ENHANCED RADIATION TOLERANCE IN SPUTTERED CU/V MULTILAYERS

A Dissertation

by

ENGANG FU

Submitted to the Office of Graduate Studies of
Texas A&M University
in partial fulfillment of the requirements for the degree of

DOCTOR OF PHILOSOPHY

August 2009

Major Subject: Materials Science and Engineering

ENHANCED RADIATION TOLERANCE IN SPUTTERED
CU/V MULTILAYERS

A Dissertation

by

ENGANG FU

Submitted to the Office of Graduate Studies of
Texas A&M University
in partial fulfillment of the requirements for the degree of

DOCTOR OF PHILOSOPHY

Approved by:

Chair of Committee,	Xinghang Zhang
Committee Members,	Karl T. Hartwig
	Lin Shao
	Haiyan Wang
Head of Department,	Tahir Cagin

August 2009

Major Subject: Materials Science and Engineering

ABSTRACT

Enhanced Radiation Tolerance in Sputtered Cu/V Multilayers. (August 2009)

Engang Fu, B.E., Dalian University of Technology;

M.E., Tsinghua University;

M.Phil. The University of Hong Kong

Chair of Advisory Committee: Dr. Xinghang Zhang

High energy particle (neutron, proton and He ions) irradiation to materials typically leads to deteriorating properties, including void swelling, blistering, embrittlement, fracture and exfoliation of surfaces. This dissertation examines size dependent radiation damage in nanostructured metallic multilayers synthesized by the magnetron sputtering technique at room temperature. It reveals the roles of interface in achieving enhanced radiation tolerance in metallic materials. The microstructure and mechanical properties of as-deposited Cu/V multilayer films are systemically investigated, providing the basis for studying radiation damage mechanisms.

Sputter-deposited Cu/V multilayers are subjected to helium (He) ion irradiation at room temperature with a peak dose of 6 displacements per atom (dpa). The average helium bubble density and lattice expansion induced by radiation decrease significantly with decreasing h, where h is individual layer thickness. The magnitude of radiation hardening decreases with decreasing h, and becomes negligible when h is 2.5 nm or less. The interactions between interfaces and radiation induced point defects and the evolution of microstructurs and mechanical behavior are discussed. This study indicates

that nearly immiscible Cu/V interfaces spaced a few nm apart can effectively reduce the concentration of radiation induced point defects.

Dose dependent radiation damage at room temperature in these Cu/V multilayers is systematically investigated with a peak dose in the range of 1-12 dpa. Peak bubble density increases with increasing dose, but it is much lower in Cu/V 2.5 nm multilayers than that in Cu/V 50 nm specimens. A similar radiation hardening trend is observed in multilayers irradiated at different fluences. Radiation hardening increases with dose and seems to reach saturation at a peak dose of 6 dpa. Negligible hardening for fine ($h \leq 2.5$ nm) multilayers is observed at all dose levels.

Thermal stability of Cu/V multilayers is revealed by in situ annealing inside a transmission electron microscope. During isothermal annealing at 600 °C grain boundary grooving occurs across layer interfaces in Cu/V 50 nm specimens, whereas Cu/V 5 nm multilayers appear rather stable. Annealing of Cu/V multilayers at 400 °C leads to hardening of multilayers, whereas softening occurs in Cu/V multilayers annealed at 600 °C. The evolution of mechanical properties during annealing is correlated to the degradation of the layer interface and the consequent reduction of interface resistance to the transmission of single dislocation.

DEDICATION

This dissertation is dedicated to:

The memory of my father, Qinghai Fu

My mother, Guirong Mu

My beloved Jing W. Fu and my daughters

My sisters and brother

ACKNOWLEDGEMENTS

I would like to thank all the people who gave me the support to complete this project. Most importantly, I would like to give my deepest and most sincere gratitude and appreciation to my doctoral advisor, Dr. Xinghang Zhang, who gave me the professional guidance, great encouragements, substantial support, and invaluable inspiration to explore my research view on the project throughout my study. Without him, the dissertation would not appear forever. His solid knowledge, strict scientific attitude, and great personality, have benefitted my whole life.

I would like to gratefully acknowledge my enthusiastic committee members: Dr. Lin Shao, Dr. Haiyan Wang, and Dr. Karl Hartwig, at Texas A&M University, who spent so much personal time helping me throughout the whole Ph.D process. They pointed out questions, offered invaluable suggestions and provided insightful feedback. Particularly, I am thankful to Dr. Lin Shao for his experimental conduct on ion irradiation and theoretical guidance on ion-solid interactions. I am thankful to Dr. Haiyan Wang for her constant support and helping in microscopy. I am thankful to Dr. Karl Hartwig for his strict scientific attitude and helping in theories and experiments.

I would like to express my sincere gratitude to Dr. Amit Misra, for his great help in offering research directions, analyzing data, and writing papers. I also want to thank Dr. Greg Swadener and Dr. Yongqiang Wang for their patience in conducting ion irradiation studies. All of them are from the Los Alamos National Laboratory.

My special thanks are given to my colleague, Dr. Jesse Carter in the Department of Nuclear Engineering at Texas A&M University, for his running accelerators and conducting ion irradiation experiments for my project with great patience. Another

colleague, Mr. Michael Martin from the same group, was invaluable in this project as well. He spent countless hours helping me on irradiation and maintaining accelerator in good condition.

I also wish to express my deep appreciation to the faculty and staff members in the Department of Mechanical Engineering at Texas A&M University for their kind assistance. Especially, I would like to thank Mrs. Jan Gerston, our program coordinator, for her patience in helping me every step for the Ph.D. Special gratitude also goes to the staff of the Microscopy Image Center (MIC) at Texas A&M University for their service in microscopy.

I am grateful to the visiting professor, Dr. J. Jang, who provided so many valuable suggestions. I wish to express my cordial appreciation to my labmates for their helps in thin film and nanolayer group at Texas A&M University, including Mr. David Foley, Mr. Steven Rois, Mr. Nan Li, Mr. Osman Anderoglu, Mr. Byoungsoo Ham, Mr. Dan Bufford, Ms. Nishitha Jetta, and Mr. Zhenxing Bi. I enjoyed a wonderful time with all of them.

I am forever indebted to my parents for their understanding, endless patience and encouragement, which fulfills my life. I would like to thank my beloved wife Jing, who always stands with me, takes great care of our family and helps me concentrate on the research. I am also grateful to my family in China for their constant support.

Lastly, I am pleased to acknowledge the financial support provided by the Advanced Fuel Cycle Initiative (AFCI) program, under grant number DE-FC07-05ID14657, funded by the Nuclear Energy Research Initiative (NERI), Office of Nuclear Energy at U.S. Department of Energy (DOE).

TABLE OF CONTENTS

Page

ABSTRACT iii

DEDICATION v

ACKNOWLEDGEMENTS vi

TABLE OF CONTENTS viii

LIST OF FIGURES x

LIST OF TABLES xviii

CHAPTER

I INTRODUCTION 1

1.1 Applications of metallic multilayers 1
1.2 Microstructure of metallic multilayers 3
1.3 Mechanical properties of metallic multilayers 10
1.4 Thermal stability of metallic multilayers 25
1.5 Radiation damage mechanisms 28
1.6 Radiation effects in metals 52
1.7 Radiation hardening 70
1.8 Difference between He, proton and neutron radiation 77
1.9 Motivation and objective 79

II EXPERIMENTAL 82

2.1 Fabrication of metallic Cu/V multilayer films 82
2.2 Ion accelerator for ion irradiation studies 88
2.3 Characterizations of metallic Cu/V multilayer films 89

III PROPERTIES OF CU/V AND AL/NB MULTILAYERS 106

3.1 Introduction 106
3.2 Experimental 107
3.3 Results 107
3.4 Discussions 111
3.5 Conclusions 116

IV INTERFACE ENABLED DEFECTS REDUCTION IN HELIUM ION IRRADIATED CU/V MULTILAYERS 117

CHAPTER Page

4.1 Introduction.. 117
4.2 Experimental.. 119
4.3 Results.. 120
4.4 Discussions.. 135
4.5 Conclusions.. 146

V DOSE DEPENDENCE OF RADIATION DAMAGE IN HELIUM ION IRRADIATED CU/V MULTILAYERS.. 147

5.1 Introduction.. 147
5.2 Experimental.. 147
5.3 Results.. 148
5.4 Discussions.. 163
5.5 Conclusions.. 178

VI THERMAL STABILITY OF CU/V MULTILAYERS.. 179

6.1 Introduction.. 179
6.2 Experimental.. 179
6.3 Results and discussions.. 180
6.4 Conclusions.. 193

VII SUMMARY AND CONCLUSIONS.. 195

BIBLIOGRAPHY.. 198

VITA.. 211

LIST OF FIGURES

FIGURE Page

1.1. Crystal structure of the tetragonal $L1_0$ ordered structure……………………….....4

1.2. Cross-sectional TEM (XTEM) images and SAD patterns of sputtered Cu/Cr multilayers with individual layer thickness of (a) 50 nm and (b) 2.5 nm……..……………...8

1.3. The plots of nanoindentation hardness as a function of $h^{-0.5}$ for Cu-based multilayer systems. The rule-of-mixture (ROM) hardnesses of single layer films for each of the three multilayer systems are indicated by horizontal dashed lines, respectively…………………………………………….12

1.4. The deformation mechanism map for Cu-based multilayers with misfit of ~ 2.5 % predicting correlation of *h* and *d* and regions with different numbers of dislocation………………………………………………...........…..14

1.5. A strengthening mechanism based on the dislocation pile-up model between layers at micrometer length scale. The strength of metallic multilayer films at length scale of sub-micro to micron is proportional to $h^{-0.5}$, where h is individual layer thickness………………………………........16

1.6. Dislocation bowing based on single dislocation model between layers at length scale of a few tenths of nanometers. The strength of metallic multilayer films is proportional to $\ln h / h$, where h is individual layer thickness...……………………………………...19

1.7. (a) The Kohler stress model based on single dislocation between layers with shear modulus mismatch at length scale of a few nanometers. The strength of metallic multilayer films is independent of h and proportional to μb^2, where μ is shear modulus and b is Burgers vector. (b) A coherency stress model due to lattice mismatch at the length scale of a few nanometers. The strength of metallic multilayer films equals to $\mu \varepsilon_{misfit}$, where μ is shear modulus and ε_{misfit} is lattice misfit between adjacent layers…………………………………………………...……….........23

1.8. Schematic diagram of classical grain-boundary grooving-driven instabilities in polycrystalline multilayers for case (a) columnar grain boundaries are laterally offset along the interface, and case (b) columnar grain boundaries are coincident............…………………………………....……27

FIGURE Page

1.9. Observations of (a) voids and (b) dislocation loops from TEM images in the irradiated stainless steel....29

1.10. A schematic of process: $d\Omega/(4\pi) = area/(4\pi R^2) = 2\pi R^2 \sin\theta_c d\theta_c / 4\pi^2$; therefore $d\Omega = area/R^2 = 2\pi \sin\theta_c d\theta_c$....32

1.11. Reduced nuclear stopping cross-sections calculated from Thomas-Fermi potential. Thick solid line indicates Lindhard's numerical result, and dashed line stands for numerical integrated solutions....37

1.12. The calculated ZBL cross section, together with other cross sections based on other four classical atom screening functions....39

1.13. Quasi-molecule formed during the collision of the moving ion and a target atom. It is divided into two regions by the Firsov plane....41

1.14. Schematic of a highly damaged volume of material, formed when the mean free path between collisions approaches the atomic spacing of the target atoms....48

1.15. Observation of stacking fault tetrahedra (SFT) from TEM micrographs of Cu, Ni and Pd irradiated at room temperature....53

1.16. TEM images of He bubbles in 12Cr-1MoVW-2Ni steel irradiated in HFIR at 600 °C to ~ 40 dpa at (a) low magnification and (b) high magnification indicating the bubbles on martensite lath boundaries, precipitate boundaries, and in the matrix....53

1.17. Photo of radiation induced swelling in 316 stainless steel rods before and after irradiation at 533 °C to a fluence of 1.5×10^{23} n/m^2 in the EBR-11 reactor....54

1.18. The shear stress-strain of Cu irradiated to different doses by proton at ambient temperature....55

1.19. Micrographs of TEM for (a) defect clusters in gold irradiated to 1.1×10^{22} n/m^2 at 200 °C and (b) stacking fault tetrahedra in silver irradiated to 4.4×10^{21} n/m^2 at 400 °C....56

1.20. Schematic of formation of dislocation loops for (a) interstitial type and (b) vacancy type....58

FIGURE Page

1.21. Temperature dependence of the void-growth rate in stainless steel under fast-neutron irradiation........65

1.22. TEM Micrograph of fuel element cladding irradiated at 510 °C to a neutron dose of 4.7×10^{22} n/cm^2........66

1.23. The strong dependence of temperature on the void swelling observed in annealed 12X18H10T flow restrictor........68

1.24. Swelling in Ni as a function of irradiation temperature for a fluence of 5×10^{19} n/cm^2........68

1.25. Dose dependent void swelling in 20 % CW 316 SS irradiated at ~ 375 °C........69

1.26. Effect of irradiation on the stress-strain behavior for (a) an austenitic (fcc) stainless steel and (b) a ferritic (bcc) steel........71

1.27. Revised version of Brinkman's displacement spike as drawn by Seeger accounting for crystallinity in the damage cascade........78

1.28. Difference in damage morphology, displacement efficiency and average recoil energy for 1 MeV different types of particles incident on Ni........79

2.1. Principle of DC magnetron sputtering........85

2.2. Magnetron (diode) cathode geometries (planar, conical, cylindrical, hollow)........85

2.3. Front view of the custom-designed DC magnetron sputter system at Los Alamos National Laboratory. There are 3 sputter guns in this system. The deposition process is fully automated through computer control. (The 3rd gun is at the back side, not visible from the front view)........87

2.4. Schematic of a circular planar magnetic cathode for (a) side view and (b) top view........87

2.5. Schematics of typical ion irradiation system components........89

2.6. The schematic outline of a TEM........93

2.7. The schematic of TEM sample preparation by ion-milling........95

FIGURE Page

2.8. Diffraction according to Bragg's law....96

2.9. Schematic representation of the cross sectional indentation....99

2.10. Schematic diagram of a loading-unloading curve during indentation, where $h_{\max}$ is maximum displacement, h_f is final depth and h_i is the intercept displacement....102

2.11. Photos of the Dektak^3 ST step profilometer....105

3.1. X-ray diffraction patterns of Cu/V multilayers. Two distinct peaks, corresponding to Cu (111) and V (110), are observed in Cu 50 nm/V 50 nm multilayers. The two peaks tend to overlap at smaller layer thickness, Cu/V 10 nm multilayers, and eventually only a single peak is observed in Cu/V 2.5 nm multilayers....108

3.2. (a) Cross-sectional TEM micrograph of as-deposited Cu/V 2.5 nm multilayer films, and (b) as-deposited Cu/V 100 nm multilayer films. Insets are selected area diffraction patterns....109

3.3. (a) Cross-sectional TEM micrograph of as-deposited Al/Nb 5 nm multilayer films. The inset is SAD pattern, and (b) Cross-sectional view of high resolution TEM (HRTEM) micrograph of as-deposited Al/Nb 5 nm multilayer films....110

3.4. Comparison of hardness vs. $h^{-0.5}$ plots for various fcc/bcc metallic multilayer systems, including Cu/Cr, Cu/Nb, Cu/V and Cu/Nb, where h is the thickness of each layer....111

3.5. The peak hardness as a function of the average biaxial modulus of the various fcc/bcc metallic multilayers. Average biaxial modulus for fcc/bcc multilayer is the average value of the biaxial moudulus between the fcc [111] and bcc [110]....115

4.1. The depth profile of helium concentration obtained from SRIM simulation of Cu/V 50 nm multilayers subjected to He ion irradiation at 50 keV with a total fluence of 6×10^{20} ions / m^2....121

FIGURE Page

4.2. XTEM images of as-deposited (a) Cu/V 50 nm, and (b) Cu/V 2.5 nm multilayers, and ion irradiated (c) Cu/V 50 nm and (d) Cu/V 2.5 nm nanolaminates. In (c) and (d), peak damage regions as indicated by two square boxes are magnified in (e) and (f), respectively....................................123

4.3. (a) A STEM image of He ion-irradiated Cu/V 50 nm multilayers with a total fluence of 6×10^{20} ions / m^2. Layer interfaces retain after radiations. (b) Semi-quantitative EDX chemical analysis along a 550 nm long line from the film surface as shown in 3a, normal to the layer interface across all three regions: the surface, peak damage and no damage region. Radiation induces insignificant change in the modulated composition profiles..125

4.4. STEM images of ion-irradiated Cu/V 2.5 nm multilayers in (a) a no damage region (~ 1100 to 1200 nm from surface), (b) a peak damage region (200-325 nm), and (c) EDX chemical analysis of the same specimen along the interface normal direction across three regions: the close-to-surface, peak damage and no damage region......................................126

4.5. (a). Comparison of He bubble density distribution along film normal direction underneath the surface in ion-irradiated Cu/V 2.5 nm and Cu/V 50 nm multilayers. Peak He bubble density is reduced by a factor of around 3 in Cu/V 2.5 nm, compared to that in Cu/V 50 nm specimen; (b). Comparison of minimum He concentration at which He bubbles are detectable in the plot of He concentration vs. irradiation depth of Cu/V 5 nm and Cu/V 50 nm simulated by SRIM program using 50 keV He^+ with a total fluence of 6×10^{20} ions / m^2; (c). Void swelling vs. $1/h$ in ion irradiated Cu/V multilayers, where h is individual layer thickness. The rule-of-mixture (ROM) void swelling in irradiated Cu and V single layer films is also shown by the horizontal dashed line...129

4.6. XRD patterns of as-deposited and ion-irradiated Cu/V 50 nm and Cu/V 2.5 nm multilayers. After radiation peak intensity decreased and peak position shifted to lower angles..132

4.7. The depth dependent evolution of lattice expansion of Cu/V 50 nm and 2.5 nm multilayer films calculated from a series of SAD studies starting from the film surface..132

FIGURE Page

4.8. (a) Comparison of hardnesses of as-deposited and ion-irradiated Cu/V multilayers as a function of h^{-1}. ROM hardness values of as-deposited and ion-irradiated films are also shown by horizontal dashed line, respectively. Hardnesses increase with decreasing h in both cases and approach peak values at h of 1 nm - 2.5 nm; (b) Hardness variation ($\Delta H = H_{ion-irradiated} - H_{as-deposited}$) of Cu/V multilayer after He ion irradiation as a function of h^{-1}. Radiation hardening in Cu and V single layer films is indicated by two horizontal dashed lines. Radiation hardening of multilayers increases with increasing h and approaches that of single layer Cu and V, and is negligible at h of 2.5 nm or less....................134

4.9. Measurement of average bubble size in ion-irradiated (a) Cu/V 50 nm and (b) Cu/V 2.5 nm multilayers through a series of defocused XTEM studies. The measured bubble sizes depend on the underfocus conditions. The real average bubble size determined from the intercepts of linear fit with y-axis (in focus condition), is ~ 0.7 nm in Cu/V 50 nm multilayers, and ~ 0.6 nm in Cu/V 2.5 nm multilayers...137

5.1. Depth profile of helium concentration from SRIM simulation in Cu/V 50 nm multilayers subjected to He ion irradiation at 50 keV with a total fluence of 6×10^{19} / m^2, 6×10^{20} / m^2 and 1.2×10^{21} / m^2, respectively...........149

5.2. STEM image of Cu/V 50 nm with He ion irradiation at a total fluence of 1.2×10^{21} / m^2...150

5.3. XTEM images of He ion irradiated Cu/V 50 nm upon peak dose of (a) 0.6 dpa, (b) 6 dpa, and (c) 12 dpa...152

5.4. XTEM images of He ion irradiated Cu/V 2.5 nm upon peak dose of (a) 0.6 dpa, (b) 6 dpa, and (c) 12 dpa...153

5.5. Peak damage XTEM images of ion irradiated Cu/V 50 nm multilayer films subjected to peak dose of (a) 0.6 dpa, (b) 6 dpa, and (c) 12 dpa..155

5.6. Figure 5.6. Peak XTEM damage images of ion irradiated Cu/V 2.5 nm multilayer films subjected to upon peak dose of (a) 0.6 dpa, (b) 6 dpa, and (c) 12 dpa...156

FIGURE Page

5.7. Comparison of Helium bubble density in the peak damage region distribution in irradiated Cu/V multilayers. Peak He bubble density is reduced by a factor of 3 in Cu/V 2.5 nm, in comparison to that in Cu/V 50 nm specimen....158

5.8. (a) and (b), XRD patterns of as-deposited and irradiated Cu/V multilayers with individual layer thickness of 50 nm and 2.5 nm; and (c) Lattice expansion ratio from XRD pattern as a function of peak dosage for ion irradiated Cu/V multilayers with individual layer thickness of 50 nm and 2.5 nm....160

5.9. (a) Comparison of radiation hardening vs. h at different radiation levels and (b) Comparison of radiation hardening vs. different radiation fluence levels....162

5.10. The comparison of the electronic and nuclear stopping powers of He ions in the Cu/V multilayer based on SRIM simulation....166

5.11. The plot of $dpa(x)$ for He ion irradiated Cu/V 50 nm upon a total fluence of $1.2 \times 10^{21} / m^2$....168

5.12. (a) and (b) show the depth dependent He concentration profiles of Cu/V 50 nm and Cu/V 5 nm multilayers predicted by SRIM simulation, respectively....170

6.1. XRD diffraction patterns of as-deposited and annealed samples at 400 °C and 600 °C for (a) Cu/V 50 nm, and (b) Cu/V 2.5 nm....182

6.2. XTEM micrographs of as-deposited (a) Cu/V 50 nm, and (b) Cu/V 5 nm....183

6.3. XTEM micrographs of annealed multilayer films at 400 °C for (a) Cu/V 50 nm, and (b) Cu/V 5 nm....185

6.4. XTEM micrographs of annealed Cu/V 50 nm multilayers at 600 °C for (a) 0 min, (b) 15 min, (c) 30 min, (d) 45 min, (e) 60 min and (f) SAD pattern after 1 hour annealing....188

6.5. XTEM micrographs of in-situ annealed Cu/V 5 nm multilayers at 600 °C for 1 hour....190

FIGURE Page

6.6. STEM image of in-situ annealed Cu/V 5 nm multilayers at 600 °C for 1 hour..191

6.7. Comparison of hardness of as-deposited and annealed Cu/V multilayers vs. h, where h is the individual layer thickness..192

LIST OF TABLES

TABLE Page

1.1. Summary of epitaxial growth of Fe-based and Co-based multilayers..................7

2.1. Correction factor for different indenter geometries..101

3.1. Calculated and experimental H-P slope of nanoscale metallic multilayers.......113

3.2. A comparison of peak hardness of several multilayers......…………..............114

CHAPTER I

INTRODUCTION

1.1 Applications of metallic multilayers

Mechanical properties of metallic multilayers have been the subject of intense studies since the first attempt to design a strong solid via using alternate layers of materials with high and low elastic constants by Koehler in 1970 [1]. Besides mechanical properties, many multilayer systems have novel and unique magnetic, thermal, optical and chemical properties. Tailoring the microstructure and interface at atomic length scale has been proven vital to achieve these properties. A popular technique to synthesize the metallic multilayer films is physical vapor deposition, which allows us to choose combinations of almost any materials. One of the most prominent characteristics of multilayer systems is their ultra high ratio of interfacial area to volume. For instance, multilayer film with an individual layer thickness of 2 nm has an interfacial area density (number of interface per unit distance along the direction normal to layer interface) of $5\times10^{8}/m$. Such a high interfacial area density plays a critical role in determining the novel properties of multilayers.

Extensive studies have shown that metallic multilayers have unique mechanical properties. Numerous multilayer systems with individual layer thickness, h, of a few nm, typically exhibit ultra high strength, approaching the 1/2 to 1/3 of the theoretical strength. The theoretical strength of metallic materials is estimated as ~ $\mu/30$, where μ is the shear modulus [2]. Such high strength can lead to improved wear resistance, making metallic multilayers promising candidates of wear resistant coatings.

This dissertation follows the style of *Journal of Nuclear Materials*.

Metallic multilayers also exhibit unusual magnetic properties, such as giant magnetoresistance (GMR). In data storage device industry, a primary goal is to store increasing amount of information while decreasing the dimensions of storage device. Since the discovery of the GMR effect, scientists and engineers keep on making impressive progress in increasing the data storage capacity. These research efforts also lead to a new exciting research area, named "spintronics" where metallic multilayers play a critical role in the electron spin dependent transport properties. The magnetizations could be altered in metallic mutilayers, a reason why metallic multilayers with very fine scale became the proving ground for the GMR effect. Since 2003 the GMR effect had become the most practical application of magnetic metallic multilayers [3]. Additionally, new classes of thin film materials, suitable for magnetic random access memory (MRAM) based devices and magnetic sensors, have been set up thanks to the discovery of GMR effect and oscillatory behavior of exchange coupling in multilayers made of transition metals.

Besides their applications enabled by unique mechanical or magnetic properties, metallic multilayers have enjoyed a number of other applications, such as x-ray optics and microelectro-mechanical systems (MEMS) [4-6]. Recently, the application of multilayer concept in designing structural materials in nuclear reactors was proposed. Studies of enhancement of radiation tolerance in nanoscale metallic multilayers are the subject of the current dissertation. The microstructure and mechanical properties of irradiated metals and alloys typically exhibit significant changes. One focus of the dissertation is to evaluate evolutions of microstructure and mechanical properties induced by radiation. Section 1.2 will review the studies of microstructure of multilayers, and

section 1.3 will summarize current understandings of their mechanical properties and strengthening mechanisms.

1.2 Microstructure of metallic multilayers

1.2.1 Single crystal multilayers

Certain applications of metallic multilayers, in data storage device for instance, necessitate the fabrication of single crystal multilayers. To promote the formation of single crystal structure, a variety of single crystal substrates have been used, including MgO, NaCl, Al_2O_3, etc. Many single crystal or highly textured magnetic materials exhibit uniaxial magnetic anisotropy along the c-axis. One of the most effective parameters for determining the magnetic properties of a medium is the preferred orientation. The bulk materials with tetragonal $L1_0$ phase, such as near equiatomic ordered alloys of CoPt and FePt, in nature are known for their high magnetocrystalline anisotropy and magnetic moment, properties desirable for high density magnetic recording media [7-9]. A typical crystal structure of the tetragonal $L1_0$ ordered structure, which consists of alternate stacking of different elements, is shown in Figure 1.1 [10]. This type of $L1_0$ ordered structure, generally produced by heat treatment of samples below the order-disorder transformation temperature, exhibits novel magnetic properties including enhanced magnetoresistance, long-range exchange coupling and large perpendicular magnetic anisotropy [11]. For metallic multilayer films, the potential applications in magneto-optical recording media require that their layer structures have $L1_0$ ordered structure. The magnetic properties of polycrystalline films depend mainly on the distribution of the c-axis of the crystals. It is difficult to study the orientation dependence of the magnetic properties of each grain in polycrystalline metals. However, by making use of epitaxy

technique, there is a possibility of preparing artificial single crystal with crystallographically different stacking such as $L1_0$ ordered phase. Atomic layer deposition techniques using molecular beam epitaxy (MBE), appropriate to control well-defined layered structures at atomic scale, have made it possible to fabricate epitaxial thin films with metastable ordered $L1_0$ phase. The advantage of MBE is this technique can easily fabricate single crystals of the ordered alloy with high degrees of structural and chemical order compared to bulk sample preparation technique accompanied by complicated heat treatment procedures.

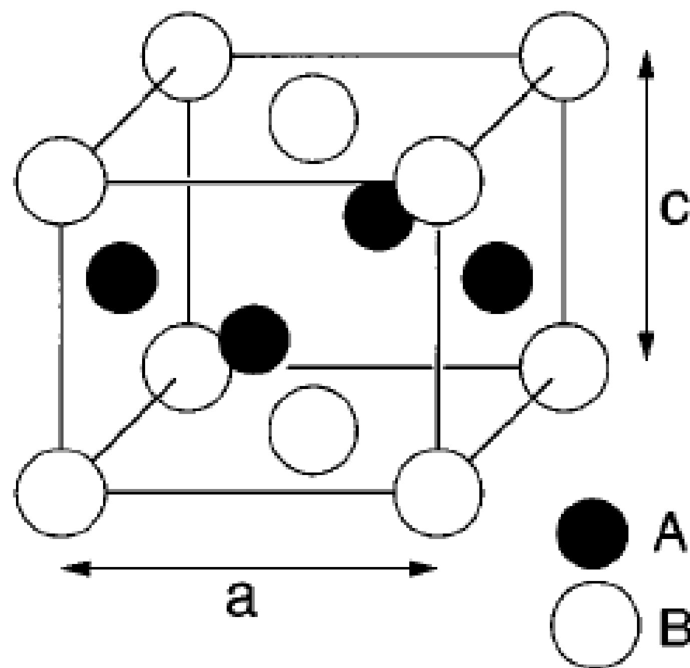

Figure 1.1. Crystal structure of the tetragonal $L1_0$ ordered structure [10].

Among the large numbers of metallic multilayer systems studied, two metallic multilayer systems with $L1_0$ structure stand out with regard to their significance. They are Co-based system, such as Co/Pt, and Fe-based system, like Fe/Pt, Fe/Pd and Fe/Au multilayers, and they exhibit very high magnetocrystalline anisotropy [12,13]. Since several groups firstly reported the good epitaxial growth of Fe/Au (100) multilayers [14-16], numerous studies have focused on the fabrication of $L1_0$ ordered single crystal type thin films [17-20]. Fe/Au ordered alloys having a phase separation and disorder consistent with their equilibrium phase diagram, and Fe/Pt having a natural $L1_0$ ordered structure around equiatomic composition according to the equilibrium phase diagram [21] were first artificially fabricated by employing alternate deposition of epitaxial monatomic stacking of bcc Fe (001) and fcc Au (001) or fcc Pt (001) layers on MgO (100) substrates under an ultra high vacuum in Mitani's group [22]. Both epitaxial films with $L1_0$ structure exhibited large uniaxial anisotropy, considerable magneto-potical Kerr rotation and perpendicular magnetization. Furthermore, M. Ohtake reported the successful preparation of Fe/Au epitaxial multilayers with $L1_0$ structure grown on the single crystal MgO (001) and MgO (011) substrates, respectively [23-25].

Co-based multilayer films including Co/Cr, Co/Cu and Co/Fe have also been widely studied for their magnetic properties, such as perpendicular magnetic anisotropy and GMR effect. In order to investigate the intrinsic magnetic properties, efforts have been made to grow well-defined single crystal magnetic films of Co and Co-alloy on various single crystal substrates to achieve desired magnetic properties [26-30]. Studies on Co-alloy/Cr bilayer films deposited on single crystal substrate of NaCl (100), Co-alloy films deposited on single crystal substrates of Cr (100) and Cr (110), and Co/Cr bilayers

grown epitaxially on MgO (100) and (110) substrates have been reported [31-33]. The mechanism of magnetization reversal in MBE-epitaxial growth of Co/Fe multilayers on MgO (001) substrates, the epitaxial growth and structures of Co/Fe magnetic multilayer films on $SiTiO_3$ (111) substrates, and epitaxial growth and texture of Co/Pr, Co/Sm and Co/Pt multilayer system have been systematically studied [34-40]. Co magnetic bilayer films with different stacking structures of fcc/hcp and hcp/fcc were successfully prepared on Al_2O_3 (0001) substrates employing Au and Cu as underlayers, and their structures and the magnetic properties were investigated by Ohtake et al. [41]. Other groups have prepared epitaxial Co thin films by employing other underlayers such as Ag, Ti, and Ru [26, 42, 44]. All these single crystal type Co-based and Fe-based multilayers with high quality epitaxial structure exhibit desired magnetic properties and are being considered to be possible candidates in the applications of perpendicular magnetic recording media and patterned media for high-density magnetic recording. Table 1.1 summarized the epitaxial growth of Fe-based and Co-based multilayer with different substrates, buffer layers and synthesis techniques.

Table 1.1. Summary of epitaxial growth of Fe-based and Co-based multilayers.

System	Substrate	Buffer layer	Deposition technique
Fe (100) /Au (100) Fe [001] /Au [001]	GaAs (100)	470 Å Au	MBE [44, 45]
Fe (110) / Au (111) Fe [001] /Au [110]	Al_2O_3 (111)	Au (111)	Alternate UHV evaporation [45]
Fe (001) / Au(001) Fe [110] /Au [100]	MgO (001)	50 Å Au	MBE [10, 24, 25]
Fe (100) / Au (or Pt) (100) Fe [100] / Au (or Pt) [110]	MgO (001)	Au (Pt)	UHV deposition with two independent e-guns [46]
Fe (001) / Pt (001) Fe [110] / Pt [100]	MgO (001)	500 Å Ag	E-beam evaporation in UHV [47]
Fe (001) / Pt (001)	MgO (001)	400Å Pt	DC magnetron sputtering [20]
Fe (112) / Au (011) Fe [110] /Au [100]	MgO (011)	50 Å Au	MBE [23]
Co 0001 /Ag (Cu, Au) 111 Co [110] /Ag [110]	Al_2O_3 (0001)	50 Å Ag	MBE [30]
Co (1120) / Cr (100) Co [0001] / Cr [011]	MgO (100)		E-beam evaporation [33, 48]
Co (1100) /Cr (211) Co [0001] / Cr [011]	MgO (110)		3 source E-beam [33, 48]
Co (001) /Cu (001) Co [001] / Cu [001]	MgO (001) or LiF (001)		MBE [49]

1.2.2 Polycrystalline multilayers

In general a majority of metallic multilayers have polycrystalline nature and yet exhibit ultra high mechanical strength. Unlike the single crystal metallic multilayers grown by epitaxy, the polycrystalline metallic multilayers can be synthesized at room temperature by sputtering technique. Typical sputtering deposition rates of metals are in the range of a few tenth of a nm/s to a few nm/s. Low deposition rate is applied to control the individual layer thickness precisely down to a few nm. Cross-sectional transmission electron microscopy (XTEM), together with selected area diffraction (SAD) techniques,

provides a conventional method to observe the microstructure of metallic multilayers. The microstructures of immiscible Cu/Nb, Cu/Cr, Cu/V, Cu/SS 304 (SS stands for stainless steel), Cu/SS 316, Cu/Ag and miscible Cu/Ni and Al/Nb have been extensively studied by several groups. Sputter-deposited metallic multilayers typically exhibit polycrystalline grains with chemically sharp and distinct interfaces between adjacent layers. XTEM images and SAD patterns of immiscible Cu/Cr multilayer with h of 50 nm and 2.5 nm deposited on Si substrates are shown in Figure 1.2 [50]. Both Cu/Cr multilayer films have polycrystalline columnar grains. When the h is greater (50 nm), the columnar grain size is on the order of the layer thickness, whereas its size is much greater than h in the Cu/Cr 2.5 nm multilayers. Furthermore, Cu/Cr 2.5 nm multilayer has stronger Cu {111} and Cr {110} fiber texture than that of Cu/Cr 50 nm specimens. This system has fcc/bcc type of immiscible interface. In other immiscible systems, such as Cu/Ag multilayers, polycrystalline nature and textures of Cu {111} and Ag {111} are observed, and this system has fcc/fcc type interface [51].

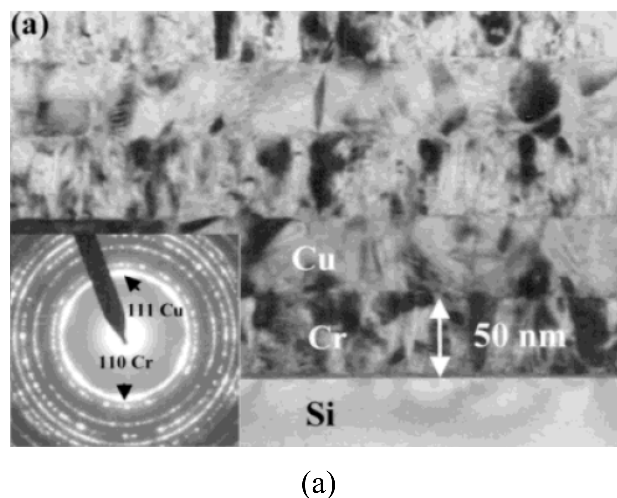

(a)

Figure 1.2. Cross-sectional TEM (XTEM) images and SAD patterns of sputtered Cu/Cr multilayers with individual layer thickness of (a) 50 nm and (b) 2.5 nm [50].

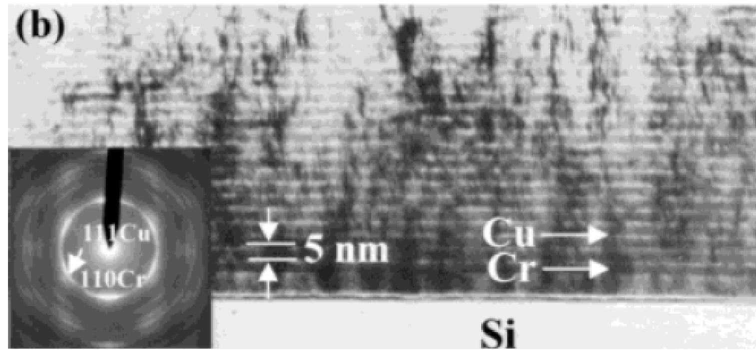

(b)

Figure 1.2 Continued.

Most of metallic multilayers with different crystal structures of metals, such as fcc/fcc, or fcc/bcc have different orientation relations along interfaces. The crystallographic orientation between layers of fcc/fcc systems could be either cube-on-cube, i.e. fcc {100}/fcc {100}, or with close-packed configurations in both components, i.e. fcc {111}/fcc {111}. In fcc structure, a close-packed {111} plane has the lowest surface energy and is typically the preferred growth direction. Hence the fcc {111} / fcc {111} multilayers are more stable than other fcc/fcc type of configurations if coherency stress in epitaxial system is not considered. On the other hand, in fcc/bcc system, the fcc {111} and bcc {110} orientation planes are preferred due to similar reasons. Two types of orientation relationships have been observed experimentally in fcc/bcc systems [52, 53]. One is so-called Kurdjumov-Sachs (K-S) orientation relationship, i.e. fcc {111} // bcc {110} and fcc <110> // bcc <111> [54]. Another type of orientation relationship is the Nishiyama-Wassermann (N-W) relation, i.e. fcc {111} // bcc {110}, fcc <110> // bcc < 001> [55, 56]. Geometrical analyses of the moiré pattern induced by overlap of two lattice planes at the interfaces [52] and the calculations of the interfacial energy of the fcc {111}/bcc {110} interfaces have been studied by several researchers to interpret the

preferred orientation relationship of two adjacent crystals [57-59]. Gotoh et al. calculated the interfacial energy of the fcc {111} / bcc {110} by assuming a sinusoidal function as an interaction potential at the interface. The results showed that K-S orientation relationship will appear in the region of the atomic diameter ratio (d_{bcc} / d_{fcc}) of (0.88, 0.96). On the other hand, the N-W orientation relationship will occur when d_{bcc} / d_{fcc} is in the range of (0.83, 0.88) and (1.02, 1.19) [60, 61]. Kobayashi and Sarma used an interaction potential with a two-fold symmetry based on the bcc {110} plane at the fcc {111} / bcc {110} to calculate the interfacial energy between them [62]. Both results are in good agreement with the experimental observations. The orientation relationships at interfaces in multilayer systems are typically examined by SAD experiments. For instance, orientation relationships of Cu {111} // Ag {111} in polycrystalline Cu/Ag multilayers and Ag {111} // Ni {111} in polycrystalline Ag/Ni multilayers have been confirmed by XTEM and SAD studies. Both systems have fcc/fcc type of interfaces [51, 63]. Furthermore, in fcc/bcc multilayer systems, the K-S orientation relationship has been observed in Cu/Nb and Cu/Cr systems [64, 65]. The driving force to form the orientation relationships between the interfaces in the metallic multilayer system lies in pursuit of minimal system energy.

1.3 Mechanical properties of metallic multilayers

1.3.1 High strength of multilayers

The mechanical properties of metallic multilayer films attract great interest because these multilayers with ultra high mechanical strength are not only promising for technological applications but also significant in providing an ideal vehicle for understanding the influence of the length scale on the fundamental deformation

mechanisms [66]. Metallic multilayer film made of alternate layers with high and low elastic constants was first proposed by Koehler in 1970 with an attempt to construct high strength material by trapping dislocations in the soft layers due to a repulsive image force [1]. After Koehler's attempt, there have been numerous experimental and theoretical studies on the mechanical properties of the metallic multilayer systems. A couple of groups reported the yield and fracture strengths of the multilayer films are on the order of GPa when the layer thickness is very small [6, 67-69]. The enhancement in the yield strength of multilayer films compared to the rule-of mixture (ROM) yield strength of single layer films for each component has been observed in the numerous metallic multilayer systems. The observed yield strength of metallic multilayers can approach 1/3 - 1/2 of the theoretical strength of the materials [70-71]. A number of models to interpret hardening mechanisms at different length scales have been proposed and developed. These include the Hall-Petch model based on the piled-ups of dislocations between layer interfaces [72-74], and 'Orowan' model based on single dislocation loop bowing within the layers [2, 75, 76].

Typical plots of the indentation hardness of Cu-based multilayer films as a function of $h^{-0.5}$, where h is the individual layer thickness, are shown in Figure 1.3 [50]. In general yield strength (estimated from one-third of hardness) increases with decreasing h, reaches a maximum or plateau at h of a few nm length scale. When h is greater than 50 nm, the indentation hardness of multilayer films is proportional to $h^{-0.5}$, following the Hall-Petch relation based on the dislocation pile-up model. The Hall-Petch type of strengthening mechanism deviates from experimental values when h is reduced to less

than 50 nm. Rather, the hardness is proportional to $\ln h / h$ at length scale of tens of nanometers. When h is reduced to a few nanometers, the peak hardness is achieved.

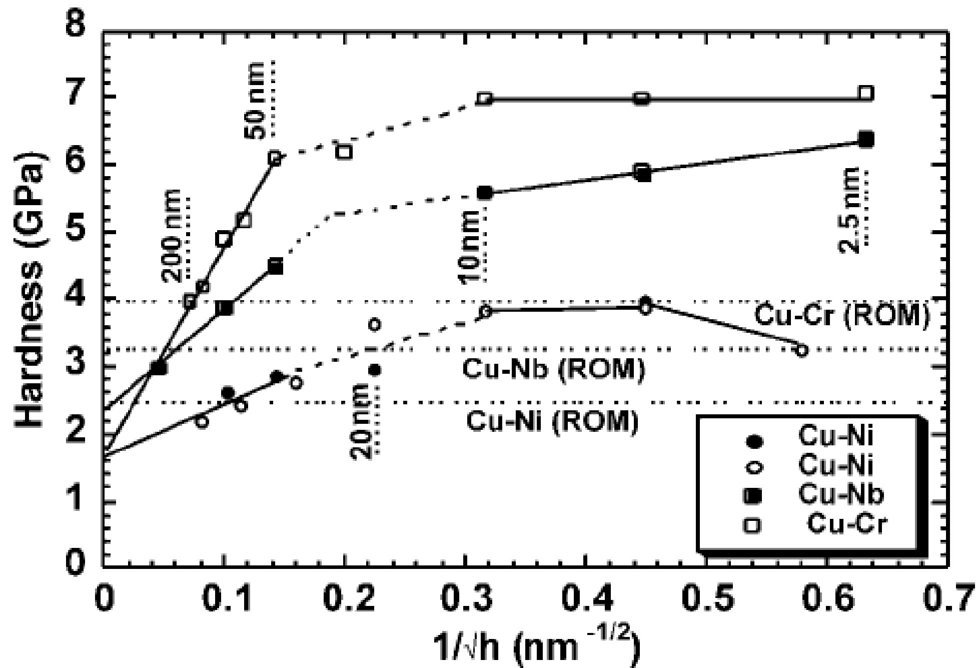

Figure 1.3. The plots of nanoindentation hardness as a function of $h^{-0.5}$ for Cu-based multilayer systems. The rule-of-mixture (ROM) hardnesses of single layer films for each of the three multilayer systems are indicated by horizontal dashed lines, respectively [50].

1.3.2 Deformation mechanisms

In polycrystalline metallic multilayer systems, two microstructural length scales of the in-plane grain size (d) and the individual layer thickness (h) are the major factors to determine the dependence of yield strength on the microstructure. Generally, the smaller one will play a dominant role at a given number (n) of dislocations. The correlation of d and h in polycrystalline metallic mutilayers has been developed by A. Misra et al. by taking dislocation-based model into account. By equating the back stresses

of the two dislocation arrays (one is interface edge array at the center of the grain, the other one is screw dislocation pile-up), the correlation of d and h can be given by the equation:

$$d = \frac{8n\lambda}{3\pi \coth(\pi h/(2\lambda))} \tag{1}$$

where λ is the spacing of the interface dislocations at the interfaces. If λ is known, the plot of d as a function of h for different dislocation numbers (n) can be given by the equation. Furthermore, for the case of $d >> h$ or $h >> d$, by considering a pile-up of edge dislocations at the interfaces and assuming $n = 1$, both critical h_t and d_t, below which pile-up is invalid, can be achieved by the equation:

$$h_t \text{ or } d_t = \frac{bn}{(1+\nu)\varepsilon_m} \tag{2}$$

where ν is Poisson's ratio and ε_m is strain. The region with pile-up and the region without pile-up are defined by the lines of h_t and d_t. In the region without pile-up, single-dislocation strengthening mechanisms including Orowan model, Koehler stress, and coherency stress will dominate the yield strength. As an example, the deformation mechanism map based on the ideas above for Cu-based multilayers with misfit of ~ 2.5 % to predict correlation of d and h and region related to deformation mechanisms and numbers of dislocations is shown in Figure 1.4. When h or d is small enough, the single dislocation model will dominate the strengthening mechanisms. At the smallest values for both h and d, non-dislocation deformation mechanisms will be applicable due to too few spaces to accommodate one dislocation. The details of the explanation can be found elsewhere [77].

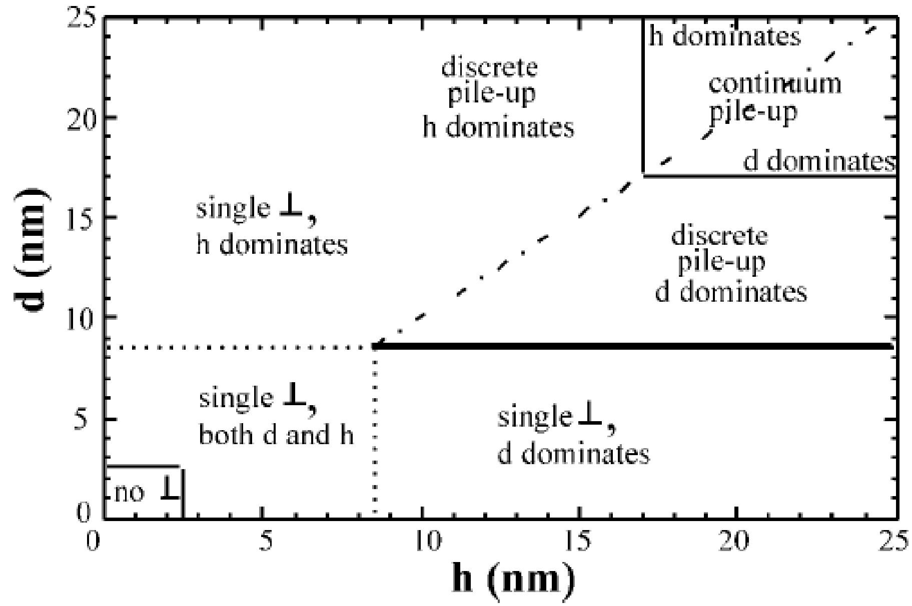

Figure 1.4. The deformation mechanism map for Cu-based multilayers with misfit of ~ 2.5 % predicting correlation of *h* and *d* and regions with different numbers of dislocation [77].

1.3.3 Strengthening mechanisms at full length scales

1.3.3.1 Continuum dislocation pile-up based strengthening mechanisms

Typical indentation hardness plots of metallic multilayer systems indicate when h is greater than 50 nm the indentation hardness of multilayer films is proportional to $h^{-1/2}$. This pronounced size effect is consistent with the classical Hall-Petch relation [78, 79], which predicts the yield strength of a polycrystalline material by

$$\sigma_{ys} = \sigma_0 + kd^{-1/2} \qquad (3),$$

where σ_{ys} is the yield strength (estimated as indentation hardness divided by a factor of 3), σ_0 is a measure of the lattice friction stress to slip, k is a material dependent constant often referred to the Hall-Petch slope and d is the average grain diameter. Although the Hall-Petch relation can be interpreted by several models, dislocation pile-up theory is the

earliest and the most prominent explanation and physical mechanism of the Hall-Petch relation. In this theory, the dislocation emitted from the source is stopped by the grain boundary (obstacle) after it propagates to the grain boundary by gliding on the slip plane. The trailing dislocations cease moving and pile up behind it because of mutual repulsion [80]. When the stress concentration of the pile-up dislocation eventually exceeds the obstacle strength, the polycrystalline materials plastically yield. The pile-up of dislocation against interlayer interfaces has been observed in the multilayer system [81]. Therefore, the most applicable model is the continuum dislocation pile-up model for multilayer systems, where h is big enough and treated similarly as grain size, according to the observation and their deformation mechanism maps. Figure 1.5 shows the dislocation pile-up strengthening mechanism between layers at micrometer length scale. The transmit slip will not cross the interfaces until the stresses due to the pile-up of dislocation plus the applied stress is greater than the barrier strength. The increasing number of dislocations increases the stresses at the tip of the dislocation pile-up. In the limit of continuum dislocations, the stress has a proportional relation with the square root of the pile-up length and its maximum can reach the theoretical yield strength levels, enough to nucleate a crack or slip in the structures. As h is reduced, the number of dislocations in the pile-ups decreases due to a smaller space between the layers for accommodating the dislocations, and thus the length of pile-up is also reduced. Consequently, stresses at the tip of pile-up are lower, making it difficult to transfer slips across interfaces, and larger applied stresses must be offered to overcome the barrier strength and accomplish the transfer.

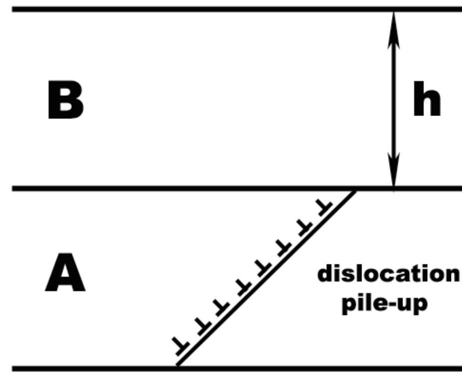

Figure 1.5. A strengthening mechanism based on the dislocation pile-up model between layers at micrometer length scale. The strength of metallic multilayer films at length scale of sub-micro to micron is proportional to $h^{-0.5}$, where h is individual layer thickness.

1.3.3.2 Strengthening mechanisms based on discrete dislocation pile-up model

The evidence from the plot of hardness vs. $h^{-0.5}$ as shown in Figure 1.3, however, shows the Hall-Petch relation deviates when h is reduced to an intermediate range, tens of nm. This indicates the continuum dislocation pile-up model does not work properly at such a length scale. The region of dislocation pile-up may transfer from continuum to discrete where few dislocations reside due to small spaces for accommodating dislocations between interfaces. Previous studies indicated the deviation from the Hall-Petch linear relationship occurred when the number of dislocations (n) in the pile-up is less than 3 for a circular pile-up ($n \leq 3$ for a double-ended pile-up and $n \leq 6$ for a single-ended pile-up). A modified Hall-Petch relation is applied at discrete pile-up region to predict the yield strength of metallic multilayer films shown below:

$$\sigma_{ys} = \sigma_0 + kh^{-a}, \ (a \neq 0.5) \tag{4}$$

where a is exponent parameter of the modified Hall-Petch model.

In several metallic multilayer systems, the values of a ranging from 0.2 to 0.6 have been adopted to fit the experimental data of yield strength by using the modified Hall-Petch relation [4]. Another estimation of exponent value of 0.35 for modified Hall-Petch in multilayer system based on the discrete pile-up model was performed by P.M. Anderson and C. Li [72]. Due to the inhomogeneous elastic properties in multilayer system, the scaling exponent a ($\neq 0.5$) in modified Hall-Petch model depends on a couple of dimensionless parameters [80]. L.H. Friedman developed a model to predict the appropriate scaling exponent for Hall-Petch behavior in the metallic multilayers by taking into account the dimensionless parameters, including the ratio of the shear moduli, the Poisson ratios, the angle of the pile-up to the interface normal, and the character of the dislocations comprising the pileup as given by the angle between the dislocation line direction and Burgers vector [80, 82]. The results by comparing with a numerical discrete dislocation simulation and with the experimental data indicate although the model solutions are expected to be worse with decreasing length scale, they are better than applying the classical Hall-Petch ($a = 0.5$) relation and give reasonable agreement with reported measurement for a couple of multilayers at intermediate length scale.

1.3.3.3 Single dislocation based strengthening mechanisms

At the length scale of a few nanometers, the continuum and discrete dislocation pile-ups models cannot operate. The region will be dominated by single dislocation and the strengthening mechanisms based on single-dislocation have been developed accordingly. Eventually at the smallest length scale, the bowing stress of a dislocation, confined by closely spaced layer interface, approaches the theoretical shear strength.

The strengthening mechanisms in the single dislocation region include the Orowan bowing model at length scale of tens of nanometers and Young's modulus mismatch model (Kohler stress) and/or lattice mismatch model (coherency stress that is only applicable in fcc/fcc or bcc/bcc multilayer systems) at a few nanometers. Other factors affecting the peak yield strength include step creation on crossing of interface by dislocations, cutting of misfit dislocations at the interfaces [83], a super-modulus effect [84] and solid solution strengthening mechanisms [85]. Overall, the total yield strength of the multilayer system is a combination of the initial stress to yield in the softer layer and the stresses that force the dislocation to penetrate the interface from the softer to harder layers. Note that the peak hardnesses in all these multilayer systems are much higher than the hardness derived from the simple rule-of-mixture (ROM) principle for the corresponding metallic multilayer systems. The ROM hardness is achieved by averaging the hardness values of single layer films for each component. Numerous multilayer systems including fcc/fcc (e.g. Cu/Ag, Ni/Au) [86, 87], fcc/bcc (e.g. Cr/Ag, Fe/Pt) [4], bcc/bcc (e.g. Fe/Cr) [4] and fcc/hcp (e.g. Al/Ti) [88] showed the similar length scale dependent hardening behaviors.

There are numerous analytical approaches to predict the yield strength of metallic multilayers. The work by Li and Anderson by studying the effects of coherency strains and interfacial misfit dislocations (dislocation sources) indicated macro-yield strength is governed by an internal source length for sufficiently small individual layer thickness [89]. Kerlavarma and Benzerga used a two-dimensional (2D) discrete dislocation plasticity framework, which incorporated some three-dimensional mechanisms through constitutive additions, to analyze the response to uniaxial tension of nanoscale

multilayers [90]. Confined layer slip mechanisms involving glide of single Orowan-type loops bounded by two interfaces were first proposed in plastic yielding of thin films on substrates by Freund and Nix [91, 76] and later developed by A. Misra et al. [2, 92, 93]. The Orowan model shown in Figure 1.6 takes into account of a single dislocation loop propagating within one layer [2, 75, 76]. A dislocation can be bowed into a semicircle within a layer of the softer phase in Orowan model, which deviates from the linear elastic behavior [2]. The shear stress in Orowan model is approximately proportional to $\ln h/h$. In the plot of mechanical behavior, the hardness of multilayer is approximately proportional to $\ln h/h$ at length scale of tens of nanometers, which is consistent with Orowan bowing model. In this model, a dislocation is emitted at the interfaces. After it glides across the layer with lower shear modulus, it will be blocked by next interface. The dislocation needs bow parallel to the interfaces on its slip plane within each layer to slip cross the interface. The stress to bow the dislocation in the softer phase is required and its value is predicted by the Orowan model.

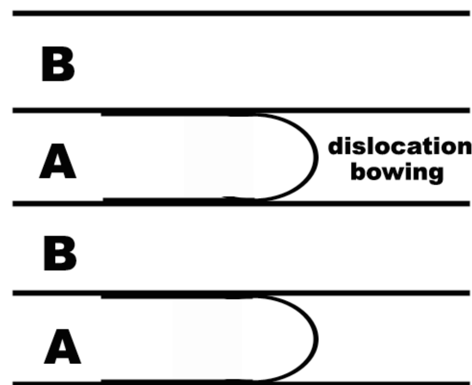

Figure 1.6. Dislocation bowing based on single dislocation model between layers at length scale of a few tenths of nanometers. The strength of metallic multilayer films is proportional to $\ln h/h$, where h is individual layer thickness [2, 75, 76].

Based on the Orowan model, a numerical analysis method of confined layer slip mechanisms to calculate the yield strength of multilayers at length scale of a few tens of nanometer to a nanometer within the region of single-dislocation ($n=1$) in the deformation mechanism maps was proposed [76, 91] and developed later by A. Misra et al. [64]. In the normal confined layer slip (CLS) model, by considering the self-energy of the dislocation segment with 60 ° deposited at the interface, the applied shear stress (τ_{cls}) required to propagate a glide dislocation with Burgers vector (b) confined to one layer can be predicted by the equation:

$$\tau_{cls} = \frac{\mu b}{8\pi h}\left(\frac{4-\nu}{1-\nu}\right)\left(\ln\frac{\alpha h}{b}\right) \tag{5}$$

where μ is shear modulus, h is the layer thickness measured parallel to the glide plane, α represents the core cutoff parameter and is often equal to 1 for compact core. The CLS model successfully predicted the trend of increasing yield strength with decreasing h. However, the prediction has a discrepancy with experiments that the strengthening rate is much faster with decreasing h than those observed experimentally [92]. In order to eliminate the discrepancy, the refinement of the CLS model was developed by taking three factors into considerations [64]. Firstly, the atomistic simulation already showed the absorption of the glide dislocation by the interface and significant spreading of the dislocation core along the Cu/Nb interface by shearing the interface after the stress field of a dislocation gliding to the interface was exerted on the interface [94]. The applied shear stress predicted in the CLS model can be reduced by the core spreading [95], so the CLS model must be refined by reducing the core cutoff parameter, α. Secondly, the elastic deformation along the interfacial region results in an interface stress (f), which can be expressed by the gradient of the interfacial energy to strain, and assist the applied

stress in the indentation hardness test of multilayer system. Its contribution to the applied stress can be given by $-f/h$, where a negative sign indicates it has the same direction with applied stress, h carries the same meaning as described before. The interface stress becomes very significant when h is on the order of a few nanometers. Thirdly, the interactions between dislocations [96, 97] instead of an isolated dislocation are considered to refine the CLS model. This consideration results in the saturation stress ($\mu b/\lambda(1-\nu)$), which is applied to estimate the resistive force from the glide array of dislocations. By considering all these three factors, the refined CLS model can be expressed as follows:

$$\tau_{cls} = \frac{\mu b}{8\pi h'}\left(\frac{4-\nu}{1-\nu}\right)\left(\ln\frac{\alpha h'}{b}\right) - \frac{f}{h} + \frac{\mu b}{\lambda(1-\nu)} \tag{6}$$

where the first term is the same as normal CLS model, $-f/h$ is the interface stress and $\mu b/\lambda(1-\nu)$ is saturation stress from the interactions between dislocations. Note the core spreading was considered by taking $\alpha < 1$. The refined CLS model was applied to a typical example of Cu/Nb multilayers and the calculated results indicated a good agreement with the experimental results until at a very small length scale of $h = 2$ nm. However, the refined CLS may not be operative when h is less than the core cut-off dimension. Alternately, other strengthening mechanisms like interface crossing will be applicable at this length scale.

When h is a few nanometers, the hardness of multilayer systems either gradually increases with decreasing h (e.g. Cu/Nb), or be independent of h (e.g. Cu/Cr), or even decreases (softening) with decreasing h (e.g. Cu/Ni) [65]. The strengthening mechanism at this length scale is dominated by the interface cutting by single dislocation. The peak

strength of the multilayer is determined by the stress required to transmit a single dislocation across the interface. Such resistance in general can be determined by Young's modulus mismatch (the Kohler stress) or lattice mismatch (a coherency stress) as shown in figure 1.7a and 1.7b. The Kohler stress model originates from the large difference in the shear modulus between layers. In system with a large modulus mismatch (typically by a factor of 2), the isotropic elasticity theory indicates a repulsive image stress exists when a dislocation in softer layer is going to cross layer interface and enter into the component with higher elastic modulus. Resolved shear stresses will be required to overcome the repulsive images stress to drive dislocations across the interfaces. This model is applicable in the multilayers with very small h where a Frank Read source can not operate inside one layer, and predicts the yield strength is independent of h. Coherency stresses that alternate from compression to tension between layers are significant in multilayers with coherent interface. They will decrease dramatically if the coherency decays due to either large misfit strain or h values of greater than the critical thickness for coherency. The applied stresses must overcome the periodic resistance of coherency stresses to drive the glide of dislocations across layer interfaces.

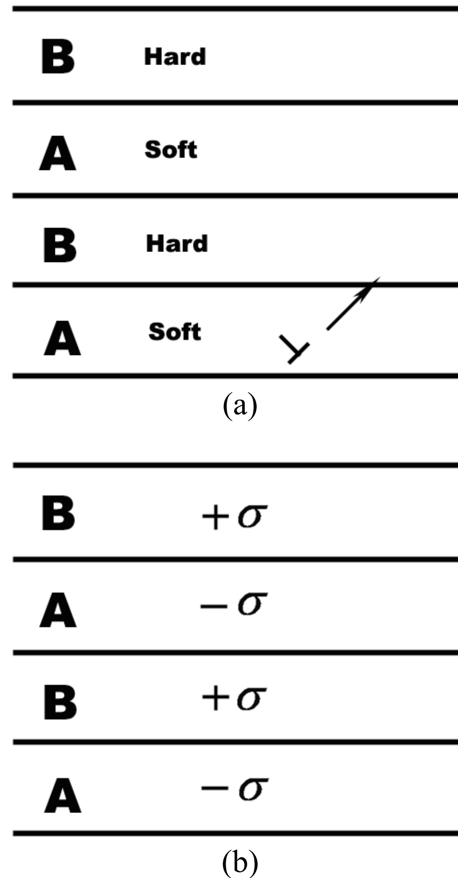

Figure 1.7 (a). The Kohler stress model based on single dislocations between layers with shear modulus mismatch at length scale of a few nanometers. The strength of metallic multilayer films is independent of h and proportional to μb^2, where μ is shear modulus. and b is Burgers vector; (b). A coherency stress model due to lattice mismatch at the length scale of a few nanometers. The strength of metallic multilayer films equals to $\mu\varepsilon_{misfit}$, where μ is shear modulus and ε_{misfit} is lattice misfit between adjacent layers [50].

At this length scale, the interface barrier strength depending on the interfacial structures will dominate, and the models involving atomic simulation of dislocation transmission across interfaces can evaluate the upper bound of the interface barrier strength. The different interfacial structures in the polycrystalline metallic multilayers were firstly taken into considerations to predict the peak strength by Hoagland et al [94]. As mentioned previously, fcc/fcc or bcc/bcc metallic multilayer systems have cube-on-

cube orientation relationship between interfaces, whereas the K-S orientation relationship is observed in the fcc/bcc multilayer systems. They distinguish interfaces with the cube-on-cube relation as transparent interfaces and with K-S orientation relationship as opaque interfaces [94].

In the fcc/fcc metallic multilayer system with transparent interfaces, the slip directions and slide planes for dislocations are almost continuous across the interfaces. The resistance is determined by several factors including the coherency stress, and cutting of misfit on the interface. For comparison, fcc/fcc multilayers of Cu/Ag with large misfit strain of 0.12 % and Cu/Ni with small misfit strain of 2.5 % were studied [98, 99]. In Cu/Ni system, the coherency stress is significant approaching 2.4 GPa, very close to the in-plane applied normal stress of 2.6 GPa required to force the lead partial to cross a coherent interface in an infinite bilayer Cu/Ni model. These studies indicate that the coherency stress plays perhaps the most critical role in determining the peak strength in multilayers with coherent interface. In Cu/Ag system, the misfit strain is too large to achieve coherency, and hence misfit dislocations form along interfaces. A high misfit strain also leads to the overlap of dislocation cores. Due to the insignificant coherency stress, the peak hardness in Cu/Ag multilayers is lower than that in Cu/Ni multilayers.

Unlike the transparent interfaces, opaque interfaces with discontinuity of slip plane and slip direction exist in the fcc/bcc metallic multilayers such as Cu/Nb. The resistance to the slip of dislocations across the interfaces is different from that in transparent interfaces due to significant variation of slip direction and slip plane. The EAM potential of Cu/Nb multilayers to examine the behavior of slip through opaque interfaces of unstressed Cu/Nb models has been applied by Hoagland et al [94]. The lead

partial of a dissociated glide dislocation, which is already contained in the Cu layer, is attracted to the interfaces, but the trailing partial is at some distance away. The trailing partial can enter the interface if a low stress is applied. However, the slip of dislocations across the interfaces and emerging into Nb layers requires very large strains, which has to be induced by a very large applied stress. A new dislocation need to be nucleated as well due to remaining of Burgers vector in Cu layers. Furthermore, the interface begins to slide in a stick-slip manner at a very low shear stress due to the low shear strength of the interface in the Cu/Nb multilayers. This weak interface provides a strong barrier to slip as the sliding of the interface initiates the core spreading of the dislocations, which loses the singularity of the dislocation enabling the dislocation to move easily through lattices.

1.4 Thermal stability of metallic multilayers

The advanced engineering applications of nanoscale metallic multilayers require they have to have high thermal stability at elevated temperature. Excellent thermal stability at elevated temperature in immiscible single crystal W/NbN multilayers has been observed [100], where W and NbN are neither miscible nor forming of intermetallic compounds. Theoretical study of the elastic stress-driven instability mechanisms has been performed in single crystal multilayers as well [101]. In polycrystalline metallic multilayers experiencing high temperature, the phenomena of layer pinch-off induced by grooves developed at columnar grain boundaries have been observed [102-104]. Figure 1.8 shows the classical mechanisms of thermal grooves at the triple-point junctions (an intersection of a grain boundary and interphase interface). Two cases of intersections are included in the model. In case 1 as shown in Figure 1.8a, grooving occurs in both layers where columnar grain boundaries are laterally offset [103]. On the other hand, case 2 in

Figure 1.8b with coincident grain boundaries in both layers indicates grooving preferentially occurs in the layer with higher grain boundary energy [105]. In both cases, the extent of groove expressed by the groove half-angle (θ is in the Figure 1.8) is determined by the ratio of the grain-boundary energy γ_{gb} to interface free energy $\gamma_{interface}$ by the equation:

$$\cos\theta = \frac{\gamma_{gb}}{2\gamma_{interface}} \tag{7}$$

Smaller θ of grooves indicates deeper grooves, which facilities the layer pinch-off. Accordingly lower ratio of the grain-boundary energy to interface free energy will lead to larger θ, which will prevent layer pinch-off by stabilizing the layered structure. Therefore enlarging half angle of grooves by selecting system with low ratios of γ_{gb} to $\gamma_{interface}$ will be one approach to develop multilayer with shallow groove and high thermal stability [103, 106, 107]. However, for the same metallic multilayer system, the in-plane grain size (d) and individual layer thickness (h) also play a critical role to determine the extent of groove during development at elevated temperature. The influences of ratio of d to h at a given metallic multilayer system on the development of thermal grooving and layer pinch-off have been studied [103, 106, 107]. Larger d/h means larger diffusion distance between two consecutive grooves on the same layer. So the grooves can keep on growing with the same half-angle without interruption. When the ratio is below a critical value, the development of grooves will be limited [108]. The study from Lewis, et al. on the annealed Cu/Nb multilayer system with ratio of d/h much larger than the critical values showed thermal grooving and also indicated higher thermal grooving in Nb than in the Cu layers due to higher ratio of γ_{gb} to $\gamma_{interface}$ in Nb [109]. On

the other hand, the study of thermal stability of Cu/Nb multilayers with h of a few tens of nanometers (lower ratio of d/h compared to Lewis' study) has been performed by A. Misra et al. [110]. In their study, the unstable quadruple points were formed by aligned grain boundaries due to the fast in-plane boundary migration and nanoscale initiated in-plane grain size. Then the quadruple points break into two triple points. The diffusive mass transport at both of triple points will occur to build up the equilibrium groove angles and finally lead to the extremely stable configuration where the layers are effectively sheared across the vertical plane formed by the overlap of sideways migrating grain boundaries. This shear of layers across the grooving triple points and an anchored structure are resistant to further instability [110].

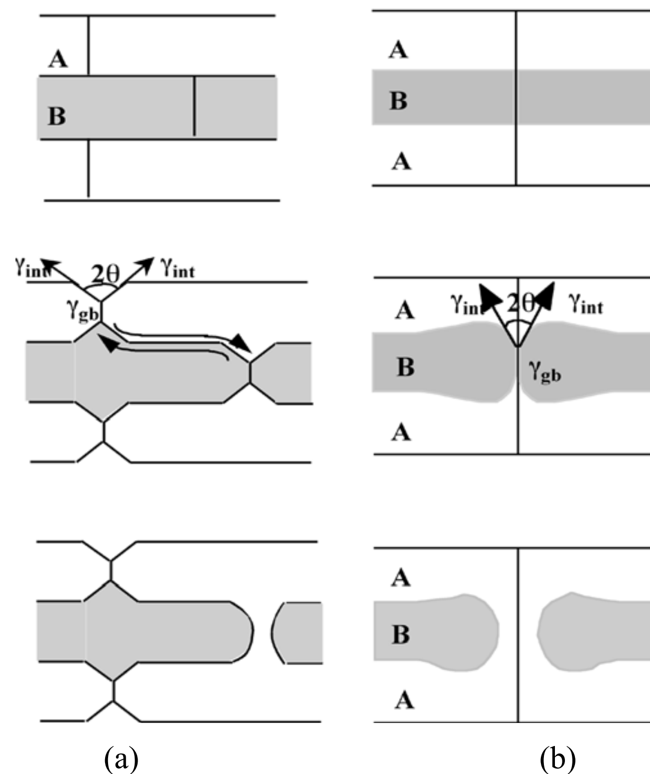

Figure 1.8. Schematic diagram of classical grain-boundary grooving-driven instabilities in polycrystalline multilayers for case (a) columnar grain boundaries are laterally offset along the interface, and case (b) columnar grain boundaries are coincident [110].

1.5 Radiation damage mechanisms

1.5.1 Introduction of ion-solid interactions

The collision of energetic ions, atoms, or molecules with condensed matter is called ion-solid interaction. The microstructure and properties of materials including mechanical, optical, electrical, and magnetic properties are sensitive to the introduction of atoms by bombardments of the solid with energetic ions. The studies on the modifications of materials by the presence of the foreign atoms have been stimulated by their potential and practical applications in the semiconductor, tribological, corrosion and optical fields. On the other hand, the violent collisions between the implanted ions and solid substrate atoms displace the lattice atoms called primary knock-on atoms (PKAs) from their lattice sites. Consequently radiation leads to atomic displacement damages, such as vacancies and interstitials, in a highly disordered region around the path of the ions [111-116]. Almost immediately following a cascade, a significant fraction of the opposite type of point defects (interstitials and vacancies) starts to recombine. However, a small fraction of the damage cascade will be left behind without recovering. This residual damage accumulates in various ways to form different extended defects such as vacancy clusters, voids and dislocation loops as shown in Figure 1.9 [117]. In certain cases, significant radiation of neutron could lead to the collapse of the ordered lattice, and the structure is transformed into an amorphous phase [116]. Radiation induced defects can significantly degrade the mechanical properties of structural materials, in form of embrittlement or loss of ductility typically accompanied by voiding swelling and radiation hardening. Several important parameters frequently used in the ion-solid interactions are discussed as follows.

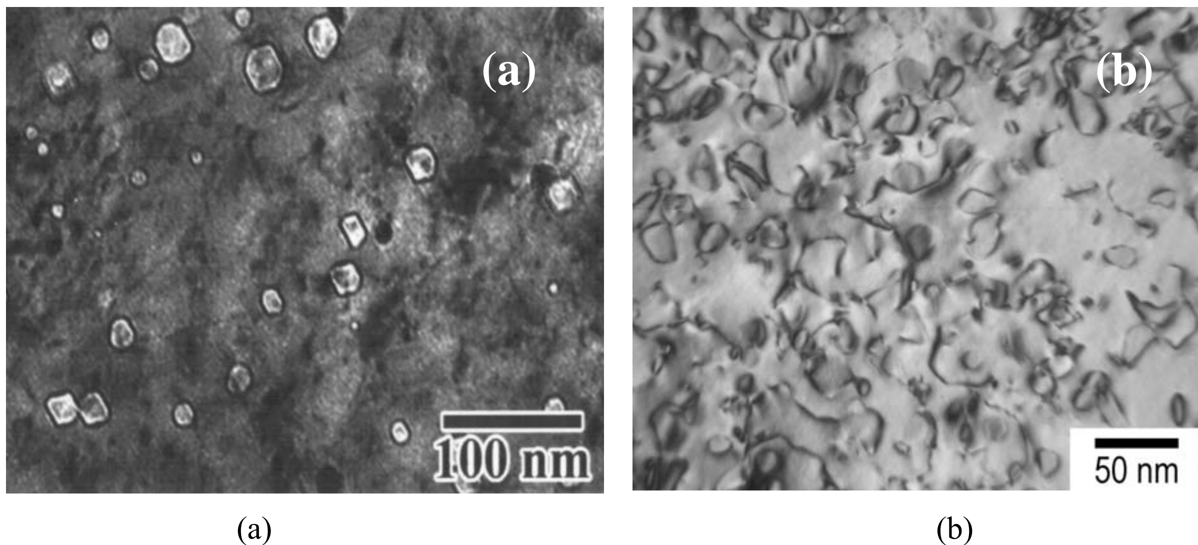

(a) (b)

Figure 1.9. Observations of (a) voids and (b) dislocation loops from TEM images in the irradiated stainless steel [117].

Ion dose is described by the number of ions per centimeter square penetrating into the solid substrate. But usually, the nomenclature of fluence is applied instead of the dose. The *flux* or *dose rate* is usually defined as the numbers of ions per centimeter square per second. The density of ion beam current is given in the unit of amperes per centimeter square. As the energetic ion comes to rest, its actual integrated distance traveled during the whole irradiation process is called *range*, whereas net penetration into solid substrate, examined along the vector of the ion's incident trajectory, is called the *projected range*. The distribution in projected ranges is defined as the range distribution or range straggling. Numerous work has been conducted to predict the range distribution. A series of collisions with the atoms and electrons lead to the loss of the energy of the energetic ions, and therefore the energetic ions slow down and eventually come to rest. The energy-loss rate (dE/dx) is depending on the incident energy, ion mass and solid substrate mass. Two different mechanisms are used to distinguish the mechanisms of

energy loss due to the collisions between energetic ions and particles in the solid substrate materials. In nuclear collisions, the energy of energetic particles is partly transmitted as translatory motion to solid substrate atoms as a whole due to collisions with nucleus. In electronic collisions, the valence electrons are excited or ejected by the energetic particles due to the deposition of the energy. Nuclear collisions and electronic collisions correspond to elastic collision and inelastic collision, respectively. Large discrete energy losses and significant angular deflection of the energetic ions are induced by nuclear collisions due to the much greater mass of nucleus compared to electrons. Therefore, nuclear collisions are the cause of the production of lattice disorder or radiation damage by displacing atoms from their equilibrium positions. Because of negligible mass of electrons with respect to ions, much smaller energy losses per collision, and negligible deflection of the ion trajectory and lattice disorder or radiation damage are the results of the electronic collisions with energetic particles [116]. Subsequent passages will describe all of these considerations or definitions in detail.

1.5.2 Ion stopping mechanisms

1.5.2.1 Scattering cross section

The definition of a cross section in nuclear and particle physics is given to express the likelihood of interaction between particles. Therefore the probability of occurrence of a particular nuclear reaction or the statistical nature of scattering events can be characterized by the cross section in the unit of area (e.g. typically centimeter square) or barn (1 barn = 10^{-24} cm^2) [116]. In the ion-solid interactions to examine the probability of ion-solid scattering events, a large number of interactions require to use differential cross section to statistically answer the questions like ‘how much energy will deposit in the

lattice from an energetic ion in a collision?' and 'what the scattering angle will be?'[116]. The definition of differential cross section in scattering is the probability to observe a scattered particle in a given quantum state per solid angle unit ($d\sigma / d\Omega$) expressed by:

$$\frac{d\sigma}{d\Omega} = \frac{Scattered\ flux / Unit\ of\ solid\ angle}{Incident\ flux / Unit\ of\ surface} \tag{8}$$

where $d\sigma$ is defined as the differential scattering cross-section, and $d\Omega$ is the solid angle of the detector [118].

Energetic particle incident with the impact factor parameters between b and $b + db$ will be scattered through angles between θ_c and $\theta_c + d\theta_c$. The probability for scattering through, also differential cross section $d\sigma$ is found by taking:

$$d\sigma = \frac{scattered}{incident} = \frac{I \cdot (2\pi b \cdot db / A)}{I / A} = 2\pi b \cdot db \tag{9}$$

where I is the number of ions incident, per unit time, over an area of A with the assumption of only one target atom in the area of A [116].

The calculation process of the solid angle of the detector is presented in Figure 1.10 [116]. The magnitude of the entire area of the sphere with the radius of R is $4\pi R^2$. The shaded ring has the area of $(2\pi)(R\sin\theta_c)(Rd\theta_c) = 2\pi R \cdot R\sin\theta_c d\theta_c$ with a ring radius of $R\sin\theta_c$ and a width of $R \cdot d\theta_c$. According to the definition of solid angle, unit solid angle can be given by:

$$d\Omega = area / R^2 = 2\pi \sin\theta_c d\theta_c \tag{10}$$

So the scattered particle in a given quantum state per solid angel unit ($d\sigma / d\Omega$) can be produced by combining equation (9) and equation (10) and the result is given by:

$$\frac{d\sigma}{d\Omega} = \frac{b}{\sin\theta_c} \cdot \left| \frac{db}{d\theta_c} \right| \tag{11}$$

In order to keep the differential cross section as a positive value, the absolute value of $db/d\theta_c$ is applied. A schematic of the process to determine equation (10) is illustrated in Figure 1.10 [116].

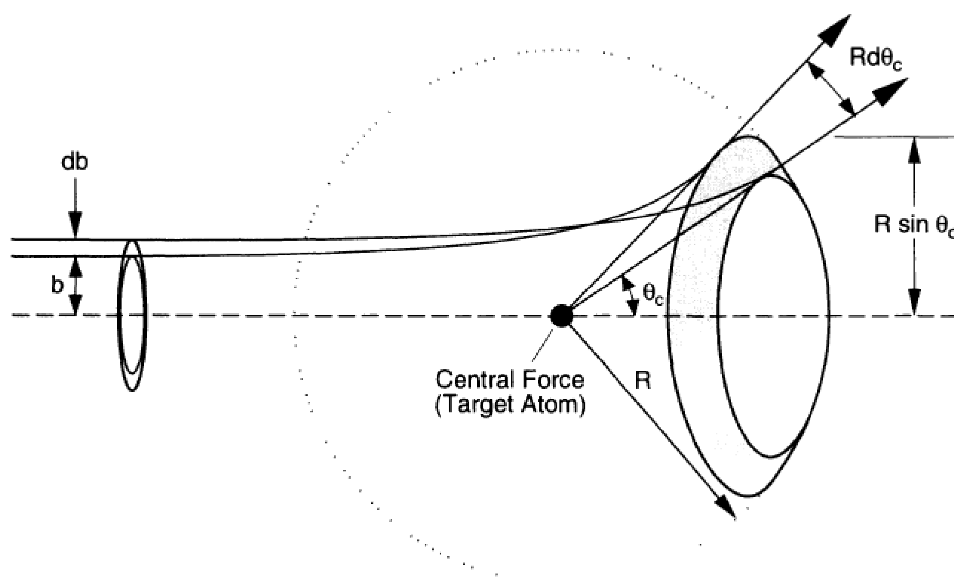

Figure 1.10. A schematic of process: $d\Omega/(4\pi) = area/(4\pi R^2) = 2\pi R^2 \sin\theta_c d\theta_c / 4\pi^2$; therefore $d\Omega = area/R^2 = 2\pi \sin\theta_c d\theta_c$ [116].

As a fundamental and important parameter to describe ion ranges and lattice disorder, differential cross section can measure the probability of scattering a projectile ion into the angle with the range from θ_c to $\theta_c + d\theta_c$ and the probability of transferring energy T in the range of T and dT to a solid target atom.

The integral cross section, often referred as cross section, is the integral of the differential cross section on the whole sphere of observation and is given by:

$$\sigma = \int \frac{d\sigma}{d\Omega} d\Omega = \int_0^{b_{\max}} d\sigma = \int_0^{b_{\max}} 2\pi b db = \pi b_{\max}{}^2 \tag{12}$$

The smaller the collision parameter, the stronger the interaction between two particles. A limitation up to $b_{\max}$ is used to define occurred scattering. The integral of differential cross section therefore can measure the effective surface area seen by the penetrating particles to have a scattering with all possible scattering angles.

The interatomic potential plays a leading role in determining the differential cross section. If the interaction between projectile particle and solid target nucleus is Coulombic only, the interactomic potential for Coulomb interaction is described by:

$$V(r) = Z_1 Z_2 e^2 / r \tag{13}$$

where Z_1 and Z_2 are the numbers of protons contained in the nucleus of projectile and target, respectively. r is the distance between the two nuclei, and e^2 =1.44 eV nm.

The differential cross section for scattering into a solid angle for the Coulombic potential is given by:

$$\frac{d\sigma(\theta_c)}{d\Omega} = \frac{b}{\sin\theta_c} \left| \frac{db}{d\theta_c} \right| = \left(\frac{Z_1 Z_2 e^2}{4E_c}\right)^2 \frac{1}{\sin^4(\theta_c/2)} \tag{14}$$

Another form of Coulomb angular differential scattering cross sections, also called the Rutherford differential cross sections, can be given by:

$$\frac{d\sigma(\theta_c)}{d\theta_c} = \frac{d\sigma(\theta_c)}{d\Omega} \frac{d\Omega}{d\theta_c} = 2\pi \left(\frac{Z_1 Z_2 e^2}{2E_c}\right)^2 \frac{\cos(\theta_c/2)}{\sin^3(\theta_c/2)} \tag{15}$$

The increase of both $d\sigma(\theta_c)/d\theta_c$ and $d\sigma(\theta_c)/d\Omega$ with decreasing θ_c indicates the Coulomb scattering process favors small-angle scattering.

The probability of an energetic ion with energy E undergoing a collision with a solid target nucleus or a scattering event is given by:

$$P(E) = N\sigma(E)dx \tag{16}$$

where N is total target atoms per unit volume, $\sigma(E)$ is the total collision cross section, and dx is the thickness where the projectile traverse.

Similarly, the probability of scattering in an energetic ion into the angular range from θ_c to $\theta_c + d\theta_c$ can be expressed by:

$$P(\theta_c) = N\sigma(\theta_c)dx \tag{17}$$

and the probability of a projectile with energy E being scattered into a solid angle traveling dx in the angular region from θ_c to $\theta_c + d\theta_c$ can be given by

$$P(E,\Omega)d\Omega = \frac{dP(E)}{d\Omega}d\Omega = \frac{d\sigma(E)}{d\Omega}N \cdot dx \cdot d\Omega \tag{18}$$

Because of $P(E,T)dT = P(E,\Omega)d\Omega,$ $d\Omega = 2\pi \sin\theta_c d\theta_c$ and the transferred energy $T = 0.5T_M(1-\cos\theta_c)$, then:

$$\frac{d\sigma(E)}{dT} = \frac{4\pi}{T_M} \cdot \frac{b}{\sin\theta_c} \left| \frac{db}{d\theta_c} \right| \tag{19}$$

where T_M is the maximum transferred energy [116].

This equation allows us to calculate the differential energy-transfer cross section at a given angular differential cross section.

The power law potential energy-transfer differential cross section can be given as follows by using the angular differential cross section and the center mass (CM) energy transfer function:

$$d\sigma(E) = 0.25\pi(2Z_1Z_2e^2)^2(M_1/M_2)\,(E_0{}^{-1}T^{-2})dT \tag{20}$$

but this function still has six major parameters. To simplicity, a universal one-parameter differential scattering cross section formula was proposed by Lindhard et al. in the reduced notation [119]:

$$d\sigma = -0.5\pi a_{TF}^2 f(t^{1'2})t^{-3'2}dt \tag{21}$$

where $f(t^{1/2}) = \lambda t^{1/2-m}[1+(2\lambda t^{1-m})^q]^{-1/q}$, a_{TF} is Thomas-Fermi screening length, and $\lambda, m, and\ q$ are fitting variables. For $f(t^{1/2})$ in Thomas-Fermi version, $\lambda = 1.309$, $m = 1/3$ and $q = 2/3$ [119, 120].

1.5.2.2 Nuclear stopping

Nuclear stopping due to nuclear elastic collisions between projectile and solid target nucleus involves large discrete energy loss and significant lattice disorder. The nuclear stopping power is the energy loss of an energetic particle undergoing the elastic collisions with solid target nucleus at per unit traveling length in the solid target. The nuclear stopping power ($\left.\frac{dE}{dx}\right|_n$) can be expressed by:

$$\left.\frac{dE}{dx}\right|_n = N\int_{T_{\min}}^{T_M} T\frac{d\sigma(E)}{dT}dT \tag{22}$$

where T_M is the maximum transfer energy and can be descried by $T_M = 4M_1M_2E/(M_1+M_2)^2$, and $T_{\min}$, the lower limit in the integration, is the minimum energy transferred. Its value is often referred to the displacement energy of the materials. The nuclear stopping cross section at a given ion energy E can be obtained by:

$$S_n(E) = \left.\frac{dE}{dx}\right|_n / N = \int_{T_{\min}}^{T_M} T\frac{d\sigma(E)}{dT}dT \tag{23}$$

Based on Thomas-Fermi atom, an equation for the calculation of stopping cross section is given by:

$$S_n(E) = \frac{C_m E^{1-2m}}{1-m}\left[\frac{4M_1M_2}{(M_1+M_2)^2}\right]^{1-m} \quad (24)$$

where m is power-law variable without unit and C_m is a power law constant. At intermediate energies, the stopping power by application of the power law approximation is energy independent and can be shown by:

$$\left.\frac{dE}{dx}\right|_n = 0.28\,(eV\ nm^2)\frac{M_1NZ_1Z_2}{(M_1+M_2)(\sqrt{Z_1}+\sqrt{Z_2})^{2/3}} \quad (25)$$

The calculation result based on the equation indicates this is reasonable approximation in the range of most of the keV energy [116].

After introduction of the reduced energy ε (proportional to ion energy) and a reduced length ρ_L [121], the reduced stopping cross section $S(\varepsilon)$ can be expressed by:

$$S(\varepsilon) = \frac{d\varepsilon}{d\rho_L}\Big|_n = \varepsilon^{-1}\int_0^{\varepsilon} f(t^{1/2})dt^{1/2} \quad (26)$$

It can be solved by the power law approximation and the power law approximation to the reduced nuclear stopping cross section is given by:

$$S_n(\varepsilon) = \lambda_m[2(1-m)]^{-1}\varepsilon^{1-2m} \quad (27)$$

The comparison of reduced nuclear stopping cross section calculated from the Thomas-Fermi potential (solid lines), and from the numerically integrated solutions indicated by dashed line is shown in Figure 1.11 [116].

Figure 1.11 indicates three energy regions. In the high-energy Rutherford regime, $S_n(E)$ decreases with ε^{-1}. In the intermediate energy regions where $m = 1/2$, $S_n(E)$ with value of 0.327 is independent of ε. In the low energy region where $m = 1/3$,

$$S_n(E) = 0.981\varepsilon^{1/3} \tag{28}$$

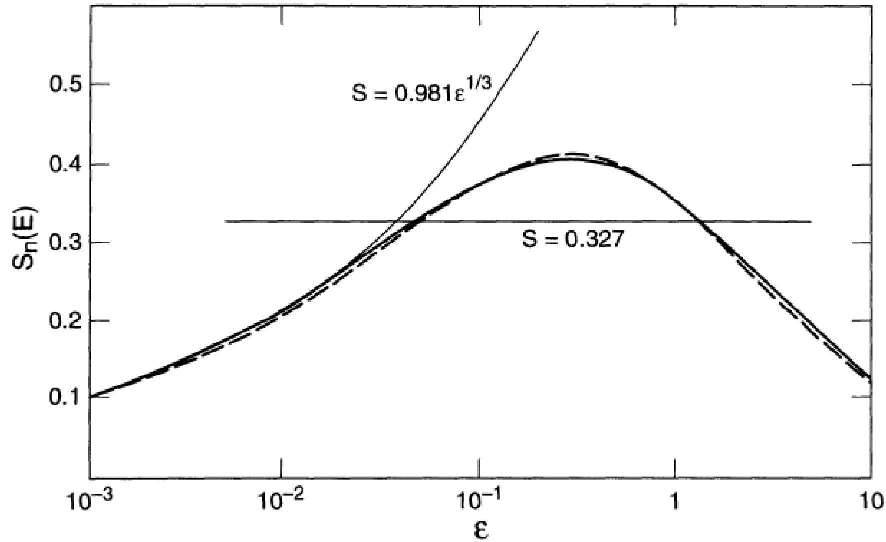

Figure 1.11. Reduced nuclear stopping cross-sections calculated from Thomas-Fermi potential. Thick solid line indicates Lindhard's numerical result, and dashed line stands for numerical integrated solutions [116].

Ziegler, Biersack, and Littmark (ZBL) universal screening function is used to provide another method to calculate stopping powers and cross sections with more accuracy and wider reduced energy. The reduced nuclear stopping cross section can be given by:

$$S_n(\varepsilon) = \varepsilon\, S_n(E)/(\pi\, a_U^{\;2}\; \gamma\; E_0) = \frac{\varepsilon}{a_U^{\;2}} \int_0^\infty \sin^2(\theta_c/2)\, d(b^2) \tag{29}$$

where a_U is the universal screening length, and $\gamma = 4M_1M_2/(M_1 + M_2)^2$ [116, 122].

Figure 1.12 shows the calculated ZBL cross section, together with other cross sections based on other four classical atom screening functions [116, 122]. After fitting to the Figure, the equation for ZBL cross section in the region of $\varepsilon < 30$ can be obtained

$$S_n(\varepsilon) = \frac{0.5 \ln(1 + 1.1383\varepsilon)}{(\varepsilon + 0.01321\,\varepsilon^{0.21226} + 0.19593\,\varepsilon^{0.5})} \tag{30}$$

and in the region of $\varepsilon > 30$

$$S_n(\varepsilon) = \ln(\varepsilon)/(2\varepsilon) \tag{31}$$

where $\varepsilon = \dfrac{32.53 M_2 E_0}{Z_1 Z_2 (M_1 + M_2)(Z_1^{0.23} + Z_2^{0.23})}$ is the ZBL reduced energy [116, 122].

If we use the relation in equation (29), for energy of E_0 ion, the ZBL universal nuclear stopping is:

$$S_n(E_0) = \frac{8.462 \times 10^{-15} Z_1 Z_2 M_1 S_n(\varepsilon)}{(M_1 + M_2)(Z_1^{0.23} + Z_2^{0.23)}} \,(eV\ cm^2\ /\,atom) \tag{32}$$

and nuclear stopping power can be calculated as follows:

$$\left.\frac{dE}{dx}\right|_n = N \cdot S_n(E_0) \tag{33}$$

where N is the atomic density [116].

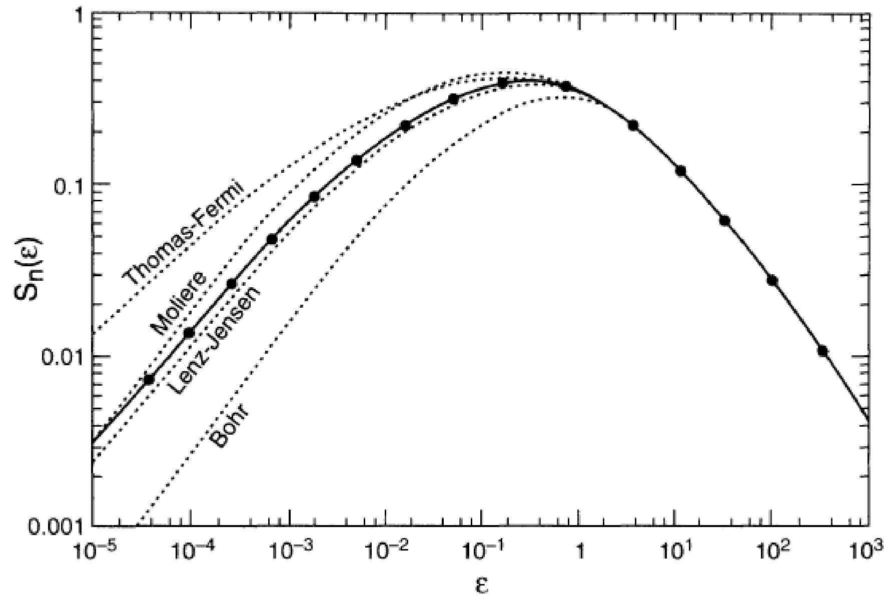

Figure 1.12. The calculated ZBL cross section, together with other cross sections based on other four classical atom screening functions [116, 122].

1.5.2.3 Electronic stopping

Another mechanism of energy loss is electronic stopping due to electronic collisions between projectile and electrons in solid target where the energy of projectile is transferred to the electrons of solid target. Because of the significant mass difference between electrons and projectiles, the electronic collisions have much lower rate of energy loss per collision, negligible deflection of the projectile direction, and insignificant displacement of atoms. In the electronic collisions, the velocities of ions determine their charge state and consequently determine the mechanisms of energy loss by electronic stooping. There are two electronic stopping regions in terms of the projectile's state of ionization or its effective charge, which is related to the ion velocities. Bohr proposed that the ion charge fraction or the effective ion charge can be expressed by:

$$\frac{Z^*}{Z} = (\frac{\upsilon_1}{\upsilon_0 Z_1^{2/3}}) \quad (34)$$

where Z is the atomic number and equals to the total number of electrons of projectile atom in ground state, Z^* is the charge of the ion, $\upsilon_0 \cong 2.2 \times 10^6\ m/s$ is the Bohr velocity of an electron in the innermost orbit of a hydrogen atom, and υ_1 is the velocity of an energetic ion [116].

For effective charge of moving ions, there are two extreme states (cases) for a projectile with charge. When an energetic ion velocity is much smaller than Bohr velocity, that is, $\upsilon < \upsilon_0 Z_1^{2/3}$, then $Z^* < Z$, which indicates that energetic ion is not fully stripped and the ion carrying its electrons tends to neutralize by capturing the electron. When an energetic ion has high velocity, i.e. $\upsilon > \upsilon_0 Z_1^{2/3}$, then $Z^* \cong Z$, which indicates the energetic ion becomes a bare nucleus. Bohr suggested that the energetic ions will lose electrons if their orbital velocities are smaller than the ion velocity. In this ion velocity regime, a sudden energy transfer occurs from the projectile to electrons in the target. The electronic stopping power will vary in different velocity regimes [116].

In the low velocity region where $\upsilon < \upsilon_0 Z_1^{2/3}$, there are three major models (Fermi-Teller, The Firsov, and Lindhard-Scharff) of electronic stopping, all of which show the stopping cross section is proportional to the energetic ion velocity.

Fermi-Teller model qualitatively exhibits the trend that electronic stopping power is proportional to the velocity of an energetic ion; however, its quantitative calculation is questionable as only valence electrons with velocities near the maximum possible velocity contribute to the energy transfer.

Firsov proposed when the energetic ion with a velocity in the region of $\upsilon < \upsilon_0 Z_1^{2/3}$ capturs the electrons in the solid target, it is slowed down by the work involved in the transfer of momentum [123]. The energetic ions have to lose a small amount of momentum to accelerate the captured electrons to reach the same velocity. He introduced that Firsov plane, which divides the quasi-molecule formed during collision where the electrons are grouped into two regions, that is, the target atom region (T-region) and the projectile region (P-region) as shown in Figure 1.13 [116,123].

Due to the momentum transfer ($m_e \upsilon$) from the projectile to the captured electron, the force on the projectile is:

$$F = m_e \upsilon \int_{S_F} 0.25\, n_e \upsilon_e dS_F \tag{35}$$

where n_e is the electron density of the solid target in the Firsov plane, υ_e is the mean electron velocity with assumption of isotropic, and S_F is Firsov plane.

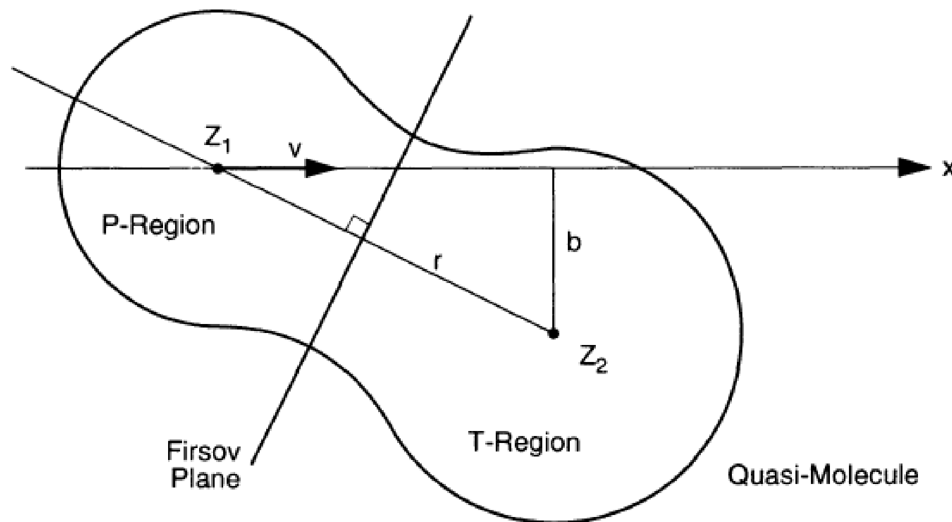

Figure 1.13. Quasi-molecule formed during the collision of the moving ion and a target atom. It is divided into two regions by the Firsov plane [116, 123].

The total losing energy of the projectile per electronic collision due to momentary transfer should be equal to the work done by the forces on the projectile at a certain distance dx. This can be expressed by:

$$T_e(b) = \int dW = \int \vec{F} \bullet d\vec{x} \tag{36}$$

and the electronic stopping power is:

$$\left.\frac{dE}{dx}\right|_e = NZ_2 \int_{b_{\min}}^{b_{\max}} 2\pi T_e(b) b db \tag{37}$$

where NZ_2 is the number of electrons per unit volume, and N is given by the atomic density in the stopping medium [116].

Substitute F into the equation, and the electron density can be calculated based on the Thomas-Fermi model of the atoms which shows the connections between the interatomic potential and the electron density. So the mean energy transferred to an atom in solid target per collision with an impact parameter is

$$T_e = \frac{0.35(Z_1 + Z_2)^{5/3} \hbar / a_0}{[1 + 0.16(Z_1 + Z_2)^{1/3} b / a_0]^5} \upsilon \tag{38}$$

So the electronic energy loss per unit distance with a cross section of $2\pi b db$ can be obtained by:

$$\left.\frac{dE}{dx}\right|_e = \int_0^\infty 2\pi T_e b db = 2\pi e^2 K_F a_0 (Z_1 + Z_2) \upsilon / \upsilon_0 = 2.34(Z_1 + Z_2) \upsilon \times 10^{-15} eV\ cm^2 / atom \tag{39}$$

where the K_F is a constant with a value of 1.08, υ_0 is Bohr velocity, and υ has an unit of $10^8\ cm/s$ [116].

Unlike the Firsov model, Lindhard and Scharff used a different interatomic potential which assumes that the twice geometrical mean of the individual Coulmb fields can represent the average interaction Coulomb field for the quasi-molecule formed by

combination of any arbitrary projectile and atom. The electronic stopping power with such an assumption is:

$$\left.\frac{dE}{dx}\right|_e = \frac{3.83 Z_1^{7/6} Z_2}{m_1^{0.5}(Z_1^{2/3} + Z_2^{2/3})^{3/2}} \tag{40}$$

The expression of Lindhard-Scharff model has wide applications [124, 125].

In the high velocity of ion region ($\upsilon > \upsilon_0 Z_1^{2/3}$), the ion is a bare nucleus and pure Coulomb interaction potential ($V(r) = Z_1 Z_2 e^2 / r$) can accurately show the interactions between projectile and electrons in the solid target.

The electron kinetic energy in this region can be obtained by:

$$T_e(b) = \Delta p_y{}^2 /(2m_e) = 2Z_1^2 e^4 /(b^2 m_e \upsilon^2) \tag{41}$$

After putting this equation into equation (37) and choosing meaningful value of $b_{\min} = Z_1 e^2 /(m_e \upsilon^2)$ and $b_{\max} = 2Z_1 e^2 (2m_e \upsilon^2 I)^{-1/2}$, the electronic stopping power with consideration of distant resonant energy transfer is:

$$\left.\frac{dE}{dx}\right|_e = \frac{4\pi Z_1^2 e^4 N Z_2}{m_e \upsilon^2} \ln \frac{2m_e \upsilon^2}{I} \tag{42}$$

where I is the average excitation energy in the unit of eV, and is roughly equal to ten times of the atomic number of the stopping atoms [116].

Although the calculations of stopping power above don't consider the shell structure of the atoms and difference of electron binding, only small derivations can be observed between the approximations and experiments [116].

1.5.3 Radiation damage mechanisms

1.5.3.1 Introduction of radiation damage

In the collisions between projectile and atoms in the solid target, the lattice atoms can be displaced from the equilibrium sites if enough energy from the projectile is transferred to them. The displaced atoms by projectile from the lattice site are defined as primary knock-on atoms (PKAs). Similarly, the energetic PKAs can induce the secondary knock-on atoms by transferring the energy, and tertiary knock-on atoms, and so on until the energy in the atoms is not enough to displace atoms. Radiation damage including point defects such as vacancies, interstitials and other types of defects in the region surrounding the ion track is the result of the displaced atoms by creating a cascade of atomic collisions. The displacement threshold energy is the minimum energy required to displace the lattice atom. The displacement energy varies for different elements, and differs in different directions for the same elements in the solid. The displacement energy in single crystal materials can be measured experimentally by monitoring electrical resistivity changes during electron irradiation at liquid helium temperatures [126]. The elastic model to calculate the displacement energy was employed by Olander [127] by examining the energy gap between the equilibrium and saddle point positions. Due to variation of displacement threshold energy, average displacement energy, often one or two times larger than the displacement threshold barrier, is calculated by weighting average over a range of displacement energy at which a displacement can occur.

1.5.3.2 PKA damage function and energy

The PKA damage function is used to describe the production of atoms displaced by a single PKA with energy of E. If the PKA has much higher energy than the

displacement energy, it will displace secondary knock-on atoms by transferring energy. The secondary knock-on displaced atom can in turn displace the other atoms. The knock-on process will continue until no atoms have energy bigger than displacement threshold energy. Finally the collision cascade is created consisting of many collisions and displacement events. The average number $\langle N_d(E) \rangle$ of atoms displaced by an energetic PKA with energy E in collision cascade is called displacement damage function. Based on the Kinchin and Pease (1955) hard-sphere model [128] and assumptions made by Olander [127] and M.W Thompson [129], the Kinchin-Pease displacement damage function for a PKA with energy of E is given by:

$$\langle N_d(E) \rangle = \begin{cases} 0 & (E < E_d) \\ 1 & (E_d < E < 2E_d) \\ 0.5E / E_d & (2E_d < E < E_c) \\ 0.5E_c / E_d & (E > E_c) \end{cases} \tag{43a}$$

where E_c is the energy in the center of mass, and E_d is the displacement energy.

After consideration of electronic stopping power and usage of realistic interatomic potential to describe the atomic interactions, the modified Kinchin-Pease damage function was obtained by Robinson, Oen and Sigmund [130-132]:

$$\langle N_d(E) \rangle = \begin{cases} 0 & E \in (0, E_d) \\ 1 & E \in [E_d, 2E_d / \xi) \\ \dfrac{\xi \nu(E)}{2E_d} & E \in [2E_d / \xi, \infty) \end{cases} \tag{43b}$$

where $\nu(E)$ is the PKA damage energy not including the energy lost to electronic stopping, ξ depends on atomic interactions and its value is around 0.8 without unit suggested by both computer simulation and analytical theory [116].

The PKA damage energy $\nu(E)$ model has been derived by Lindhard et al. in 1963 [133] based on which a detailed analytical approach of NRT model has been developed by Norgett, Robinson, and Torrens [134] and is given by:

$$\nu(T) = T - \eta(T) = T / [1 + kg(\varepsilon)] \quad (44)$$

where T is PKA energy, $k = 0.1337 amu^{1/2} Z^{2/3} / M^{1/2}$ is the reduced electronic energy-loss factor and $g(\varepsilon) = \varepsilon + 0.40244\varepsilon^{3/4} + 3.4008\varepsilon^{1/6}$ is Lindhard's function and can be expressed by this analytical form by Robinson [135]. The reduced energy of ε can be expressed by:

$$\varepsilon = T / [86.93\ eV \cdot Z^{7/3}] \quad (45)$$

On the other hand, the projectile's energy and mass determine the damage density deposited on the solid target during the ion irradiation. The reduced damage energy in a specific region is approximately given based on the comparison of calculation and experimental results [133, 136]:

$$\nu_p(\varepsilon) \cong 0.8\varepsilon \quad (46)$$

where ε and Z_1 are in the range of $\varepsilon < 1$ and $Z_1 > 5$, respectively. The laboratory damage energy can be given below by taking advantage of the relationship of $\nu_p(\varepsilon)/\varepsilon = \nu_p(E)/E$:

$$\nu_p(E) \cong 0.8E \quad (47)$$

1.5.3.3 Damage production rate and DPA

According to modified Kinchin-Pease function, the damage production rate of displacement number per unit volume $N_d(x)$ at a depth of x is:

$$N_d(x) = 0.8F_D(x)\phi/(2E_d) \quad (48)$$

where ϕ is dose in the unit of ion/cm^2 and $F_D(x)$ is the deposited energy depth distribution function without considering the electronic energy losses from recoiling target atoms.

The extent of irradiation damage can be expressed by displacements per atom, also called dpa. Radiation damage at 1 dpa level means that in the irradiated region, on the average, every atom has been displaced once from its original lattice site. Due to the relationship of $dpa(x) = N_d(x)/N$, dpa as a function of depth at a given dose can be expressed by:

$$dpa(x) \approx 0.8F_D(x)\phi/(2NE_d) \quad (49)$$

By integrating $dpa(x)$ and making use of $\nu_p(\varepsilon) \cong 0.8\varepsilon$ in the range of $\varepsilon < 1$ and $Z_1 > 5$, the total dpa over the energy range of (E_0, E_d) approximately equals to:

$$dpa \cong N_d(\nu_p(\varepsilon))\phi/(NR) \cong 0.4\nu(0.8\varepsilon)\phi/NRE_d \quad (50)$$

where $N_d\nu_p(\varepsilon)$ is the modified Kinchin-Pease damage function for calculating damage energy.

1.5.3.4 Displacement and thermal spikes

In ion-solid interactions, a spike is defined as a high density cascade that occurs in a limited volume in which the majority of atoms are temporarily in motion [137, 138]. The studies by Brinkman [139] showed that when the average distance traveled by a projectile with energy E between displacement collisions with target atoms approaches the atomic spacing of solid target, a heavily damaged region formed where every displaced atom is forced away from the ion or PKA path can produce displacement spike,

which creates a volume of material composed of a core of vacancies surrounded by a shell of interstitial atoms as shown in Figure 1.14 [139]. Usually the time to form the displacement spike is the same as the period of PKA energy from E to the rest [138].

After the displacement spike, the energy of the moving atoms or ions smaller than the displacement threshold energy will be shared between the neighboring atoms and hence diminish as lattice vibrations or in the form of heat. This localized heating is called thermal spike, and will last for several picoseconds to be quenched to the ambient temperature [116].

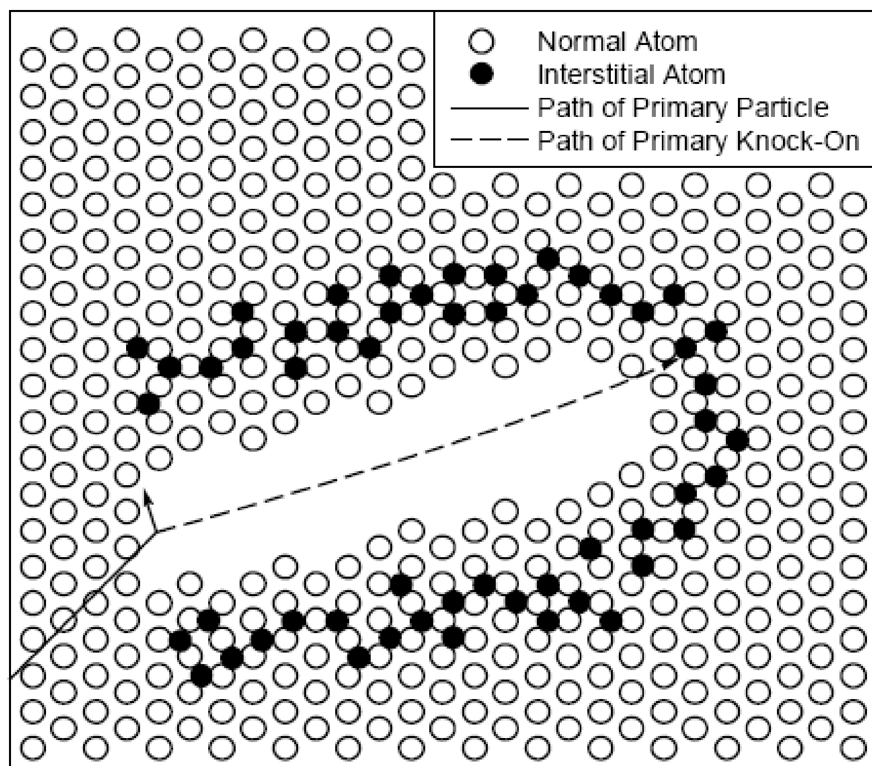

Figure 1.14. Schematic of a highly damaged volumeo f material, formed when the mean free path between collisions approaches the atomic spacing of the target atoms [139].

1.5.3.5 SRIM simulation based on Monte Carlo

Numerous techniques including transmission electron microscopy, positron annihilation spectroscopy, X-ray scattering and small angle neutron scattering have been used to analyze radiation damage and radiation effects, however, it is very challenging to capture the temporal development of the collision cascade and the resolution of many techniques are not yet sufficient to image individual defects. Hence computer simulations have been extensively used to understand the spatial and temporal development of the collision cascade. Major simulation techniques include the binary collision approximation (BCA), molecular dynamics (MD), and the kinetic Monte Carlo (KMC) method. KMC, used for ion-solid interactions, depends on a binary collision model and is the most powerful method to predict long-time dynamics at the mesoscale with little questionable assumptions. It allows for a more rigorous treatment of elastic scattering and leads to accurate determination of angular and energy distributions. Among a large number of KMC computer simulation code, the program of stopping and range in the matters (SRIM) developed over decades by Ziegler et al. is the most commonly cited to determine ion range, damage distributions and angular and energy distribution of backscattered and transmitted ions in irradiated materials [122].

SRIM is a group of programs [140]. The stopping and range of ions (up to 2 GeV/amu) into matter can be calculated by SRIM by using a quantum mechanical treatment of ion-atom collisions. The interaction between the ion and atom is Coulomb and thus there is a screened Coulomb collision including exchange and correlation interactions between the overlapping electron shells. The long range interactions in the ions create electron excitations and plasmons within the target, which are described by

including a description of the target's collective electronic structure and interatomic bond structure when the calculation is setup (tables of nominal values are supplied). The effective charge including a velocity dependent charge state and long range screening due to the collective electron sea of the target describe the charge state of the ion within the target [141].

SRIM can provide much useful information related to ion-solid interactions. For an example, dpa, which is a relative measure of lattice damage, can be written as:

$$dpa = D(\frac{10^7 nm}{cm})(\frac{dose(ions/cm^2)}{N(atoms/cm^3)}) \tag{51}$$

where D is the number of displaced atoms per ion per Å thick of target materials, and is a direct output of SRIM simulations.

1.5.3.6 Radiation damage in metals

The radiation damage in the metals involves a series of microscopic events, which precede the appearance of macroscopic changes in the irradiated materials and the time scale for these events is less than 10^{-11} second. The studies on radiation damage in irradiated materials are concerned with the density and configuration of the point defects including vacancies and interstitials induced by bombardment of projectiles. Because the binding energy of lattice atoms is typically lower compared to the energy transferred to the lattice atoms from the projectile, on the order of tens to hundreds of eV during radiation, radiation damages composed of displaced atoms certainly occur. Almost immediately following a cascade, a majority of point defects (interstitials and vacancies) start recombining and the structure recovers to its original state. However, a small fraction of the damage cascade (point defects) will be left behind without recovering. The remaining interstitials and vacancies forms the foundations of the most observed

radiation damage effects. An atom located between the regular lattice sites in crystalline solids is called interstitial. Interstitials of the same type of matrix atoms is called self-interstitial atoms (SIA), and impurity interstitials are different from matrix atoms. Multiple interstitials can be formed by the agglomeration of mobile SIAs due to their strong interactions. A vacancy is another type of point defect in a crystal. Single vacancy is a lattice site where the lattice atom is missing. Multiple vacancies composed of several vacancies are often observed in irradiated materials. The formation energy of point defects is given by [111]:

$$E_f = 4\pi r_a^2 \sigma - 12\pi r_a \sigma^2 / \mu + 6\pi r_a \sigma^2 / \mu \tag{52}$$

where σ is the surface energy per unit area, μ is shear modulus and r_a is the atom radius. Due to greater r_a induced by interstitial, the formation energy of vacancies is smaller than that of interstitials. The vacancies have low formation energies of smaller than 2 eV and high migration energy of greater than 0.5 eV. Conversely SIAs have high formation energy of greater than 2 eV and low migration energy of smaller than 0.15 eV. The comparison indicates the vacancies are much less mobile than SIAs. The equilibrium concentration of point defects can be expressed by [111]:

$$C = \exp(S_f / k)\exp(-E_f /(kT)) \tag{53}$$

where S_f is entropy, k is Boltzmann's constant, T is temperature and E_f is formation energy of point defects. Because of the higher formation energy of interstitial, the equilibrium concentration of vacancies is much higher than that of SIAs. The solutes or impurities in the lattice can often act as efficient raps for vacancies because the binding of vacancies with solute or impurity can lower the overall free energy of solid.

These vacancies and interstitials can form vacancy clusters and interstitials loops to reduce the overall energy of the irradiated materials further. Subsequent section will introduce the point defects clusters in the form of void, dislocation loops, and the consequent radiation effect of these clusters.

1.6 Radiation effects in metals

1.6.1 Introduction of radiation effect

Radiation effects are the macroscopic events, including void swelling, hardening, embrittlement and fracture, many of which degrade the performance and properties of irradiated materials. Radiation induced vacancies and interstitials accumulate in various ways to form extended defects such as vacancy clusters, voids and dislocation loops, which could lead to the collapse of the ordered lattice, and in some cases, the crystalline structure can be transformed into an amorphous state [116]. Stacking fault tetrahedra (SFT) shown in Figure 1.15 [142] as a result of agglomeration of vacancies is frequently observed in irradiated metals with faced-centered cubic (FCC) structure, such as Au, Cu, Ni, Pd and stainless steel [142-148]. A high concentration of vacancy clusters and SFT is observed in FCC Cu, whereas interstitial loops seem to prevail in irradiated V [149]. In fusion reactors, besides the aforementioned displacement damages, a high concentration of He atoms created via (n, α) or other transmutation reactions typically leads to a large number of He bubbles shown in Figure 1.16 [150] where He atoms combined with vacancy clusters in irradiated structural metals.

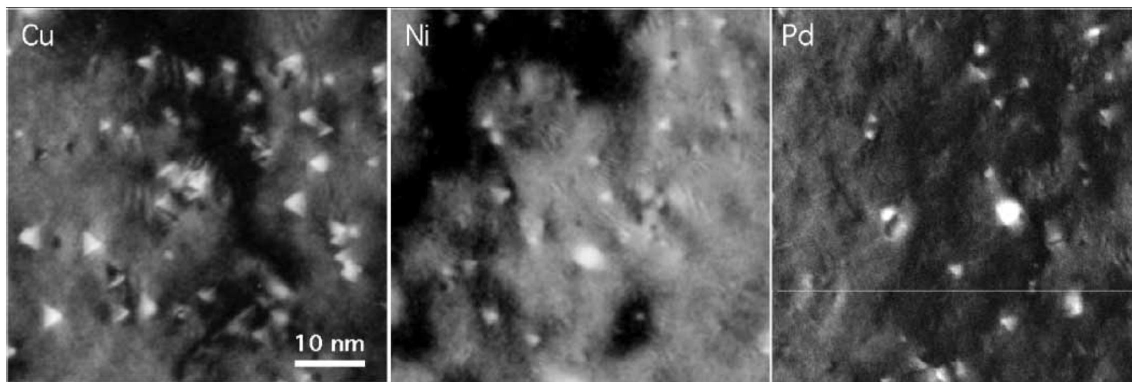

Figure 1.15. Observation of stacking fault tetrahedra (SFT) from TEM micrographs of Cu, Ni and Pd irradiated at room temperature [142].

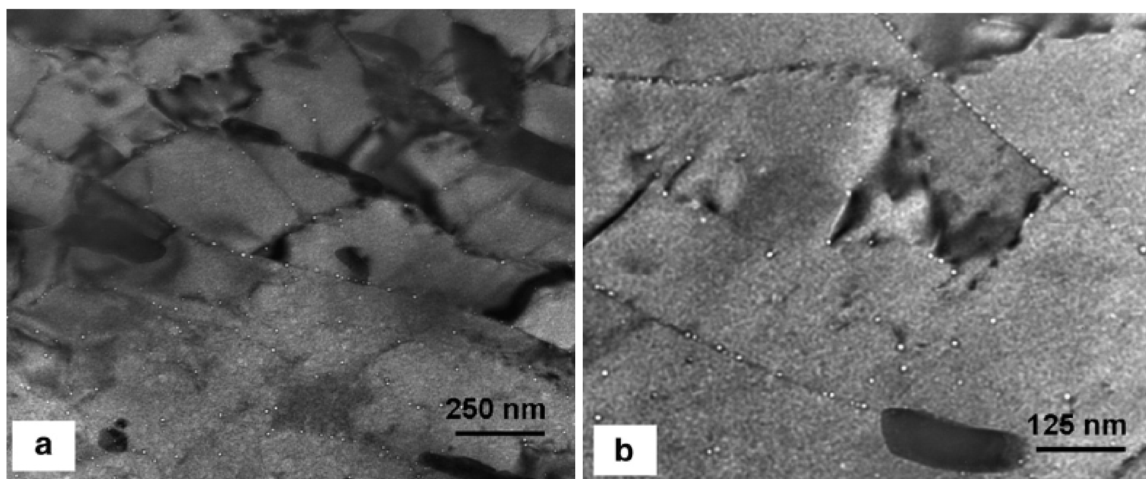

Figure 1.16. TEM images of He bubbles in 12Cr-1MoVW-2Ni steel irradiated in HFIR at 600°C to ~ 40 dpa at (a) low magnification and (b) high magnification indicating the bubbles on martensite lath boundaries, precipitate boundaries, and in the matrix [150].

Macroscopically, void swelling, as shown in Figure 1.17 [151], frequently occurs in structural steels as a result of the growth of vacancy clusters [152, 153], and can significantly degrade the mechanical properties of structural materials, in the form of embrittlement and loss of ductility typically accompanied by radiation hardening. Degradation of mechanical properties, manifested as radiation induced embrittlement and

loss of ductility, is a serious challenge to the application of structural alloys in nuclear reactors. Early studies on neutron irradiated FCC (such as Cu) and BCC (such as V) metals showed that pronounced hardening is due to the presence of radiation-induced point defects, dislocation loops, SFT, and He bubbles [154-156]. The shear strength of proton irradiated Cu increases with the extent of damage as shown in Figure 1.18 [157]. The increase of yield strength is approximately 200-300 MPa in Cu and V irradiated at a damage level of ~ 1 dpa [158]. Significant void swelling, ~ 14 %, has been observed in neutron radiated 316L stainless steels [159].

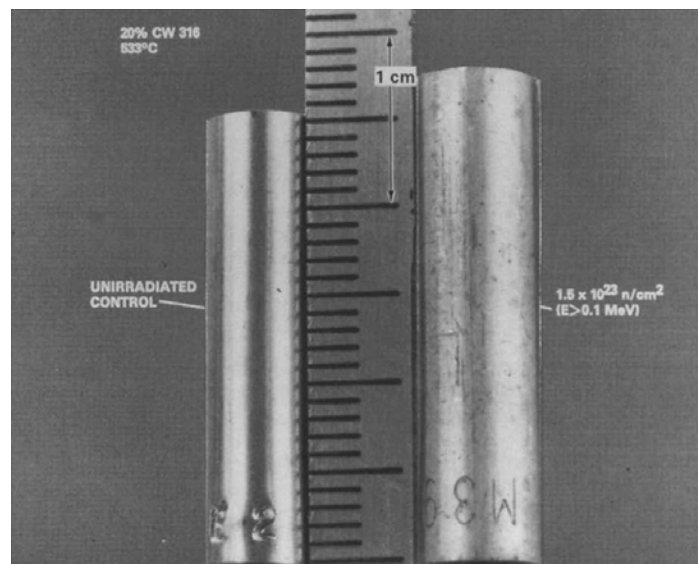

Figure 1.17. Photo of radiation induced swelling in 316 stainless steel rods before and after irradiation at 533 °C to a fluence of 1.5×10^{23} n/m^2 in the EBR-11 reactor [151].

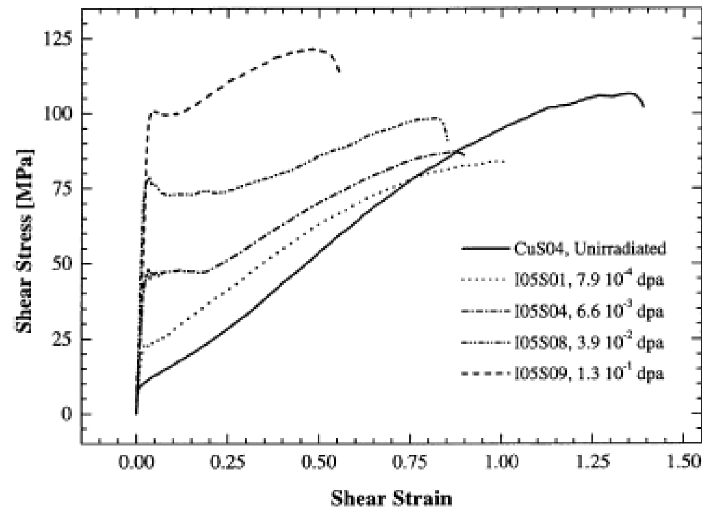

Figure 1.18. The shear stress-strain of Cu irradiated to different doses by proton at ambient temperature [157].

1.6.2 Defect clusters and dislocation loops

Collision cascade (or displacement spike) is composed of a shell of interstitials surrounding a core of vacancies. In addition to single interstitial and vacancy in cascade, most of defects are their clusters. Interstitial clusters are created either in the transition between collision and thermal spike or during thermal spike where the short-range diffusion of interstitial is induced by elastic interaction between neighboring interstitials. Vacancy clusters are created inside the core of the cascade as shown in Figure 1.14. Their structures are strongly dependent on the solid target structure [160, 161]. In FCC metal, such as Cu, the configuration of the smallest interstitial cluster has the form of two <100> dumbbells and it changes to a set of <110> dumbbells or a set of <110> crowdions as the size of clusters increases. For vacancy cluster in Cu, the most stable configurations are the SFT and faulted clusters on {111} crystallographic planes. Figure 1.19 shows radiation induced vacancy type dislocation loop and SFT observed by TEM in gold and

silver [162]. In BCC metal, like α-Fe, small interstitial cluster with number of SIAs smaller than seven has configuration of a set of <111> crowdions and big interstitial cluster with more than 7 SIAs has two configurations of <111> and <110> crowdions. The crowdions in metals can be transformed into interstitial type dislocation loops during later development. The most stable configurations of a set of di-vacancies concentrated on two adjacent {100} planes and a set of first nearest neighbor vacancies on a {110} plane are the major vacancy cluster in BCC metal such as α-Fe. The interstitial clusters will invariably grow to interstitial type dislocation loops, while vacancy clusters can either grow to vacancy type dislocation loop from collapsed platelets or agglomerate into 3D cluster, which is called void.

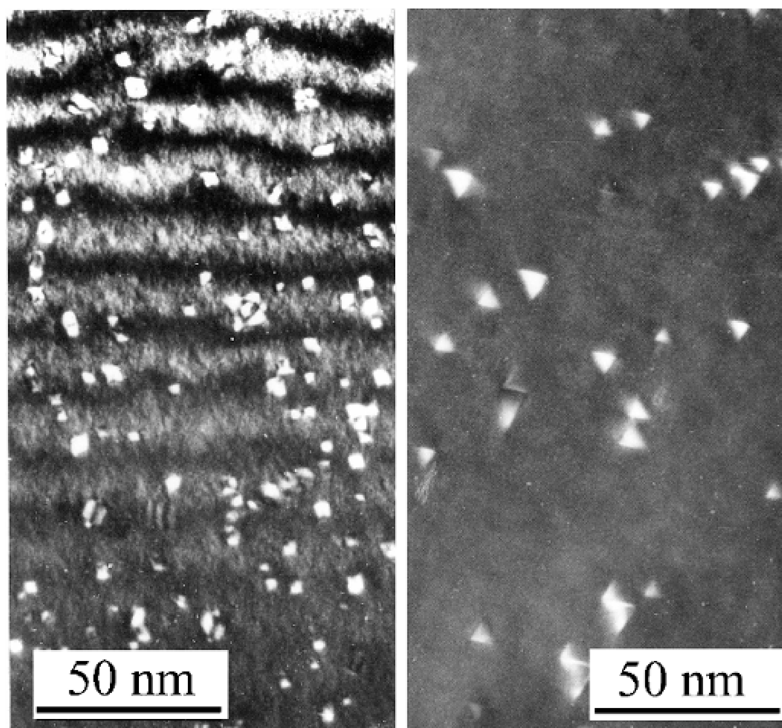

Figure 1.19. Micrographs of TEM for (a) defect clusters in gold irradiated to 1.1×10^{22} n/m^2 at 200 °C and (b) stacking fault tetrahedra in silver irradiated to 4.4×10^{21} n/m^2 at 400 °C [162].

Dislocation loops including interstitial and vacancy type developed from the defects clusters are of importance in determining the influence of radiation on both microstructure and mechanical properties. A dislocation loop is the result of the defect agglomeration and is formed by the condensation of vacancies or interstitials into roughly circular disks followed by collapse of the atom planes adjacent to the platelet [127]. Figure 1.20 shows the schematic diagram of the formation of dislocation loop for (a) interstitial type and (b) vacancy type [127]. The collapse of interstitial shell in the cascade onto a close-packed plane results in an extrinsic stacking fault and the condensation of vacancy core leads to the intrinsic fault. The dislocations loops are called Frank sessile dislocation loop or Frank loops, which are not mobile because its glide plane defined by the projection of the loop perimeter and Burgers vector are perpendicular to the plane of the loop. The diameter of a Frank loop can change by absorbing or emitting the point defects. For an example, additions of more interstitial causes interstitial type dislocation loop grow, but cause vacancy type dislocation loop shrink. The immobile frank loops can unfault by reacting with other type of loop to form a perfect loop. For an instance, the Shockley dislocation react with Frank dislocation to form a mobile dislocation at the original position of Frank dislocation due to the interior of the loop in perfect stacking region with the neighboring (111) plane [127]. This unfaulted dislocation is usually called a prismatic loop. In irradiated FCC metals, SFT has very common three dimension stacking fault configuration, which evolve either directly from vacancy clusters induced in cascade or from consuming of vacancy type Frank loop. The detail of formation of SFT can be found elsewhere [111].

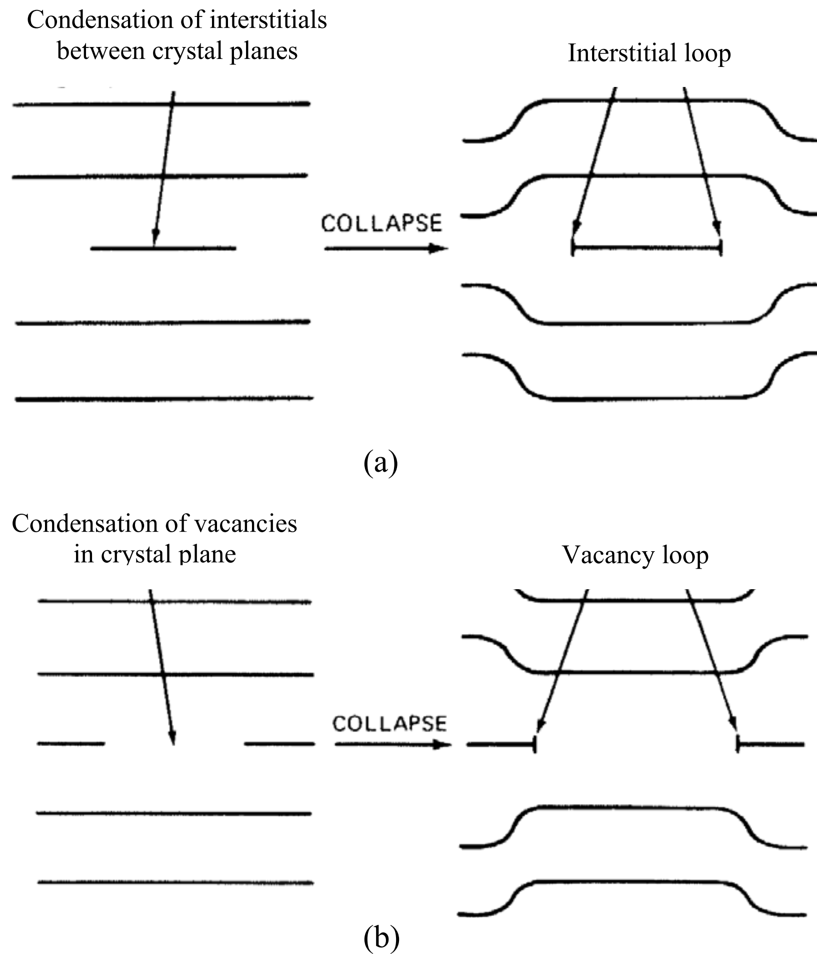

Figure 1.20. Schematic of formation of dislocation loops for (a) interstitial type and (b) vacancy type [127].

Many studies on determining the nucleation rate of dislocation loops have been performed. In a classical model [127], the energy of a Frank dislocation loop without unfaulting is:

$$E_{Loop} = 2\pi\mu b^2(\sqrt{3}\Omega m/(\pi a_0))^{1/2} + E_{Stacking\ \ fault} \quad (54)$$

where μ is shear modulus, b is Burgers vector, Ω is the atomic volume, m is number of interstitial, and a_0 is lattice parameter. Based on the equation above, Russel et al. [163] estimated that the dislocation loop energy ε_m, by using a slightly different formula to calculate strain energy of the loop and neglecting the stacking fault energy, is:

$$\varepsilon_m = \begin{array}{ll} 420kJ/mole & m=1 \\ 500m^{1/2}kJ/mole & m>1 \end{array} \quad (55)$$

where m is the number of point defects. According to this equation at a given interstitial supersaturation of 10^{17}, the emission rates can be given by:

$$\alpha_i(2) \approx 3\times10^4 \beta_i(1),\ \alpha_i(3) \approx 6\times10^5 \beta_i(2) \quad (56)$$

where $\alpha_i(m)$ is the loop emission rate and $\beta_i(m)$ is the rate at which a loop size of m captures interstitial [127]. However, due to the inappropriate energy formula for di-interstitials and tri-interstitials and crude analytic method, an advanced model to analyze the loop nucleation based on chemical reaction-rate theory has been developed by Hayns who considered presentence of vacancies and the kinetics of annealing of point-defects [164]. There are four reactions including reactions between vacancies and di- and tri-interstitials to the nucleation of interstitial cluster:

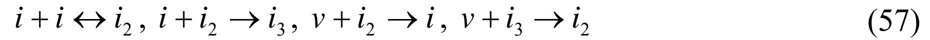

$$i+i \leftrightarrow i_2,\ i+i_2 \rightarrow i_3,\ v+i_2 \rightarrow i,\ v+i_3 \rightarrow i_2 \quad (57)$$

so the forward rate of reaction 1 and the rate of the reverse of reaction 1 can be given as:

$$R_{1f} = \beta_i(1)C_i \text{ and } R_{1r} = \alpha_i(2)N_2 \quad (58)$$

Similarly, the rate of reaction 2, 3 and 4 can be written as:

$$R_2 = \beta_i(2)N_2,\ R_3 = \beta_v(2)N_2, \text{ and } R_4 = \beta_v(3)N_3 \quad (59)$$

where $\beta_i(m) = z_{m,i}\Omega D_i C_i / a_0^{\ 2}$ is the arrival rate of interstitials at a cluster of size m, $z_{m,i}$ is the number of sites surrounding an interstitial cluster with m interstitial from which a single interstitial can jump to form interstitial cluster having $m+1$ interstitials. $\beta_v(m) = z_{m,v}\Omega D_v C_v / a_0^{\ 2}$ is the rate for an interstitial cluster with m interstitials to

capture vacancies and $z_{m,v}$ is the number of locations surrounding an interstitial cluster with m interstitials from which a vacancy reduces the number of interstitial by one jump. By taking into account of $N_2 = N_3$, the nucleation rate of loop during steady-state nucleation is given by:

$$I_{loop} = (1 - \beta_v / \beta_i)\beta_i N_2 \tag{60}$$

where $\beta_i N_2$ is the nucleation rate in the absence of vacancies, and the rate of loop nucleation is decreased by a factor of $(1 - \beta_v / \beta_i)$, when the vacancy supersaturation is achieved in the irradiated metals [127].

1.6.3 The nucleation and growth of voids and bubbles

Interstitial clusters can grow to the interstitial type dislocation loops in irradiated materials. Void, a 3D vacancy cluster is one of two results of agglomeration of vacancies in irradiated materials. A large number of studies on understanding void nucleation and growth have been performed experimentally and theoretically, since Cauthorne and Fulton [165] first observed voids in the irradiated materials. Void nucleation refers to the rate at which tiny embryos of these defect clusters start to appear in the lattice, and it includes two types of nucleations: homogeneous and heterogeneous nucleation. Homogeneous nucleation is the buildup of tiny clusters by accidently encountering of many single point defects which are performing random work in the lattice. Heterogeneous nucleation is the appearance of voids on structural features different from that of the solid, including impurity gases, incoherent precipitate particles, dislocation loops, thermal spike zone, etc. The supersaturation of radiation induced vacancies in the irradiated materials is the force to drive the nucleation of the void, and it can be written as:

$$S_V = C_V / C_V^0 \quad (61)$$

where $C_V^0 = N_s \exp(-\varepsilon_v / kT)$ is the concentration of vacancies at thermal equilibrium conditions, $N_s = 1/\Omega$ is the number of atom sites in a unit volume of solid, and ε_v is the vacancy formation energy [111, 127].

The number of vacancy absorbed must be greater than that of interstitial absorbed by vacancy cluster for growing void. It is therefore important to know the void distribution function in the equilibrium conditions. Equilibrium void distribution function, giving the number of vacancy clusters in each cluster, has been developed based on supersaturation of vacancy and is written as follows:

$$N^0(m) = N_s \exp(m \ln S_V - \xi m^{2/3}) \quad (62)$$

where ξ is a constant without units, and its values are in the range of 10 - 30 [127].

This equilibrium void distribution function is derived from thermodynamics. When at equilibrium the rate for capturing one single vacancy by vacancy clusters with size of m equals to rate for emitting one vacancy from the clusters with size of $m+1$ and can be expressed by:

$$\beta_v(m) N^0(m) = \alpha_v(m+1) N^0(m+1) \quad (63)$$

where $\beta_v(m)$ and $\alpha_v(m)$ carry the same meaning as before, but this time the clusters are of vacancy type. $\beta_v(m)$ can be approximately expressed by $\beta_v(m) \cong a_o D_v C_v m^{1/3}$ given that $a_o / R < 1$. Where a_o is lattice constant, D_v is the diffusion coefficient of vacancy and C_v is the concentration of bulk vacancy. So the emission rate is given by [127]:

$$\alpha_v(m+1) \cong a_o D_v C_v^0 m^{1/3} \exp(2\xi m^{-1/3} / 3) \quad (64)$$

The comparison of the capture and emission rate indicates that $\beta_v(m)$ increases but $\alpha_v(m)$ decreases with the increase of m. When m of the cluster reaches to a certain minimum size, it will continue to grow into a full-fledged void. The nucleation current or nucleation rate (I) termed for a flow rate of voids is the net rate where the size of clusters grow from m to $m+1$ per unit volume and can be expressed by the rate at which the size of cluster from $m+1$ to m minus the rate at which the size cluster from m to $m+1$.

$$I = \beta_v(m)N(m) - \alpha_v(m+1)N(m+1) - \beta_i(m+1)N(m+1) \tag{65}$$

where $N(m)$ is the nonequilibrium void distribution function in a steady-state. The first and second term stands for the capture of vacancies and interstitials, respectively, and the third term represents the emission of vacancies. The emission of interstitials has been neglected in the equations due to very large formation energy of interstitials.

Because $\beta_v(m)N^0(m) = \alpha_v(m+1)N^0(m+1)$, the nucleation rate can be modified to:

$$\begin{aligned} I &= \beta_v(m)\{N(m) - N(m+1)[N^0(m)/N^0(m+1) + \beta_i/\beta_v]\} \\ &= \beta_v(m)[N(m) - N(m+1)(h(m)/h(m+1))] \\ &= \beta_v(m)h(m)[N(m)/h(m) - N(m+1)/h(m+1)] \end{aligned} \tag{66}$$

where $\beta_i/\beta_v = D_iC_i/D_vC_v$ is called arrival-rate ratio and plays an important role in determining nucleation rate, and $h(m)$ is a defined function [127].

When a derivative is approximately used to express the difference of $[N(m)/h(m) - N(m+1)/h(m+1)]$, so

$$I = -\beta_v h \frac{d(N/h)}{dm} \tag{67}$$

After integrating, the solution for nucleation rate is:

$$I = [\frac{1}{2\pi}(\frac{d^2 \ln h}{dm^2})_{m_c}]^{1/2} \beta_v(m_c)h(m_c) \tag{68}$$

where m_c is obtained by $(d \ln h / dm)_{m_c} = 0$. Therefore the nucleation rate can be determined by both vacancy capture rate of void and near function $h(m)$'s minimum [127].

By far, the nucleation rate of void is derived based on sufficient supersaturation of readily mobile point defects to create void embryo. It is well accepted that the He atoms created by transmutation reaction act as the immobile stabilized site for void nucleation. Indeed previous studies have suggested the gas atoms are always involved in the process of void nucleation [166-168]. A couple of theories about void nucleation accounting for He atoms in the metal have been proposed and can be found elsewhere [169-172].

The prediction of void growth can be described as the rate of change of the void radius at any instant time during irradiation, which is termed as void growth law with the assumption of spherical void and its growth controlled by the diffusion of interstitials and vacancies from the lattice of solid to the void surface. When some gas is contained in the void, the growth law is given by:

$$\frac{dR}{dt} = \frac{\Omega}{R}[D_v(C_v - C_{vR}) - D_i(C_i - C_{iR})] \tag{69}$$

where C_v and C_i are the vacancy and interstitial concentration in the solid, C_{vR} and C_{iR} are the vacancy and interstitial concentration at the bubble surface. If the void does not contain gas, i.e. the pressure inside the void is zero, the void growth rate can be expressed by:

$$\dot{R} = \frac{dR}{dt} = \frac{\Omega}{R}[D_v(C_v - C_v^0 \exp(\frac{2\gamma\Omega}{RkT})] - D_i C_i)] \tag{70}$$

where $C_v^0 = \exp(s_v / k)\exp(-\varepsilon_v / kT)/\Omega$ is the thermodynamic equilibrium vacancy concentration for a solid without stress, s_v and ε_v are the vacancy entropy and energy of formation, respectively [127].

Also the void growth rate can be described by [173]:

$$\dot{R} = \dot{R}_0 F(\eta) + \dot{R}_e \tag{71}$$

where $\dot{R}_e$ is the void-shrinkage term, $\dot{R}_0$ is the void growth rate without homogeneous recombination and thermal emission ($C_v^0 = 0$), and the factor $F(\eta) = 2[(1+\eta)^{1/2} - 1]/\eta$ is a factor related to the effect of homogeneous recombination during void growth, and η is a temperature dependent-constant without unit .

In the void growth model, the vacancy diffusion coefficient D_v and the equilibrium vacancy concentration C_v^0 determine the η . The reduction of D_v with decreasing temperature results in the increase of η . Consequently, both $F(\eta)$ and $\dot{R}_e$ become small at low temperature, and thus void growth stops. At very high temperature, $\dot{R}_e$ becomes increasingly negative whereas η reduces and $F(\eta)$ approaches unity. There is a temperature range, at which the void growth rate reaches a maximum value, corresponding to the observed maximum swelling temperature. The dependence of the void growth rates on temperature for typical fast reactor conditions is shown in Figure 1.21 [127, 173].

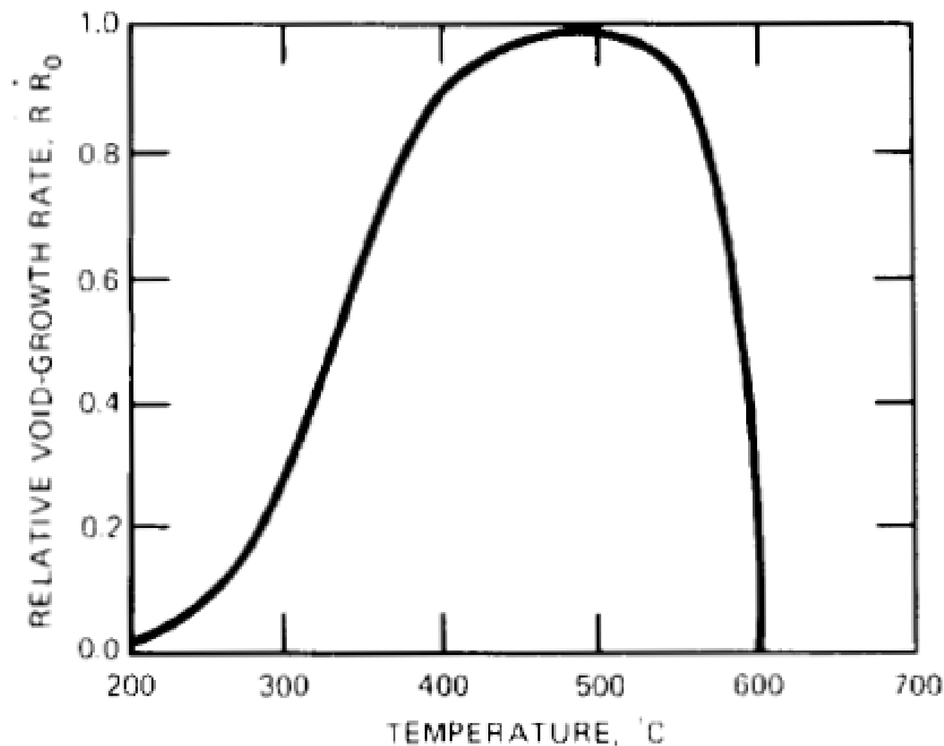

Figure 1.21. Temperature dependence of the void-growth rate in stainless steel under fast-neutron irradiation [127, 173].

1.6.4 Void swelling

Embrittlement induced by excessive hardening at low temperature or helium agglomeration at grain boundaries at high temperature is the most detrimental radiation effect in the structural materials in the reactors before void swelling was found. It came as somewhat of a shock when void swelling was first reported by Cawthorne and Fulton in the stainless steel fuel claddings irradiated in a test reactor [165]. Figure 1.22 shows the TEM micrograph of neutron irradiated stainless steel at 510 °C to a dose of 4.7×10^{22} cm^{-2}. As much as 7 % void swelling was observed at a neutron fluence which was about 25 % of the target fluence for a commercial reactor [165].

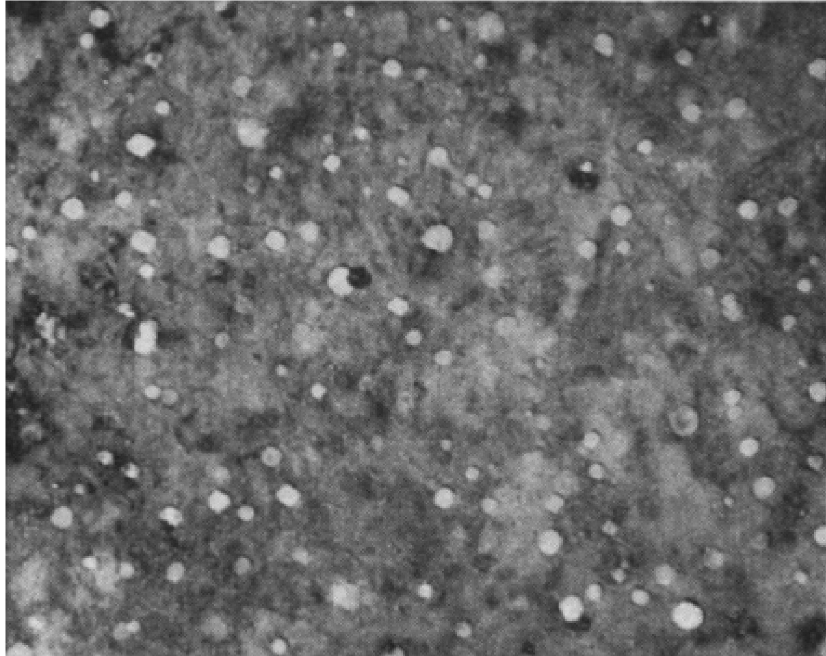

Figure 1.22. TEM Micrograph of fuel element cladding irradiated at 510 °C to a neutron dose of 4.7×10^{22} n/cm^2 [165].

Void swelling is a volume increase in a material caused by the collection of interstitial atoms as extra planes in the lattice and void formation and growth. It is expressed as $\Delta V / V$. The origins of void swelling are described as follows. A large number of Frenkel pairs are induced by collision cascade between the energetic projectiles and atoms in the solid. Most of the Frenkel pairs eventually recombine or migrate to the sinks in the solid where they lost their identity. The effective sinks include dislocations, precipitates, and grain boundaries. However, a small fraction of interstitials and vacancies remain uncombined. If the temperature is high enough so that they become mobile, the interstitials can agglomerate into interstitial type dislocation loops and the vacancies can agglomerate in the form of either 2D vacancy type dislocation loops or 3D

clusters termed void. The collections of interstitials and void growth cause the solid swell. As described above, the void growth is difficult at low temperature due to the difficulty of the defects migration. At high temperature, the defects are highly mobile, but they are preferred to be trapped by the sinks. Thus it indicates that void swelling is not favored at high temperature. At intermediate temperature, the defects are mobile but not removed by recombination or migration to sinks due to insufficient mobility. Void swelling reaches its maximum as shown in Figure 1.21. So the irradiation temperature plays an important role in determining the void swelling. Void swelling was observed in most metals and alloys in the temperature range of 0.3 to 0.6 T_m, where T_m is the melting point. Unfortunately the temperature range for void swelling in stainless steel overlaps with the temperature where liquid metal fast breeder reactors are operative. The strong dependence of temperature on the void swelling is indicated in the void swelling observed above 300 °C in annealed 12X18H10T with the following chemical composition: 0.12% C, 18% Cr, 10% Ni, 0.7% Ti, 0.8% Si, and 1.5% Mn [174] flow restrictor, as shown in Figure 1.23 [175].

With the increase of temperature, the density and size of void increases significantly, and so does the magnitude of void swelling. Another example of the effect of irradiation temperature on the void swelling, as shown in Figure 1.24 [176], correlated well with the production of void growth model.

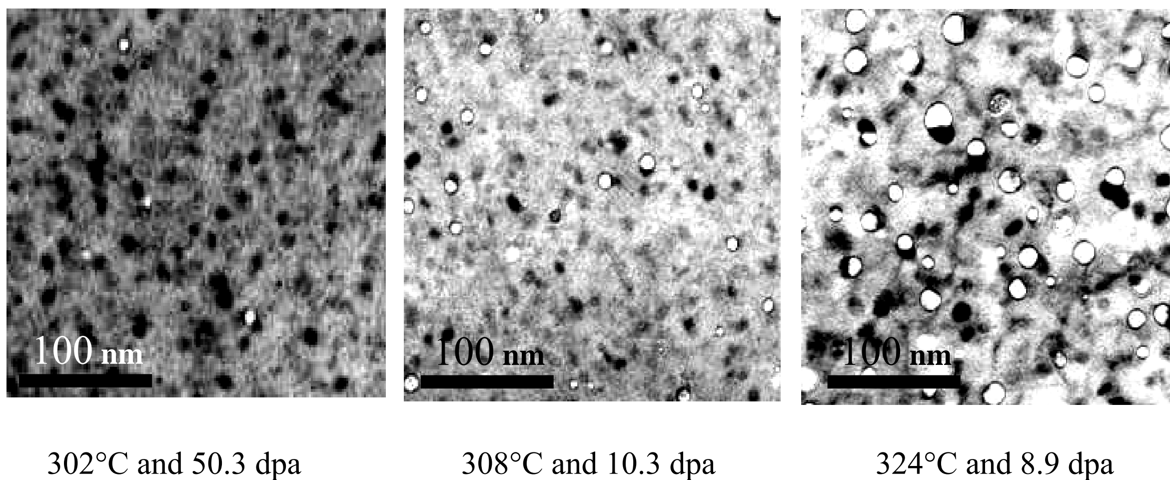

302°C and 50.3 dpa 308°C and 10.3 dpa 324°C and 8.9 dpa

Figure 1.23. The strong dependence of temperature on the void swelling observed in annealed 12X18H10T flow restrictor [175].

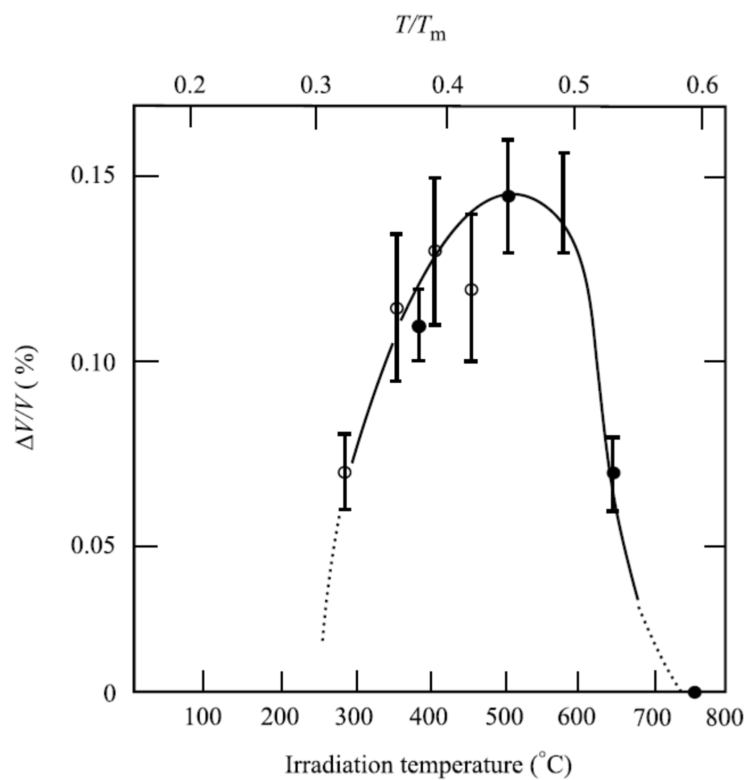

Figure 1.24. Swelling in Ni as a function of irradiation temperature for a fluence of 5×10^{19} n/cm^2 [176].

The magnitude of void swelling depends strongly on radiation dose as well. Void swelling is an increasing function of the irradiation dose and can be described empirically by a power law function [127]:

$$\Delta V / V = A(D)^n \tag{72}$$

where A is a constant, D is dosage, and n is the exponent greater than unity.

Void swelling increases with increasing dosage, however, there appears to be an incubation period, i.e., generally, void swelling only becomes noticeable after a certain dosage is reached, and then scales almost linearly with dose. Figures 1.25 shows the TEM micrographs of void swelling in 20 % cold worked 316 SS as a function of dose. The size and density of void increase with increasing dose.

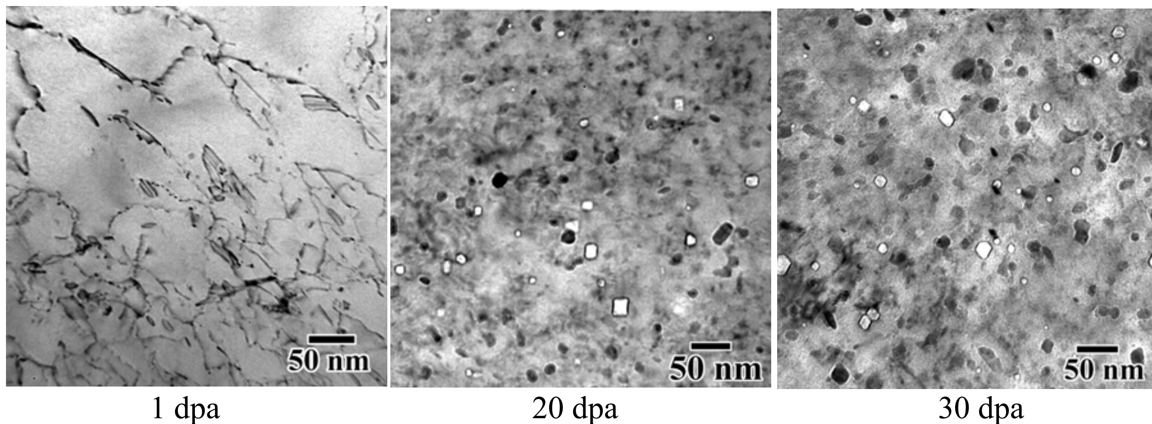

Figure 1.25. Dose dependent void swelling in 20 % CW 316 SS irradiated at ~ 375 °C [117, 177].

The incubation period depends strongly on the nature of the material, the alloying elements, dose and temperature, and it increases with temperatures. The dose rate and stress are also important parameters that affect void swelling. Other parameters affecting

void swelling and incubation period include chemical composition, transmutation gas, sink strength, crystal structure, etc.

1.7 Radiation hardening

In general, radiation hardening refers to the increase of yield strength and ultimate tensile strength (stress) of the metals and alloys. It occurs over a wide temperature range, and is most pronounced when the irradiation temperature is lower than one third of the melting point. Radiation hardening is also a function of the total fluence of radiation. Radiation hardening can be affected by many parameters, including point defect clusters, impurity, dislocation loops (interstitial or vacancy type), dislocations and their networks, voids and bubbles, and precipitates. Most of these defects are produced by the collisions between the energetic particles and atoms in the solid during irradiation as described previously in section 1.5.3. Compared to larger defect clusters, such as dislocation loops and voids, point defects and impurity atoms are considered to play a minor role in radiation hardening. Here we focus on the review of radiation hardening by dislocation loops and voids (bubbles). Reviews on radiation hardening by other factors can be found elsewhere [127]. The typical radiation hardening at temperatures of below 1/2-1/3 of T_m in FCC and BCC steels is indicated by engineering stress-strain curves as shown in Figure 1.26 [111].

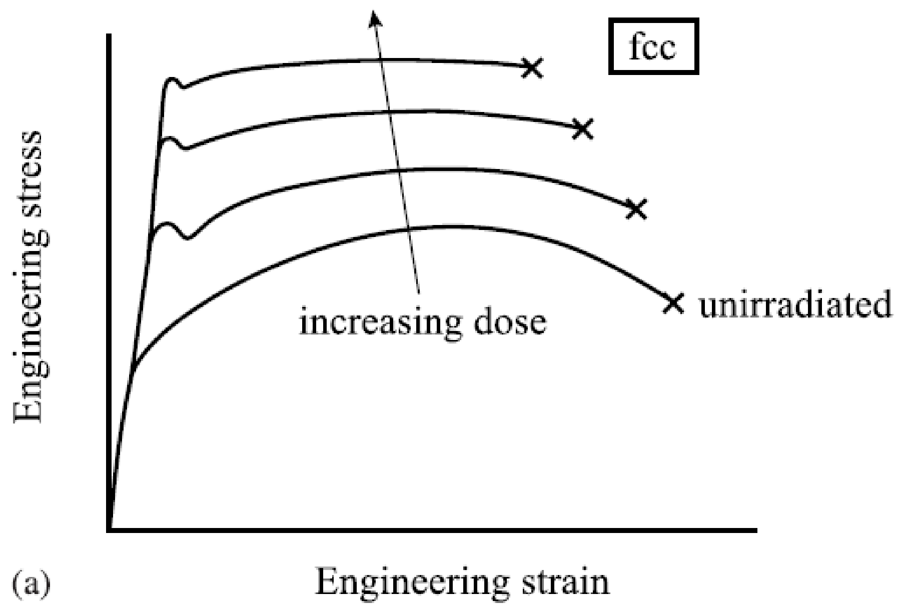

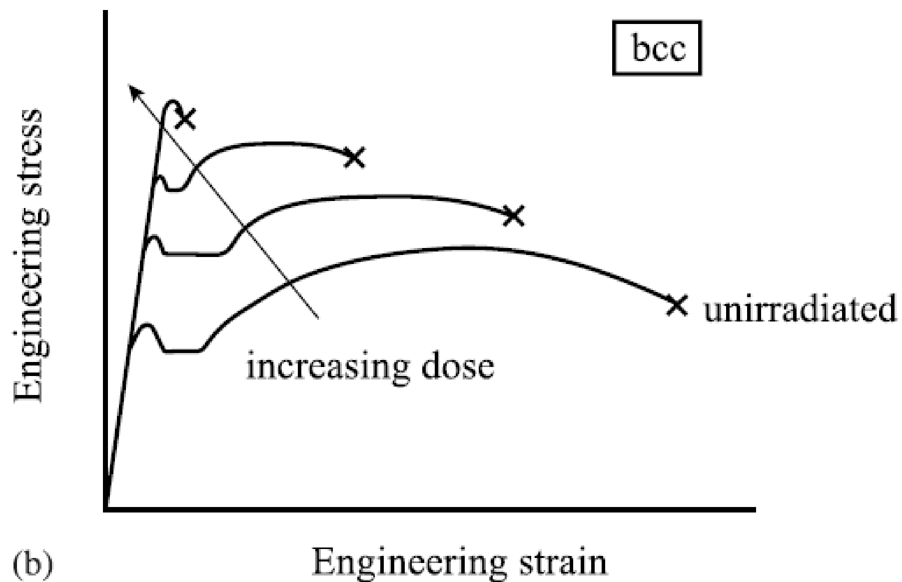

Figure 1.26. Effect of irradiation on the stress-strain behavior for (a) an austenitic (fcc) stainless steel and (b) a ferritic (bcc) steel [111].

In both FCC and BCC steels, the magnitude of radiation hardening, indicated by the increase of yield strength, increases with increasing dose.

There are basically two types of strengthening mechanisms that account for radiation hardening in metals. One is called source hardening, i.e. the increase of stress to activate the glide of dislocations. The applied stress needed to release or activate a dislocation onto its glide plane is defined as the unpinning or unlocking stress. The other strengthening mechanism is termed as friction hardening, which is the resistance from the natural or radiation-induced obstacles, such as dislocation loops and voids, which impede the glide of the dislocation. Although the strengthening mechanisms are categorized into these two groups, there is often unclear distinction due to many characteristics of the radiation induced deformation that has been attributed to the source hardening. Subsequent passage will describe these two strengthening mechanisms in terms of the obstacles induced by radiation.

1.7.1 Source hardening

Figure 1.26 shows the source hardening, manifested by the yield drop, observed in irradiated FCC and BCC metals. Radiation induced defect clusters in the vicinity of Frank-Read sources could be the reason for developments of source hardening. These defect clusters act as obstacles to raise the stress that is needed to expand dislocation loops and induce dislocation multiplications. If a sufficient stress is reached to release the source, the mobile dislocations will destroy the small defect clusters such as dislocation loops and thus reduce the stress required to continue deformation. Singh et al. [178] derived that the shear stress σ_S in the source hardening can be given by:

$$\sigma_S = \frac{0.4\mu b}{l}\left(\frac{r}{y}\right)^2 \tag{73}$$

where l is the spacing between edge character loops, r is the radius of loops, and y is a stand-off distance from the straight edge dislocation and was suggested via observed

microstructure to be $\sim 1.5r$. Therefore, $\sigma_S = 0.09\mu b / l$ is much less than that required to initiate a Frank-Read source by bowing of dislocation, which can be expressed by $\sigma_{FR} = \mu b / l$.

1.7.2 Friction hardening

The friction hardening mechanisms, that describe the impedance to the glide of dislocations, can be classified into two types: long range and short range. The total friction stress to move dislocations can be given by:

$$\sigma_F = \sigma_{LR} + \sigma_{SR} \tag{74}$$

where σ_F is the friction stress, σ_{LR} is the long range stress and σ_{SR} is the short range stress [127].

1.7.2.1 Long range stresses

Long range stress is induced by interaction among dislocations via their stress fields. It results from the repulsive interaction between a moving dislocation and components of the dislocation network of the solid. The long range force, also called interaction forces between the loop and the network dislocation at an angle of zero can be approximately given by [111]:

$$F_{LR} = \frac{\mu b^2}{2\pi(1-\nu)r} \tag{75}$$

so the stress required to overcome long range force of F_{LR} is:

$$\sigma_{LR} = \frac{F_{LR}}{b} = \frac{\mu b}{2\pi(1-\nu)r} \tag{76}$$

Taking a Poisson's ratio of $\nu = 1/3$ for typical ductile metals, the distance between dislocations is $r = 1/(\pi\rho_d)^{1/2}$, where ρ_d is the density of dislocation, so the long range stress is:

$$\sigma_{LR} \approx \mu b(\pi\rho_d)^{1/2}/4 \approx \alpha\mu b\sqrt{\rho_d} \tag{77}$$

Note that the long range stress on the mobile dislocation increases with increasing dislocation density. For an example, the process of cold working, unfaulting of prismatic loops induced by radiation, or work hardening can increases the long range stress via increasing the dislocation density.

1.7.2.2 Short range stresses

The short range stress refers to the stress that occurs between a very close moving dislocation and an obstacle on its glide plane. This indicates the short range stress is active only when the moving dislocation comes very close to or in contact with the obstacle. The moving dislocation will be exerted a force from the obstacle. The short range stress can be grouped into two types: athermal and thermal stress. The athermal stress is independent of temperature and involves bowing of a dislocation around the obstacle. In the thermal stress mechanism, the moving dislocation is required to cut through or climb over the obstacle. The energy to overcome the barrier by cutting through the obstacle or climbing of dislocation is partly assisted by thermal fluctuations. Higher temperature results in the lower thermal component of the short range stresses. For spherical obstacles, the distance l between obstacles can be given by [111]:

$$l = 1/(Nd)^{1/2} \tag{78}$$

where d is the diameter of the spherical objects, and N is a concentration of these spherical objects which are randomly distributed throughout the solid.

1.7.2.3 Precipitate, void (bubble) and dislocation loop hardening

Precipitation induced hardening refers to the increased strength produced by impenetrable obstacle through which a dislocation line moves only by bowing around them. Bowing will continue until two edges of the dislocation touch and annihilate each other due to their opposite signs. This process is called "pinch-off" and exactly the same as that occurs in a Frank-Read source. Then the dislocation will be free to move continuously until it touches the next obstacle. The short range stress due to an array of obstacles of density N and size of d is approximately given by [111]:

$$\sigma_S \approx \alpha \mu b \sqrt{Nd} \tag{79}$$

where $\alpha = \ln(0.5l / r_c)/(2\pi)$ and r_c is the dislocation core radius.

A relation between the applied yield stress σ_y and the resolved shear stress σ_S is described by $\sigma_y = M\sigma_S$, where M is the Taylor factor. So

$$\sigma_y = \alpha M \mu b \sqrt{Nd} \tag{80}$$

In FCC and BCC metals, M is an upper limit for the ratio of uniaxial yield strength to resolved shear strength and equals to 3.06 as suggested by Stoller and Zinkle [179]. Therefore, the increase in the yield strength $\Delta\sigma_y$ due to the precipitate with size of d and density of N is expressed as follows:

$$\Delta\sigma_y = \alpha M \mu b \sqrt{Nd} \tag{81}$$

This is the so called dispersed barrier hardening model. Like precipitate, the void and bubbles are also considered to be hard barriers. But the difference between them is that the dislocation segments touch the surface of void or bubble at 90 degree and leave no dislocation loop surrounding the void or bubble after moving through them. Following

the dispersed barrier model, radiation hardening due to void or bubble is usually written as $\Delta\sigma_y = \alpha M \mu b \sqrt{Nd}$, but this time α has a very small value of ~ 0.16.

1.7.2.4 Dislocation loop hardening

The dislocation loops including interstitial and vacancy type will provide the resistance to the motion of dislocation if the slip plane of a moving dislocation is close to or intersects a loop. The dislocation will experience a significant resistance if its glide plane lies close to the center of the dislocation loop. The dislocation loop induced the increase in the yield stress of the metal and alloy is given by [127]:

$$\sigma_S = F_{\max} /(b_e l) \tag{82}$$

where b_e is the burgers vector of the moving dislocation, l is the spacing of the loops on the glide plane, and $F_{\max}$ is the maximum force to overcome the loop resistance. $F_{\max}$ can be approximately expressed by [127]:

$$F_{\max} = \frac{\alpha \mu b_e b_1}{2(1-\nu)} (\frac{R_1}{y})^2 \tag{83}$$

where α is a numerical coefficient on the order of unity, and depends on the relative orientations and the Burgers vector of the loop and the dislocation line. Kroupa and Hirsch [180] proposed that the average of $F_{\max}$ induced by the distributed loops uniformly in a slab of thickness $2R_1$ is approximately $\mu b_e b_1 / 8$, so the stress due to dislocation loops is written by:

$$\sigma_s = \mu b_1 /(8l) \tag{84}$$

Furthermore, the bulk of experimental evidence on loop induced hardening give the stress as follows:

$$\sigma_s = \mu b(2R_1N_1)^{1/2}/\beta \tag{85}$$

where N_1 is the loop concentration and β is a constant between 2 and 4.

Another form of the stress due to dislocation loop is written as:

$$\Delta\sigma_y = \alpha M\mu b\sqrt{Nd}\text{ , with } \alpha = 0.1 \tag{86}$$

1.8 Difference between He, proton and neutron radiation

Figure 1.14 shows the cascade as a displacement spike with a high core density of vacancies surrounded by an interstitial shell. Based on this picture, Seeger revised the picture by taking account into the crystallinity such as focused energy packets (focusons), and long range transport of mass by replacement collisions and channeling, and termed the vacancy core a depleted zone, as shown in Figure 1.27 [181]. The distribution of damage energy can be described by the definitions of the deposited energy depth distribution $F_D(x)$ and primary recoil spectrum.

By using the nuclear sopping power and range given by the power law potential the deposited energy depth distribution is written by:

$$F_D(x) = \frac{T(1-x/R)^{(1/(2m)-1)}}{2mR} \tag{87}$$

where T is the PKA energy, R is the PKA range, and $m = 1/s$ is the power law exponent.

By using the K-P model and $\xi = 0.8$, the displacement rate as a function of depth in units of dpa can be written by:

$$dpa(x) = N_d(x)/N = 0.4F_D(x)\phi/(NE_D) \tag{88}$$

And the total dpa produced over all the recoil range by replacing $F_D(x)$ with E_D is $dpa \cong 0.4E_D/(NRE_d)$.

The weighted average recoil spectra for Coulomb potential is:

$$W_c(T) = (\ln T - \ln E_d)/[(\ln \gamma E_i) - \ln E_d] \tag{89}$$

and for hard-sphere potential is:

$$W_h(T) = (T^2 - E_d^{\,2})/E_d^{\,2} \tag{90}$$

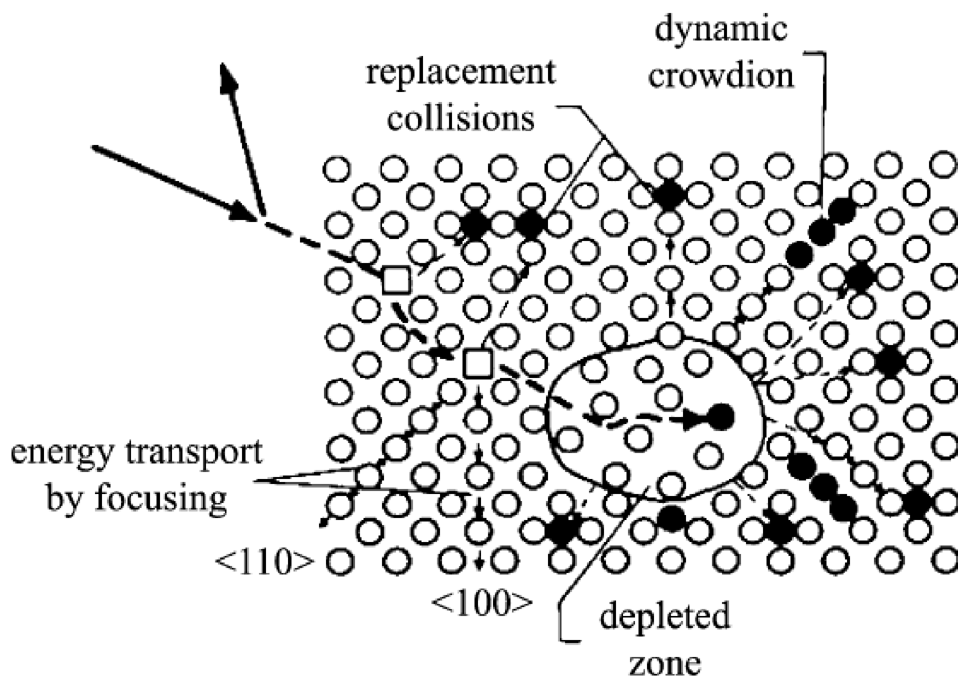

Figure 1.27. Revised version of Brinkman's displacement spike as drawn by Seeger accounting for crystallinity in the damage cascade [181].

Proton irradiation can be described well by the Coulomb potential while neutron irradiation is matched by hard sphere potential well. The screened Coulomb is the best approximation for heavy ion irradiation and its collisions can create many PKAs with low energy. Coulomb force increases slowly as the particle approaches the target in the Coulomb model, and the repulsive force goes to infinity only when the distance between

particles and atoms is at the hard sphere radius in hard sphere model. The hard sphere tends to create fewer PKAs with higher energy.

Radiation induced damages by different types of particles including electrons, protons, heavy ions and neutrons have been illustrated in Figure 1.28 [182]. The electrons and protons, which are light particles, produce isolated Frenkel pairs or small clusters. Conversely, heavy particles like heavy ions and neutrons induce large clusters damage.

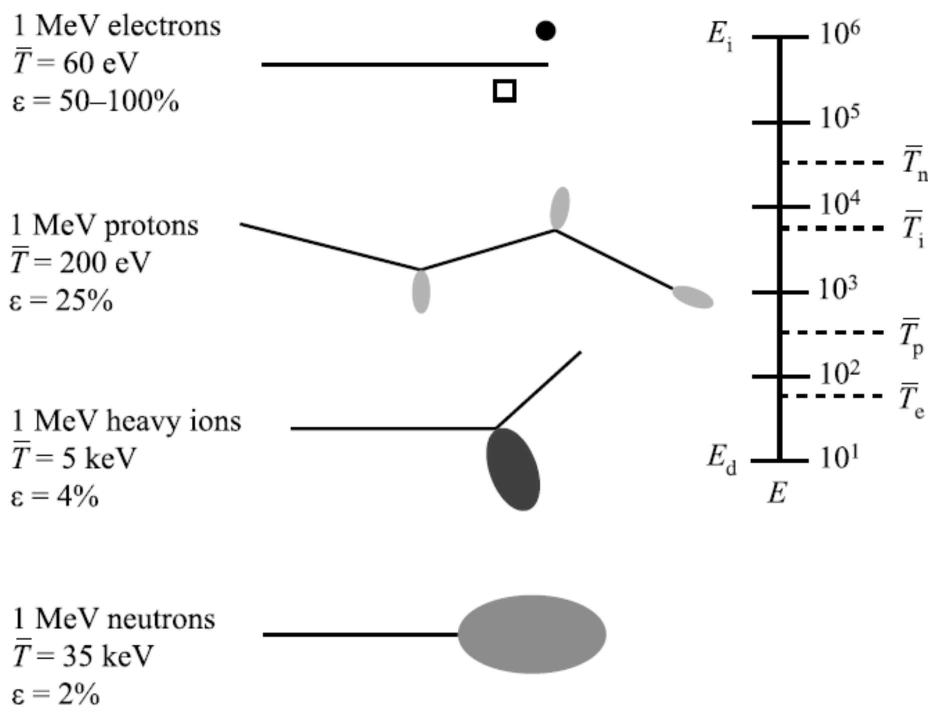

Figure 1.28. Difference in damage morphology, displacement efficiency and average recoil energy for 1 MeV different types of particles incident on Ni [182].

1.9 Motivation and objective

The national nuclear energy- and defense-related missions require the development of highly radiation resistant (tolerant) materials to be used in extreme

radiation environment. Basically, radiation damage in solid is induced by violent collisions between the energetic particles (neutrons, protons, and ions) and target atoms. Radiation damage could lead to the collapse of the ordered lattice, and the structure could be transformed into an amorphous phase. Failure of structural metals in advanced nuclear reactors is typically a consequence of deteriorating materials properties due to long term radiation, including void swelling, blistering, embrittlement, fracture and exfoliation of surfaces. Nanoscale materials often have new and technologically useful properties. Understanding radiation response of materials in this extreme state of matter is great relevance to fundamental science and to a wide range of materials applications under harsh environments. We attempt to attack such grand challenge by using a novel concept derived from our previous studies of nanostructured metallic composites.

Recently we discovered that certain multilayer composites possess unusual resistance to the accumulation of radiation-induced damage when individual layers are very thin, on the order of a few nanometers. The idea of exploring radiation tolerant metallic multilayer materials comes from the following rationale: It is well known that radiation induced defects tend to migrate to the interfacial regions in irradiated materials [183]. Nanostructured metallic multilayers have a large volume fraction of interfacial regions. These interfacial regions are expected to act as effective sinks for radiation induced defects. Due to the high diffusivity of solute atoms along interfaces, especially at medium to high temperatures, these interfacial regions may become freeways to “pipe out” defects at a high rate. Recovery processes may occur simultaneously with defect generation/accumulation in nanostructured metallic multilayers and therefore maintain their ability to continuously absorb radiation damages without significant void swelling

or blistering. Materials possessing a high volume fraction of interfacial regions may therefore be more radiation tolerant than conventional polycrystalline materials.

The goal of the study is to explore the fundamental radiation tolerance mechanisms through which certain types of interfaces in metallic multilayers may attract radiation induced point defects and facilitate the annihilation of unlike point defects by increasing their diffusivity along layer interfaces. We hypothesize that multilayer metals with immiscible interfaces have enhanced radiation tolerance than their bulk counterpart given that interfaces would function as defect sinks. We also suspect that there could be considerable size effect on interaction between interface and point defects because the volume fraction of atoms at interfaces increases monotonically with decreasing individual layer thickness. The major tasks of this research include (1) the fabrication of metallic multilayers with immiscible layer interfaces; (2) the exploration of size effect (layer thickness) on the microstructure and mechanical properties of multilayers before and after irradiation; and (3) the mechanisms of interaction of layer interfaces with radiation induced point defects. Because the capability of interface to absorb radiation induced point defects will decay due to the loss of interfaces, a major factor to consider is the stability of interfaces in a multilayer system. FCC Cu and BCC V were selected as the candidates in this study because of their ultra low solid solubility. The mutual solid solubility between Cu and V, is very limited, approximately 2.5 wt. % Cu in V matrix at 800 °C. Furthermore, the Cu and V system has a positive heat of mixing of ~ 5 kJ/mol, indicating high resistance of the interface to radiation induced mixing. The project will establish a new scientific approach to understanding the fundamental physics that governs the radiation response of metallic nanocomposites at nanoscale.

CHAPTER II

EXPERIMENTAL

2.1 Fabrication of metallic Cu/V multilayer films

A popular class of technique to synthesize the metallic multilayer films is physical vapor deposition (PVD), which allows us to deposit almost any metallic materials. In PVD process, the vapor particles are ejected from a source (target) and are deposited on the substrate to form thin film. One of the PVD techniques, molecular beam epitaxy (MBE), can deposit well-defined layer structures with the precision at atomic level by using a very low deposition rate. Another advantage of MBE is to synthesize single crystals or epitaxial films with high quality. In comparison, as one of the most widely used methods to deposit thin films, magnetron sputtering typically produces polycrystalline metallic materials at much higher deposition rates.

When energetic particles such as accelerated ions bombard the solid target surface, the target atoms from the solid surface are scattered backward due to collision cascade between the energetic particles and the target atoms. This phenomenon is called sputtering. Sputtering was discovered in 1852 by W.R. Grove in the investigation of discharge tubes where the film deposition on the anode place was observed [184]. Later sputtering was used to deposit metal films for mirrors and other applications. During the sputtering process, collision cascade between energetic inert gas ions and atoms within the target material occurs after positive inert gas ions are generated (usually Ar^{+} by the process of $Ar + e^{-} \rightarrow Ar^{+} + e^{-} + e^{-}$) and accelerated to target surface. One or more of the surface or near-surface atoms are kinetically dislodged by the impact of the energetic particle to the target. These dislodged atoms having considerable kinetic energy by

transferring from the initial particles, move deeper into the target material and dislodge extra atoms. This knock-on process only stops when the energy in the projectile or displaced atoms is smaller than the displacement energy. The residual energy is absorbed to generate phonons and this raises the local temperature. These atoms on or near the surface may be dislodged to leave surface by overcoming the surface binding energy due to enough energy transferred from the ions or other knock-on atoms, and are deposited on the substrate surface. These atoms are known as sputtered atoms and the process is termed as sputtering deposition.

The number of atoms (molecules) ejected from a target surface per incident ion is defined as sputtering yield Y. The magnitude of sputtering yield depends on factors including the details of energy transfer between incident and target atoms, mass and energy of incident ion, type of discharge gas, mass and binding energy of target atom, incident angle of the projectile. The sputter yield can be obtained either from the simulation such as SRIM in which collisions between the energetic ions and the paths are calculated by using collision potential, or from the experiments [185]. The empirical expression of sputter yield $Y(\alpha)$ as a function of incident angle is given by [186]:

$$Y(\alpha) = \frac{Y(0)}{(\cos^f \alpha)} \exp[f \cdot \cos \alpha_{opt} (1 - \frac{1}{\cos \alpha})] \tag{91}$$

where $Y(0)$ is the sputter yield at normal incidence to the target and α_{opt} is the incident angle corresponding to the maximum yield. The increase of the incidence angle of the energetic ions results in a smaller fraction of their energy deposited to the target. This leads to less sputtering. So sputter yield has a peak value at a certain angle [187]. In equation 91, f is a function of surface binding energy E_b of target, mass of recoil atoms m_r and discharge gas m_p atoms, and can be expressed by:

$$f = (E_b)^{1/2}[0.94 - 1.33 \times 10^{-3} \frac{m_r}{m_p}] \quad (92)$$

Sputter yield has a unit of atoms/ion, so the sputtering or deposition rate are in the unit of atoms$\cdot$cm$^{-2}s^{-1}$ atoms. But usually, the deposition rate is defined as the thickness of thin film deposited per second with the unit of nm/s by converting mass to thickness using the density. Experimentally, the deposition rate can be calculated based on the thickness of deposited thin film at a given time.

The sputter deposition is often practiced in plasma, which can be generated by a voltage applied across a cathode and an anode in the vacuum chamber. In most cases, the grounded chamber wall is treated as the anode, and the cathode is then biased negatively. The types of source for sputtering deposition include dc diodes, rf diodes and magnetrons.

Sputter-deposition of thin films has a wide range of applications, including architectural glass, semiconductors, automobiles' coatings and surface analysis by etching patterns. Since the transverse magnetic field normal to the electric field is applied to increase the ionization efficiency of electrons by increasing their path length in the sputtering, which is so called magnetron sputtering. The principle of DC magnetron sputtering is illustrated in Figure 2.1 [188]. During the magnetron sputtering process, secondary electrons close to the target will be trapped by a magnetic field where the electrons follow helical paths around the magnetic field lines. The confinement of electrons leads to more ionizing collisions with neutral gaseous atoms (such as Ar) near the target surface than would otherwise occur during a regular sputtering process, and in turn leads to a higher deposition rate. The sputtered atoms are neutrally charged and so are unaffected by the magnetic trap.

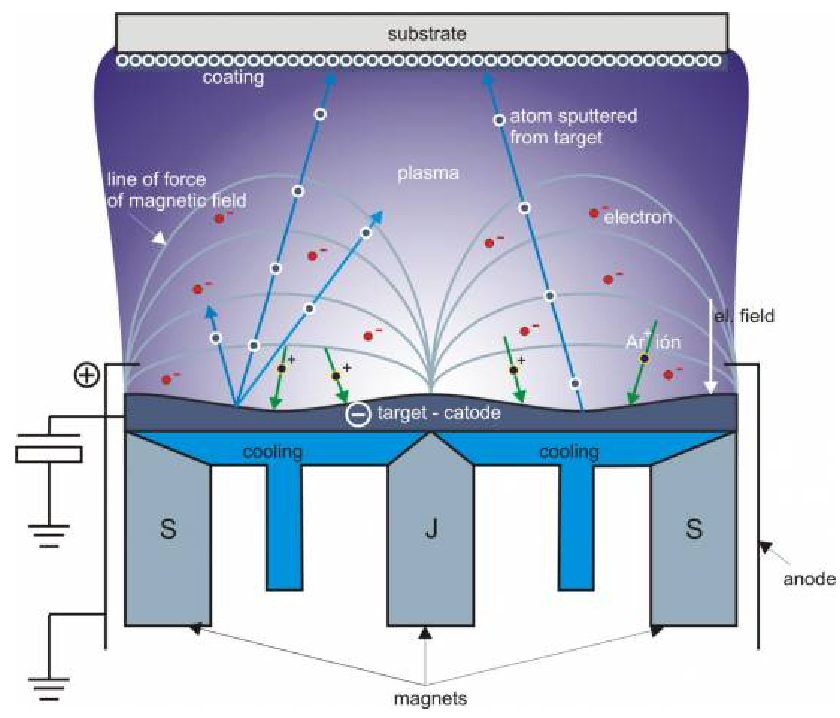

Figure 2.1. Principle of DC magnetron sputtering [188].

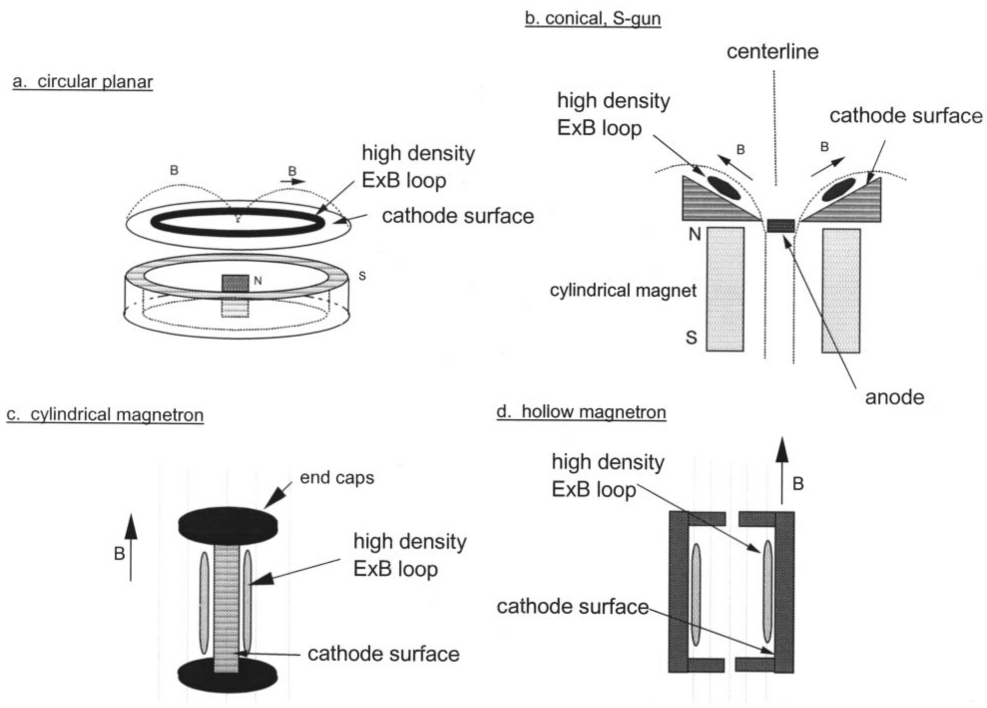

Figure 2.2. Magnetron (diode) cathode geometries (planar, conical, cylindrical, hollow) [189, 190].

There are a number of target geometries as shown in Figure 2.2 [189], including planar, conical, cylindrical and hollow, all of which are based on the same closed-loop effect [189, 190].

The advantages of magnetron sputtering are as follows. (1) There is almost no restriction on target material; (2) The sputtered films typically exhibit a better adhesion on the substrate than evaporated films; and (3) Magnets in the magnetron enable lower pressures to be used. When sputtering metals by using DC magnetron sputtering technique, the good conductivity of metals guarantees a discharge-free sputtering of the targets.

The fabrication of multilayer films in the study was performed by using DC magnetron sputtering system, shown in Figure 2.3. A typical magnetron sputtering system includes a vacuum chamber, controlling system operated by a computer, a load-lock system for loading sample, sputter guns, and sample stage for holding substrate. Three sputter guns with circular planar magnet cathode shown in Figure 2.4 are used in the custom-designed sputter system [189]. Prior to deposition, the chamber was evacuated to a base pressure of 5×10^{-8} - 1×10^{-7} torr. Pre-sputtering of Cu and V is typically performed to clean the target for avoiding contamination before depositing thin film. The substrate temperature during deposition was kept at room temperature. No heating or cooling was applied to the substrate during deposition. The deposition rate is varied in the range of 5-10 Å/s by controlling the dc power to the magnetron gun and the distance between targets to substrate. HF etched Si (100) and Si (100) with a native 1 μm thick SiO_2 layer were used as Cu/V multilayer film substrates for different purposes. The selection of Si (100) with a native 1 μm thick SiO_2 layer as substrate considers avoiding

the diffusion between the Si and multilayer films in annealing study. The multilayer films grown on HF etched Si (100) were used to prepare TEM samples.

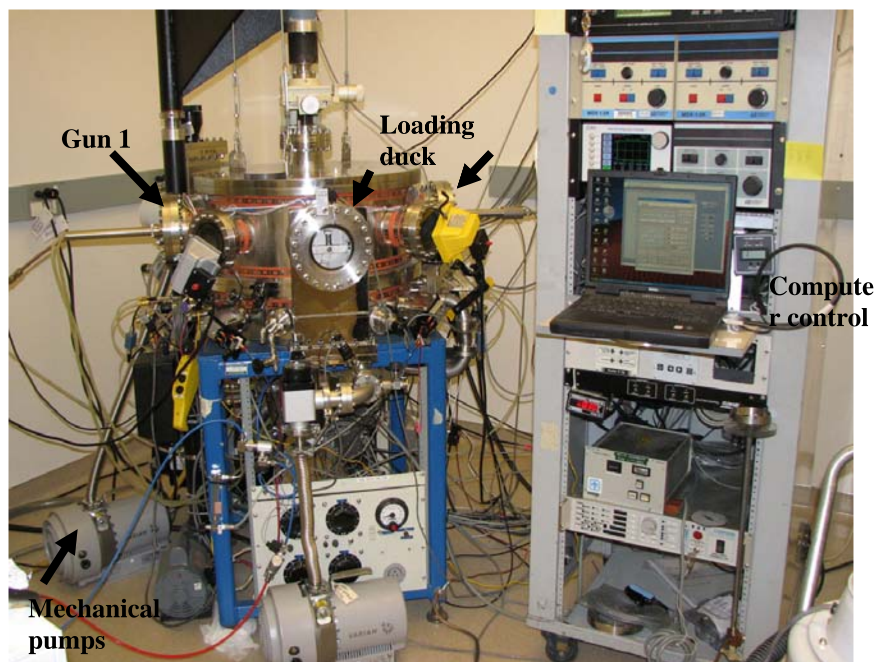

Figure 2.3. Front view of the custom-designed DC magnetron sputter system at Los Alamos National Laboratory. There are 3 sputter guns in this system. The deposition process is fully automated through computer control. (The 3rd gun is at the back side, not visible from the front view).

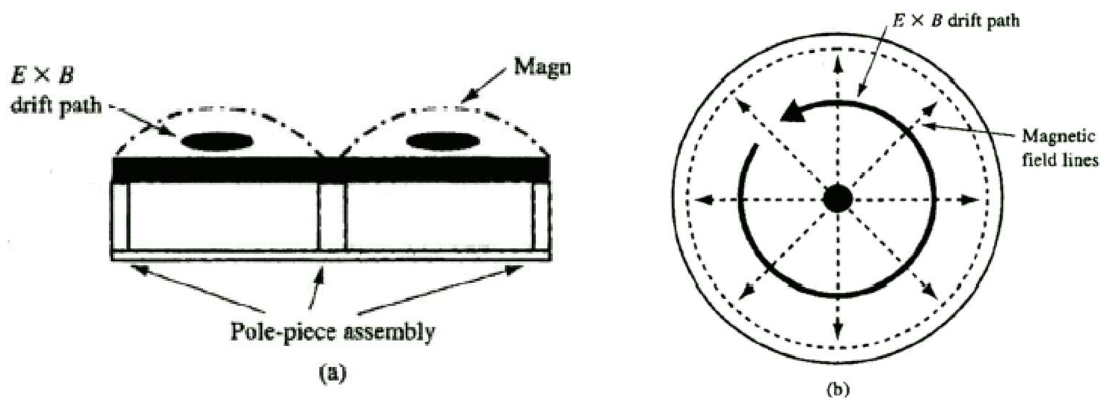

Figure 2.4. Schematic of a circular planar magnetic cathode for (a) side view and (b) top view [189].

2.2 Ion accelerator for ion irradiation studies

The basic elements in the typical ion accelerators illustrated in Figure 2.5 included ion source, acceleration column, mass separator, beam sweeping and target chamber. A wide variety of ion beams with sufficient intensity for irradiation can be produced by different types of ion sources such as protons, neutrons, helium, hydrogen, etc. [116]. The total fluence (ion dose) varies with the irradiation time and beam current density.

In this dissertation, He ion implantation at energy up to 150 keV with a fluence level up to $10^{17}/cm^2$ was performed in accelerator laboratory at Texas A&M University (TAMU) and ion beam materials lab in Los Alamos National Laboratory (LANL). The Accelerator Laboratory in TAMU is one of the largest university ion irradiation facilities in USA. A total of five accelerators are able to deliver virtually all ions in the elemental table with ion energy from a few hundred to a few MeVs. The lab provides unique capabilities to perform irradiation studies on various nuclear materials. The key facility in the study in the Accelerator Laboratory is a 150 kV Ion Accelerator (with a universal ion source). He ions were used for irradiation of Cu/V multilayers.

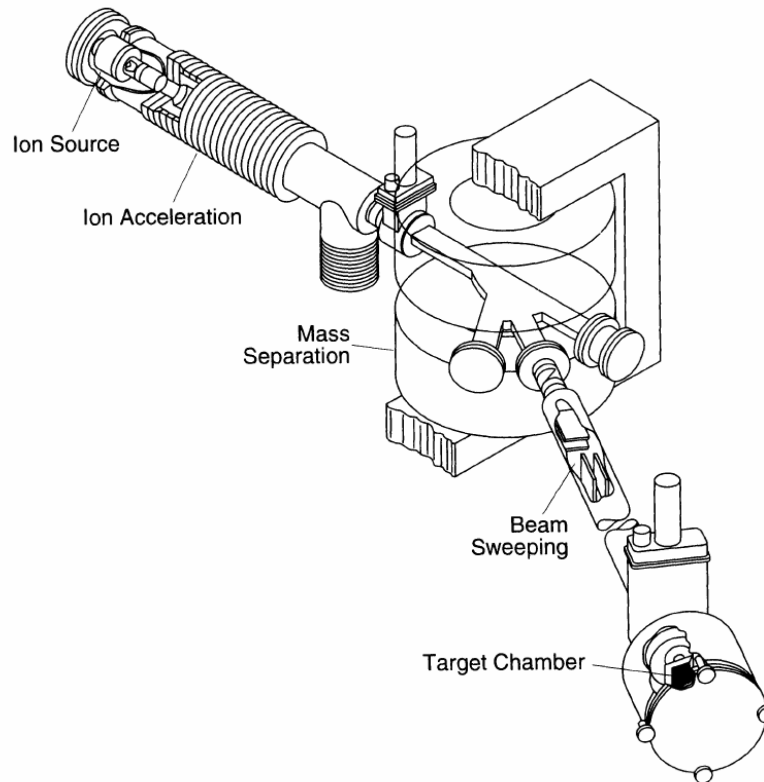

Figure 2.5. Schematics of typical ion irradiation system components [116].

2.3 Characterizations of metallic Cu/V multilayer films

Void swellings and radiation hardening are two of the major radiation effects in the irradiated metallic materials, and were extensively studied in the current project. Experiments were focused on detailed microstructure examination of ion-irradiated multilayered composites by transmission electron microscopy (TEM), scanning transmission electron microscopy (STEM) and x-ray diffraction (XRD), and the evolutions of mechanical properties examined by nanoindentation technique. TEM offers the details of microstructural changes, such as He bubbles, voids and dislocation loops. STEM can provide chemical information at nanometer length scales and therefore is helpful for checking interface morphology and chemistry before and after ion irradiation.

XRD determined the evolution of texture and lattice distortion originated from defect accumulation. These experiments were intended to examine the development of stable defect clusters as a function of proximity to interfaces or grain boundaries and the associated evolution of interface stability and chemistry that developed with irradiation. Mechanical properties (hardness and modulus) of multilayer coatings were studied by nanoindentation technique.

2.3.1 Transmission electron microscopy (TEM)

2.3.1.1 Transmission electron microscopy (TEM)

Transmission electron microscopy (TEM) is critical in evaluation of microstructure in sputtered Cu/V multilayer films, such as interface features, film structures and radiation damage. TEM is a microscopy technique whereby an electron beam is transmitted through an ultra thin specimen, interacting with the specimen as electrons pass through. An image is formed from the interaction of the electrons transmitted through the specimen, which is magnified and focused onto an imaging device, such as a fluorescent screen, as is common in most TEM microscopes, on a layer of photographic film, or to be captured by a CCD camera [191].

A typical TEM is composed of four systems: illumination, electromagnetic lens, sample stage and holder, and imaging system as shown in Figure 2.6 [192]. The illumination system provides a stream of monochromatic electrons by electron source composed of a cathode and an anode. Usually a heated tungsten or LaB_6 filament emits electrons, which are then confined into a loosely focused beam by a negative cap. The positive anode accelerates the focused beam, most of which will pass through the tiny hole in the center of the anode to form a stream of monochromatic electrons. When the

stream passes through the electromagnetic lens system, it is tightly focused to a small, thin, coherent beam with a well-defined energy by condenser lenses and metal aperture. The first condenser lens determine the general size range of the final spot that strikes the sample and the second condenser lens can adjust the size of the spot on the sample. The metal aperture, a thin disk with a small circular through-hole, is applied to restrict the electron beam and knock out high angle electrons before striking the specimen. The well-defined beam by electromagnetic lens system strikes the specimen, which is sitting in the sample holder, and parts of it are transmitted. The sample holder is a platform equipped with a mechanical arm for holding the specimen and controlling its position. Three types of transmitted electrons after interactions between the electron beam and specimen are collected to provide the sample information. The unscattered electrons are the incident electrons, which are transmitted through the thin specimen without any interaction occurring inside the specimen. The contrast generated by the unscattered electrons varies in terms of specimen thickness as the transmission of unscattered electrons is inversely proportional to its thickness. Elasticity scattered electrons are the incident electrons that are scattered to leave their original path by atoms in the specimen in an elastic fashion without loss of energy. The pattern generated by elasticity scattered electrons can provide the information regarding the orientation, atomic arrangements and phases present in the area being examined because all electrons scattered by the same atomic spacing will be scattered by the same angle, which follows Bragg's Law. Inelastically scattered electrons, which are incident electrons that interact with specimen atoms in a inelastic fashion, loosing energy during the interaction can be used to get either electron energy loss spectroscopy (EELS) or Kirkuchi bands. After transmitting the specimen, the electron

beam is focused by the objective lens into an image system consisting of another electromagnetic lens system and a screen. In the electromagnetic lens system, objective lens is used to re-focus the electrons after they pass through the specimen and projective lens can enlarge the image and project it onto the screen with a phosphorescent plate. The objective aperture can enhance the contrast of the image by blocking out high-angle electrons, and the projective aperture offers the functions to examine the periodic diffraction of electrons by ordered arrangement of atoms in the specimen. The image is formed in a similar way to photography after the electrons strike the phosphor plate and can be observed as it glows when it is hit by electrons.

Selected area diffraction (SAD) is a method in which the SAD pattern is produced on the display screen of the microscope when parallel electrons transmitted through a small area of the thin foil specimen determined by intermediate lens aperture size and are diffracted according to the Bragg's law. The SAD patterns of polycrystalline or nanocrystalline materials are composed of a transmitted beam and a number of rings. It can prove the information on the periodicities in the lattice, and hence the atomic positions, such as amorphous or crystalline, crystallographic features, orientation relationship of the interface, and so on.

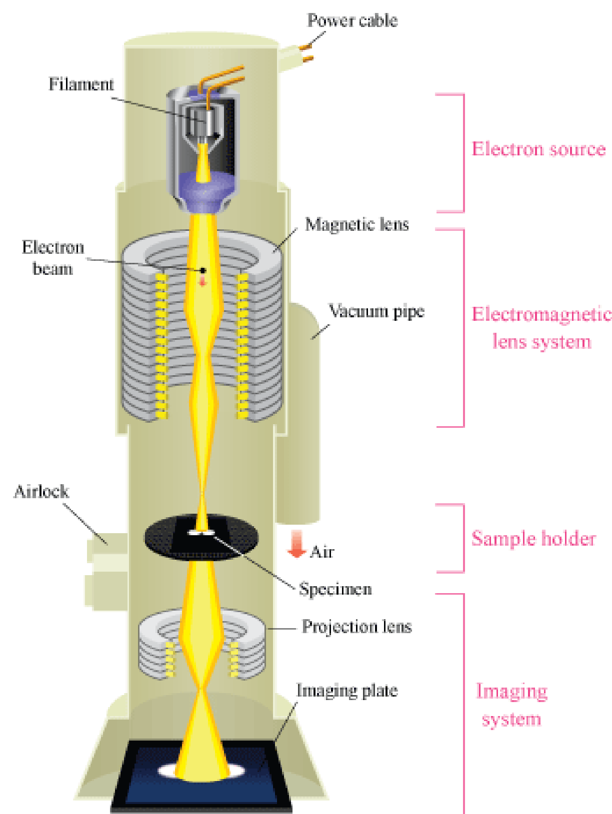

Figure 2.6. The schematic outline of a TEM [192].

Another type of TEM is a scanning transmission electron microscope (STEM). The electron optics focuses the beam into a narrow spot which is scanned over the sample in a raster when the electrons pass through the specimen. The contrast of different materials in STEM is directly related to their atomic numbers. STEM is typically accompanied by chemical analysis techniques, such as mapping by energy dispersive X-ray (EDX) spectroscopy, electron energy loss spectroscopy (EELS), and annular dark-field imaging (ADF) due to the rastering of the beam across the sample. After the introduction of a high-angle ADF detector into STEM, images with atomic resolution can be obtained.

TEM and STEM were performed in the microscopy and imaging center (MIC) at TAMU equipped with two transmission electron microscopes. One is JEOL JEM-2010 equipped with Gatan SC1000 ORIUS CCD camera (Model 832), using 200 kV accelerating voltage with a LaB_6 filament. This is a high-resolution analytical TEM microscope with 0.23 nm point resolution. The STEM and EDX were performed by the FEI Tecnai G2 F20 microscope with Fischione ultra-high resolution STEM HAADF detector (0.23 nm in the STEM image mode) and Oxford instruments EDX detector with a spatial resolution of ~ 1-2 nm.

2.3.1.2 Preparation of cross-sectional TEM (XTEM) samples

Sample preparation for TEM studies, whether cross-sectional or plan view, is a challenge because of the tiny dimensions of specimens required for the experiment. Typically a TEM holder has about 3 mm space for the sample to be analyzed. However the thickness of the electron transparent specimens is on the order of nanometers. Usually, TEM samples can be prepared by conventional thinning and focused ion beam cutting (FIB). Ion milling is the most commonly used method for solid samples and was used in the study. Figure 2.7 shows several steps for a TEM sample to become electron transparent. The bulk sample was firstly cut into thin slices with around 0.6 mm thickness. Then the sample was grinded and polished to around 60 μm thick and was punched to get a 3 mm diameter disks. After that, the disk was dimpled until the thickness in the center reaches about 10 to 20 μm. The last step is to ion mill the sample in the ion milling machine until it is penetrated.

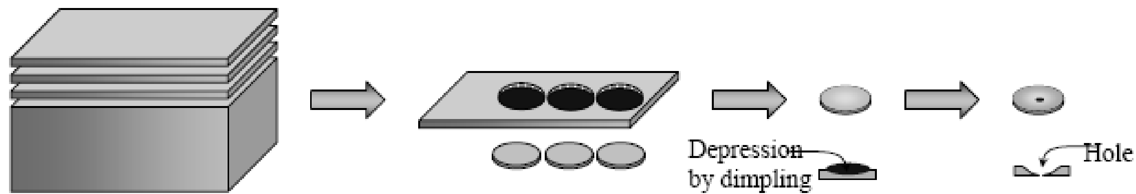

Figure 2.7. The schematic of TEM sample preparation by ion-milling [193].

Particularly, when preparing cross-sectional TEM (XTEM) samples for multilayer films on substrates, a small piece of specimen is bonded by using M-bond to another piece of Si, and the sandwich is pressed to cure at about 100 °C for 3 hours. Once the sample is cured, mechanical grinding and polishing were performed from both sides of the sandwiches to eventually ~ 60 μm. Then the sample is further thinned by Gatan dimpler to 30 μm, followed by ion milling to obtain an electronically transparent TEM specimen.

2.3.2 X-ray diffraction (XRD)

X-ray diffraction is a powerful and non-destructive tool for the structural study of multilayer films. No sample preparation is required in this quick and versatile technique. XRD was extensively utilized in this study especially for the comparison of the crystallinity of as-deposited and ion irradiated multilayer films.

In the XRD experimental, the multilayer thin film samples are exposed to a monochromatic beam of x-rays from a Cu-K_α source, which is used to investigate the crystal structure. The wavelength of these x-rays is of the same order as the interatomic distance (a few Å), which allows atomic structure of the deposited thin film to be studied. The thin film sample scatters the incident x-ray beam in all directions. However, due to the periodic arrangement of atoms on specific crystallographic planes in the crystalline

solid thin film, the scattered x-rays mutually reinforce each other in certain directions, giving rise to a strong (high-intensity) diffracted beam by constructive interference. The position (angle θ) of the diffracted beam is given by the Bragg's law (93):

$$n\lambda = 2d\sin\theta \qquad (93)$$

where n is the order of diffraction, λ is the wavelength for the incident x-ray beam, d is the spacing between planes that contribute to diffraction, and θ is the angle between incident beam and the crystallographic plane. An x-ray detector such as a Geiger counter or a scintillation counter, mounted on a movable arm, detects the diffracted beam. From the intensity and position of the diffracted beam, various interplanar spacings, crystal structure, and orientation of the thin film are determined. From equation (93), a basic condition for the waves reflected from a given set of planes to be in phase with one another is set that the difference of path lengths for waves reflected from successive planes must be an integral multiple of the wave length, i. e. n = 1, 2, etc.. Figure 2.8 shows diffraction according to Bragg's law.

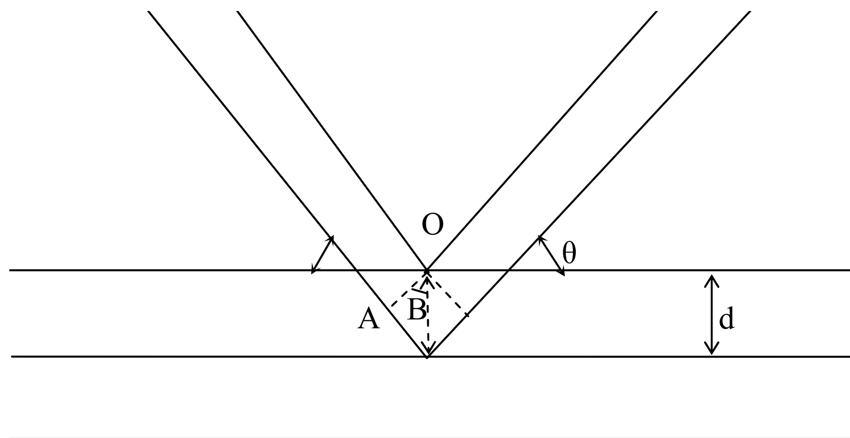

Figure 2.8. Diffraction according to Bragg's law.

XRD was performed in the study by two Bruker powder diffractometers (D8-Focus Bragg-Brentano and D8-Vario) in the X-ray Diffraction Laboratory at the Department of Chemistry in TAMU. Bruker-AXS D8 advanced Bragg-Brentano X-ray powder diffractometer (XRD) is equipped with Cu-K_α source anode, D8 Goniometer, automatic divergence slit, graphite monochromator on the diffracted beam and Lynxeye PSD for detection. The divergent x-ray beam of filtered or monochromatized radiation impinges on the flat face of a sample. This sample is rotated at precisely one-half of the angular speed of the receiving slit so that a constant angle between the incident and diffracted beams is maintained. The receiving slit is mounted in front of the counter on the counter tube arm, and behind it is usually fixed with a scatter slit to ensure that the counter receives radiation only from the portion of the sample illuminated by the primary beam.

The angle between the direct x-ray beam and the diffracted beam is 2θ, where θ is the Bragg angle for each set of crystal planes. This is called the 2θ method. The divergent x-ray beam of filtered or monochromatized radiation impinges on the flat face of a sample. The sample is rotated at precisely half of the angular speed of receiving slit so that a constant angle between the incident and diffracted beam is maintained.

2.3.3 Nanoindentation

2.3.3.1 Definition of hardness

The mechanical properties of a material reflect its response or deformation to an applied load or force. Hardness is one of the important mechanical properties of a material and indicates its resistance to localized plastic deformation or to permanent penetration by another hard material. Hardness can be measured by performing carefully

designed laboratory experiments that replicate as close as possible the service conditions [194]. Measuring hardness involves two steps. Firstly a small and hard indenter is pressed into the material with a load F and the displacement is composed of elastic and plastic deformation; secondly when the indenter is retracted, the elastic deformation is recovered and only the residual area A (plastic deformation) is measured [195]. Figure 2.9 shows the schematic diagram of the cross-section of an indentation [196]. The harder the material, the smaller and shallower is the indent. The hardness is defined by:

$$H = \frac{F}{A} \tag{94}$$

where H is hardness, F is load and A is residual area.

Based on the hardness definition, quantitative hardness measurement techniques have been developed over the years and they include Rockwell hardness test, Brinell hardness test, Vickers and knoop microhardness tests [197]. These conventional hardness test methods satisfy the need of hardness measurement for bulk materials with larger dimensions; however, their load and indenter size limit applications in materials with at least one dimension in the micrometer or nanometer length scale such as thin film, particle, second phase, nanowire, etc. Micro-scale or nano-scale materials are often subjected to extreme conditions and their hardnesses are different from that of the bulk materials due to dimensional constraints. So a novel approach to measure the hardness of micro- or nano-scale materials is desirable. Nanoindentation technique combined with high resolution record of indentation depth and load and corresponding data analyses was developed to perform the hardness measurement of small structures [195].

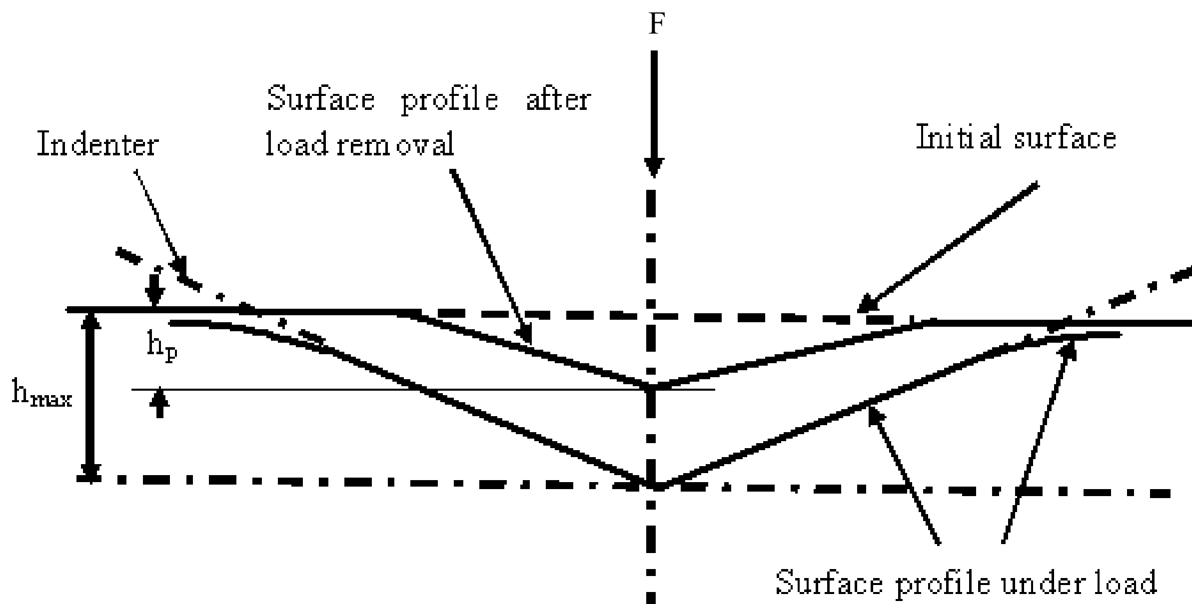

Figure 2.9. Schematic representation of the cross sectional indentation [196].

2.3.3.2 Determination of indentation hardness

The nanoindentation instrument must have the capability of applying and recording the predetermined load and displacement with very high resolution during indentation, and use powerful computational method to perform the indentation load displacement analysis and obtain the mechanical properties directly from the load-displacement data.

The hardness of materials measured by nanoindentation is referred as indentation hardness (H_{IT}) and it is determined by equation:

$$H_{IT} = \frac{F_{\max}}{A_c} \tag{95}$$

where $F_{\max}$ is the maximum applied force and A_c is the projected (cross-sectional) area of the contact between the indenter and the test piece determined from the load-displacement curve. A_c can not be measured directly and is an area function, which

describes the shape of the indenter tip. It can be expressed as a mathematic function relating to the depth of contact of the indenter with the test piece h_c ($A_c = f(h_c)$) [198].

The indentation hardness measurement process is similar to the conventional techniques. Hardness values are directly obtained from the load-displacement curve, but they are sensitive to the details of the analysis. Data analysis methods include elastic contact model [199-201], continuous stiffness method [202], and Herzian contact solution for spherical indenters [203, 204]. Among these, the analysis based on elastic contact model developed and refined by Oliver and Pharr in 1992 [201] is the most commonly used nanoindentation analysis method, and is used to determine the indentation hardness of thin film in the dissertation as well. It assumed: (1) deformation upon unloading is purely elastic; (2) the compliances of the samples and of the indenter tip can be combined as springs in series and (3) the contact can be modeled using an analytical model for contact between a rigid indenter of defined shape with a homogeneous isotropic elastic half space using equation:

$$S = \frac{2E_r\sqrt{A_c}}{\sqrt{\pi}} \tag{96}$$

where S is the contact stiffness, A is the contact area, and E_r is the reduced modulus [201].

Based on these assumptions, contact depth h_c can be expressed by:

$$h_c = h_{\max} - \varepsilon(h_{\max} - h_i) \tag{97}$$

where $h_{\max}$ is the maximum depth, and h_i, the intercept depth, is the intercept of the tangent to the load-displacement data at the maximum load on unloading with the depth

axis [201]. The correction factor ε, a function of the shape of the indenter tip, for different indenter geometries is shown in Table 2.1 [198].

Table 2.1. Correction factor for different indenter geometries [198].

Indenter Geometry	ε
Flat punch	1
Conical	2(π-2)/π=0.73
Berkovich, Vickers	3/4
Paraboloid of revolution (includes spherical)	3/4

The procedure for data analysis to obtain indentation hardness is as follows: The slope of the fit at $F_{\max}$ is used to obtain h_i, and $h_{\max}$ at $F_{\max}$ is acquired in load-displacement curve shown in Figure 2.10 [205]. Correction factor ε is determined by the shape of indenter tip. So the contact depth h_c can be obtained by inputting $h_{\max}$, h_i and ε according to equation (97). The project area A_c is a function of shape of indenter tip. For a Vickers indenter, a pyramid shape indenter with a square base, $A_c = 24.5 \times h_c{}^2$ and for a perfect Berkovich indenter, a diamond pyramid with triangular base, $A_c = 23.96 \times h_c{}^2$ [198]. The obtained h_c is put into the area function to get A_c. Finally the indentation hardness can be obtained according to equation (95).

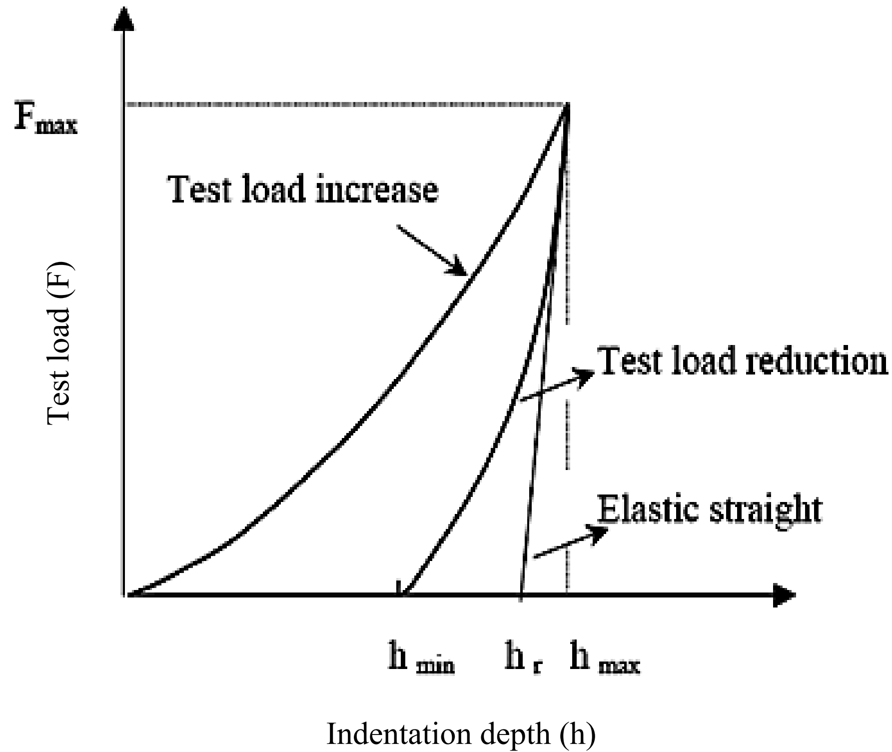

Figure 2.10. Schematic diagram of a loading-unloading curve during indentation, where $h_{\max}$ is maximum displacement, h_f is final depth and h_i is the intercept displacement [205].

2.3.3.3 Determination of indentation modulus

The elastic contact model assumes that the compliances of the samples and the indenter tip can be combined as springs in series, so

$$\frac{1}{E_r} = (\frac{1-v_{indenter}{}^2}{E_{indenter}}) + (\frac{1-v_{IT}{}^2}{E_{IT}}) \tag{98}$$

where E_r is called reduced modulus, $E_{indenter}$ is the modulus of indenter and E_{IT} is modulus of the tested materials. $v_{indenter}$ and v_{IT} is the Poisson's ratio of the indenter and the tested materials, respectively. In the contact model, the contact stiffness describes the slope of the tangent of load-displacement curve during unloading cycle and can be

expressed by equation (96) [201]. So reduced modulus is obtained by a rearrangement of equation (96) as:

$$E_r = \frac{S\sqrt{\pi}}{2\sqrt{A_c}} \tag{99}$$

According to equation (98), the E_{IT}, modulus of the tested materials can be expressed by:

$$E_{IT} = (1 - V_{IT}{}^2)/(\frac{1}{E_r} - (\frac{1 - v_{indenter}{}^2}{E_{indenter}}) \tag{100}$$

E_r can be obtained according to equation (99) after contact stiffness, the slope of the tangent, is acquired from loading-unloading curves. So combining the equation (99) and (100), finally the E_r can be obtained according to the following equation

$$E_{IT} = (1 - V_{IT}{}^2)/(\frac{2\sqrt{A_c}}{S\sqrt{\pi}} - (\frac{1 - v_{indenter}{}^2}{E_{indenter}}) \tag{101}$$

The indentation modulus is comparable to the Young's modulus of the material.

Accurate quantitative measurements of indentation hardness and modulus may be obtained by nanoindentation measurements. However, results from this technique are influenced by many factors such as tip geometry, machine compliance, time-dependent displacements, surface roughness, indentation size, etc. [195, 206-209].

2.3.3.4 Measurement of thin film hardness

The nanoindentation measurements in our study were performed by the Fischerscope HM2000XYp measurement system, which measures the indentation hardness according to ISO 14577. Basically, the hardness measured with Fischerscope HM2000XYp is determined from the area of the indenter displacement under load. The indentation depth and a constant, specific to each indenter, are used to calculate the area

of the indenter displacement. The positioning devices consist of the holding device for the measuring head and a microscope with an attached video camera for viewing the test area in a video image that is shown on the computer monitor. Manually adjustable XY measuring stage and programmable XY measuring stage are equipped in the tester. The coordinates of the measurement points can be stored and visited automatically in sequence. A Vickers indenter was used as the indenter. The load range is from 0.4 to 2000 mN and the maximum indentation depth of the indenter is 150 μm [210]. The tested materials in our study in the nanoindentation measurement are thin films grown on silicon substrate. For an example, the hardness and indentation modulus of Cu/V multilayer thin films were measured based on an average of 9-12 indents at different indentation depths at room temperature with the same loading rate. The maximum indentation depth was kept at ~ 200 nm for all specimens [211]. The low surface roughness of the thin film (a few nm) leads to a negligible roughness effect. The total thicknesses of the films are ~ 2 μm, so the maximum depth is kept at below 200 nm, which satisfies the one-tenth of film thickness "rule of thumb" to eliminate the substrate effect [201, 212].

2.3.4 Profliometer

The Dektak^3 Stylus Profilometer shown in Figure 2.11 can measure small vertical features ranging in height from 10 to 65,000 nm. The height position of the diamond stylus generates an analog signal which is converted into a digital signal stored, analyzed and displayed. The radius of diamond stylus is 12.5 microns, and the horizontal resolution is controlled by the scan speed and scan length.

There is a horizontal broadening factor which is a function of stylus radius and step height. This broadening factor is added to the horizontal dimensions of the steps. The stylus tracking force is factory-set to 50 milligrams. The scanning head contains a viewing camera, a motor driven stylus and analog electronics to detect and amplify the transducer signal.

Before helium (He) ion irradiation, the samples with 5 × 10 mm in dimension were partially masked to avoid ion irradiation in the masked regions. After irradiation experiments, the difference in height (step height) between the irradiated and masked regions was measured by using a Dektak^3 Stylus profilometer with a Z height resolution of better than 1 nm.

Figure 2.11. Photos of the Dektak^3 ST step profilometer [213].

CHAPTER III

PROPERTIES OF CU/V AND AL/NB MULTILAYERS *

3.1 Introduction

Nanostructured metallic multilayers have received broad attention due to their high mechanical strength [1, 6, 214, 215]. The yield strength of certain metallic multilayers, estimated as 1/3 of nanoindentation hardness [216], can approach 1/2 to 1/3 of the lower-bound estimate of theoretical strength limit of $\mu/30$, (where μ is the shear modulus) [217]. The evolution of film hardness as a function of layer thickness has been studied, and various strengthening mechanisms have been proposed [2, 72, 79, 218-223]. At micron to submicron length scale, the yield strength of multilayers is proportional to $h^{-0.5}$, where h is the individual layer thickness, a phenomenon that can be explained by Hall-Petch model of dislocation pile-ups at layer interfaces. Furthermore, Hall-Petch slope is a measure of the strength of interface barrier for slip transmission and determines the rate of strength increase with decreasing h. However, in the tens of nanometers regime, the deformation mechanism may involve glide of single dislocation, in the form of Orowan loops, leading to a $\sigma_y \propto \ln(h)/h$ relation [2, 218]. In the limit of a few nanometers, the strength of the multilayer may be determined by the stress to transmit a single dislocation across the interfaces. Factors such as shear modulus mismatch and lattice parameter mismatch may determine the transmission stress, Koehler stress or coherency stress, for single dislocation [1, 99, 224]. Molecular dynamics simulations have shown that in fcc/fcc systems, such as Cu/Ni, coherency stress determines the peak strength of multilayers [94]. In fcc/bcc systems with incoherent interfaces, such as

---

*Reprinted with permission from “Mechanical Properteis of Sputtered Cu/V and Al/Nb Multilayer films” by E.G Fu, Nan Li, A. Misra, R.G. Hoagland, H. Wang, X Zhang, 2008. *Materials Science and Engineering A*, 493, 283-287, Copyright [2007] by Elsevier B.V.

Cu/Nb, a weak interface leads to dislocation core spreading and creates a strong barrier for the transmission of slip activity [94].

In this chapter, we report on the mechanical properties of two fcc/bcc multilayer systems, Cu/V and Al/Nb. Comparisons of their mechanical properties with Cu/Cr and Cu/Nb studied previously provide insight on the factors that determine strengthening mechanisms and peak strength in these multilayer films.

3.2 Experimental

Cu/V and Al/Nb multilayers with individual layer thickness ranging from 1 nm to 200 nm were deposited at room temperature on Si (100) substrates with native SiO_2 layer by DC magnetron sputtering technique. A base pressure of $\leq 5 \times 10^{-8}$ torr ($\sim 6.67 \times 10^{-6}$ Pa) is reached prior to deposition. The number of bilayers deposited was such that the total multilayer film thickness was kept at ~ 1.6 - 2 μm. The deposition rate for various metals was kept at a few Å/sec or higher. X-ray diffraction (XRD) experiment was performed by using Bruker-AXS D8 VARIO high-resolution X-ray diffractometer. Transmission electron microscopy (TEM) was performed on a JEOL 2010 operated at 200kV, and high resolution TEM (HRTEM) was performed on a JEOL 3000F operated at 300kV. The hardness and indentation modulus of films were measured by means of an indentation load and depth sensing apparatus, a commercial Fischerscope HM200, using a Vickers indenter. The maximum indentation depth was kept at about 200 nm for all experiments.

3.3 Results

Distinct Cu (111) and V (110) peaks are observed in XRD patterns of Cu/V 50 nm multilayers as shown in Figure 3.1. The two peaks start to overlap at smaller layer

thickness and eventually, at a layer thickness of 2.5 nm, only one broad peak is observed centered at a two-theta value between Cu (111) and V (110).

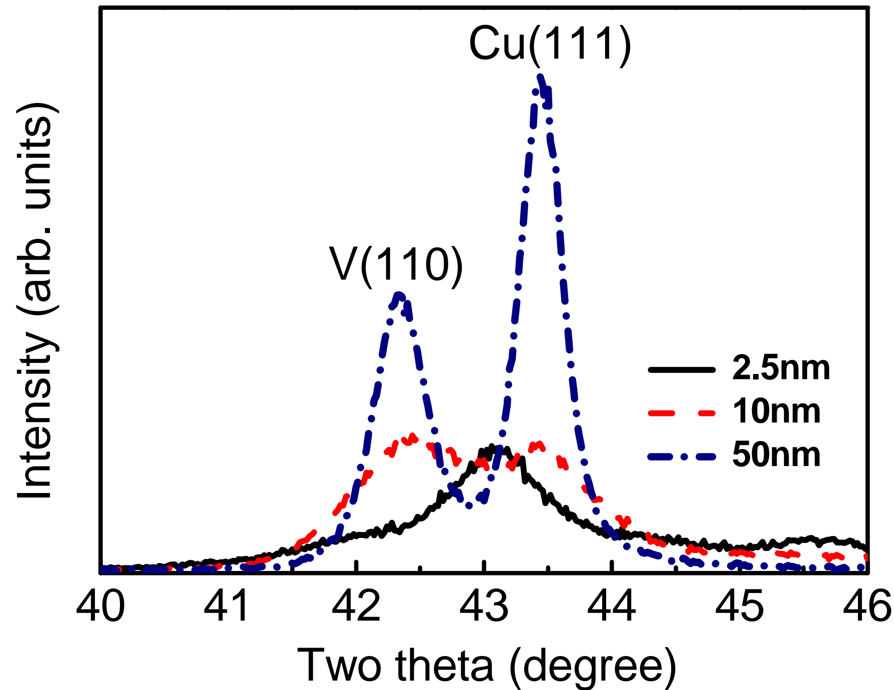

Figure 3.1. X-ray diffraction patterns of Cu/V multilayers. Two distinct peaks, corresponding to Cu (111) and V (110), are observed in Cu/V 50 nm multilayers. The two peaks tend to overlap at smaller layer thickness, Cu/V 10 nm multilayers, and eventually only a single peak is observed in Cu/V 2.5 nm multilayers.

Figure 3.2a is the cross-sectional TEM micrograph of as-deposited Cu/V 2.5 nm multilayer films. The layer interface between Cu and V is clearly distinguishable. The inserted selected area diffraction pattern (SAD) indicates a strong fiber texture with Kurdjumov-Sachs (K-S) orientation relationship, i.e. {111}Cu // {110}V and <110> Cu // <111>V. The columnar grain sizes of Cu and V are much greater than layer thickness. The cross-sectional TEM micrograph and the corresponding SAD pattern of Cu/V 100

nm multilayers are shown in Figure 3.2b. Both constituents have polycrystalline microstructures without a strong texture. The cross-sectional TEM micrograph of as-deposited Al/Nb 5 nm multilayer films is shown in Figure 3.3a. No significant intermixing is observed. Furthermore, such multilayer films have strong fiber texture, Al {111} and Nb {110}, with a K-S orientation relationship similar to that of Cu/V 2.5 nm multilayers. Microstructures of as-deposited Al/Nb multilayers with individual layer thickness of 50 nm, not shown here, or greater exhibit weaker texture as compared to the 2.5 nm layer thickness.

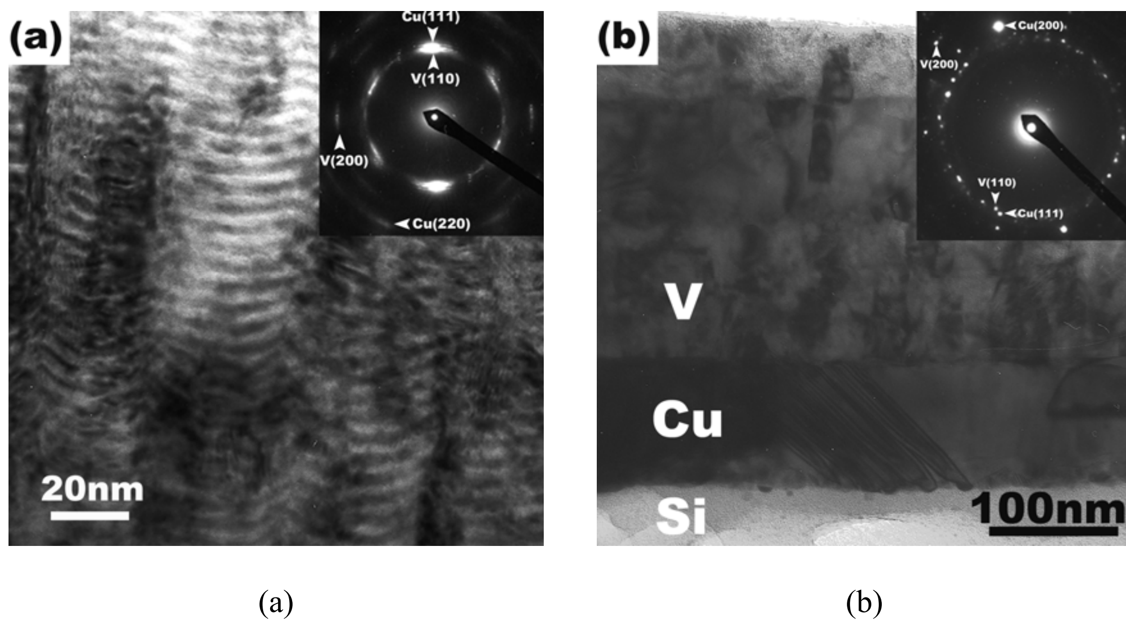

(a) (b)

Figure 3.2. (a) Cross-sectional TEM micrograph of as-deposited Cu/V 2.5 nm multilayer films, and (b) as-deposited Cu/V 100 nm multilayer films. Insets are selected area diffraction patterns.

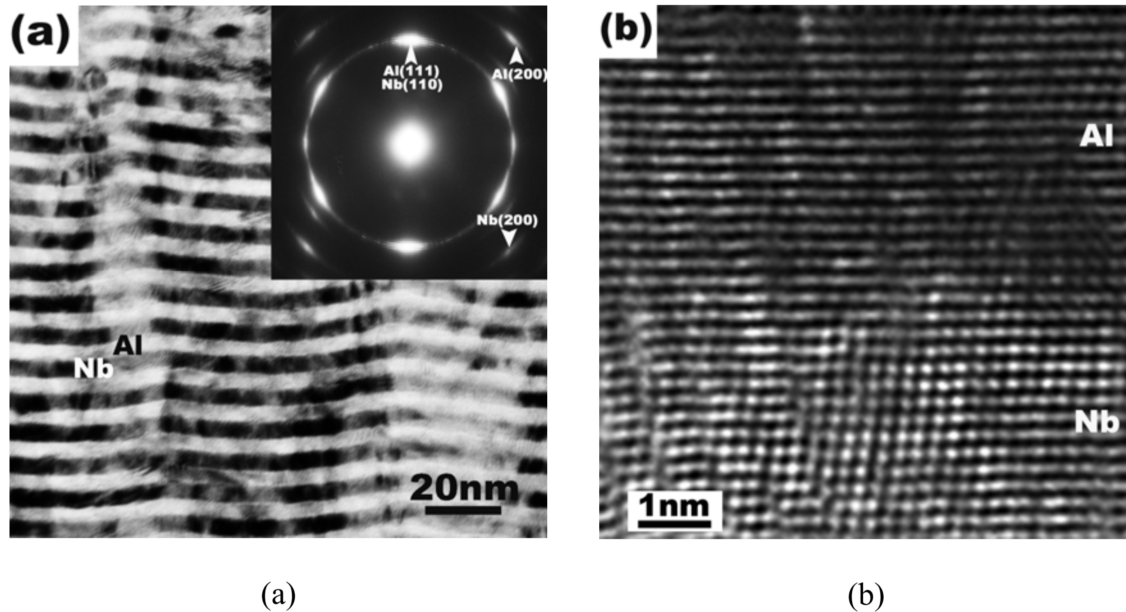

(a) (b)

Figure 3.3 (a) Cross-sectional TEM micrograph of as-deposited Al/Nb 5 nm multilayer films. The inset is SAD pattern, and (b) Cross-sectional view of high resolution TEM (HRTEM) micrograph of as-deposited Al/Nb 5 nm multilayer films.

HRTEM micrograph of interface of Al/Nb 5 nm multilayers shown in Figure 3.3b indicates little intermixing along interfaces. Fast Fourier transform from the micrograph has confirmed a K-S orientation relationship, and more importantly shows that atomic arrangement is such that Al{111} and Nb{110} atomic planes are continuous across interface.

The hardnesses of Cu/V and Al/Nb multilayers are plotted as a function of $h^{-1/2}$, as shown in Figure 3.4. The hardness data of Cu/Cr and Cu/Nb metallic multilayers [93] are also shown in the same plot for comparison. When layer thickness is greater than ~ 50 nm, the hardnesses of all multilayers increase approximately linearly versus $h^{-1/2}$ with decreasing layer thickness. The Hall-Petch slope is the highest for Cu/Cr multilayer, followed by Cu/Nb, Cu/V and Al/Nb multilayers. Such linear relation is quickly deviated at smaller layer thicknesses. Peak hardnesses are approached at approximately the

smallest layer thickness for all systems, except in Cu/Cr system, where the peak hardness is approached at 10 nm individual layer thickness and stays constant thereafter. Among these four systems, the peak hardnesses of Cu/Cr and Cu/Nb, almost identical at ~ 6.8 GPa, are the highest, and Al/Nb has the lowest peak hardness at ~ 4.8 GPa.

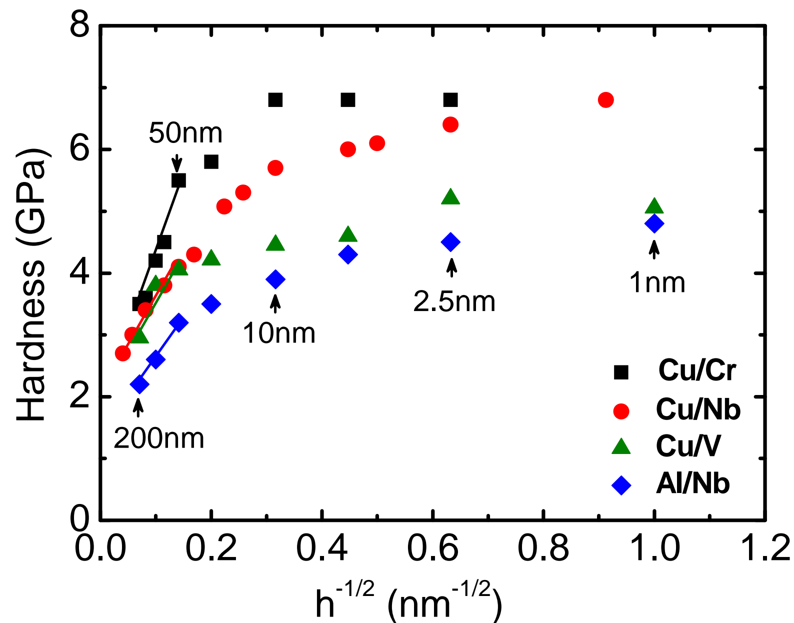

Figure 3.4. Comparison of hardness vs. $h^{-0.5}$ plots for various fcc/bcc metallic multilayer systems, including Cu/Cr, Cu/Nb, Cu/V and Cu/Nb, where h is the thickness of each layer.

3.4 Discussions

3.4.1 Microstructure of multilayer films

The mutual solubility between Cu and V is very small, approximately 2.5 wt% Cu in V matrix at 800 °C [21]. Such immiscible nature, derived from thermodynamics, is consistent with the observation of chemically discrete interfaces in all Cu/V multilayer films. Cu/V multilayer with smaller individual layer thickness (10 nm or less) has

stronger fiber texture with K-S orientation relationship, whereas a weaker texture is observed in Cu/V multilayers at layer thicknesses of 50 nm or greater. The evolution of texture intensity and K-S orientation relationship are similar in Al/Nb multilayer films. Although phase diagram shows the formation of several intermetallic phases between Al/Nb [21], we did not observe significant intermixing, and no new phases are identified by either XRD or TEM in current studies. The retention of interface between miscible Al and Nb is partly attributed to the fact that all deposition was performed all at room temperature at which there is not sufficient thermal energy to promote inter diffusion. Furthermore heating was prohibited during TEM specimen preparations. We have studied the microstructures of Cu/Cr and Cu/Nb previously. Both systems have fcc/bcc type of layer interfaces, and the texture and K-S orientation relationship are similar to the current cases. Examination of phase diagrams of Cu/Cr and Cu/Nb indicates that both systems are basically immiscible [21].

3.4.2 Comparison of Hall-Petch slope of fcc/bcc multilayer systems

The phenomena that hardness is proportional to $h^{-1/2}$ at layer thickness of 50 nm or greater in all cases can be explained by the Hall-Petch model, based on dislocation pile-ups at layer interfaces [77]. Dislocation pile-ups become more and more difficult at smaller layer thicknesses. The deviation from the Hall-Petch linear relationship occurs when the number of dislocations (n) in the pile-up is less than 2 for a circular pile-up ($n \leq 3$ for a double-ended pile-up and $n \leq 6$ for a single -ended pile-up) [225-227]. Hall-Petch slope, k, is a measure of interface barrier strength for slip transmission and can determine the rate of strength increase with decreasing h. Hall-Petch slope was calculated using:

$$k = 0.18\mu\sqrt{b} \tag{102}$$

where μ and b are the shear modulus and the magnitude of Burgers vector of the stiffer component of the multilayers, respectively [228]. The magnitude of Burgers vector is $a\sqrt{2}/2$ in fcc phase and $a\sqrt{3}/2$ in bcc phase, where a is lattice parameter. The calculated k values for each multilayer system are given in Table 3.1. Briefly the experimental Hall-Petch slopes are in good agreement with that of calculated values. For instance, in Cu/Nb and Cu/V systems, Cu is the stiffer phase. Therefore the calculation predicts that the Hall-Petch slope of the two systems shall be the same. This is precisely what the experimental results have shown in Table 3.1. In Cu/Cr, the calculated k based on the stiffer component, Cr is slightly lower than experimental result. In Al/Nb multilayers, the calculated slope based on the stiffer Nb phase is similar to experimental value. These studies indicate that in thicker multilayer composites, at length scale of tens of nanometers or greater, the interface barrier strength of multilayers could be dominated by the strength of the stiffer component.

Table 3.1. Calculated and experimental H-P slope of nanoscale metallic multilayers.

Metallic multilayers	Cu/Cr	Cu/Nb	Cu/V	Al/Nb
Average shear modulus* (GPa)	70	42	46	31
Calculated k, (MPa$\sqrt{m}$)	0.29	0.14	0.14	0.11
Experimental k (MPa$\sqrt{m}$)	0.33	0.16	0.15	0.12

* Shear modulus (GPa): Cu (46), Cr (93), Nb (38), V (46), and Al (25)

3.4.3 Comparison of peak hardnesses of various fcc/bcc multilayer systems

The peak hardnesses of four fcc/bcc multilayer systems are listed in Table 3.2, together with the heat of mixing and mismatch strain between fcc {111} and bcc {110} interplanar spacing. The peak hardness is the highest for Cu/W [230], then Cu/Cr and Cu/Nb, followed by Cu/V and Al/Nb in descending sequence. We will attempt to understand the difference in their peak hardness based on factors that may determine the interface barrier strength, including average shear modulus and modulus mismatch and dislocation core spreading along interfaces.

At layer thickness of a few nanometers, the metallic multilayer films typically reach peak hardness, and thereafter, the hardness varies very little with layer thickness. At length scales of a few nanometers, dislocation pile-ups are less likely; instead the strength of multilayer films is dominated by the strength of interface barrier to the transmission of single dislocation [50, 231].

Table 3.2. A comparison of peak hardness of several multilayers.

System	Average biaxial modulus (GPa)	Indentation modulus (GPa)	Mismatch strain* (%)	Heat of mixing (kJ/mol) [229]	Peak hardness (GPa)
Cu/W	415	228	13.1	22	8.9
Cu/Cr	296.5	170	2.3	12	6.8
Cu/Nb	211.5	115	10.5	3	6.8
Cu/V	228	111	2.5	5	5.2
Al/Nb	138	95	0.02	-18	4.8

Mismatch strain between the fcc {111} and bcc {110} interplanar spacing

In earlier literature, it was postulated that the Koehler stress plays a dominant role in determining the peak strength, especially in systems with large elastic modulus mismatch [1]. We examine this by plotting the peak hardness as a function of the average biaxial modulus of the multilayers. A plot of the peak hardness versus average biaxial modulus revealed essentially identical trends as in Figure 3.5. The average biaxial modulus for each multilayer system is the average value of biaxial modulus between fcc [111] and bcc [110]. The biaxial modulus for each metal is taken from the paper by D. Baral et al. [232]. While there is a general trend of the peak hardness scaling with the modulus, there are significant departures from this trend as well. For an example, Cu/Nb is significantly harder than Cu/V in spite of similar moduli, and Cu/Cr and Cu/Nb have similar peak strengths in spite of a large difference in moduli. Thus, the peak strengths of these fcc/bcc multilayers cannot be interpreted solely based on the Koehler stress.

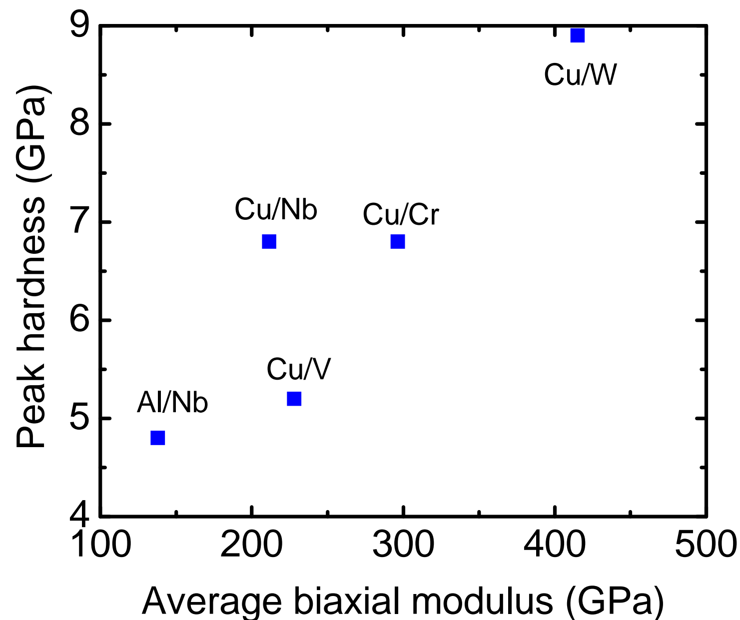

Figure 3.5. The peak hardness as a function of the average biaxial modulus of the various fcc/bcc metallic multilayers. Average biaxial modulus for fcc/bcc multilayer is the average value of the biaxial moudulus between the fcc [111] and bcc [110].

Molecular dynamics simulations of slip transmission across the incoherent Cu/Nb interfaces revealed that these interfaces have low shear strengths [231]. As a result, the stress field of a glide dislocation can locally shear the interface and lead to dislocation core spreading along the interface plane. This trapping of the glide dislocation in the interface plane due to core spreading makes the slip transmission difficult. The extent of core spreading is inversely proportional to the interfacial shear strength and may be the key to determining the interface barrier to slip transmission in incoherent fcc/bcc interfaces. The interfacial shear strength (and hence the core spreading and the peak strength of the composite) of fcc/bcc interfaces with Kurdjumov-Sachs orientation relationship may depend on a combination of factors such as heat of mixing, lattice parameter mismatch and the atomic structure of the interface. This will be investigated via atomistic modeling in our future work.

3.5 Conclusions

The mechanical behavior of sputter-deposited Cu/V and Al/Nb multilayer films is compared with that of Cu/Nb and Cu/Cr. All systems are all fcc/bcc type with incoherent interfaces, and with Kurdjumov-Sachs orientation relationship. The Hall-Petch slope scales with the shear moduli of the stiffer layer, but a similar scaling was not observed between the peak strength and the moduli of the fcc/bcc multilayers investigated. The peak strength depends on the interface barrier to slip transmission which for fcc/bcc incoherent interfaces may depend on the low shear strength of the interface that allows dislocation core spreading along the interface.

CHAPTER IV

INTERFACE ENABLED DEFECTS REDUCTION IN HELIUM ION IRRADIATED CU/V MULTILAYERS *

4.1 Introduction

Radiation-induced defects and evolutions of mechanical properties in proton, neutron, synchrotron and ion irradiated metallic materials have been extensively studied [233-238]. During radiation the interactions between energetic projectile particles and the atoms of the irradiated materials lead to atomic displacement damages, such as vacancies, interstitials, and their agglomerations in the form of vacancy clusters, voids and dislocation loops [111-115]. Stacking fault tetrahedra (SFT) as a result of agglomeration of vacancies are frequently observed in numerous irradiated metals and alloys with faced-centered cubic (FCC) structure, such as Au, Cu, Ni, Pd and austenitic stainless steel [142-148]. A high concentration of vacancy clusters and SFTs are observed in FCC Cu, whereas interstitial loops seem to prevail in irradiated BCC V [149]. In fusion reactors, besides the aforementioned displacement damages, a high concentration of He atoms created via (n, α) or other transmutation reactions typically leads to a large number of He bubbles in irradiated structural metals [239-241]. Radiation induced void swelling can cause significant dimensional instability and degrade the mechanical properties in the form of embrittlement. Significant void swelling, ~ 14 %, has been observed in neutron radiated 316L stainless steels [159]. Radiation hardening has been extensively studied in irradiated FCC and BCC monolithic metals, such as Cu and V [154, 155, 157, 242-246]. The yield strengths of neutron irradiated Cu and V both increase with the extent of

*Parts of this chapter are reprinted with permission from "Size Dependent Enhancement of Helium Ion Irradiation Tolerance in Sputtered Cu/V Nanolaminates" by E.G Fu, J. Carter, G. Swadener, A. Misra, L. Shao, H. Wang, X Zhang, 2009. *Journal of Nuclear Materials*, 385, 629-632, Copyright [2008] by Elsevier B.V.

damage, displacement-per-atom (dpa). The increase of yield strength is approximately 200-300 MPa in bulk coarse-grained Cu and V irradiated at a damage level of ~ 1 dpa [158].

Microstructural control has been shown to be effective in suppressing radiation damage. Significant reduction of void swelling has been recognized in a series of ferritic / martensitic (F/M) steels [247-251] with BCC or BCT structures. Also, oxide-dispersion-strengthened alloys, with nanoscale oxides uniformly distributed in F/M steels, have shown superior void swelling resistance and high temperature thermal stability [252]. A high density of dislocations in cold-worked 316L stainless steel can moderately alleviate void swelling at low temperatures [235]. The aforementioned studies have shown that grain or phase boundaries may act as sinks for radiation induced point defects and their clusters, where recombination of interstitial and vacancy could occur and such recovery process assists the interfaces in maintaining their ability to continuously absorb point defects [183, 253-256]. Increasing the volume fraction of grain or phase boundaries thus appears beneficial to alleviating radiation-induced damage. Metallic multilayer films possess very large interfacial areas. Recent studies show that immiscible Cu/Nb multilayers, particularly those with a layer thickness of a few nm, are extremely resistant against He ion irradiation-induced intermixing [257]. He bubbles are barely detectable in irradiated Cu/Nb 2.5 nm multilayers, suggesting the extraordinary capability of Cu/Nb interface in reducing point defect concentration compared to their bulk counterparts [46]. Atomistic simulations show that pairs of extended jogs formed by misfit dislocations along interfaces can effectively lower the point defect formation energy, and such

interfaces become virtually inexhaustible sinks for point defects and catalysts for efficient Frenkel pair recombination [259].

Despite these studies, the effect of the volume fraction of interfaces on radiation induced evolutions of microstructure and mechanical properties has not been studied systematically. The preliminary studies showed the reduction of He bubble density and suppression of radiation hardening in He ion irradiated Cu/V multilayers [260]. In this chapter, we provide a complete analysis of radiation induced defects, lattice distortion, void swelling, and evolution of hardness, and explain the mechanisms that lead to enhanced radiation tolerance in nearly immiscible Cu/V multilayers.

4.2 Experimental

Cu/V multilayer films with equal individual layer thickness ranging from 1 to 200 nm were synthesized on HF etched Si (100) substrates by using DC magnetron sputtering at room temperature. The deposition rate was approximately 1 nm/s. The total thicknesses of Cu/V multilayers were kept at 1.6-2 μm. A base pressure of 6.6×10^{-6} Pa was reached prior to depositions and argon partial pressure during sputtering was ~ 0.5 Pa. Before helium (He) ion irradiation, the samples with 5 × 10 mm in dimension were partially masked to avoid ion irradiation in the masked regions. After irradiation experiments, the difference in height (step height) between the irradiated and masked regions was measured by using a Dektak^3 Stylus profilometer with a Z height resolution of better than 1 nm. The ion irradiations were performed at room temperature using 50 keV He ions. A total fluence of 6×10^{20} / m^2 was achieved in 4 hours at a constant beam current of 2 μA. Baseline pressure in the ion implanter was less than 1×10^{-5} Pa. The temperature rise of specimens due to beam heating was estimated to be less than 50 ºC.

The microstructure of Cu/V multilayer films was characterized by Bruker-AXS D8 advanced Bragg-Brentano X-ray powder diffractometer (XRD). The XTEM samples of Cu/V, prepared by dimpling and ion-milling, were examined in a 200 kV JEOL 2010 TEM equipped with a Gatan SC1000 ORIUS CCD camera. The scanning TEM (STEM) and energy dispersive X-ray (EDX) analysis for identifying the elemental composition and the interface integrity of the specimens were performed by the FEI Tecnai G2 F20 with Fischione ultra-high resolution STEM HAADF detector (0.23 nm in the STEM image mode) and Oxford instruments EDX detector with a spatial resolution of ~ 1 nm. The hardness and indentation modulus of films were measured based on an average of 9-12 indents at different indentation depths at room temperature, by a Fischerscope HM2000XYp micro/nano indenter using a Vickers indenter with the same loading rate. Hardness and indentation modulus were measured as a function of indentation depth, up to a maximum depth of ~ 200 nm for all specimens. The plots of hardness vs. indentation depth are typically used in a depth range of 100 - 200 nm for accurate determination of average film hardness values.

4.3 Results

4.3.1 SRIM simulation

The stopping and range of ions in matter (SRIM) computer program based on Monte Carlo method [140] was used to compute the depth profile of the concentration of implanted He at an energy of 50 keV and a total fluence of 6×10^{20} ions/m^2. The simulation, as shown in Figure 4.1, predicts that, in Cu/V 50 nm multilayer, He concentration initially increases with the increase of the penetration depth, reaches a peak value of ~ 5 at.% at a depth of ~ 200 nm, and decays thereafter. The peak damage

induced by He collisions in multilayers is approximately 6 dpa, and the radiation damage extends to a maximum depth of ~ 380 nm underneath the film surface upon 50 keV He ion irradiations.

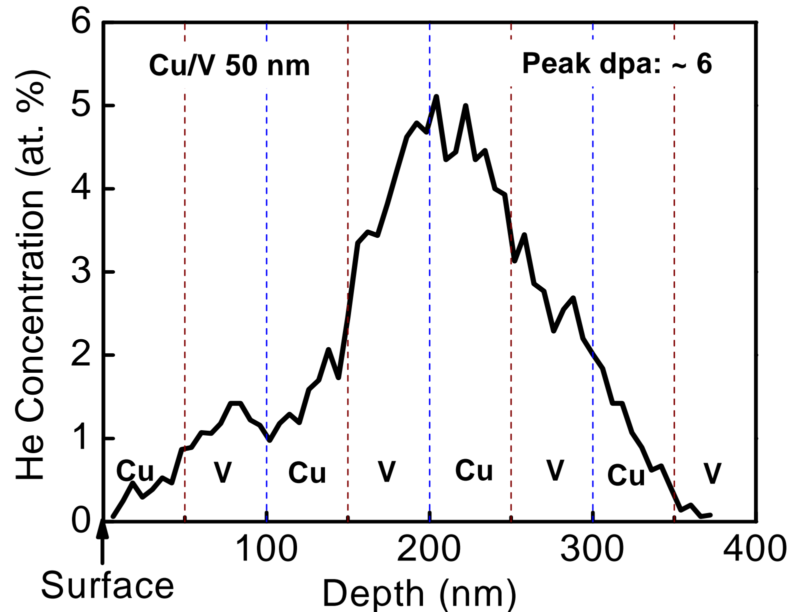

Figure 4.1. The depth profile of helium concentration obtained from SRIM simulation of Cu/V 50 nm multilayers subjected to He ion irradiation at 50 keV with a total fluence of 6×10^{20} ions / m^2.

4.3.2 Evolutions of microstructures examined by TEM

Bright field XTEM micrographs of the as-deposited and ion irradiated Cu/V 50 nm and Cu/V 2.5 nm multilayers are compared in Figure 4.2. For all layer thicknesses, the as-deposited Cu/V multilayers possess polycrystalline columnar grain structures with clearly defined layer interfaces and Kurdjumov-Sachs (K-S) orientation relationship: Cu {1 1 1} // V {1 1 0} // interface, and Cu <1 1 0> // V <1 1 1>. The columnar grain size in as-deposited Cu/V 50 nm is on the order of the individual layer thickness, h, whereas the

columnar grain size is much greater than h in the as-deposited Cu/V 2.5 nm specimen. Cu/V 2.5 nm multilayer has stronger fiber textures of Cu {111} and V {110} than Cu/V 50 nm. After He ion irradiation, de-focused XTEM experiments were performed to reveal defects induced by He ion irradiation across the entire thickness of the Cu/V 50 nm and Cu/V 2.5 nm specimens. Figure 4.2c and 4.2d show the under-focus XTEM images of these specimens after He ion irradiation. Superimposed on the images are two depth profiles of He concentration (solid curves starting from surfaces) obtained from SRIM simulations [140] of Cu/V 50 nm and Cu/V 5 nm nanolaminates by using experimental radiation parameters. The simulated maximum He concentration is ~ 5 at. % at a depth of around 200 nm underneath film surfaces where the peak displacement per atom (dpa) is approximately 6. These de-focused bright field XTEM images across the entire radiation region indicate that the number of He bubbles follows the concentration profile reaching a maximum at a depth of ~ 200 nm underneath the film surface. Inserted SAD patterns indicate irradiated films have similar texture as before. Peak damage regions outlined by a box in Figure 4.2c and 4.2d, are compared in Figure 4.2e and 4.2f. Careful examination of these Figures shows that white dots, typical signatures of He bubbles, appear in both Cu and V. Comparisons of the two micrographs show similar size of He bubbles, ~ 1 nm in diameter, and the density of He bubbles in Cu/V 50 nm specimen is much greater than that in irradiated Cu/V 2.5 nm multilayers.

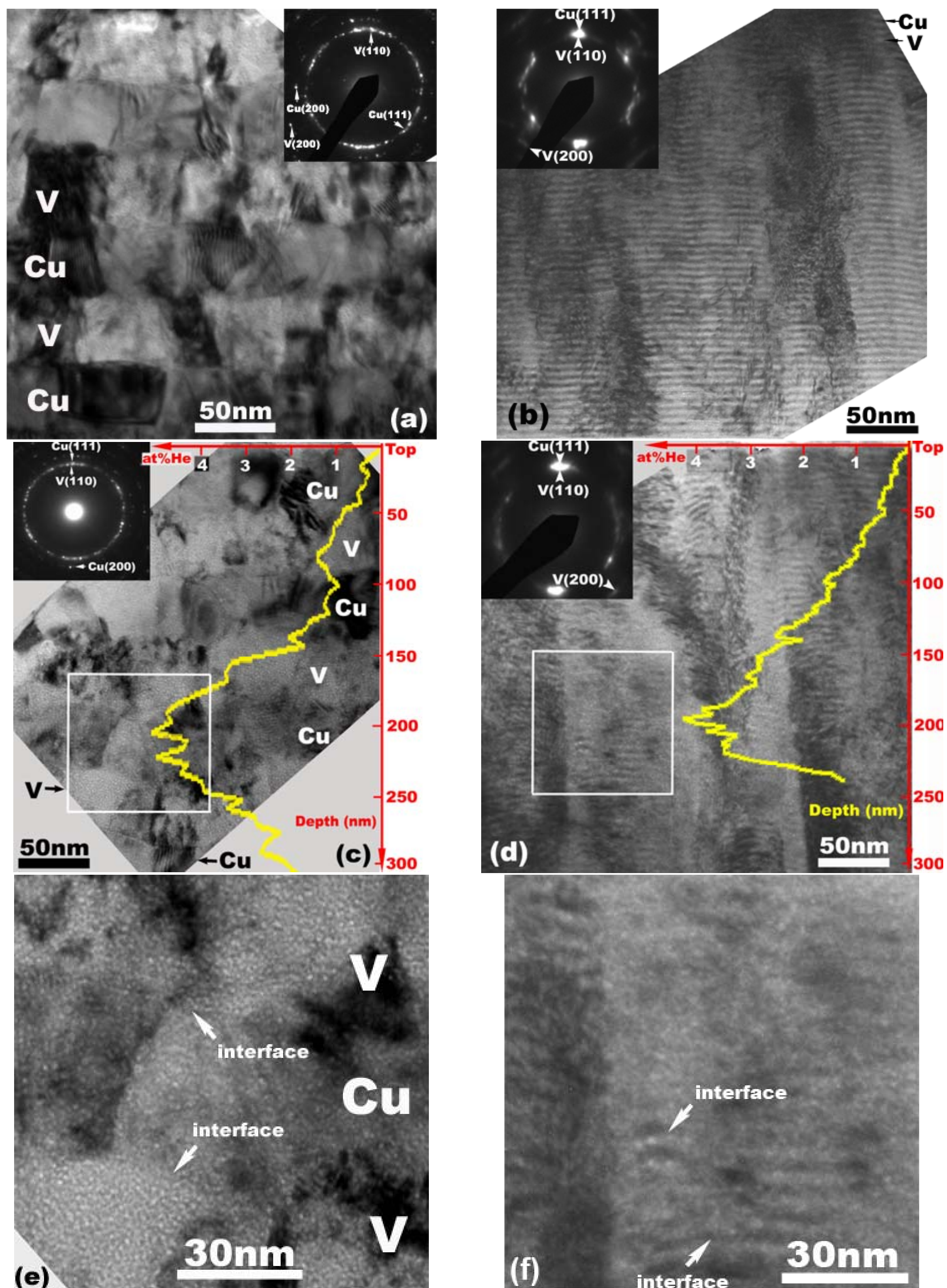

Figure 4.2. XTEM images of as-deposited (a) Cu/V 50 nm, and (b) Cu/V 2.5 nm multilayers, and ion irradiated (c) Cu/V 50 nm and (d) Cu/V 2.5 nm nanolaminates. In (c) and (d), peak damage regions as indicated by two square boxes are magnified in (e) and (f), respectively.

4.3.3 Evolutions of microstructure examined by STEM technique and chemical analyses

STEM experiments were performed to examine the chemical integrity of layer interface after irradiation. A STEM micrograph of ion irradiated Cu/V 50 nm specimen is shown in Figure 4.3a. The brighter layers are Cu, sandwiched by the darker V layers. Three different regions predicted by SRIM simulation were examined: (i) a surface region with low-to-medium damage; (ii) a peak damage region at a depth of around 200 nm; and (iii) a no damage region that is deeper than the ion range. Chemically abrupt layer interfaces were observed in all three regions with the interfaces in the peak damage region being rougher than those in less irradiated or unirradiated regions. Furthermore, semi-quantitative chemical composition analysis via EDX was performed in the same specimen along a straight line, 550 nm in length as shown in Figure 4.3a, normal to the layer interface across all three regions. As shown in Figure 4.3b, the composition profiles for the three regions are essentially the same (no discernable sign of intermixing), indicating that radiation induced interdiffusion across layer interface, if any, is under the spatial resolution limit of such technique.

Similarly, the geometric and chemical integrity of interfaces of irradiated Cu/V 2.5 nm in the unirradiated and peak damage regions are compared in Figure 4.4a and 4.4b. The comparison of STEM micrographs shows qualitatively that layer interfaces remain chemically modulated after He ion irradiation. Chemical analyses of the same specimen with an EDX spatial resolution of 1-2 nm is shown in Figure 4.4c. Insignificant change in the peak-to-valley distances indicates that layer interfaces in Cu/V 2.5 nm specimens were essentially unchanged after ion irradiations.

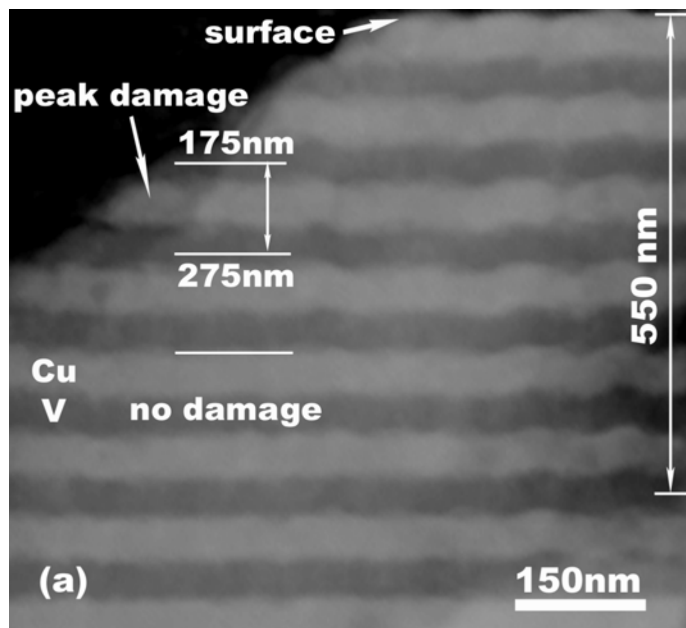

(a)

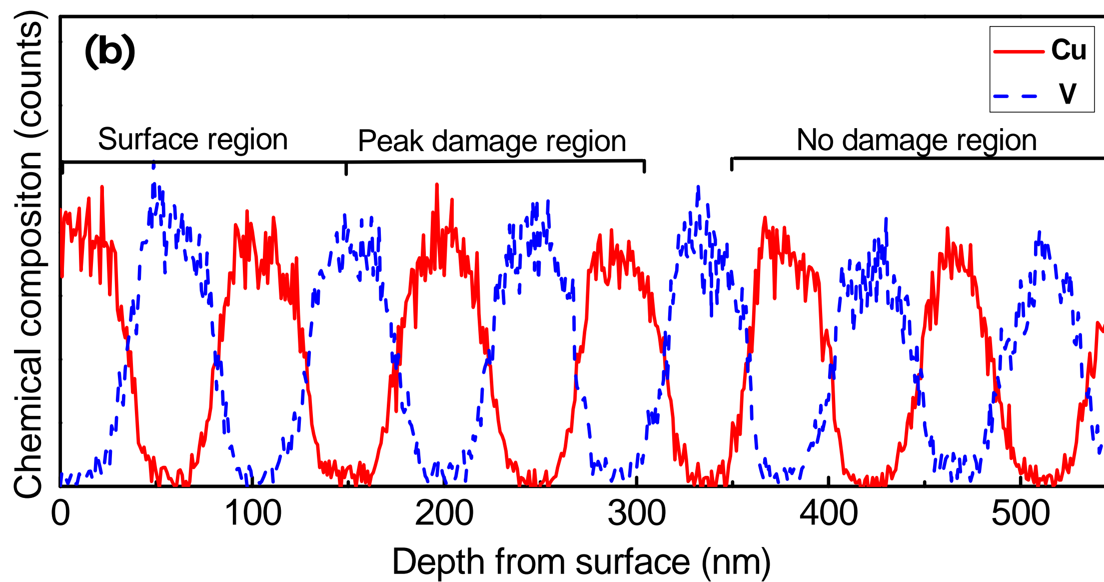

(b)

Figure 4.3. (a) A STEM image of He ion-irradiated Cu/V 50 nm multilayers with a total fluence of 6×10^{20} ions / m^2. Layer interfaces retain after radiations. (b) Semi-quantitative EDX chemical analysis along a 550 nm long line from the film surface as shown in 3a, normal to the layer interface across all three regions: the surface, peak damage and no damage region. Radiation induces insignificant change in the modulated composition profiles.

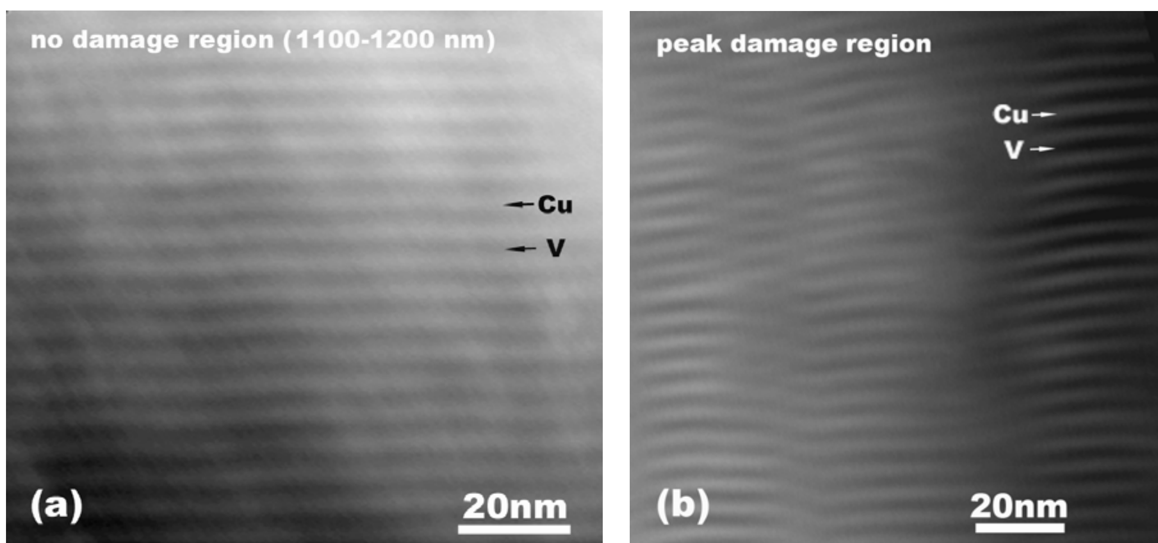

(a) (b)

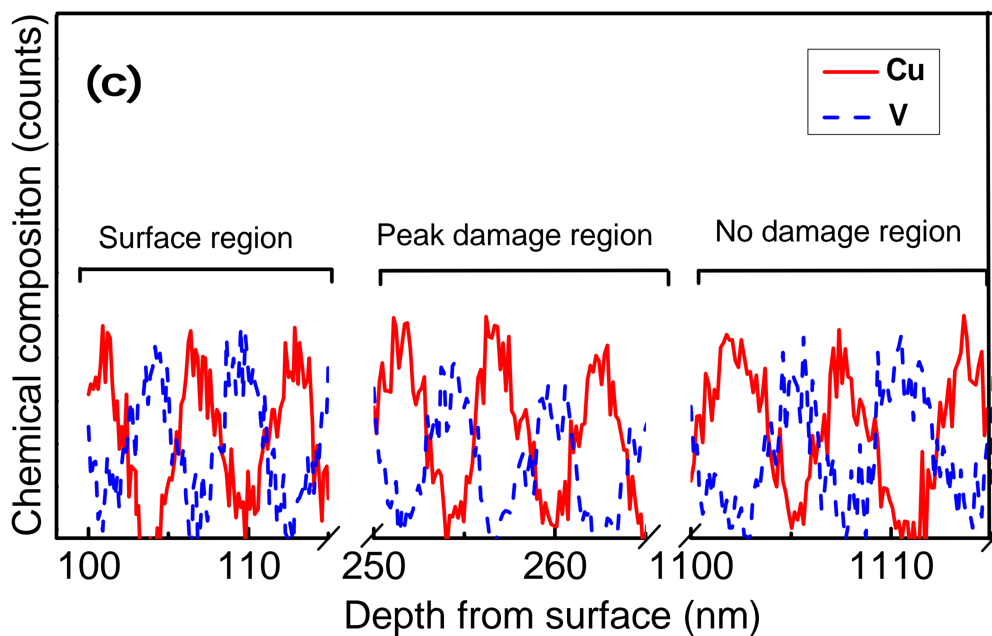

(c)

Figure 4.4. STEM images of ion-irradiated Cu/V 2.5 nm multilayers in (a) a no damage region (~ 1100 to 1200 nm from surface), (b) a peak damage region (200-325 nm), and (c) EDX chemical analysis of the same specimen along the interface normal direction across three regions: the close-to-surface, peak damage and no damage region.

4.3.4 He bubbles and void swelling measurements

XTEM was used to examine the influence of layer thickness on bubble density in ion irradiated Cu/V multilayers. Figure 4.5a shows He bubble density as a function of depth from the film surface in irradiated Cu/V 50 nm and Cu/V 2.5 nm multilayers. He bubble density (number per unit volume) was calculated from TEM micrographs taken at an under-focused condition (-400 nm) where similar bubble sizes (~ 1 nm) are observed in all irradiated specimens, and sample thickness is assumed to be ~ 25 nm. In both cases, the He bubble density increases rapidly to a maximum at a depth of ~ 200 nm, where the helium concentration reaches a peak as shown in Figure 4.1.

One major difference in the two cases is that the peak He bubble density in the Cu/V 50 nm multilayer is around 3 times greater than that of Cu/V 2.5 nm specimen. On the other hand, the peak bubble density of irradiated Cu/V 50 nm multilayer is still lower than that of single layer polycrystalline Cu films, as shown by the horizontal dashed line in Figure 4.5a, irradiated at the same condition.

From the XTEM studies, we also attempted to estimate the threshold concentration of He that leads to the formation of visible He bubbles. Figure 4.5b shows the SRIM simulation of depth dependent He concentration profiles of Cu/V 5 nm and Cu/V 50 nm multilayers. The vertical dotted and dashed lines, obtained from the TEM images, indicate the depth range over which bubbles are observed in TEM images of irradiated Cu/V 2.5 nm and 50 nm multilayers. The intersection of the vertical dotted lines with the SRIM simulated He concentration profiles indicates that the minimum He

concentration at which the bubbles are observed is approximately 1 at.% at ~ 80 nm underneath the film surface in Cu/V 2.5 nm multilayer. At larger layer thickness, Cu/V 50 nm, bubbles are resolved very close to the surface, ≈ 10 nm. The analysis shown in Figure 4.5b indicates a critical helium concentration of approximately 0.28 at.% in Cu/V 50 nm multilayer.

To provide a rough estimate of radiation-induced void swelling, the step height across the irradiated and masked (no radiation) region was measured by a profilometer and the results are shown in Figure 4.5c. The magnitude of void swelling in multilayers clearly decreases with decreasing h. The void swelling in irradiated Cu/V 2.5 nm multilayer is approximately 2 times lower than that in Cu/V 50 nm multilayers. Furthermore, void swelling in all irradiated Cu/V multilayers is less than rule-of-mixture (ROM) void swelling in irradiated single layer Cu and V films, shown as the horizontal dashed line in Figure 4.5c.

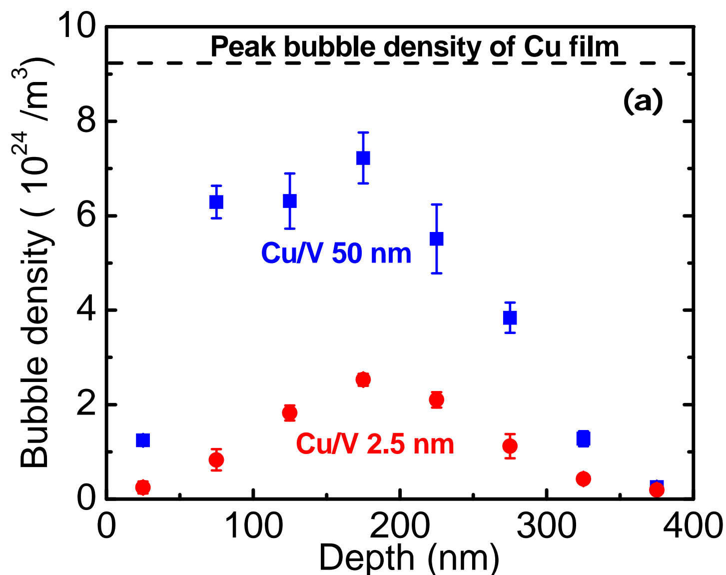

(a)

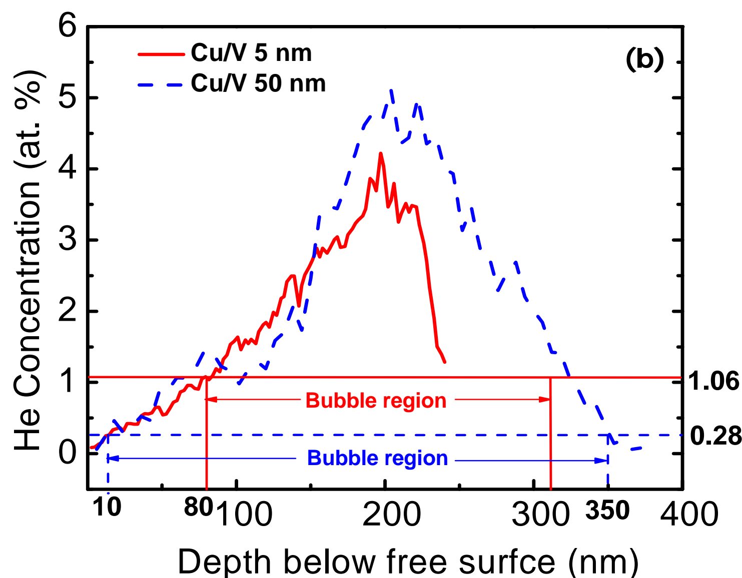

(b)

Figure 4.5 (a). Comparison of He bubble density distribution along film normal direction underneath the surface in ion-irradiated Cu/V 2.5 nm and Cu/V 50 nm multilayers. Peak He bubble density is reduced by a factor of around 3 in Cu/V 2.5 nm, compared to that in Cu/V 50 nm specimen; (b). Comparison of minimum He concentration at which He bubbles are detectable in the plot of He concentration vs. irradiation depth of Cu/V 5 nm and Cu/V 50 nm simulated by SRIM program using 50 keV He^+ with a total fluence of 6 $\times$ 10^{20} ions / m^2; (c). Void swelling vs. $1/h$ in ion irradiated Cu/V multilayers, where h is individual layer thickness. The rule-of-mixture (ROM) void swelling in irradiated Cu and V single layer films is also shown by the horizontal dashed line.

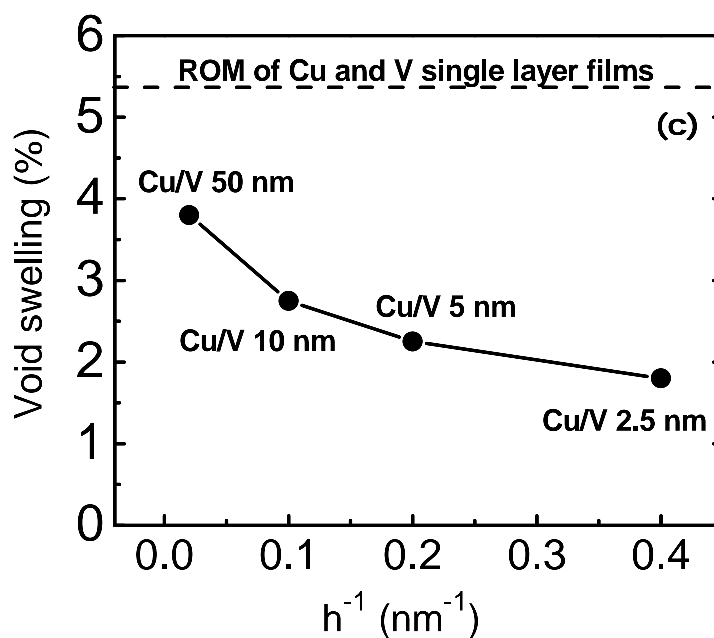

(c)

Figure 4.5 Continued.

4.3.5 Lattice distortions examined by x-ray and electron diffraction

All the as-deposited and irradiated samples were characterized by XRD, and V (110), Cu (111) and Si (400) (as a reference peak) diffraction peaks are present in all diffraction patterns. XRD patterns of as-deposited and irradiated Cu/V multilayers with individual layer thickness of 50 and 2.5 nm (Cu/V 50 nm, and Cu/V 2.5 nm) are shown in Figure 4.6. V (110) and Cu (111) peaks are well separated in Cu/V 50 nm specimen, but they overlap in Cu/V 2.5 nm multilayer. The V (110) and Cu (111) peaks in the He ion irradiated Cu/V 50 nm multilayers were shifted to lower angles by 0.45° and 0.06°, corresponding to ~ 1.1 % and 0.13 % of lattice expansion, respectively. The overlapped peaks in Cu/V 2.5 nm multilayers showed peak shift with the same trend (i.e. lattice

expansion), but at a smaller magnitude (0.11 % of lattice expansion) than those observed in the irradiated Cu/V 50 nm specimen.

Systematic SAD experiments were performed, with an aperture size of 100 nm in diameter, to examine the localized variation of lattice distortions along the irradiation path. Depth dependent lattice expansions, calculated from a series of SAD patterns along the implantation path, are shown in Figure 4.7 for Cu/V 2.5 nm and Cu/V 50 nm multilayers. The dependence of lattice expansions on implantation depth is similar to the variation of He bubble density vs. depth, as shown in Figure 4.5a. The peak lattice expansion in Cu/V 2.5 nm specimens is ~ 1.2 %, ~ 2-3 times lower than that in Cu/V 50 nm multilayers, ~ 2.5 %. The average lattice expansion is ~ 0.51 % and 1.30 % in Cu/V 2.5 nm and Cu/V 50 nm multilayers, respectively. Both values are larger than those obtained by XRD studies, which typically yield the average lattice parameters of the whole specimen. Given the difficulty of distinguishing Cu (111) from V (110) in SADs, the average values of the two are used in the calculations. Overall, the XRD measurements are more precise in estimating the lattice strain, if specimens are uniformly strained through thickness. The strains measured from SAD patterns, however, indicate the variation in strain with depth and show the correlation between the depth dependence of helium bubble density (Figure 4.5a) and depth dependence of strain (Figure 4.7).

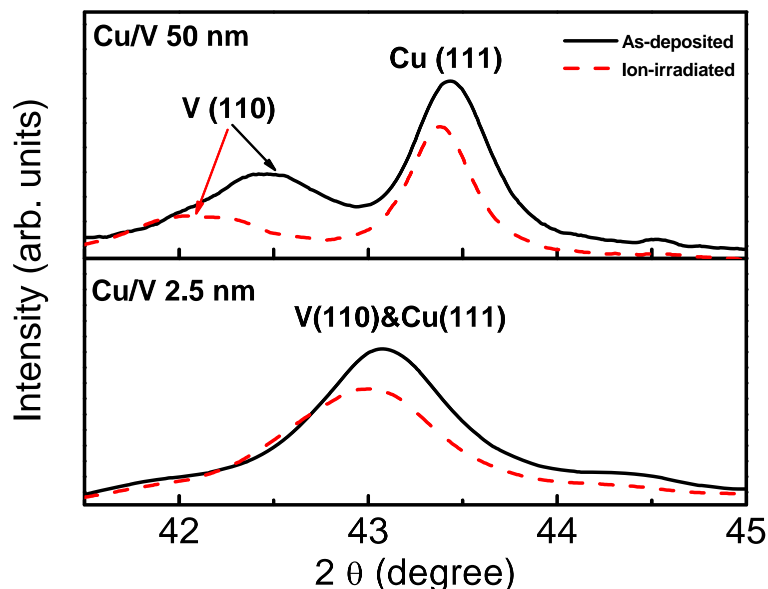

Figure 4.6. XRD patterns of as-deposited and ion-irradiated Cu/V 50 nm and Cu/V 2.5 nm multilayers. After radiation peak intensity decreased and peak position shifted to lower angles.

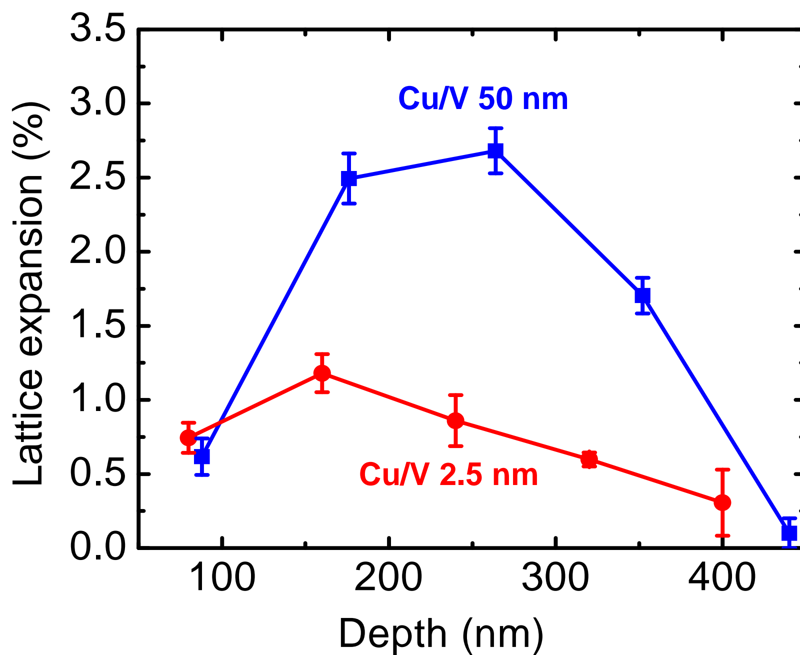

Figure 4.7. The depth dependent evolution of lattice expansion of Cu/V 50 nm and 2.5 nm multilayer films calculated from a series of SAD studies starting from the film surface.

4.3.6 Irradiation hardening

Hardnesses of as-deposited (shown by spheres) and ion-irradiated (shown by squares) Cu/V multilayers vs h^{-1} are plotted in Figure 4.8a, where h is the individual layer thickness. The hardness of as-deposited Cu/V increases monotonically with decreasing h, and approached peak values at h of 2.5 nm or less. He ion irradiation in general leads to the increase of film hardness (radiation hardening). But the magnitude of radiation hardening diminished continuously with decreasing h, and became negligible at $h \leq 2.5\,\text{nm}$. To test the reproducibility of radiation hardening effect, two more sets of deposition, irradiation and hardness measurements were performed and results (not shown here) are reproducible. ROM hardness values of as-deposited and ion irradiated films are also shown by horizontal dashed lines in the same plot, respectively, with an ROM hardness increase of ~ 1 GPa after irradiation. In order to examine hardness variation in more detail, the change of hardness between the as-deposited and ion irradiated Cu/V specimens, ΔH, as a function of h^{-1}, was plotted in Figure 4.8b. The magnitude of ΔH increases with increasing h and approaches the values of radiation hardening in single layer Cu and V films.

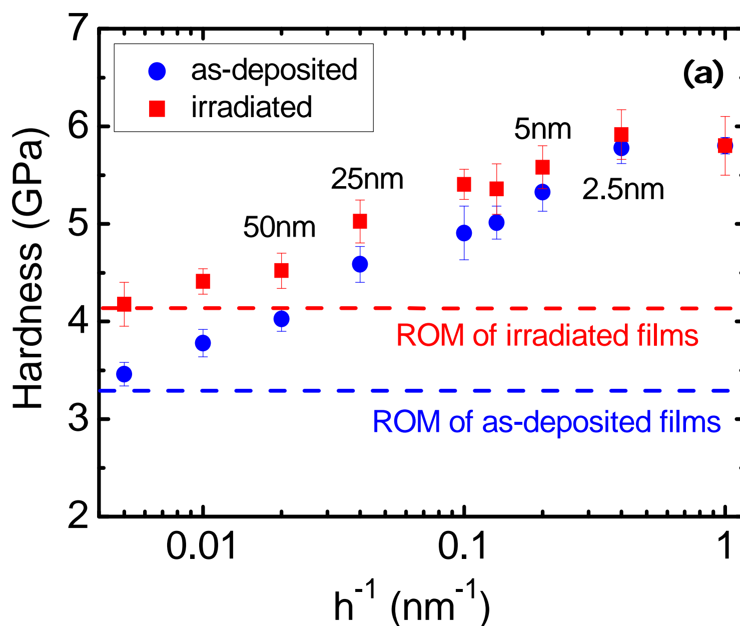

(a)

Figure 4.8. (a) Comparison of hardnesses of as-deposited and ion-irradiated Cu/V multilayers as a function of h^{-1}. ROM hardness values of as-deposited and ion-irradiated films are also shown by horizontal dashed line, respectively. Hardnesses increase with decreasing h in both cases and approach peak values at h of 1 nm - 2.5 nm; (b) Hardness variation ($\Delta H = H_{ion-irradiated} - H_{as-deposited}$) of Cu/V multilayer after He ion irradiation as a function of h^{-1}. Radiation hardening in Cu and V single layer films is indicated by two horizontal dashed lines. Radiation hardening of multilayers increases with increasing h and approaches that of single layer Cu and V, and is negligible at h of 2.5 nm or less.

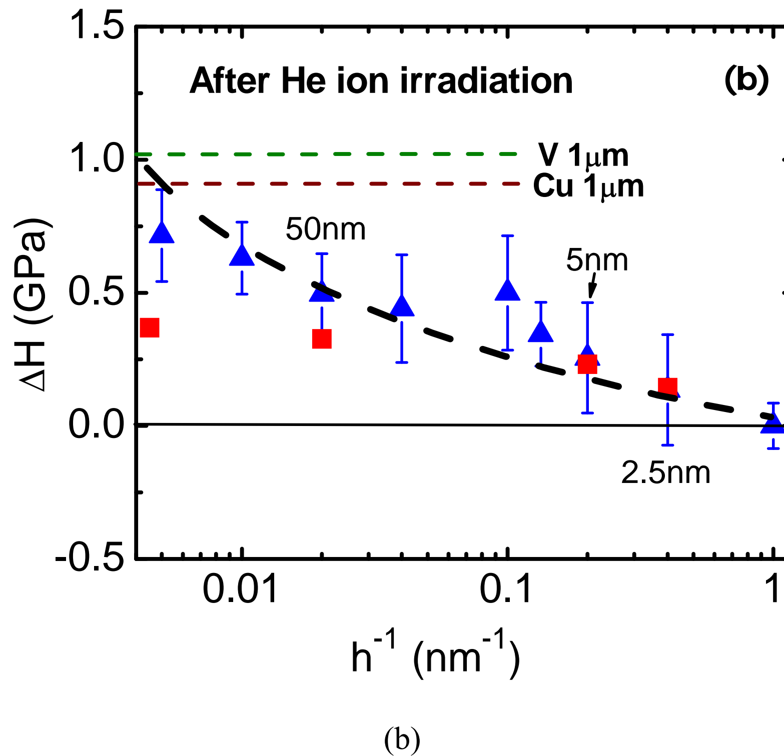

(b)

Figure 4.8 Continued.

4.4 Discussions

We will first examine the evolution of microstructures, including the retention of layered morphology, generation of He bubbles and lattice distortions, and then the implication of these microstructural changes on irradiation hardening.

4.4.1 Morphological stability of Cu/V layer interfaces

An energetic ion beam can induce ion mixing at interfaces between dissimilar materials. Such energetic ion induced ballistic mixing can effectively induce the formation of new phases or even completely destruct layer interfaces in miscible systems, such as Cu/Au [261], Hf/Ti [262], Fe/W [263] and Al/Nb [264]. However, in Cu/V system with a positive heat of mixing, ~ 5 kJ/mol [229], a chemically driven demixing process may have occurred simultaneously during irradiation experiments. Hence the

strong demixing tendency led to the retention of Cu/V layer interfaces. Similar phenomena have been observed in several other immiscible systems, such as Cu/W [261], Cu/Nb [257] and Hf/Ni [262]. The mutual solid solubility between Cu and V is very limited, approximately 2.5 wt. % Cu in V matrix at 800 °C [21]. Intermixing at the level of a few at.% is below the detection limit of the STEM technique used in this study, although some indication of the increased interface roughness was noted in Figure 4.2e and 4.3a. The curvature of interfaces as shown in Figure 4.4a and 4.4b is typically observed in TEM analyses of columnar grains [211, 265, 266], and is a consequence of the island growth mechanism of sputtered films.

4.4.2 Radiation induced He bubbles and lattice distortion

We now attempt to analyze radiation induced defect concentration and corresponding lattice distortion in multilayers. The primary radiation damage event in crystalline metals is the displacement of one or more atoms, and consequently vacancies, self-interstitials and foreign elements are created in crystal lattices [267]. In bulk FCC metal with low-to-medium stacking fault energy (SFE), such as Cu (γ_{SF} = 39 mJ/m^2) [142], approximately 90 % of neutron radiation-induced defects are stacking fault tetrahedra (SFT) at a density of 2-6 × 10^{23} /m^3 at a damage level of 0.01 - 0.9 dpa [149]. In BCC bulk V, radiation induced defects are mostly dominated by interstitial loops, 2 nm in diameter, at a density level of 1-2 × 10^{23} /m^3 [149, 268]. Helium will rapidly combine with vacancies and vacancy clusters to form bubbles.

He bubbles have been observed in most irradiated Cu/V multilayers. The size and density are crucial to depict the He bubbles. To determine the He bubble size, a series of XTEM images of ion irradiated Cu/V 50 nm and Cu/V 2.5 nm were taken at different

under-focus conditions. Figure 4.9a and b show that the bubble image size increases with increasing magnitude of de-focus distance. The average bubble size at in-focus condition, determined by the intercept of linear fit with y axis, is 0.7 ± 0.2 nm, and 0.6 ± 0.2 nm in irradiated Cu/V 50 nm, and Cu/V 2.5 nm specimens, respectively. Such analysis indicates that the average bubble size depends very little on h of the multilayers, and provides the basis for accurate determination of He bubble density. The reduction of He bubble density in Cu/V 2.5 nm specimen by a factor of approximately 3 compared to that in irradiated Cu/V 50 nm and Cu films indicates that vacancy concentration must have been dramatically reduced.

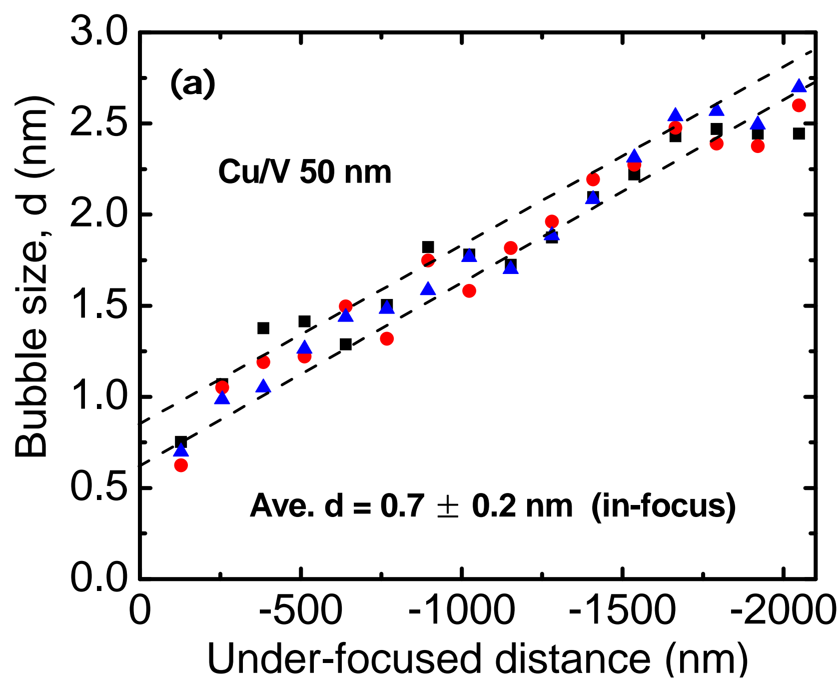

(a)

Figure 4.9. Measurement of average bubble size in ion-irradiated (a) Cu/V 50 nm and (b) Cu/V 2.5 nm multilayers through a series of defocused XTEM studies. The measured bubble sizes depend on the underfocus conditions. The real average bubble size determined from the intercepts of linear fit with y-axis (in focus condition), is ~ 0.7 nm in Cu/V 50 nm multilayers, and ~ 0.6 nm in Cu/V 2.5 nm multilayers.

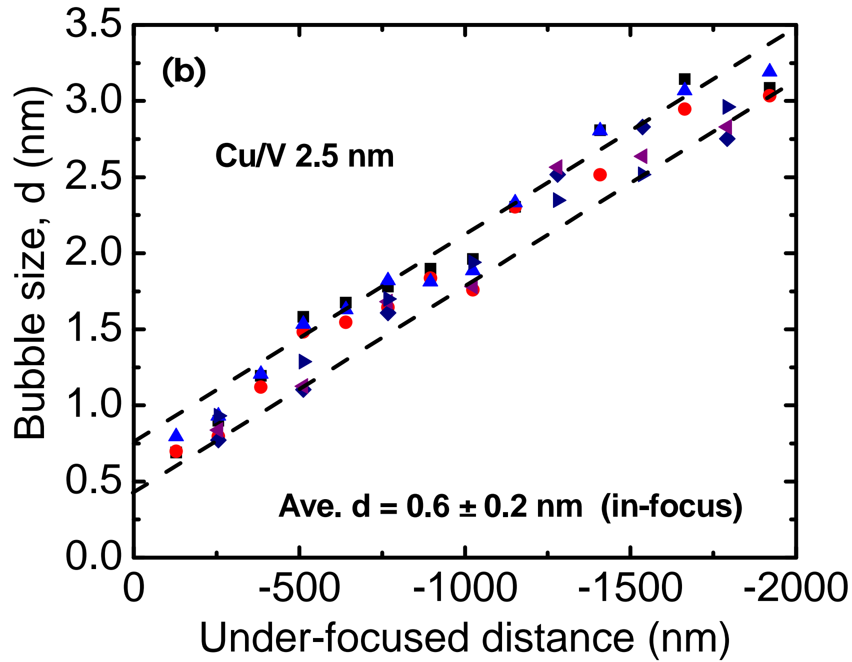

(b)

Figure 4.9 Continued.

The equilibrium distribution function of He bubbles with the number of vacancies, n, and gas atoms, x, can be expressed by [111]:

$$\rho^0(n,x) = M_x \exp\{n \ln S_V - \xi n^{2/3} + x \ln(\frac{MHn\Omega}{xkT})\} \tag{103}$$

where M_x is the number of gas-atom clusters per unit volume composed of x gas atoms, S_V is the supersaturation of vacancies, ξ is a temperature dependent constant, M is the overall He concentration in metals, H is the Henry's law constant for the dissolution of He in the metal, and Ω is the atomic volume of metals. S_V can be expressed by:

$$S_V = \frac{C_V}{C_{V_0}} \tag{104}$$

where C_V and C_{V_0} is the vacancy concentration and thermal equilibrium vacancy concentration, respectively. ξ can be written as:

$$\xi = (36\pi\Omega^2)^{1/3} \frac{\gamma}{kT} \tag{105}$$

where γ is the surface energy of solid.

Inspection of equation (103) shows that for Cu/V 2.5 nm and Cu/V 50 nm multilayers, the major difference in the two systems is the first term in the bracket, S_V. Hence, assuming the thermal equilibrium vacancy concentration is similar in both systems, the reduced He bubble density at smaller layer thickness should be a direct evidence of reduced vacancy concentration, C_V, in multilayers, via annihilation with interstitials.

It is generally accepted that radiation induced defects tend to migrate to the interfacial regions, such as grain boundaries and interfaces [183]. These interfacial regions are expected to act as effective sinks for radiation induced defects. The interfacial area density (number of interface per unit length along the direction normal to the layer interfaces) in Cu/V 2.5 nm multilayers is 20 times higher than that in Cu/V 50 nm multilayers. It is likely that defect migration along interface is facilitated, an event that leads to enhanced annihilation of opposite type defects. Mathematically, the reduced supersaturation of vacancies could also be affected by C_{V_0} to certain extent, which is dependent on temperature and vacancy formation energy in thermal equilibrium state. Recent MD simulation studies of Cu/Nb multilayer films showed the formation energies of vacancies are significantly lower at Cu/Nb interfaces than in the perfect crystals of the neighboring elements [269]. Hence it is likely that when h in the multilayer is reduced to

a few nm length scale, the value of C_{V_0} is slightly increased due to the interface effect. As a result the capacity of defect storage in multilayer is enhanced and reduces the supersaturation of vacancies. The reduction of He bubble density in multilayers is thus a combined effect of enhanced defect storage capacity (increasing C_{V_0}) and increased probability of defect annihilation at interfaces (decreasing C_V).

Lattice expansion is observed in XRD and TEM-SAD analyses as shown in Figure 4.6 and 4.7. There are several factors that may contribute to lattice distortions, including dissolution of solute atoms, vacancies, He bubbles, interstitials, and interstitial loops. Interstitials are mobile and may migrate to interfaces or form loops, and hence the contribution of interstitials to lattice expansion can be neglected. Our TEM analysis reveals that interstitial loop density in multilayers is low, thus interstitial loop induced lattice expansion is insignificant and will not be considered further. From Cu-V phase diagram [266], it is evident that up to 2 at. % of Cu can be dissolved in V. Assume that ion irradiation induces slight intermixing by incorporating a maximum of 2 wt % Cu into V, and by using the lattice parameters of Cu and V ($a_{Cu} = 3.615$ Å , $a_V = 3.027$ Å), one can estimate a lattice expansion of ~ 0.46 % in V. However the peak lattice expansion is ~ 2.5 % in Cu/V 50 nm multilayers as revealed by SAD studies in Figure 4.7. Also, the intermixing zone is unlikely to extend over several tens of nanometers given that the microscopy characterization (Figures 4.3 and 4.4) revealed the preservation of discrete, compositionally modulated layered structure. In the ion irradiated Cu/V 50 nm specimen, the variations of He bubble density and lattice expansion with implantation depth follow a similar trend (i.e. a maximum at approximately 200 nm below the surface). This

observation implies that pressurized He bubbles may account for much of the observed lattice expansion.

Pressurized He bubbles could lead to lattice expansion based on the point source dilatation mechanism [270]. The pressure due to point source (He bubbles in this case) dilatation can be expressed as:

$$P = \frac{\mu \delta v}{\pi r_0^3} \tag{106}$$

where μ is the shear modulus of the metal matrix, and δv is the volume expansion induced by internal pressure, and r_0 is the radius of bubbles. If we assume that the lattice expansion due to He bubble is approximately 2 % (= 2.5 %-0.46 %) in V, given μ = 46 GPa for V and a bubble radius of 0.5 nm, the pressure is estimated to be ~ 3.8 GPa. By using the EOS of He [271, 272], the molar volume of He is estimated to be 6.29 cm^3/mol, or approximately 1.3 He atoms per vacancy in V. A similar result, 1.1 He atoms per vacancy in Cu is obtained. This compares well with literature values (1.4 He/vacancy in He bubbles of 4 GPa pressure in V, and 1.0 He/vacancy in He bubbles of 2.8 GPa pressure in Cu [273]).

4.4.3 Mechanical integrity and hardening mechanisms

In conventional metals, radiation hardening is contributed by interaction of dislocations with two types of radiation-induced defects: strong obstacles, such as interstitials, interstitial loops, SFTs and precipitates, and relatively weak obstacles, such as He bubbles [156, 267, 274]. The interaction of glide dislocations with Cu/V interfaces is not expected to change significantly given the retention of chemically abrupt interfaces after radiation. As noted in previous reviews of obstacle-controlled strengthening, the

dispersed barrier model [181] is appropriate for strong obstacles induced hardening. An alternative hardening relationship was developed by Friedel-Kroupa-Hirsch (FKH) for weak obstacles [180, 275]. The contribution of He bubbles to radiation hardening is negligible at low He concentration and becomes significant only above a critical He concentration around 1 at. % [276-278]. The SRIM simulation results predict the average He concentration is around 1.9 at. % in Cu/V 50 nm multilayers and 1.6 at. % in Cu/V 5 nm multilayers, respectively. When the bubble size is very small, He bubbles are treated as the weak obstacle. The FKH model is applied to estimate the He bubbles induced enhancement of yield strength, $\Delta\sigma$, by:

$$\Delta\sigma = \alpha M \mu b d N^{\frac{2}{3}} \quad (107)$$

where α is typically taken as ~ 1/8 [279]. M is the Taylor factor taken as 3.06 for equiaxed FCC and BCC metals, and μ is the shear modulus of 46 GPa for both Cu and V; b is the Burgers vector of the primary glide dislocations. The magnitude of Burgers vector in FCC Cu is $a_{Cu}/\sqrt{2} = 0.3615/\sqrt{2} = 0.25562$ nm, and it is $a_V\sqrt{3}/2 = 0.3027 \times \sqrt{3}/2 = 0.26218$ nm in BCC V. The diameter of He bubbles (d), ~ 1 nm, and their average number density (N) across the radiation damage region are obtained from TEM measurements (Figure 4.5a and 4.9). Radiation hardening, estimated as three times of the calculated $\Delta\sigma$ indicated by red square, is compared with experimental values in Figure 4.8b. It is evident that insignificant radiation hardening in multilayers at smaller h (a few nm or less) can be described well by He bubble induced hardening. However, He bubble induced hardening alone clearly underestimates the experimental values for single layer Cu and V film, and multilayers with greater h (h =

50 nm for instance). The above analyses with a constant α value of 1/8 show that the magnitudes of radiation hardening due to He bubbles alone are less than experimental measurement, implying radiation hardening contributions from other factors, presumably interstitial loops.

We noticed that, in spite of a rather high He bubble density, the average distance between He bubbles (λ, estimated as $1/\sqrt{Nd}$ [111]) is ~ 25 nm, a length scale where Orowan type of dislocation bowing between bubbles is a reasonable mechanism. Depending on the difference between inter bubble separation (λ) and the individual layer thickness, h, radiation hardening in multilayers could be categorized into three regimes. (i) For $h << \lambda$, at a few nm length scale, the yield strength of the multilayers is expected to be controlled by the smaller length scale, h, with minimal contribution from He bubbles. (ii) When h is comparable to λ, radiation hardening from bubbles will become more evident. (iii) Finally when h is much greater than λ, on the order of hundreds of nm, the magnitude of radiation hardening approaches that of single layer films, and significant hardening by irradiation-induced defects is expected. In addition to He bubbles, other defects, such as interstitial loops will also become important. At small h, interstitials are expected to migrate to interface sinks and hence, loops may not form within layers.

The interstitial loops are typically treated as the strong barriers to the trespassing of the dislocations in the radiation studies. The dispersed barrier model based on straightforward geometrical considerations for obstacles intersecting the dislocation slide plane is the most appropriate model to describe the increase in yield strength, $\Delta\sigma$, for polycrystalline metal, and can be expressed by:

$$\Delta\sigma = M\alpha'\mu b\sqrt{Nd} \tag{108}$$

Where M, μ, b, N and d carry the same physical meanings as defined previously in equation (107), but this time the defect clusters are interstitial loops. α' is a parameter that depends on the average barrier strength of the radiation-induced defect clusters. Recent studies estimate that α' is 0.26 for V, and 0.2 for Cu [149]. By subtracting the contribution of He bubble induced hardening from the measured values, the average interstitial loop density with an assumption of size of 2 nm is estimated as 0.5×10^{23} /m^3 for Cu/V 50 nm multilayer. This is comparable to the interstitial loop density of 6.7×10^{23} /m^3 and 2.3×10^{23} /m^3 in neutron-irradiated polycrystalline pure Cu and V metals subjected to a total dose of 0.92 dpa and 0.69 dpa, respectively [149]. Future experiments are planned in the authors' laboratory to determine the density of interstitial loop.

Finally we noticed that the underestimation of radiation hardening by He bubbles alone could also be attributed to use of a constant α value of 1/8 in equation (107). Our analysis shows that an α value varying from 1/8 (for Cu/V with smaller h) to ~ 1/3 (single layer Cu or V) can fit the experimental results of radiation hardening well. An increasing α value would indicate a greater number of helium atoms per bubble or higher pressure inside bubbles. At higher h, less interface area is available to trap He. So a higher concentration of helium may be trapped in the bubbles within the layers, making bubbles stronger barriers for the glide of dislocations. In the mean time, a higher pressure inside He bubble in multilayers of greater h or single layer films would lead to greater lattice expansion as evidenced by electron and X-ray diffraction studies. To elucidate this

hypothesis future studies are needed to determine the pressure in bubbles or number of He atoms per bubbles in Cu/V multilayers of different *h*.

4.4.4 The significance of Cu/V interface in enhancing radiation resistance in multilayers

Our study clearly demonstrates that in the nearly immiscible Cu/V system, layer interfaces play significant roles in enhancing radiation resistance of the multilayers, manifested as reduced He bubble density and less radiation hardening. Based on this study the fundamental mechanisms of interface-driven enhancement of radiation tolerance can be interpreted as follows.

(1) Interfaces (between Cu and V) act as sinks for defects (vacancies, interstitials and helium atoms), since defect formation energy is lower at interfaces than in crystal lattices [269]. Furthermore MD simulations of Cu/Nb interface show that misfit dislocations evolve into extended jog pairs and significantly increase the sink capacity of Cu/Nb interfaces [259]. Since the immiscible Cu/V has similar interface (fcc/bcc type with K-S orientation relationship) comparing to immiscible Cu/Nb, we anticipate that the Cu/V interface will also have high sink capacity for point defects.

(2) Interfaces promote annihilation of unlike defects as defects have high mobility and delocalized cores [259] at interfaces. The recent MD simulation studies [259, 269] have shown that interfaces will athermally absorb and annihilate point defect within 2 ps after their generation up to a distance of approximately 1 - 2 nm from the interface. With an interface spacing of 2.5 nm in Cu/V 2.5nm multilayers, the distance between cascade events and interfaces is expected to be small enough to allow direct interaction without the need for diffusion. So the annihilation process in these very fine nanolayers should occur almost instantaneously with the collision cascades. Whereas in bulk lattices (Cu/V

100 nm instance), the interface-defect interactions will depends on both the length and time scales.

(3) Interfaces also have a high solubility for helium, and hence, such an effect combined with reduced vacancy concentration due to enhanced annihilation defers the bubble nucleation to higher helium concentration.

(4) Interfaces in Cu/V multilayers can significantly reduce the densities of defect clusters such as interstitial loops, stacking fault tetrahedra, and more importantly He bubbles, and hence, dramatically alleviate void swelling and suppress irradiation hardening. Furthermore the significance of interface is also manifested from a clear size (layer thickness) dependent reduction of void swelling and irradiation hardening. When the individual layer thickness is ~ 100 nm or greater, the radiation tolerance of multilayer decays and approaches that of bulk materials.

4.5 Conclusions

The evolution of microstructure and mechanical properties of sputtered Cu/V multilayers subjected to 50 keV He ion irradiation were investigated systematically. Irradiated multilayer interfaces remain chemically abrupt even in the peak damage region upon a total dosage of ~ 6 dpa. Such immiscible layer interface can effectively reduce the overall concentration of He bubbles and void swelling, the magnitude of which reduces at smaller individual layer thickness. These multilayers also show clearly a monotonic suppression of radiation hardening at smaller layer thickness due to the effective attraction and facilitated annihilation of Frenkel pair defects. Multilayers with immiscible layer interface hence may offer a promising approach in alleviating void swelling and radiation hardening.

CHAPTER V

DOSE DEPENDENCE OF RADIATION DAMAGE IN HELIUM ION IRRADIATED CU/V MULTILAYERS

5.1 Introduction

The previous chapter has shown that immiscible Cu/V interface can effectively alleviate radiation induced void swelling and suppress radiation hardening in He ion irradiated Cu/V multilayers. However, the limit that Cu/V multilayer can sustain radiation damage remains unclear. In this chapter we discuss the exploration of the capacity of these interfaces in absorbing radiation induced defects spanning a fluence of 6×10^{19} to 1.2×10^{21} / m^2.

5.2 Experimental

Cu/V multilayer films of nominally identical individual layer thickness, *h*, ranging from 1 to 200 nm were deposited on HF etched Si (100) substrates using a DC magnetron sputtering technique at room temperature. The total film thickness is 1.5-2 μm in all cases. The first deposited layer on the silicon substrate was always vanadium. A deposition rate of a few Å/s for Cu and V metals was used. The base pressure of the vacuum system was better than 6.67×10^{-6} Pa prior to deposition. The pressure of Ar was typically ~ 0.5 Pa during deposition. He ion irradiations were performed at room temperature with ion energy of 50 keV in an ion accelerator with He gas ion source. The dose rate was kept at a constant of 4.2×10^{-4} dpa/s. The total fluences of He ion irradiation were set to 6×10^{19}, 6×10^{20} and 1.2×10^{21} / m^2, corresponding to the peak displacements per atom (dpa) of 0.6, 6 and 12 based on SRIM simulation of He ion irradiated Cu/V 50 nm multilayer. A base pressure of better than 1×10^{-5} Pa was

obtained in the ion irradiation chamber prior to irradiation experiments. Details of fabrication and helium ion irradiation are given in the earlier chapters.

X-ray powder diffractometer (XRD) with the model of Bruker-AXS D8 Advanced Bragg-Brentano equipped with a LynxEye linear position sensitive detector was used to characterize the microstructure of Cu/V multilayer films. Microstructure of ion irradiated films was examined in JEOL 2010 TEM microscope, and images were recorded by Gatan SC1000 ORIUS CCD camera. Cross-sectional TEM (XTEM) specimens were prepared by using a dimple grinder followed by ion milling with argon ions. The hardness and indentation modulus of multilayer films were measured by a Fischerscope HM2000XYp micro-indenter with a Vickers indenter at room temperature. The indentation depths range from 100 to 200 nm, and at least of 9-12 indents were performed at each depth to obtain an average hardness value.

5.3 Results

5.3.1 SRIM simulation

The simulation of He ion irradiation on the Cu/V multilayer was performed by the stopping and range of ions in matter (SRIM) computer program based on Monte Carlo method [140]. The nominal individual layer thickness of Cu/V multilayer in the simulation was 50 nm. Three ion irradiation fluences, 6×10^{19}, 6×10^{20} and 1.2×10^{21} / m^2, corresponding to real experiments were simulated with a He ion energy of 50 keV. The corresponding peak damages, induced by He collision and calculated from the output of simulation, were 0.6 dpa, 6 dpa and 12 dpa, respectively. Figure 5.1 shows the variation of He concentration as a function of the ion penetration depth predicted by SRIM for the three cases. In all cases with the increase of irradiation depth, He

concentration increases to the peak value at a depth of around 200 nm and then decreases to zero at depth of 380 nm. Higher total fluence results in greater He concentration and thus higher radiation damage. The He concentration at the total fluence of 1.2×10^{21} / m^2 is twenty times greater than that in the specimen radiated at a fluence of 6×10^{19} / m^2. The maximum implantation depth is the same in all three cases due to the usage of the identical He ion energy.

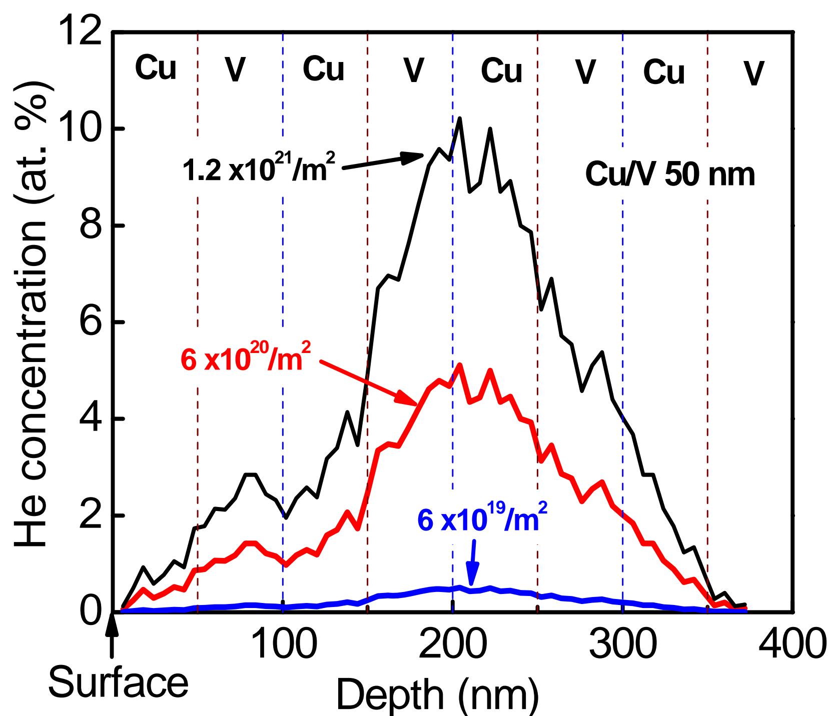

Figure 5.1. Depth profile of helium concentration from SRIM simulation in Cu/V 50 nm multilayers subjected to He ion irradiation at 50 keV with a total fluence of 6×10^{19} / m^2, 6×10^{20} / m^2 and 1.2×10^{21} / m^2, respectively.

5.3.2 Evolutions of microstructures examined by STEM and TEM

The examination of the chemical integrity of layer interface after irradiation was performed by STEM based on the contrast of different materials. Figure 5.2a shows a STEM micrograph of ion irradiated Cu/V 50 nm specimen. The darker layers are V, sandwiched by the brighter Cu layers. This STEM micrograph examined three different regions of the sample predicted by SRIM simulation. These three regions include a film surface region with low to medium damage, a peak damage region at a depth of around 200 nm, and a no damage region that is deeper than the ion projected range. STEM image clearly shows chemically abrupt layer interfaces in all the three regions. This indicates the remaining of integrity of interface structure after high dose He ion irradiation.

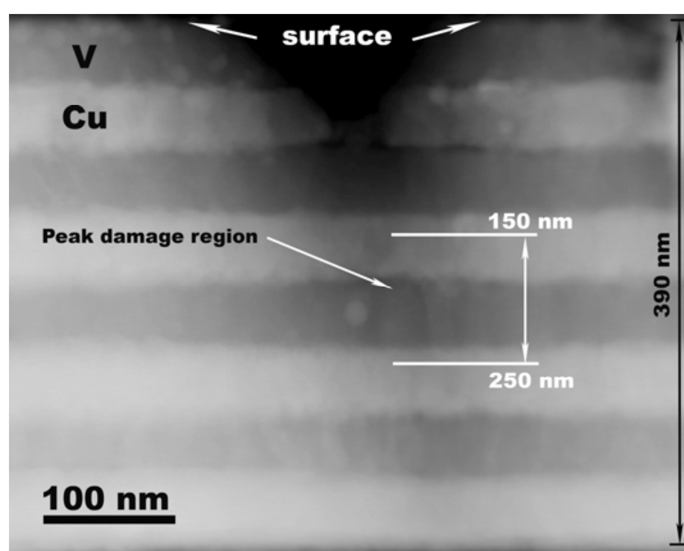

Figure 5.2. STEM image of Cu/V 50 nm with He ion irradiation at a total fluence of $1.2 \times 10^{21} / m^2$.

Furthermore, semi-quantitative chemical composition analysis via EDX (not shown here) indicates that the composition profiles for the three regions are essentially

the same, implying that radiation induced interdiffusion across layer interface, if any, is under the spatial resolution limit of such a technique.

XTEM micrographs in the previous chapters show the sputtered Cu/V 50 nm and 2.5 nm multilayer samples, having columnar grain structure, exhibit distinguishable interfaces without significant intermixing. The interfaces in both samples have Kurdjumov-Sachs (K-S) orientation relationship, i.e. Cu {111} // V {110} and Cu <110> // V <111>, with weak fiber texture in Cu/V 50 nm and strong fiber texture in Cu/V 2.5 nm sample. The depth profile of He bubble distribution in ion irradiated Cu/V multilayer films indicates the He bubble density increases to peak value at a depth of 200 nm and then decreases to zero at a depth of 380 nm. The radiation damage in terms of He bubbles across the entire radiation depth in the irradiated Cu/V multilayers with various radiation levels were examined by XTEM. Figure 5.3a-5.3c compare the de-focused TEM micrographs of Cu/V 50 nm multilayer after He irradiation to a total fluence of $6 \times 10^{19} / m^2$, $6 \times 10^{20} / m^2$, and $1.2 \times 10^{21} / m^2$. Insets in the Figures show the corresponding selected area diffraction (SAD) patterns. The white boxes labeled in the Figures are estimated to be peak damage regions and details will be provided in the following Figures. The numbers of He bubbles in Cu/V 50 nm sample irradiated at the highest fluence are much higher than that in Cu/V 50 nm multilayer with the lowest fluence. This indicates that higher fluence leads to more significant radiation damage, consistent with the SRIM predictions. The comparison of SADs shows no significant change in the texture after ion irradiation. The defocused TEM images of the irradiated Cu/V 2.5 nm to a total fluence of $6 \times 10^{19} / m^2$, $6 \times 10^{20} / m^2$, and $1.2 \times 10^{21} / m^2$ are shown in Figure 5.4a-

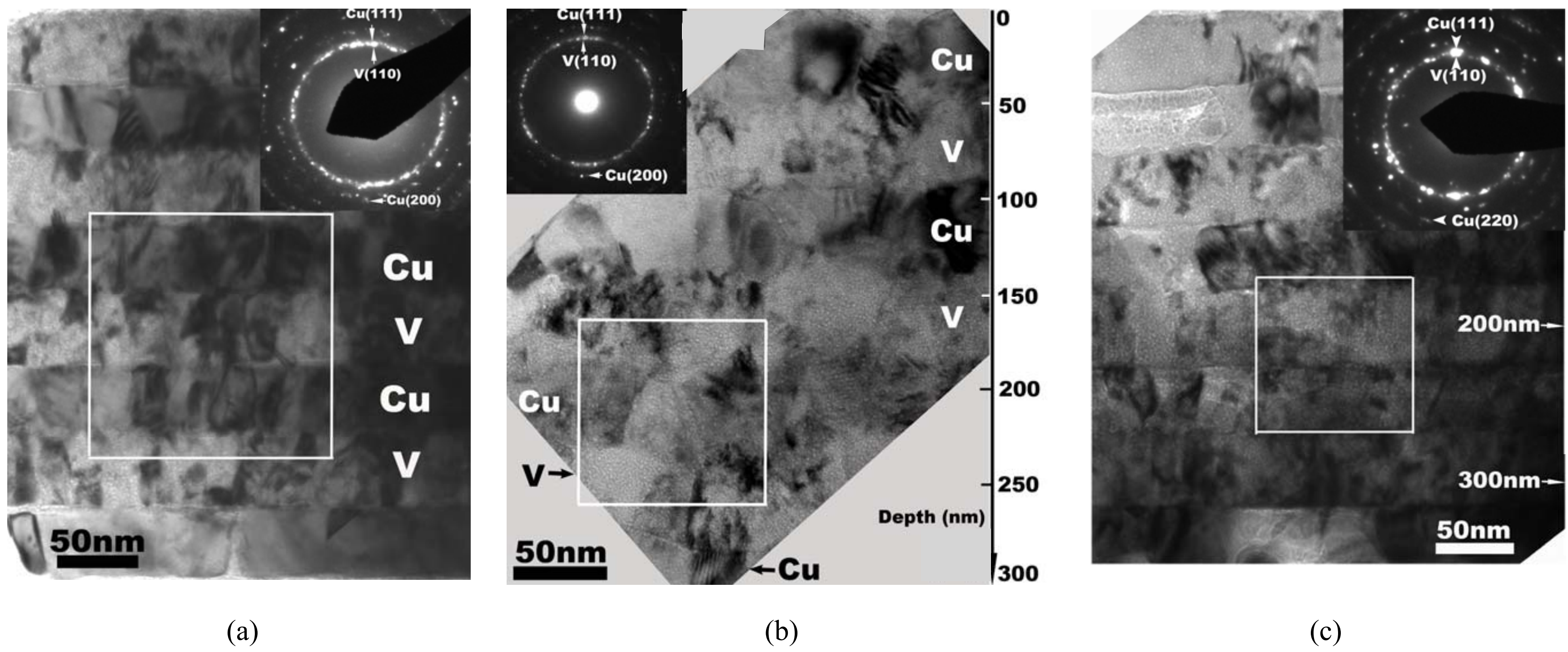

(a) (b) (c)

Figure 5.3. XTEM images of He ion irradiated Cu/V 50 nm upon peak dose of (a) 0.6 dpa, (b) 6 dpa, and (c) 12 dpa.

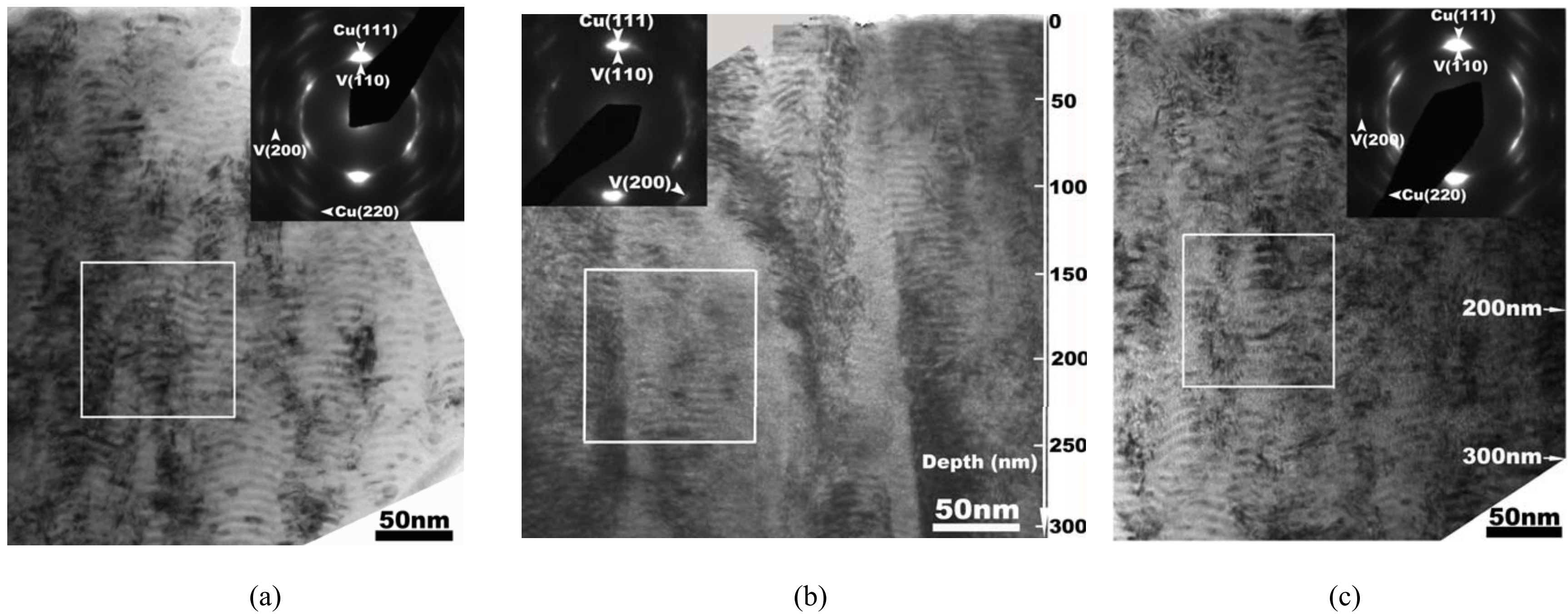

Figure 5.4. XTEM images of He ion irradiated Cu/V 2.5 nm upon peak dose of (a) 0.6 dpa, (b) 6 dpa, and (c) 12 dpa.

5.4c, respectively. Similar trend is observed, i.e. higher dose leads to great concentration of He bubbles. However, no significant He bubbles are observed in ion-irradiated Cu/V 2.5 nm at a flucence of $6 \times 10^{19}/m^2$. The comparison of numbers of He bubbles in the irradiated Cu/V 50 nm (Figure 5.3) and Cu/V 2.5 nm (Figure 5.4) at the same radiation fluence indicates the Cu/V 50 nm multilayer films have much more He bubbles than the Cu/V 2.5 nm samples. At the lowest irradiation fluence in the study, irradiated Cu/V 2.5 nm multilayer has no detectable He bubbles, however, irradiated Cu/V 50 nm does. All the Figures show clear interfaces between Cu and V without apparent intermixing in the irradiated Cu/V multilayers.

Next, the focus will be to compare the *peak damage regions* of Cu/V multilayers subjected to different radiation fluences. Figure 5.5a-5.5c show under-focused XTEM micrographs of the peak damage regions, labeled by the boxes in Figure 5.3, in the irradiated Cu/V 50 nm multilayers subjected to the different dosages. He bubbles appeared in all peak damage regions. The number of He bubbles in Cu/V 50 nm at a peak dose 0.6 dpa is much less than those irradiated at higher doses. The interfaces in all peak damage regions are clear without significant intermixing.

Figure 5.6a-5.6c show the under-focused XTEM micrographs of the peak damage region, labeled by boxes in Figure 5.4a-5.4c, of Cu/V 2.5 nm multilayers ion irradiated to a total fluence of $6 \times 10^{19} / m^2$, $6 \times 10^{20} / m^2$, and $1.2 \times 10^{21} / m^2$. In the peak damage region in all ion irradiated 2.5 nm, the interfaces between Cu and V remain abrupt without significant mixing. With the increase of the ion irradiation dose, the number of He bubbles increases in the peak damage region. However, no bubbles are detected in Cu/V 2.5 nm subjected to a radiation fluence of $6 \times 10^{19} / m^2$. The number of He bubble

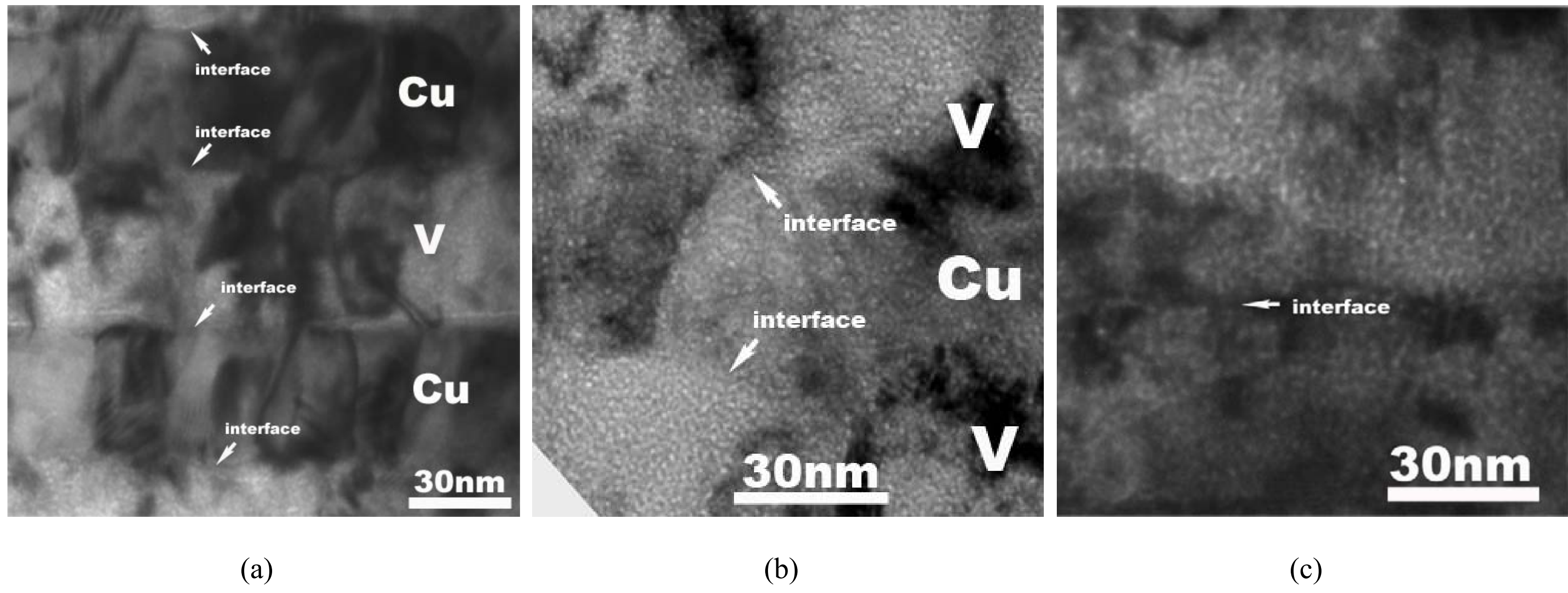

(a) (b) (c)

Figure 5.5. Peak damage XTEM images of ion irradiated Cu/V 50 nm multilayer films subjected to peak dose of (a) 0.6 dpa, (b) 6 dpa, and (c) 12 dpa.

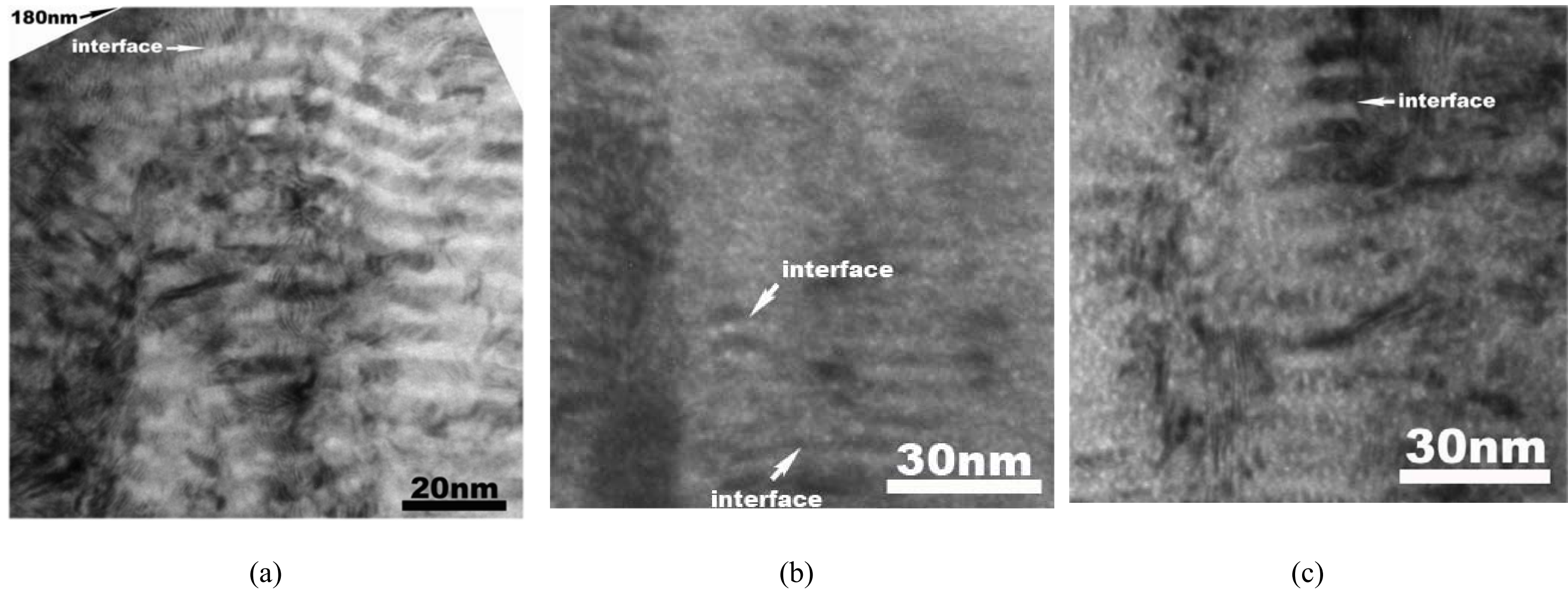

(a) (b) (c)

Figure 5.6. Peak XTEM damage images of ion irradiated Cu/V 2.5 nm multilayer films subjected to upon peak dose of (a) 0.6 dpa, (b) 6 dpa, and (c) 12 dpa.

increases with the increase of the total fluence from 6×10^{20} /m^2 to 1.2×10^{21} / m^2.

Overall, layer interfaces retain in all irradiated multilayers in spite of a high He concentration and a highest fluence of 1.2×10^{21} / m^2. The SAD patterns (not shown here) for all the samples indicate the orientation relationship between the Cu and V at interfaces remains unchanged, and no extra diffraction spots are identified. The comparison between ion irradiated Cu/V 50 nm and Cu/V 2.5 nm subjected to the same dose indicates that Cu/V 50 nm multilayers contain more radiation damage in terms of He bubbles, compared to ion irradiated Cu/V 2.5 nm multilayer specimens.

5.3.3 Peak He bubble density evolution

To compare the radiation damage quantitatively at various fluences, a plot of peak He bubble density, counted from TEM micrographs taken with an under-focus distance of -400 nm, as a function of fluences for ion irradiated Cu/V 50 and 2.5 nm multilayers samples is shown in Figure 5.7. Overall, the bubble density in the peak damage regions of irradiated Cu/V 50 nm multilayer is a factor of 3 higher than that in irradiated Cu/V 2.5 nm multilayer at the same radiation dose. The peak He bubble density increases with increasing fluence and reaches saturation at the fluence of 6×10^{20} / m^2 in ion irradiated Cu/V 50 nm multilayers. The He bubble density increases continuously with increasing fluence in irradiated Cu/V 2.5 nm multilayer. Although the peak helium bubble density shows the trend to reach saturation in irradiated Cu/V 2.5 nm at a fluence of 1.2×10^{21} / m^2, it is speculated that the Cu/V 2.5 nm multilayer may reach the same level of peak helium peak bubble density as Cu/V 50 nm multilayer after it is subjected to even higher total helium ion fluence.

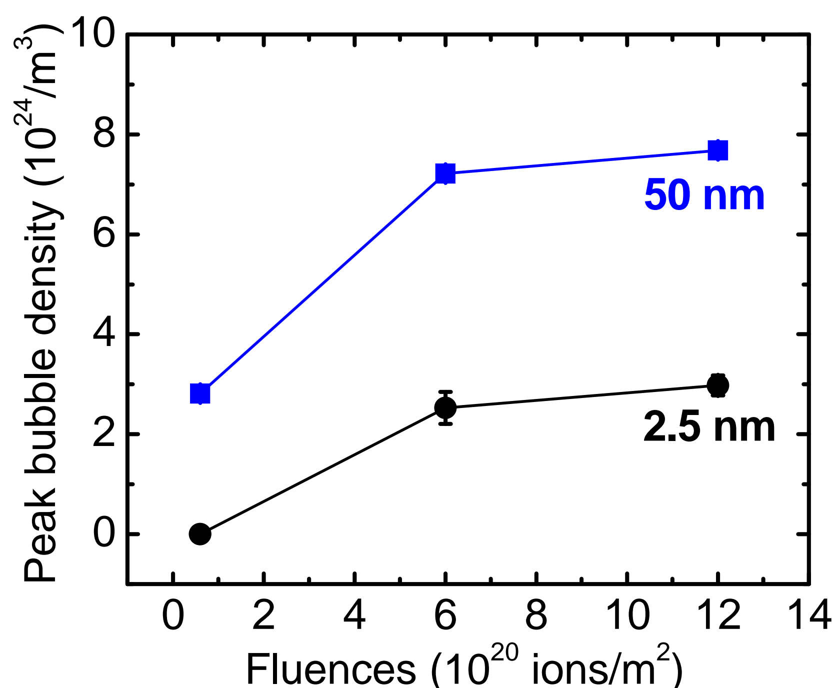

Figure 5.7. Comparison of Helium bubble density in the peak damage region distribution in irradiated Cu/V multilayers. Peak He bubble density is reduced by a factor of 3 in Cu/V 2.5 nm, in comparison to that in Cu/V 50 nm specimen.

5.3.4 Lattice expansion examined by XRD

The lattice expansion was deduced from the shift of the diffraction peak position of Cu/V multilayers with Si (100) substrates before and after irradiations with various fluences characterized by X-ray diffraction (XRD) shown in Figure 5.8. Si (400) peak from Si substrate is used as a reference for calibration purpose. Two distinct peaks of V (110) and Cu (111) are observed in all Cu/V 50 nm multilayer samples shown in Figure 5.8a. With the increase of total fluences, labeled by peak damage of 0.6 dpa, 6 dpa and 12 dpa, respectively, both the V (110) and Cu (111) peaks shifted to the lower angle. Also the magnitude of peak shift in V (110) is more significant, compared to that of Cu (111) peak. Similarly, the comparison of peak shift in XRD patterns of the Cu/V 2.5 nm

multilayers is shown in Figure 5.8b. An overlapped V (110) and Cu (111) peak is observed in all Cu/V 2.5 nm multilayer samples. After He ion irradiation at different fluence levels, the peak shift of overlapped peak to the low angle increases insignificantly, and the peak shift is much smaller than that observed in irradiated Cu/V 50 nm multilayers.

The lattice expansion deduced from the peak shift of XRD patterns as a function of fluence in Cu/V 50 nm and Cu/V 2.5 nm is shown in Figure 5.8c. At the lowest fluence 0.6×10^{19} / m^2, the lattice expansion in V layer is 0.15 % in Cu/V 50 nm multilayers, however, its lattice expansion increases to 1.38 %, when the fluence increases to 1.2×10^{21} / m^2. The expansion of lattice parameter in Cu layer subjected to the highest fluences of 1.2×10^{21} / m^2 is 0.36 %, which is also higher than that (0.08 %) in the sample subjected to the lower fluence. Much smaller position shift of the overlapped peak in Cu/V 2.5 nm multilayers shows that magnitude of lattice expansion in Cu/V 2.5 nm specimens is much smaller than that in Cu/V 50 nm specimen subjected to the same irradiation fluence.

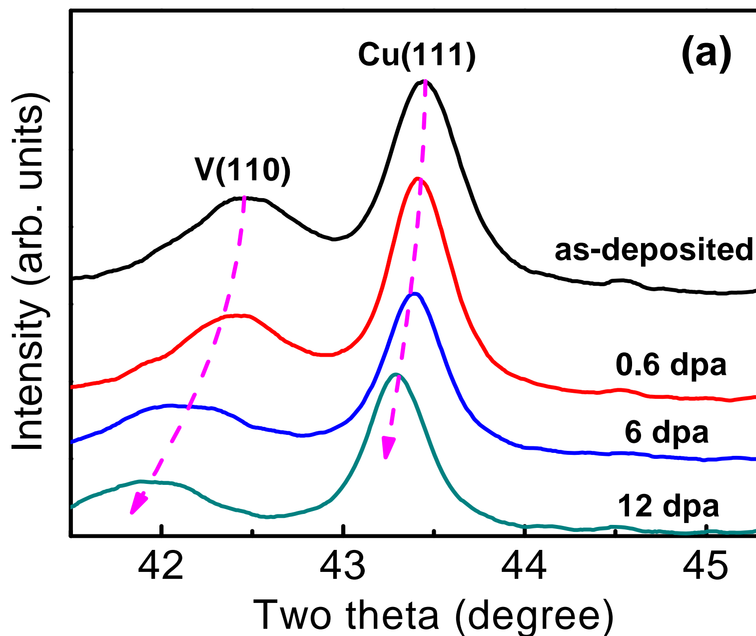

(a)

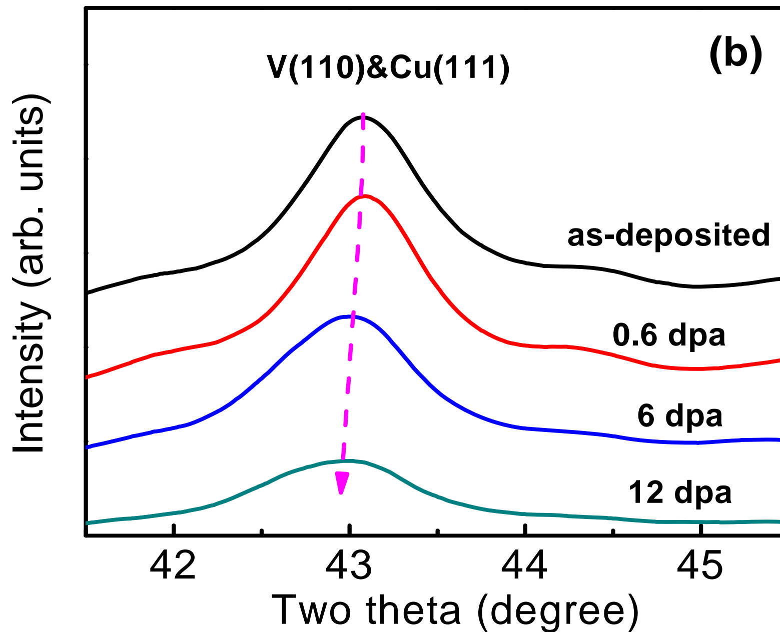

(b)

Figure 5.8. (a) and (b) XRD patterns of as-deposited and irradiated Cu/V multilayers with individual layer thickness of 50 nm and 2.5 nm; (c) Lattice expansion ratio from XRD pattern as a function of peak dosage for ion irradiated Cu/V multilayers with individual layer thickness of 50 nm and 2.5 nm.

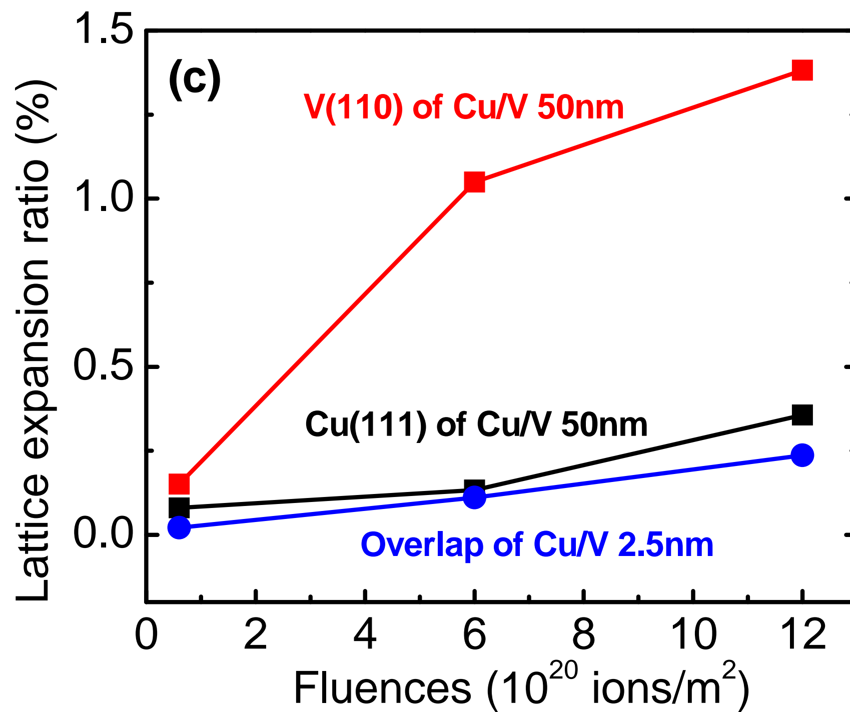

(c)

Figure 5.8 Continued.

5.3.5 Dose dependent radiation hardening

To examine dose dependent radiation hardening, the hardness of irradiated Cu/V multilayers were measured by nanoindentation technique. Dose rate was essentially the same during radiation experiments and loading rate was kept constant during nanoindentation. Figure 5.9a shows the evolution of hardness change (radiation hardening) at different fluence levels as a function of h. The trend of radiation hardening in specimens irradiated at different fluences is similar, i.e., radiation hardening is more significant at greater h and decreases with decreasing h. A greater fluence (from 6×10^{19} / m^2 to 6×10^{20} / m^2) leads to more significant radiation hardening when h > 1 nm. Hardening is negligible for fine ($h \leq 2.5$ nm) multilayers at all fluence levels in the study.

No radiation hardening is observed in Cu/V 1 nm multilayers even at a fluence of 6 × 10^{21} / m^2. The hardness enhancement seems to reach a saturation value at a fluence of 6 × 10^{20} / m^2. The hardness enhancement in Cu/V multilayer with greater *h* is more significant at higher dose. The hardness increases in Cu/V multilayer films with different individual layer thicknesses as a function of radiation fluence is compared in Figure 5.9b. Overall the hardness increases with the increase of fluence in all these three Cu/V multilayer films. However, the magnitude of hardness increase in Cu/V 2.5 nm is much less than that in Cu/V 10 nm and Cu/V 50 nm multilayers subjected to the same radiation fluence.

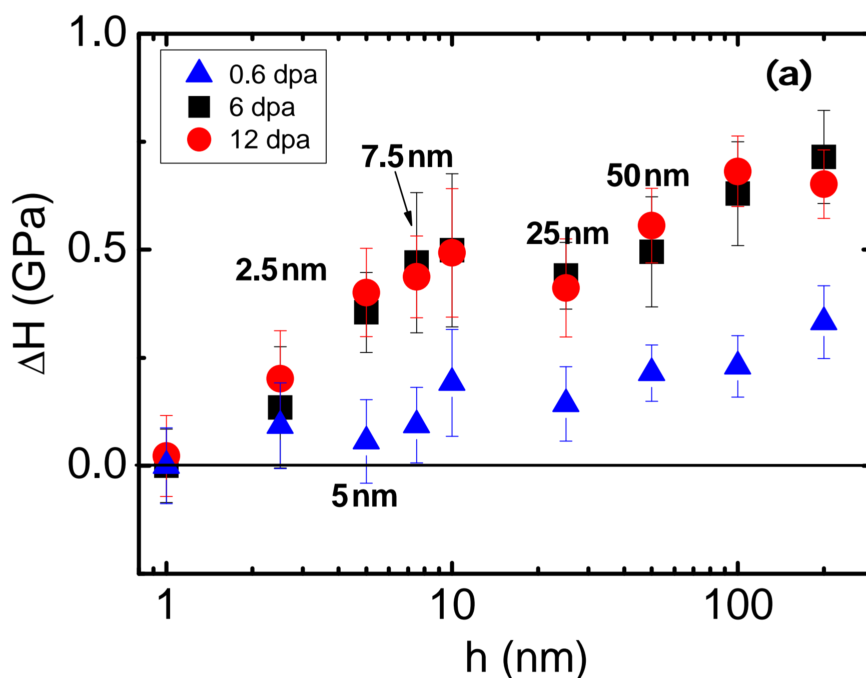

(a)

Figure 5.9. (a) Comparison of radiation hardening vs. *h* at different radiation levels; (b) Comparison of radiation hardening vs. different radiation fluence levels.

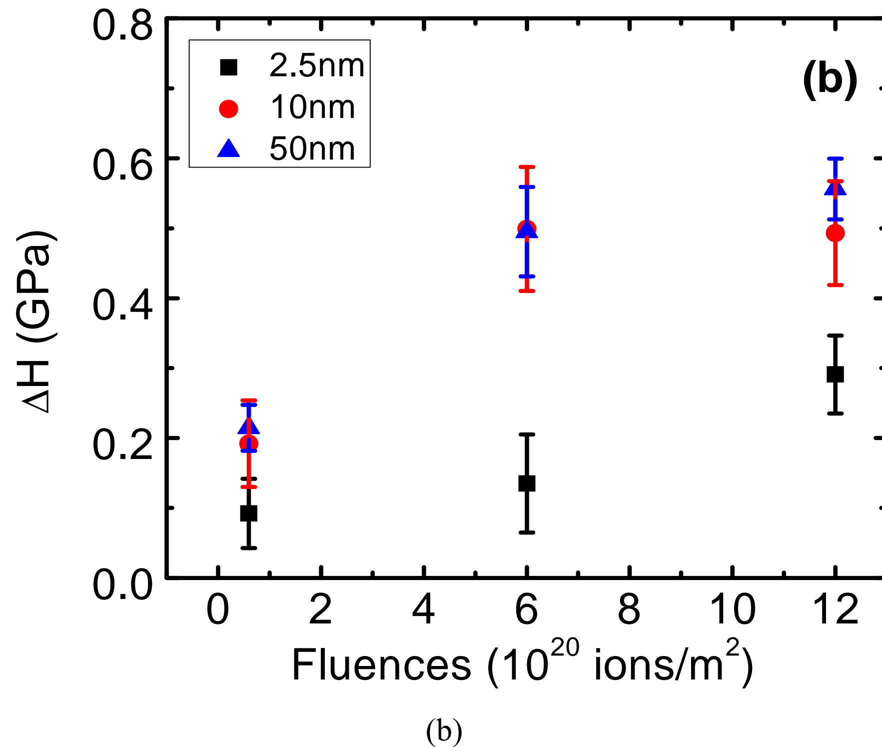

(b)

Figure 5.9 Continued.

5.4 Discussions

5.4.1 Interfacial stability upon high dose

Ion mixing along the interfaces between dissimilar materials induced by bombardment of energetic particles has frequently been observed in many miscible systems such as Cu/Au [261], Hf/Ti [262], Fe/W [263] and Al/Nb [264], however, as for the immiscible Cu/V interface, the chemical analysis study shown in Figure 5.2 has shown clear interfaces without significant intermixing. The simulation for Cu recoil atoms into V layer and V recoil atoms into Cu layer due to He ion irradiation has been performed by SRIM computer code using the experimental ion energy of 50 keV. The distribution of recoil atoms into layers can be well fitted by Gauss function:

$$f(x) = ae^{-\frac{(x-b)^2}{2c^2}} \tag{109}$$

where a, b, and c are constant. The parameter c is related to the full width at half maximum (FWHM) of the peak. The value of FWHM of diffusion regions in He ion irradiated Cu/V from SRIM simulation is within the range from 9 Å to 14 Å. The ion mixing region along the interface at a depth of 150 nm has the maximum FWHM value of 14 Å, which is above the limitation of STEM resolution and can be detected by chemical analysis. However, no significant ion intermixing region with a length of 1.5 nm along the interface between layers was observed by the STEM and EDX. When the fluence increases to 1.2×10^{21} / m^2, both STEM (Figure 5.2) and XTEM micrographs of irradiated Cu/V 50 nm and Cu/V 2.5 nm (Figure 5.3c and 5.4c) still show clear interface without intermixing. There is a very limited mutual solid solubility between Cu and V. According to the phase diagram, only approximately 2.5 wt % Cu can be dissolve in V at 800 °C, which results in a positive heat of mixing of ~ 5 kJ/mol [229]. The positive heat of mixing leads to a driving force for de-mixing process between Cu and V. The competition result between mixing and de-mixing is that the de-mixing process canceled the influence of ion mixing on the Cu/V interface. Therefore, no significant ion intermixing between Cu/V was observed. Similar phenomena showing a lack of irradiation induced intermixing have been observed in several multilayer systems such as Cu/W [261], Cu/Nb [257] and Hf/Ni [262], which are all immiscible systems and have positive heat of mixing.

5.4.2 Radiation induced He bubbles and lattice expansion

Radiation damage, such as He bubbles, has been observed in the irradiated Cu/V multilayers. The interactions between the projectiles and the atoms in the solid result in

the collision cascade, composed of the vacancy clusters core and interstitial shell. After collision, the recombination of interstitial and vacancy occurs immediately by which most of point defects recover to the original site. However, a small fraction of interstitial and vacancy will remain in the matrix and develop to either the dislocation loops or voids. He atoms introduced by ion irradiation can combine with vacancy clusters and thus form He bubbles. The density of He bubbles is a direct measure of the magnitude of radiation damage. Radiation damage during ion solid interactions can be described by the modified Kinchin-Pease displacement damage function. When the energy of the implanted particles is greater than the minimum displacement energy of atoms, the modified Kinchin-Pease displace damage function is given by:

$$\langle N_d(E) \rangle = \frac{\xi \nu(E)}{2E_d} \tag{110}$$

where $\langle N_d(E) \rangle$ is the vacancy-interstitial pairs (Frenkel pairs) generated by a primary knock-on effect, E_d is minimum displacement energy, and ξ is parameter suggested to be 0.8 by both analytical theory and computer simulations. $\nu(E)$ is nuclear stopping power and is given by $\nu(E) = dE/dx$ [116].

This equation is used to calculate the Frenkel pairs and estimate the radiation damage. Before that, the nuclear and electronic stopping power is required. It is well known that the contribution to ion stopping in solids originates from two different mechanisms: nuclear and electronic stopping [116]. Nuclear stopping, the loss of energy by ion-target nucleus collisions, plays a dominant role in displacing the atoms from their lattice sites. In the case of electronic stopping, ions lose energy by collision with target electrons. The nuclear and electronic stopping power can be obtained through SRIM

simulation, but their stopping power as a function of projected range can not be obtained directly from SRIM. Firstly, a table regarding stopping powers as a function of energy can be calculated by SRIM. After that the energy can be converted into the corresponding depth for 50 keV He ions. The comparison of the electronic and nuclear stopping powers of He ions in the Cu/V multilayer based on SRIM simulation is shown in Figure 5.10. Electronic stopping is reduced with increasing depths, while nuclear stopping increases with increasing of depth and reaches the peak at a depth of the range between 150 nm and 200 nm, which is consistent with the depth where peak damage region was observed experimentally in Figure 5.3 and 5.4.

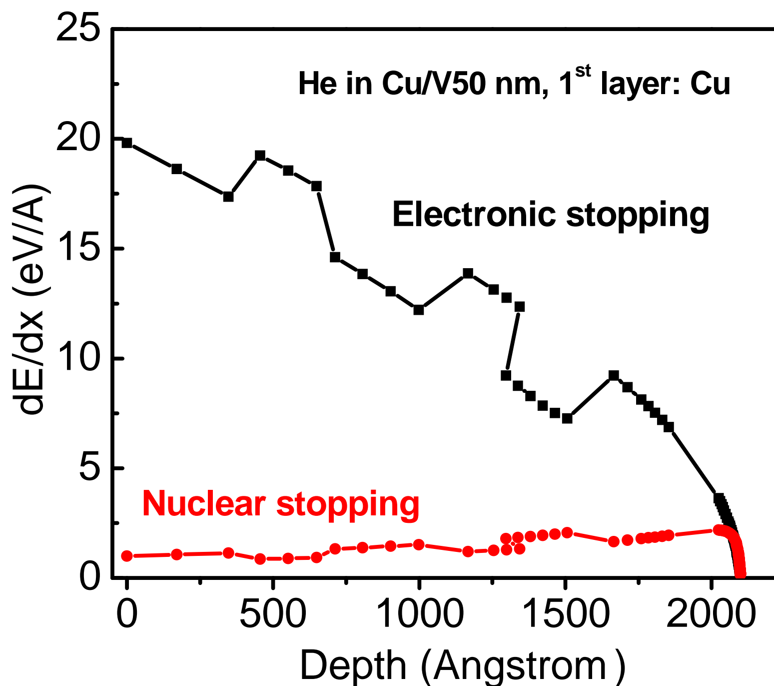

Figure 5.10. The comparison of the electronic and nuclear stopping powers of He ions in the Cu/V multilayer based on SRIM simulation.

Based on the nuclear stopping power functions, the Frenkels pairs generated by a primary knock-on effect as a function of depth can be calculated. At a given total fluence ϕ, the displacements per atom (dpa) as a function of depth is given by [116]:

$$dpa(x) \cong \frac{N_d(x)}{N} = \frac{0.8\phi}{2NE_d} \cdot \left.\frac{dE}{dx}\right|_n \tag{111}$$

where $N_d(x)$ is the Frenkel pairs generated by knock-on effect at a given fluence of ϕ, N is the atomic density of the solid, and $\left.\frac{dE}{dx}\right|_n$ is nuclear stopping power as a function of depth. Another approach to calculate $dpa(x)$ is given by SRIM simulation, which uses the same analytic method as above. The SRIM simulation can provide the value of *D*, which has the unit of displaced atoms per ion per unit thickness. In the calculation, the $dpa(x)$ is given by [116]:

$$dpa(x) = D \cdot \phi / N \tag{112}$$

Based on this analytic method, the plot of $dpa(x)$ for He ion irradiated Cu/V 50 nm upon a total fluence of 1.2×10^{21} / m^2 is shown in Figure 5.11. The peak radiation damage is around 12 dpa at a depth of 150 nm in Cu layer. Similarly, the plot of $dpa(x)$ in He ion irradiated Cu/V 50 nm at 6×10^{19} / m^2 and 6×10^{20} / m^2 has the same distribution of radiation damage, but corresponding magnitude of dpa is smaller than that irradiated to a flucence of 1.2×10^{21} / m^2 by a factor of 20 and 2, respectively. This is the reason why higher irradiation fluence level results in heavier radiation damage, observed in both irradiated Cu/V 50 nm (Figure 5.3) and Cu/V 2.5 nm (Figure 5.4) where the He bubbles are more frequently observed in Cu/V multilayers upon higher fluence of He ion irradiation.

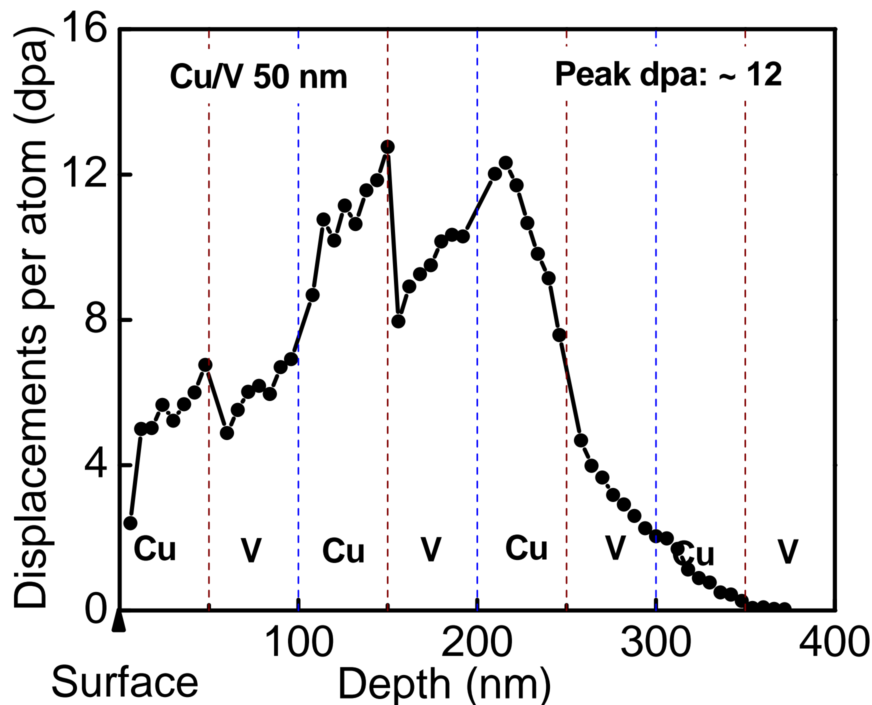

Figure 5.11. The plot of $dpa(x)$ for He ion irradiated Cu/V 50 nm upon a total fluence of 1.2×10^{21} / m^2.

The SRIM simulation results predict the similar irradiation damage generated at the same irradiation fluence based on the calculation method above, however, it is noted that the comparison of de-focused XTEM micrographs of the irradiated Cu/V multilayer samples (comparing Figure 5.3a-3c with Figure 5.4a-4c orderly) indicates the irradiated Cu/V 2.5 nm samples have less radiation damage with respect to the Cu/V 50 multilayer sample subjected to the same fluence levels.

Figure 5.12a and 5.12b show the depth dependent He concentration profiles of Cu/V 50 nm and Cu/V 5 nm multilayers predicted by SRIM simulation, respectively. The simulation assumes no interface effect to the radiation damage. The vertical dashed lines, obtained from the de-focused TEM images of Figure 5.3 and Figure 5.4, indicate the depth range over which bubbles are observed (assuming similar results of He

concentrations between Cu/V 5 nm and Cu/V 2.5 nm). The intersection of the vertical dashed lines with the SRIM simulated He concentration profiles indicates that the minimum He concentration at which the bubbles are observed. In Cu/V 50 nm upon the highest fluence in the study, the minimum He concentration where the bubbles are detectable is approximately 0.27 at. % at ~ 5 nm underneath the film surface. This value is very similar with that in Cu/V 50 nm multilayer upon the lowest fluence, although the depth where the bubbles can be observed is around 140 nm. On the other hand, the threshold of He concentration in Cu/V 2.5 nm upon the highest fluence is around 1.8 %. Note the He concentration introduced into Cu/V 2.5 nm at the lowest fluence of 6×10^{19} / m^2 in the study is smaller than the threshold of He concentration, so no He bubbles are observed. This indicates the Cu/V 2.5 nm has higher threshold of He concentration to form the He bubbles and thus has more radiation tolerance than that with greater h.

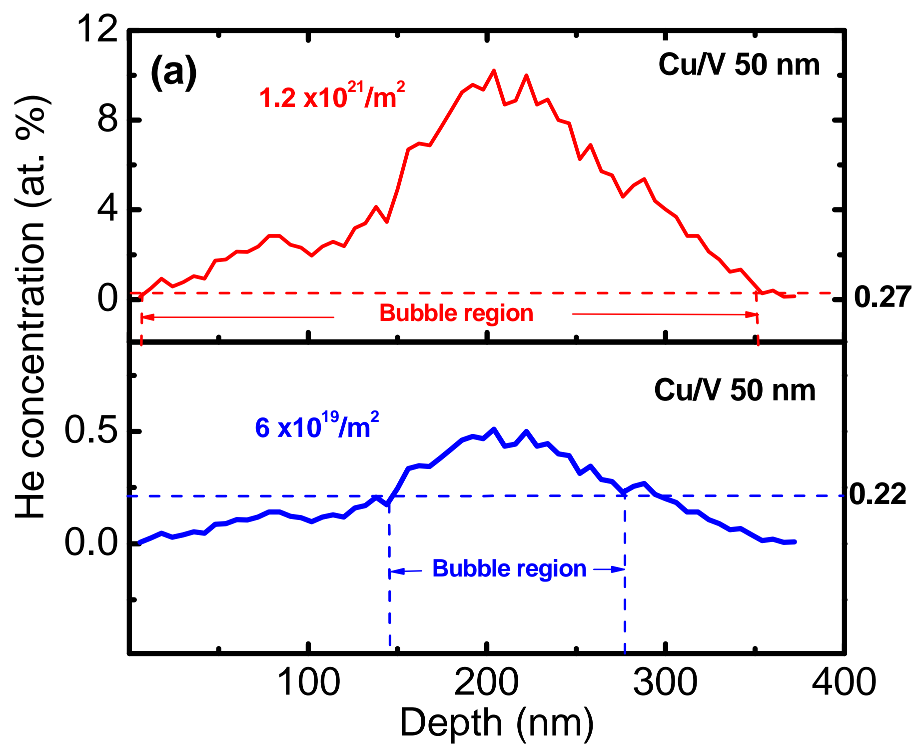

(a)

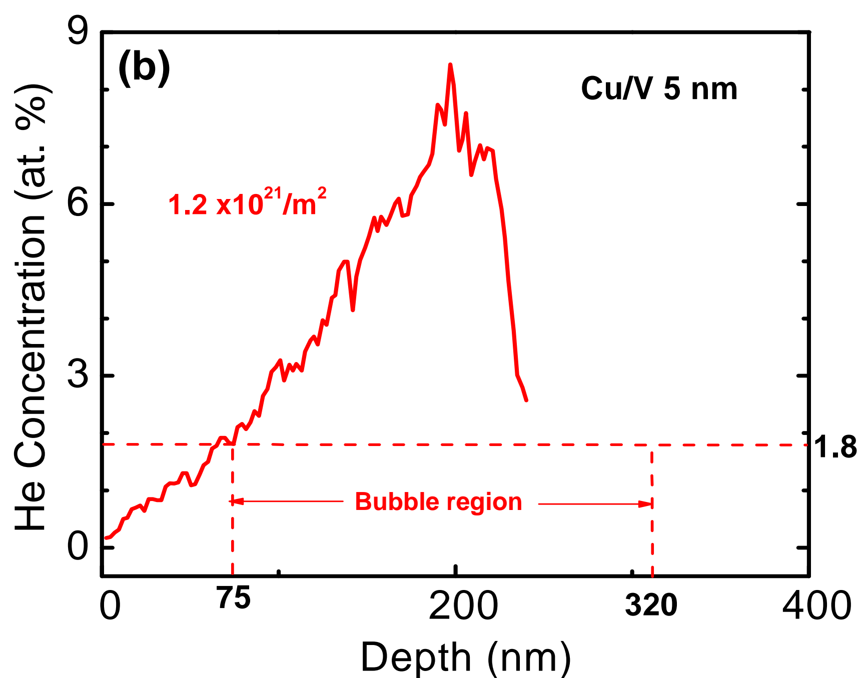

(b)

Figure 5.12. (a) and (b) show the depth dependent He concentration profiles of Cu/V 50 nm and Cu/V 5 nm multilayers predicted by SRIM simulation, respectively.

On the other hand, the aforementioned discussions are based on the assumption that the interfacial regions do not trap or reduce the radiation damage. However, it is well accepted that grain or phase boundaries may act as sinks for radiation induced point defects and their clusters, where recombination of interstitial and vacancy could occur and such recovery process assists the interfaces in maintaining their ability to continuously absorb point defects [183, 253-256]. The Cu/V 2.5 nm has 20 times of volume fraction of interfacial region as the Cu/V 50 nm nanlayers at a given total thickness. This means the Cu/V 2.5 nm may have less radiation damage than that predicted by SRIM simulation due to the strong effect of interfaces. This hypothesis has been confirmed by the experimental observation of both de-focused XTEM of peak damage regions in Figure 5.5 and Figure 5.6, and the peak bubble density in Figure 5.7. In the peak damage regions, the irradiated Cu/V 2.5 nm has less radiation damage in terms of He bubbles compared to Cu/V 50 nm upon the same fluence of irradiation. Consequently, the peak bubble density in irradiated Cu/V 2.5 nm is much lower than that in irradiated Cu/V 50 nm at the same fluence level as well. In the previous chapter, we already discussed the phenomena of reduction of He bubble density in irradiated Cu/V 2.5 nm with respect to the irradiated Cu/V 50 nm. The equilibrium distribution function of He bubbles with the number of vacancies, n, and gas atoms, x [111]:

$$\rho^0(n,x) = M_x \exp\{n \ln S_V - \xi n^{2/3} + x \ln(\frac{MHn\Omega}{xkT})\} \tag{103}$$

is determined by $S_V = \frac{C_V}{C_{V_0}}$ in Cu/V 2.5 nm and Cu/V 50 nm multilayers.

The interfacial regions are expected to act as effective sinks for radiation induced defects due to the tendency of point defect migration to the interface. Cu/V 2.5 nm has

smaller C_V due to the annihilation of vacancies with interstitials and larger value of C_{V_0} due to the interface effect. The reduction of He bubble density in multilayers is thus a combined effect of enhanced defect storage capacity (increasing C_{V_0}) and increased probability of defect annihilation at interfaces (decreasing C_V).

The magnitude of the peak shift in both peak Cu (100) and peak V (110) in irradiated Cu/V 50 nm increases with the increase of radiation fluence. In Cu/V 2.5 nm sample, the magnitude of peak shift increases very small even subjected to the highest fluence of 1.2×10^{21} / m^2 in the study. This observation results in the conclusion that the peak shift in Cu/V 50 nm is more significant than that in Cu/V 2.5 nm. Peak shift is related to the change of d-spacing or lattice parameter induced by defects. More peak shift implies more radiation damage. In Cu/V 2.5 nm, less peak shift indicates a large number of interface can effectively absorb the radiation induced point defects.

Lattice expansion deduced from XRD studies shown in Figure 5.8c provides another means to evaluate the radiation damage level. A couple of factors can contribute to lattice distortions, such as dissolution of solute atoms, vacancies, He bubbles, interstitials, and interstitial loops. The studies in the previous chapter indicated insignificant contributions to lattice distortion from interstitials and interstitial loops. Up to 2 wt. % of Cu can be dissolved in V according to phase diagram, so the maximum lattice expansion induced by dissolution of Cu in V is 0.46 % with assumption of a maximum of 2 wt % Cu into V. Other major contribution to lattice expansion is the He bubbles according to previous studies. Pressurized He bubbles could lead to lattice expansion based on the point source dilatation mechanism [270]. The less lattice expansion in Cu/V 2.5 nm compared to Cu/V 50 nm confirms again the Cu/V multilayer

with smaller h has less defects and thus has more radiation tolerance than that with greater h.

5.4.3 Radiation hardening mechanisms

Radiation hardening and its strengthening mechanism together with the effect of interface in irradiated Cu/V multilayer films have been discussed in Chapter IV. The increase of the hardness after irradiation is attributed to the interactions of dislocations with two types of radiation-induced defects, which are strong obstacles, such as interstitials, interstitial loops, SFTs and precipitates, and relatively weak obstacles, such as He bubbles [156, 267, 274]. Based on this description, the dispersed barrier model for strong obstacles and FKH model for weak obstacles were applied to explain and estimate the radiation hardening in irradiated Cu/V multilayer films, respectively. The previous study indicated He ion irradiation results in the increase of film hardness (radiation hardening) when the individual layer thickness is greater. However the magnitude of radiation hardening is reduced continuously with decreasing h, and became negligible at $h \leq 2.5\,\text{nm}$. In the irradiated Cu/V multilayer with a few nanometer length scale, the negligible radiation hardening was consistent with the estimation of He bubbles induced hardening based on the FKH model. This indicates the He bubbles play a dominant role in the radiation hardening of the irradiated Cu/V multilayers at small length scale. As the radiation fluence varies to the Cu/V multilayers with small h, radiation hardening changes slightly based on the distribution of He bubbles. But the magnitude of radiation hardening remains low. For an example, the estimation of He bubble induced radiation hardening in irradiated Cu/V 2.5 nm multilayer with a fluence of 1.2×10^{21} / m^2 is 0.12 GPa, according to FKH model, which is very close to the experimental observation of

radiation hardening of 0.2 GPa. The difference between them could be attributed to the other defects induced hardening at higher radiation fluence.

On the other hand, when the irradiated Cu/V multilayers have greater h, radiation hardening is induced not only by the He bubble but also by other defects, such as interstitial loops. The interstitial loop induced hardening can be estimated by the dispersed barrier model based on the fact that they are treated as the strong obstacles to the trespassing of the dislocations. Due to the difficulty to quantify interstitial loop density from the XTEM experiments, it is very hard to estimate the interstitial loop induced hardening by obtaining the interstitial loop density. But dispersed barrier model can be used to estimate average interstitial loop density assuming a known interstitial loop induced hardening. In this study, it is given by subtracting the He bubble-induced-hardening from the observed experimental hardening. The estimation of average interstitial loop density with an assumption of size of 2 nm is estimated as 0.7×10^{23} /m^3 for Cu/V 50 nm multilayer upon 1.2×10^{21} / m^2 He ion irradiation fluence, which is on the same order of the interstitial loop density of 6.7×10^{23} /m^3 and 2.3×10^{23} /m^3 in neutron-irradiated polycrystalline pure Cu and V metals subjected to a total dose of 0.92 dpa and 0.69 dpa, respectively [149].

In addition to the similar trend of the radiation hardening observed in irradiated Cu/V multilayers upon He ion irradiation with various fluences, another significant observation is the saturation of radiation hardening when the irradiation fluence reaches a certain value. The dispersed barrier hardening model indicates the magnitude of radiation hardening increases as $N^{1/2}$, where N is the defect density. In the absence of mechanisms for the destruction of obstacles, N is proportional to the total fluence of ion

irradiation, so the radiation hardening should be proportional to $(\phi)^{1/2}$ and can be expressed by [127]:

$$\Delta\sigma_S \propto (\phi)^{1/2} \tag{113}$$

where $\Delta\sigma_S$ is the increase of yield strength and ϕ is the radiation fluence. At low doses, the radiation hardening is estimated accurately and can be fitted with a $(\phi)^{1/2}$ dependence quite well by the equation above. This equation indicates radiation hardening will continue to increase with increasing radiation fluence without a limit. Hence it will clearly overestimate the hardening once the radiation induced defect density reaches saturation. At higher doses, the radiation saturation is usually because of cascade overlap [280, 281]. In trying to account for saturation of radiation hardening, Makin and Minter proposed that the displacement cascade can not create new zone in the neighborhood of an existing zone or cluster because the reduced volume available for new zones formation cause it harder to form as the concentration increases [282]. They suggested a two parameter equation to predict radiation hardening:

$$\Delta\sigma_S = A[(1-\exp(-B\phi)]^{1/2} \tag{114}$$

where A and B are regression coefficients. This expression shows a progress transition from the low-dose region with $(\phi)^{1/2}$ dependence to the saturation regime with an asymptotic value A at very high dose [158].

For simplicity, in this study the power-law expression will be used to evaluate the saturation of radiation hardening:

$$\Delta\sigma_S = m\phi^n \tag{115}$$

where m and n are regression coefficients, ϕ is the radiation fluence, and can be replaced by dpa [283-284].

When the radiation dose is greater than the saturation dose, the exponent n for Cu and V is 0.01 and 0.13, where the saturation dose is 0.05 dpa for Cu and 0.003 dpa for V, respectively [158]. The corresponding coefficient m, representing the magnitude of radiation hardening, is 290 MPa for Cu and 280 MPa for V, respectively [158]. In the case the saturation dose is much smaller than the present study, so the coefficient of m and n can be used to estimate the saturation of radiation hardening in the irradiated Cu/V multilayers. When h is 50 nm in the Cu/V multilayer irradiated up to a total fluence of 1.2×10^{21} / m^2, the average dose deduced from Figure 5.11 is 6 dpa in Cu layer and 4 dpa in V layer. The estimation of radiation hardening is the average value of the hardening contributed from both Cu and V layers. By incorporating the dose, m and n, the calculation of radiation hardening based on power-law expression is 0.85 GPa in Cu/V 50 nm irradiated by fluence of 1.2×10^{21} / m^2. Similarly, the calculated value for radiation hardening in irradiated Cu/V 50 nm with a flucence of 6×10^{20} / m^2 is 0.81 GPa. Both values are slightly greater than the experimental data of 0.6 GPa and 0.5 GPa of radiation hardening in irradiated Cu/V 50 nm multilayer upon these two fluences, respectively. The slight difference between the calculation and experiment value could be due to the reduction of radiation damage (dpa) induced by the effect of interface. Better regression coefficients of m and n for this case can be obtained by fitting the experimental data based on the power-law expression.

Compared to Cu/V 50 nm multilayer, Cu/V 5 nm multilayer has much larger volume fraction of atoms at interfacial regions. Previous study shows the interfacial

region can significantly reduce the radiation damage, so the regression parameters used in estimating hardening by power-law expression in irradiated Cu/V 50 nm multilayer will deviate to evaluate the hardening in irradiated Cu/V 5 nm multilayers due to a higher density of interfaces. For an example, by using the m and n of regression coefficients together with the radiation damage from SRIM for irradiated Cu/V 5 nm, the radiation hardening is estimated to be 0.86 GPa and 0.82 GPa, which is much greater than the experimental value of 0.40 GPa and 0.36 GP in irradiated Cu/V 5 nm with fluence of 1.2 × 10^{21} / m^2 and 6 × 10^{20} / m^2, respectively. The discrepancy could be due to the reduced radiation damage induced by greater density of interfacial region in irradiated Cu/V 5 nm, whereas the SRIM failed to consider the strong interfacial effect. On the other hand, regression coefficients of m and n can be fitted according to the experimental values in irradiated Cu/V 50 and Cu/V 5 nm multilayers with various fluences based on the power-law equation when radiation damage is known. For an example, the fitting power-law expression based on experimental data multilayer with various fluences of 6 × 10^{20} / m^2, 1.2 × 10^{21} / m^2, and 1.8 × 10^{21} / m^2 for irradiated Cu/V 50 nm is:

$$\Delta\sigma_S = 131.4\,(\phi/10^{20})^{0.180} \tag{116}$$

where $m = 131.4\ MPa$ and $n = 0.180$, and for irradiated Cu/V 5 nm is:

$$\Delta\sigma_S = 106.7\,(\phi/10^{20})^{0.123} \tag{117}$$

where $m = 106.7\ MPa$ and $n = 0.123$. The values for the exponent $n = 0.180$ and $n = 0.123$ are within the range of 0.07-0.18 and 0.01-0.24 in the high-dose regime in BCC and FCC metals, respectively [158]. This fitting expression could evaluate the radiation hardening in irradiated Cu/V 50 nm and irradiated Cu/V 5 nm with various fluences, which are greater than the saturation dose.

5.5 Conclusions

The dose dependent evolution of microstructure and mechanical properties of sputtered Cu/V multilayers subjected to 50 keV He ion irradiation were investigated systematically. The interfaces in all immiscible Cu/V multilayers remain clear without significant intermixing even at the total fluence of 1.2×10^{21} / m^2, corresponding to a peak damage of 12 dpa. A nearly immiscible interface between Cu and V is believed to play a significant role to avoid ion mixing. With increasing the total fluences, the peak He bubble density increases, but it is a factor of 3 lower in irradiated Cu/V 2.5 nm multilayers, compared to Cu/V 50 nm multilayers. Higher radiation fluences results in greater radiation damage, except at very small h (2.5 nm or less). The threshold He concentration to form He bubbles is greater in irradiated Cu/V 2.5 nm multilayer than that in Cu/V 50 nm. Interface enhanced radiation tolerance is explained by a combined effect of enhanced defect storage capacity and increased probability of defect annihilation at interfaces.

At all fluences, radiation hardening is greater in Cu/V multilayer with greater h, but it becomes negligible when h is at the length scale of a few nm. The saturation of radiation hardening in Cu/V multilayers at greater fluences was discussed based on an empirical power-law expression. The saturation of radiation hardening in irradiated Cu/V with greater h is close to the calculation, but the saturation behavior in Cu/V multilayer with small h deviates. The saturations of radiation hardening in both irradiated Cu/V 50 nm and Cu/V 2.5 nm yield new fitting coefficients.

CHAPTER VI

THERMAL STABILITY OF CU/V MULTILAYERS

6.1 Introduction

The study in the chapter V has shown the interfacial stability upon high He ion irradiation up to a fluence of 1.2×10^{21} / m^2. XTEM micrographs of irradiated Cu/V 50 nm and Cu/V 2.5 nm multilayers show clear interface without significant ion-induced-mixing due to very limit mutual solid solubility between Cu and V. The chemical and morphological stability of the interface is also important at high temperatures since most metallic materials will be applied at these temperatures. This chapter, therefore, is aimed at exploring the thermal stability of interfaces at elevated temperatures.

6.2 Experimental

A series of Cu/V multilayers with individual layer thickness, h, ranging from 1 to 200 nm were deposited by dc magnetron sputtering technique at room temperature on oxidized Si substrates with 1 μm thick SiO_2. The details regarding synthesis of immiscible Cu/V multilayers can be found in the previous chapters, but this time for annealing study, the SiO_2 instead of HF etched Si (100) was used as the substrates for growing Cu/V multilayers. This is due to the reason that V or Cu will react with Si and they will diffuse into each other under high temperature [285]. Consequently, the Cu/V multilayers will be contaminated and peeled off from substrate after high temperature annealing. SiO_2 is inert to the Cu or V under high temperature, so it will be stable without reacting with thin films during annealing.

To investigate the thermal stability of Cu/V multilayers, a series of ex-situ annealing experiments on Cu/V films deposited on oxidized Si substrates were carried

out in a vacuum tube furnace at 400 °C and 600 °C for 1 hour. The tube furnace is equipped with a diffusion pump and resistive heater. Samples were placed in a ceramic boat inside the quartz furnace tube under a vacuum of 5×10^{-6} torr or better. The samples remained at room temperature during pump-down. After the vacuum level and furnace temperature were stable, the furnace was slid over the tube to heat the sample for the specified time. The furnace was pulled away from the tube and the samples were allowed to cool under vacuum. To cool from 600 °C to 300 °C takes about a minute, but it takes nearly half an hour to cool down continuously to room temperature.

X-ray diffraction (XRD) experiment was performed by using Bruker-AXS D8 VARIO high-resolution X-ray diffractometer to characterize the annealing induced structure changes. The microstructure of annealed multilayers was examined by cross sectional TEM (XTEM) in 200 kV JOEL 2010 equipped with Gatan SC1000 ORIUS CCD camera, which is used to capture the images. Heating stage for in-situ heating was attached to the TEM for observing real time microstructure changes and interfacial stability with the varying of temperature. A dimple grinder followed by ion milling with argon ions was used to thin XTEM specimens. The hardness and indentation modulus of films were measured by means of an indentation load and depth sensing apparatus, a commercial Fischerscope HM2000XYp, using a Vickers indenter. The maximum indentation depth was kept at about 200 nm for all experiments.

6.3 Results and discussions

6.3.1 X-ray diffraction

X-ray diffraction patterns of Cu/V 50 nm and Cu/V 2.5 nm multilayers annealed at 400 °C and 600 °C were shown in the Figure 6.1a and 6.1b, respectively. Two

significant diffraction peaks have been observed in the as-deposited Cu/V 50 nm multilayers in Figure 6.1a. The peaks become stronger and sharper and tend to shift to the standard position of bulk V (110) and Cu (111) after annealing at 400 °C. Cu (111) peak becomes even sharper and stronger at 600 °C. It is unclear why V (110) peak disappears at such a temperature as shown in Figure 6.1a. We noticed that the surface layer, V, in Cu/V 50 nm samples, was oxidized after high temperature annealing experiments.

The overlap of V (110) and Cu (111) peaks has been observed in as-deposited Cu/V 2.5 nm multilayers in the previous studies. After annealing at 400 °C for an hour, as shown in Figure 6.1b, the overlapped peak intensity is higher than that in as-deposited samples, indicating the release of the constraint along layer interfaces originated from lattice mismatch of ~ 2.5 % between Cu (111) and V (110). The overlapped peak of V (110) and Cu (111) already separated completely into V (110) peak and Cu (111) as the annealing temperature increased to 600 °C.

The overlap of V (110) and Cu (111) peaks in XRD in the as-deposited Cu/V 2.5 nm indicates a large tensile stress in Cu (compressive stress in V) caused by the lattice mismatch between V (110) ($d_{(110)}$ = 2.1411 Å) and Cu (111) ($d_{(111)}$ = 2.0817Å). As h increases from 2.5 nm to 50 nm, the overlapped peak separated into two independent peaks of V (110) and Cu (111), indicating a diminished interface induced tension (compression) in Cu (V). On the other hand, in the annealed Cu/V 2.5 nm multilayers, as the annealing temperature increases, the overlap peak tends to separate and eventually separate into two independent peaks when the annealing temperature reaches 600 °C, indicating the influence of annealing temperature in diminishing constraint along layer interface. The intensity of two distinguished peaks observed in as-deposited Cu/V 50 nm

multilayers increases with increasing annealing temperature up to 400 °C, but V (110) peaks disappears at annealing temperature of 600 °C. This could be due to the oxidation of V layers during annealing.

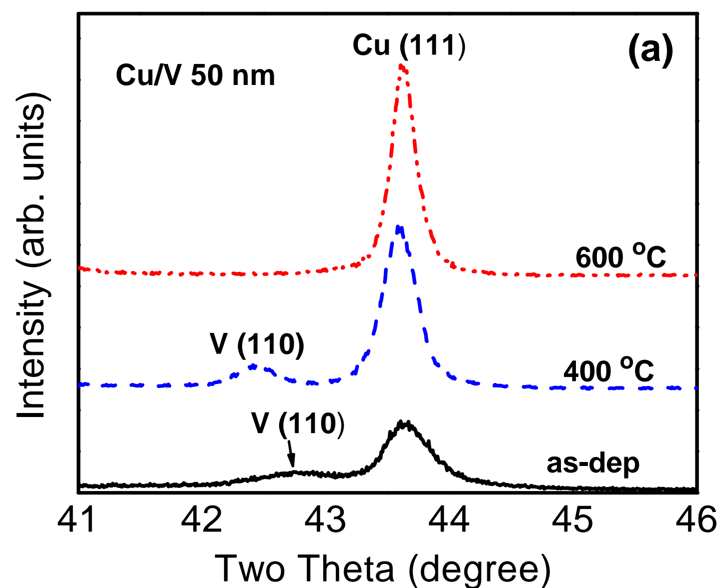

(a)

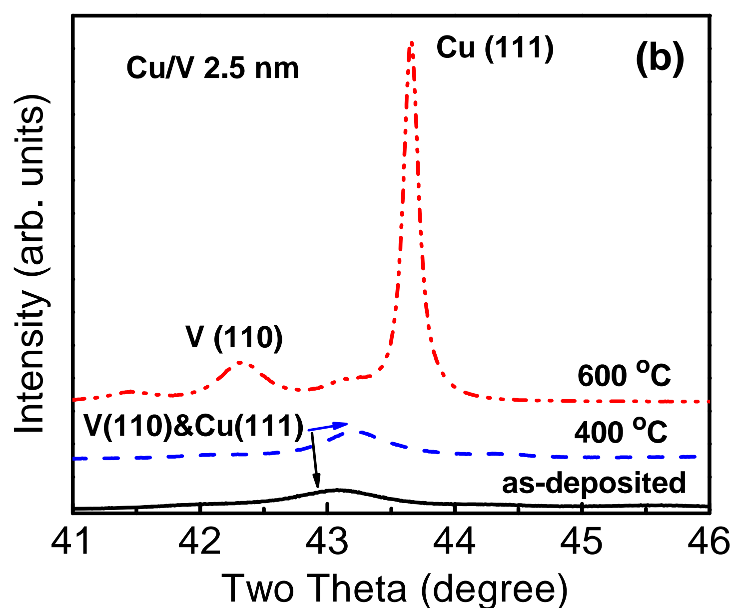

(b)

Figure 6.1. XRD diffraction patterns of as-deposited and annealed samples at 400 °C and 600 °C for (a) Cu/V 50 nm, and (b) Cu/V 2.5 nm.

6.3.2 Evolutions of microstructures examined by XTEM

The sputtered Cu/V 50 nm and 2.5 nm multilayer samples grown on the HF Si (100) have columnar grain structure and distinguishable interfaces without significant intermixing, which has been shown in the previous chapters. Figure 6.2a and 6.2b show the bright field XTEM micrographs of as-deposited Cu/V 50 nm and Cu/V 5 nm samples. The insets are corresponding selected area diffraction (SAD) patterns. Both Cu/V 50 nm and Cu/V 5 nm multilayer films exhibit flat and distinguished interface without mixing and have polycrystalline grains, confirmed by the diffraction rings in the corresponding SAD patterns. The crystallographic plane orientation is determined after careful examination of interplanar distance. The results in both samples indicate Cu (111) plane is parallel to V (110) plane, typical features of Kurdjumov-Sachs (K-S) orientation relationship, i.e., Cu {111} // V {110} and Cu <110> // V <111>.

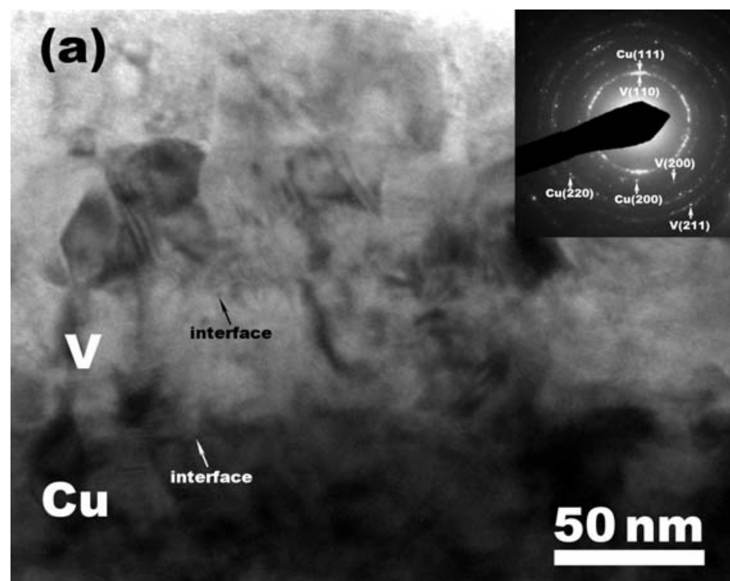

(a)

Figure 6.2. XTEM micrographs of as-deposited (a) Cu/V 50 nm, and (b) Cu/V 5 nm.

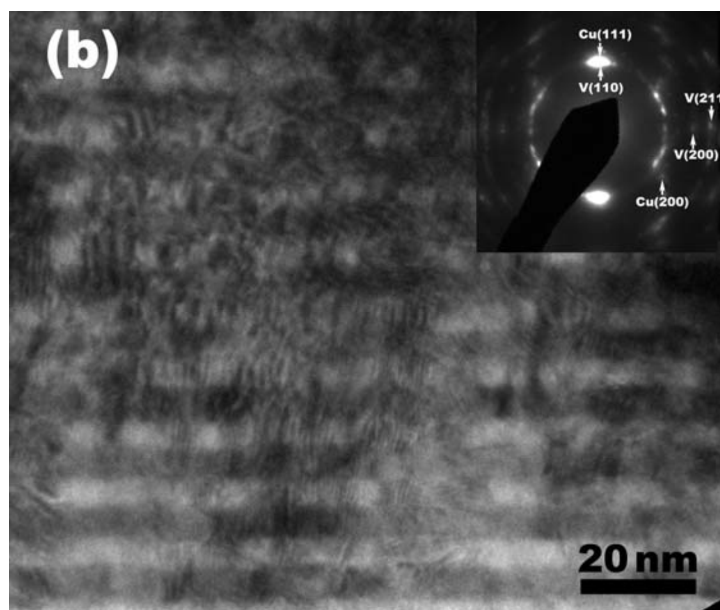

(b)

Figure 6.2 Continued.

Figure 6.3a and 6.3b shows the XTEM micrographs of Cu/V 50 nm and Cu/V 5 nm multilayer films annealed in vacuum at 400 °C for 1 hour. The interfaces in annealed Cu/V 50 nm multilayer samples remain stable, but the average column grain sizes have increased to around 60 nm, a factor of 2 compared to that of as-deposited Cu/V 50 nm multilayers, which have an average grain size of 30 nm. The corresponding SAD patterns, shown in the inset of the XTEM images, have more diffraction dots indicating the possibility of oxide formation. The XTEM image of annealed Cu/V 5 nm multilayer shows insignificant changes of microsctructures including the column grain size. But like the annealed Cu/V 50 nm samples, more diffraction dots appeared in corresponding SAD patterns shown in the inset of micrographs. The clearly distinguishable layer interface between Cu and V in annealed Cu/V 5 nm multilayers indicates insignificant intermixing along layer interface. The XTEM studies of annealed Cu/V 50 nm and 5 nm multilayer

films indicates their interfaces are thermally stable at the annealing temperature of 400 °C.

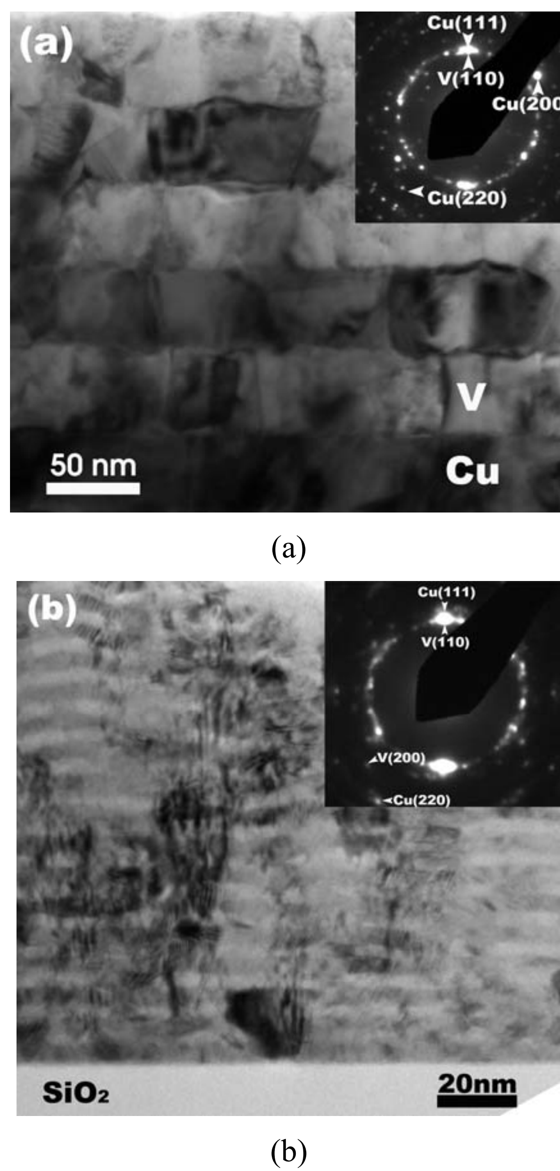

(a)

(b)

Figure 6.3. XTEM micrographs of annealed multilayer films at 400 °C for (a) Cu/V 50 nm, and (b) Cu/V 5 nm.

Grain growth is observed in annealed Cu/V 50 nm multilayers, but annealed Cu/V 5 nm multilayer has less grain growth. The grain growth kinetics in multilayer films may differ significantly from the common three dimensional grain growth kinetics. In general, the 3D grain growth model is given by:

$$(d - d_0) \propto \sqrt[\alpha]{t} \tag{118}$$

where d is the real time grain size, d_0 is the initial grain size at the beginning of the grain growth, t is the time and α is a fitting parameter [286]. This equation predicts that grains grow with increasing annealing period at a given temperature. However, it was reported that grain growth in the annealed Cu/Nb multilayer is quite different. After the initial grain growth following the 3D grain growth model, a sharp increase of grain growth occurs when the annealing time is greater than a certain time, which is related to the individual layer thickness of the Cu/Nb multilayer. For greater h, this characteristic becomes much larger [286]. The sharp increase of the grain grow is believed to be attributed to the fact that fast diffusion along the interfaces occurred. After this early jump, the grain growth will follow a logarithmic time law, which is given by:

$$d_{particle} = A(T)\ln(t) + consta(d_0, T) \tag{119}$$

where T is the temperature, t is annealing time, $A(T)$ is the coefficient, proportional to the temperature [286].

In order to examine the interfacial stability with the time, the in-situ annealing experiments were performed in TEM by using a heating stage. Figure 6.4a-e compared the microstructural changes of Cu/V 50 nm multilayer kept at 600 °C for increasing periods. Figure 6.4a shows the XTEM image of the Cu/V 50 nm multilayer films when the sample temperature just reached 600 °C. The layer interfaces appear rougher. After

15 minutes, as shown in Figure 6.4b, at the same temperature, some grains in Cu layer start to grow in all directions. Half an hour later, as shown in Figure 6.4c, the grain highlighted by dash lines appear spheroidized. When the annealing time reached 45 minutes, as shown in Figure 6.4d, the Cu grain seems to grow into the neighboring V layers, but the grain growth ceases in the direction parallel to layer interfaces. After 60 minutes of in-situ annealing, no obvious grain growth in the lateral direction is observed, but the Cu grain appears to almost completely penetrate the downward V layer, and joins together with another Cu layer. We notice that a majority of layer interface remains distinguishable at this annealing stage. The SAD pattern of multilayers in Figure 6.4e is shown in Figure 6.4f, and reveals the existence of the phases of vanadium oxide. Figure 6.5 shows the Cu/V 5 nm multilayers annealed at 600 °C for 1 hour. Interestingly the interfaces appear mostly intact after annealing, indicating outstanding thermal stability of layer interfaces. This observation is confirmed again by STEM study of Cu/V 5 nm in-situ annealed at 600 °C for 1 hour. The STEM image of in-situ annealed Cu/V 5 nm shown in Figure 6.6 indicates film keeps clear column grain and clear interfaces without intermixing after 600 °C annealing for 1 hour. The comparison between annealed Cu/V 50 nm and Cu/V 2.5 nm annealed at 600 °C for 1 hour indicates that Cu/V 5 nm multilayers may have greater thermal stability, compared to Cu/V 50 nm multilayer specimen, an intriguing phenomenon.

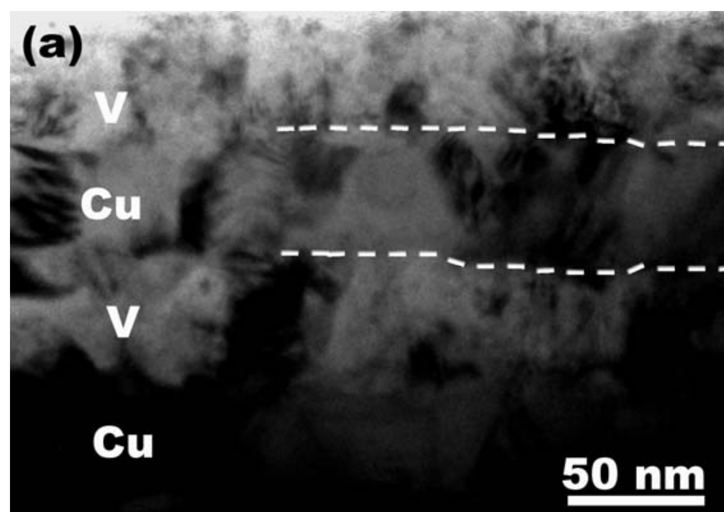

(a)

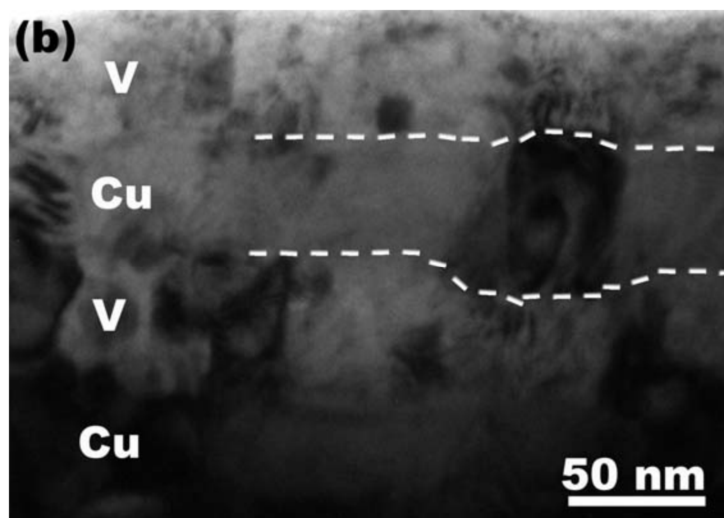

(b)

Figure 6.4. XTEM micrographs of annealed Cu/V 50 nm multilayers at 600 °C for (a) 0 min, (b) 15 min, (c) 30 min, (d) 45 min, (e) 60 min and (f) SAD pattern after 1 hour annealing.

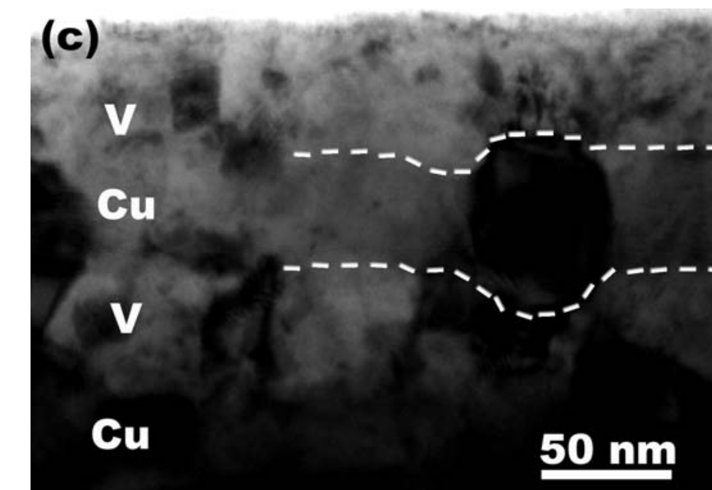

(c)

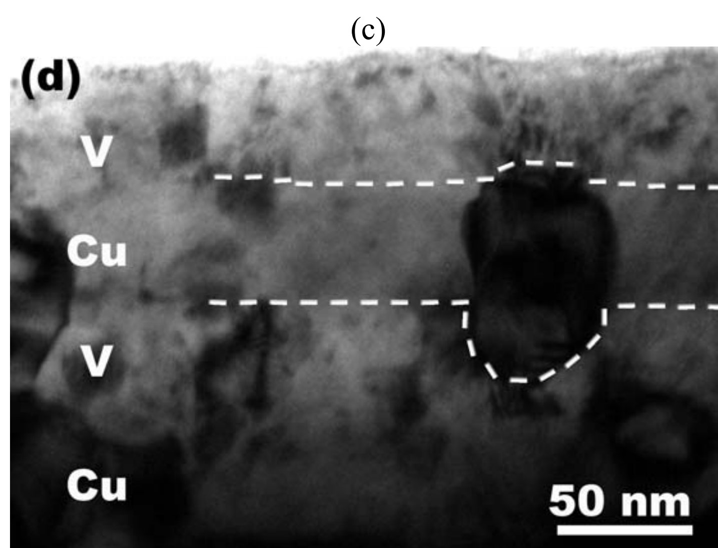

(d)

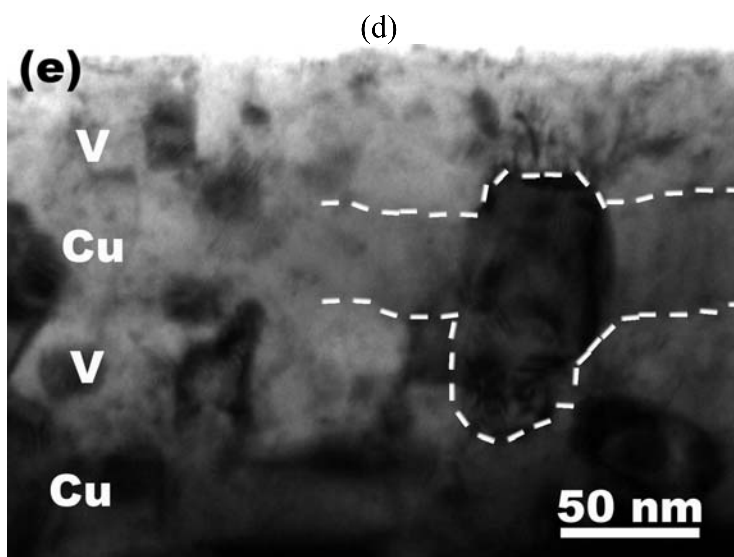

(e)

Figure 6.4 Continued.

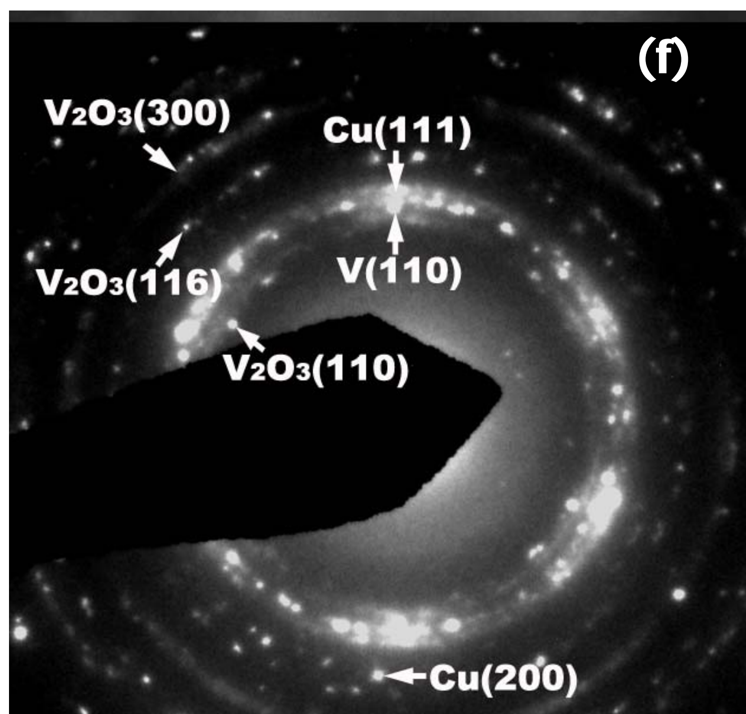

(f)

Figure 6.4 Continued.

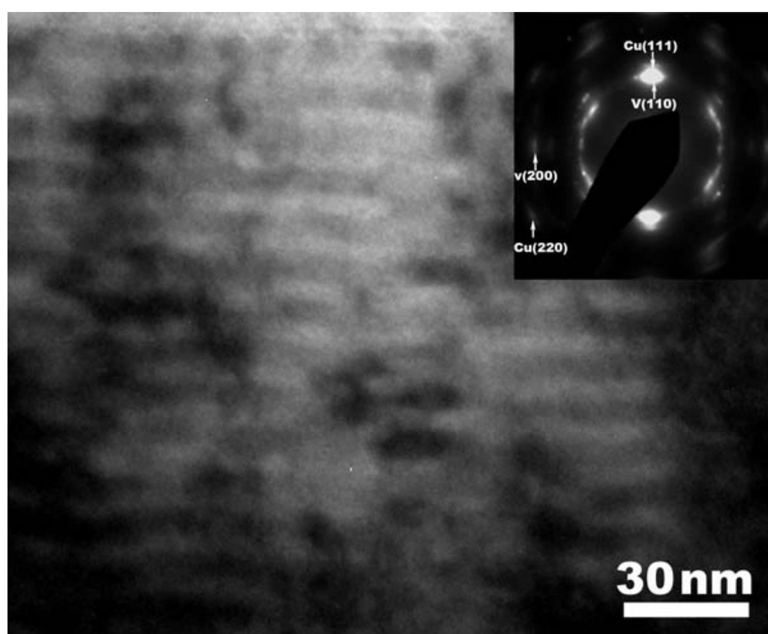

Figure 6.5. XTEM micrographs of in-situ annealed Cu/V 5 nm multilayers at 600 °C for 1 hour.

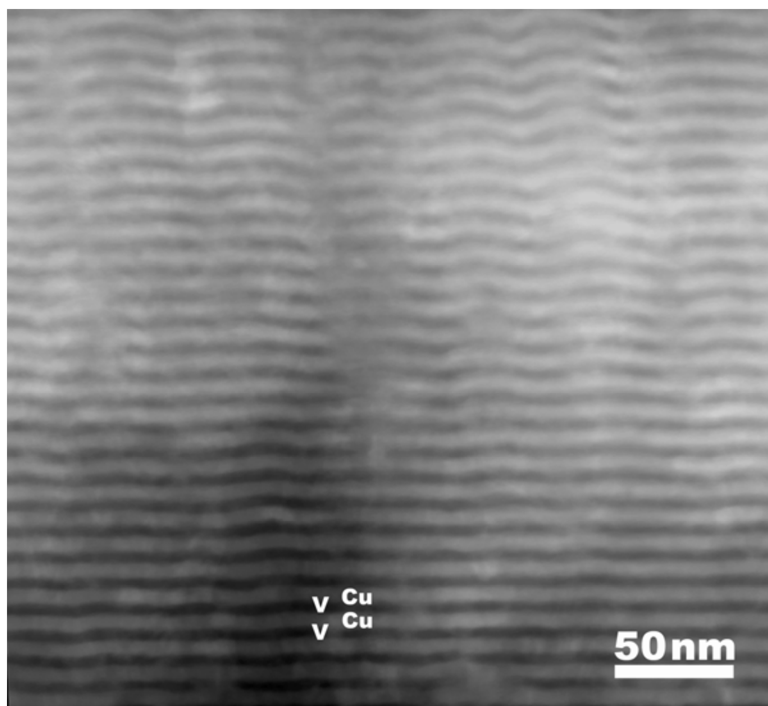

Figure 6.6. STEM image of in-situ annealed Cu/V 5 nm multilayers at 600 °C for 1 hour.

6.3.3 Evolution of hardness of Cu/V multilayers after annealing

The mechanical properties of the Cu/V multilayers films at different annealing temperatures were examined by nanoindentation technique. Figure 6.7 shows the indentation hardness of as-deposited and annealed Cu/V multilayers films as a function of h. At 400 °C, when h > 25 nm, hardness of multilayer barely change; when $h \leq 25$ nm, hardening is observed and the magnitude of hardening increases with decreasing h. On the other hand, annealing at 600 °C induces softening at h across all length scale, and softening is more significant at smaller h. In general, the yield strength of multilayer films are determined by both the layer thickness and the in-plane grain size, similar to additive film thickness and grain size contributions to yield strength noted in single layer thin metal films on substrates [287, 288]. The smallest dimension of the two typically

determines the strength of materials as the confinement of dislocation activities is more significant by this dimension. In multilayers, this parameter is typically the individual layer thickness since in general the columnar grain sizes are either comparable or much greater than *h*. When Cu/V multilayer with greater *h* was annealed at 400 °C, no significant hardness change is observed. This is consistent with the fact that the morphology of multilayers (layer thickness) retained after annealing. Although the average grain size increased from 30 to 60 nm after annealing, the hardness is still dominated by layer interface confined dislocation activities.

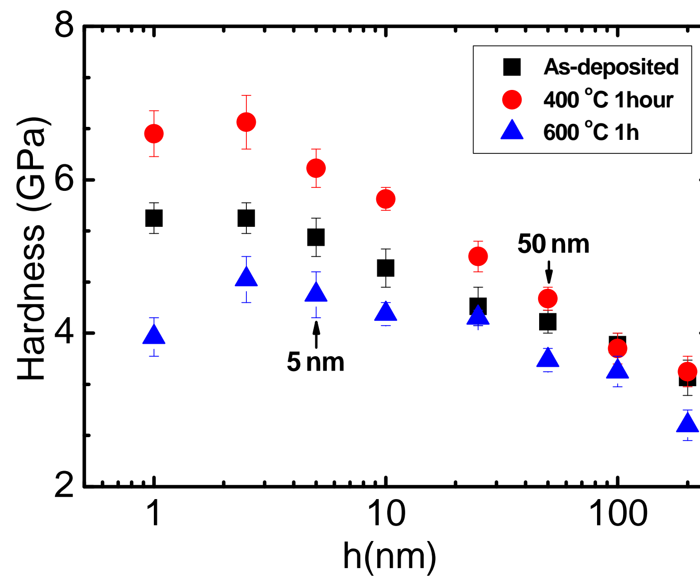

Figure 6.7. Comparison of hardness of as-deposited and annealed Cu/V multilayers vs. *h*, where *h* is the individual layer thickness.

The significant variation of hardness in multilayers of smaller *h* annealed at different temperatures and a drastic different trend is more complicated to interpret. In general V (110) has greater lattice parameter than Cu (110), the formation of K-S

orientation relationship indicates that V will be in compression in-plane and Cu will be in tension in-plane. Such alternating stress would have an effect on the propagation of dislocations across layer interfaces. At 400 °C, when h is 50 nm, XRD spectrum (Figure 6.1a) has shown that the out-of-plane lattice parameter of V has become greater. This would indicate that the in-plane lattice parameter of V is getting smaller, and a greater compressive stress shall develop. Our previous studies [289] have shown that a compressive stress will lead to greater measured film hardness. The increase of compressive film stress shall be more significant at smaller h, and hence the magnitude of hardening could be greater when h is smaller.

The reduction of film hardness after annealing 600 °C is likely due to the loss of integrity of interfaces as shown by in situ annealing studies. XRD studies (Figure 6.1b) also show that when h is a few nm, a single overlapped peak split into Cu (111) and V (110) peaks indicating the loss of constraint along layer interfaces, although in situ TEM studies show that layer structure retains. The degradation of interfaces lowers the barrier strength of interface. As a result, dislocation can propagate by slip across interface due to a lower resistance from interface. We also notice that the oxidation of V can lead to high strength vanadium oxides, ~ 21 GPa [290]. However the fact that higher temperature annealing leads to softening together with factor that a majority of V remains metallic suggest that the hardening observed in multilayer annealed at 400 °C is unlikely to be due to the formation of oxides.

6.4 Conclusions

Annealing induced evolution of microstructure and mechanical properties of sputtered Cu/V multilayers was systematically investigated by in situ and ex situ

methods. Annealed multilayers exhibit stronger texture with the increase of annealing temperature. The interfaces in all annealed Cu/V multilayers at 400 °C are stable without significant intermixing, although grain growth was observed in annealed Cu/V 50 nm multilayers. As the annealing temperature increases to 600 °C, grains grow across the interfaces in Cu/V 50 nm multilayers and degrade the integrity of layer interfaces. Interface morphology seems more stable in Cu/V 5 nm multilayers. Annealing (at 400 °C) induced hardening could be related to increasing compressive stress in multilayers as indicated by XRD experiments, whereas softening after annealing at 600 °C is due to the loss of constraint along layer interface and consequently a lower barrier resistance.

CHAPTER VII

SUMMARY AND CONCLUSIONS

(1) Metallic Cu/V multilayers have been synthesized by magnetron sputtering at room temperature. The films have individual layer thickness, *h*, varying from 1 nm to 200 nm. The microstructure and mechanical properties of Cu/V multilayers were studied systematically. The mechanical properties of sputter-deposited Cu/V and Al/Nb multilayers are compared to that of Cu/Nb and Cu/Cr. All systems are of fcc/bcc type with incoherent interfaces, and have Kurdjumov-Sachs orientation relationship. The Hall-Petch slope scales with the shear moduli of the stiffer components in multilayers, but a similar scaling was not observed between the peak strength and the moduli of the fcc/bcc multilayers. The peak strength depends on the interface barrier resistance to slip transmission of single dislocations, which for fcc/bcc incoherent interfaces may depend on the low shear strength of the interface that allows dislocation core spreading along the interface.

(2) The evolution of microstructure and mechanical properties of sputtered Cu/V multilayers subjected to 50 keV He ion irradiation was investigated systematically. Irradiated multilayer interfaces remain chemically abrupt even in the peak damage region upon a total fluence of 6×10^{20} ions/m^2. Such immiscible layer interface can effectively reduce the overall concentration of He bubbles and void swelling, and such phenomenon becomes more prominent at smaller *h*. These multilayers also show clearly a monotonic suppression of radiation hardening at smaller layer thickness due to the effective attraction and interface facilitated annihilation of Frenkel pair defects. Multilayers with immiscible layer interface hence may offer a promising approach in alleviating void

swelling and radiation hardening. These findings illustrate remarkable radiation tolerance in Cu/V multilayers with small h.

(3) We systematically investigated the dose dependent evolution of microstructure and mechanical properties of sputtered Cu/V multilayers subjected to 50 keV He ion irradiation. The interfaces in all immiscible Cu/V multilayers remain chemical abrupt with little intermixing even at the total fluence of 1.2×10^{21} / m^2, corresponding to a peak damage of 12 dpa. A nearly immiscible interface between Cu and V is believed to play a significant role in preventing ion mixing. With increasing the total fluences, the peak He bubble density increases, but it is a factor of 3 lower in irradiated Cu/V 2.5 nm multilayers, compared to Cu/V 50 nm multilayers. Higher radiation fluences results in greater radiation damage, except at very small h (2.5 nm or less), where radiation induced void swelling and hardening are minimal. The threshold He concentration to form He bubbles is greater in irradiated Cu/V 2.5 nm multilayer than that in Cu/V 50 nm. Interface enhanced radiation tolerance is explained by a combined effect of enhanced defect storage capacity and increased probability of defect annihilation at interfaces. At all fluences, radiation hardening is greater in Cu/V multilayer with greater h, but it becomes negligible when h is at the length scale of a few nm. The saturation of radiation hardening in Cu/V multilayers at greater fluences was discussed based on an empirical power-law expression. The saturation of radiation hardening in irradiated Cu/V with greater h agrees with the literature, but the saturation behavior in Cu/V multilayer with small h deviates and yields new fitting coefficients.

(4) The results of ex-situ vacuum annealing and in-situ TEM annealing studies on Cu/V multilayer composites reveal their thermal stability up to 400 °C. At this

temperature, the texture becomes stronger in annealed Cu/V multilayers with the retention of chemically modulated layer interfaces. Grain growth across layer interface occurs at higher annealing temperature, 600 °C, in Cu/V 50 nm multilayer, whereas interfaces remain distinguishable in annealed Cu/V 5 nm multilayer. Annealing of multilayers at 400°C leads to hardening and could be a consequence of increasing compressive stress in the multilayers, while the softening of annealed multilayer at 600 °C is due to the loss of constraint along layer interface between Cu (111) and V (110), and hence a lower interface barrier resistance to the transmission of single dislocation.

BIBLIOGRAPHY

[1] J.S. Koehler, Phy. Rev. B 2 (1970) 547.

[2] J.D. Embury, J.P. Hirth, Acta Metall. Mater. 42 (1994) 2051.

[3] S.S.P. Parkin, X. Jian, C. Kaiser, A. Panchula, K. Roche, M. Samant, Proceedings of IEEE 91 (2003) 661.

[4] B.M. Clemens, H. Kung, S.A. Barnett, MRS Bull. 24 (1999) 20.

[5] P.M. Anderson, T. Foecke, P.M. Barnett, MRS Bull. 24 (1999) 27.

[6] G.S. Was, T. Foecke, Thin Solid Films 286 (1996) 1.

[7] D.J.Craik, Platinum Met. Rev. 16 (1972) 129.

[8] A.S. Darling, Platinum Met. Rev. 17 (1963) 96.

[9] K.R. Coffey, M.A. Parker, J.K. Howard, IEEE Trans. Magn. 31 (1995) 2737.

[10] K. Takanashi, S. Mitani, M. Sano, H. Fujimori, H. Nakajima, A. Osawa, Appl. Phys. Lett. 67 (1995) 1016.

[11] J.A.C. Bland, B. Heinrich, Ultrathin Magnetic Structures, Springer, Berlin, 1994.

[12] A. Sakuma, J. Phys. Soc. Jpn, 63 (1994) 3053.

[13] T. Klemmer, D. Hoydick, H. Okumura, B. Zhang, W. A. Soffa, Scr. Metall. Mater. 33 (1995) 1793.

[14] T. Okuyama, Jpn. J. Appl. Phys. 30 (1991) 2053.

[15] Y. Suzuki, H. Kikuchi, M. Taninaka, T. Katayama, S. Yoshida, Appl. Surf. Sci, 60-61 (1992) 820.

[16] A. Fuss, S. Demokritov, Grünberg, W. Zinn, J. Magn. Magn. Mater. 103 (1992) L221.

[17] M. Watanabe, M. Homma, Jpn. J. Appl. Phys. 335 (1996) L1264.

[18] D. Weller, A, Moser, L. Folks, M.E. Best, W.E. Lee, M.F. Toney, M. Schwickert, J.-U Thiele, M.F. Doerner, IEEE Trans. Magn. 36 (2000) 10.

[19] T. Shiama, K. Takanashi, Y.K. Takahashi, K. Hono, Appl. Phys. Lett. 81 (2002) 1050.

[20] T. Seki, T. Shima, K. Takanashi, Y. Takahashi, E. Matsubara, K. Hono, Appl. Phys. Lett. 82 (2003) 2461.

[21] T.B. Massalski, J.L. Murray, L.H. Bennet, H. Baker, Binary Alloy Diagrams, American Society for Metals, Metals Park, Ohio, 1986.

[22] K. Takanashi, S. Mitani, M. Sano, H. Fujimori, Appl. Phys. Lett. 67 (1995) 1016.

[23] M. Ohtake, F. Kirino, M. Futamoto, Jpn. J. Appl .Phys. 46 (2007) L895.

[24] M. Ohtake, Y. Yasui, F. Kirino, M. Futamoto, Phys. Stat. Sol. (b) 244 (2007) 4503.

[25] M. Ohtake, M. Futamoto, F. Kirino, Jpn. J. Appl. Phys. 47 (2008) 3450.

[26] H. Gong, M. Rao, D.E. Laughlin, D.N. Lambeth, J. Appl. Phys. 85 (1999) 4699.

[27] M. Futamoto, K. Terayama, K. Sato, Y. Hirayama, IEICE Trans. Electron E85-C (2002) 1733.

[28] D. Weller, G.R. Harp, R.F.C. Farrow, A. Cebollada, J. Sticht, Phys. Rev. Lett. 72 (1994) 2097.

[29] Y. Kageyama, T. Suzuki, Trans. Magn. Soc, Jpn. 5 (2005) 89.

[30] M. Ohtake, Y. Akita, M. Futamoto, f. Kirino, J. Appl. Phys. 101 (2007) 09D122.

[31] M. Mirzamaani, C.V. Jahnes, M. A. Russak, J. Appl. Phys. 69 (1991) 5169.

[32] B.Y. Wong, D.E. Laughlin, D.N. Lambeth, IEEE Trans. Magn. 27 (1991) 4733.

[33] A. Nakamura, M. Koguchi, M. Futamoto, Jpn. J. Appl. Phys. 34 (1995) 2307.

[34] A. Kohn, C. Wang, A.K. Petford-Long, S.G. Wang, R.C.C. Ward, J.Appl. Phys. 103 (2008) 063918.

[35] M. Ohtake, K Shikada, F. Kirino, M. Futamoto, J. Mag. Mag. Mater. 320 (2008) 3096.

[36] A. Singh, R. Tamm, V. Neu, S. Fähler, C.-G. Ortel, W. Skrotzki, L. Schultz, B. Holzapfel. J. Appl. Phys. 97 (2005) 093902

[37] D.J. Keavney, E.E. Fullerton, D. Li, C.H. Sowers, S.D. Bader, K. Goodman, J. G. Tobin, R. Carr, Phys. Rev. B 57 (1998) 5291.

[38] A.K. Patra, V.Neu, S. Fähler, H. Wendrock, L. Schultz, J. Appl. Phys. 100 (2006) 043905.

[39] A.K. Patra, V. Neu. S. Fähler, R. Groetzschel, S. Bedanta, W. Kleemann, L. Schultz, Phys. Rev. B 75 (2007) 184417.

[40] I. Zana, G. Zangari, M. Shamsuzzoha, J. Magn. Magn. Mater. 292 (2005) 266.

[41] M. Ohtake, M. Futamoto, F. Kirino, N. Fujita, N. Inaba, J. App. Phys. 103 (2008) 07B522.

[42] K.M. Krishnan, T. Takeuchi, Y. Hirayama, M. Futamoto, IEEE Trans. Magn. 30 (1994) 5115.

[43] C. Cesari, J.P. Faure, G. Nihoul, K. Le Dang, P.Veillet, D. Renard, J. Magn. Magn. Mater. 78 (1989) 296.

[44] K. shintaku, Y. Daitoh, T. Shinjo, Phys. Rev. B 47 (1993) 14584.

[45] T. Okuyama, Jpn J. Appl. Phys. 30 (1991) 2053.

[46] S. Mitani, K. Takanashi, H. Nakajima, K. Sato, R. Schreiber, Grunberg, H. Fujimori, J. Magn. Magn. Mater. 156 (1996) 7.

[47] M. Sakurai, J. Appl. Phys. 76 (1994) 7272.

[48] A. Nakamura, M. Futamoto, Jpn. J. Appl. Phys. 32 (1993) 1410.

[49] É.S. Mushailov, P.D. Kim, I.A. turpanov, G.V. Bondarenko, G. N. Nondarenko, S. É. Mishina, JETP Lett. 71 (2000) 195.

[50] A. Misra, H. Kung, Adv. Eng. Mater. 3 (2001) 217.

[51] J. McKeown, A. Misra, H. Kung, R.G. Hoagland, M. Nastasi, Scripta Mater. 46 (2002) 593.

[52] L.A. Bruce, H. Jaeger, Phil. Mag. A 38 (1978) 223.

[53] E. Bauer, Appl. Surf. Sci. 11-12 (1982) 479.

[54] G. Kurdjumov, G. Sachs, Z. Phys. 64 (1930) 325.

[55] Z. Nishiyama, Sci. Rept. Tohoku Univ. 23 (1934) 638.

[56] G. Wassermann, Arch. Eisenhüttenw. 16 (1933) 647.

[57] J. H. van der Merwe, Phil. Mag. 45 (1982) 127.

[58] R. Ramirez, A. Rahman, I.K. Schuller, Phys. Rev. B 30 (1984) 6208.

[59] Y. Gotoh, I. Arai, Jpn. J. Appl. Phys. 25 (1986) L583.

[60] Y. Gotoh, M. Uwaha, I. Arai, Appl. Surf. Sci, 33-34 (1988) 443.

[61] Y. Gotoh, H. Fukuda, Surf. Sci. 223 (1989) 315.

[62] A. Kobayashi, S. Das, Sarma, Phys. Rev. B 35 (1987) 8042.

[63] J.A. Ruud, F. Spaepen, T.R. Jervis, J. Appl. Phys. 75 (1994) 4969.

[64] A. Misra, J.P. Hirth, R.G. Hoagland, Acta Mater. 53 (2005) 4817.

[65] A. Misra, M. Verdier, Y.C. Lu, H. Kung, T.E. Mitchell, M. Nastasi, J.D. Embury, Scripta Mater. 39 (1998) 555.

[66] H. Kung, T. Foecke, MRS Bull. 24 (1999) 2.

[67] S.L. Lehoczky, J. Appl. Phys. 49 (1978) 5479.

[68] R.L. Bickerdike, D. Clarke, J.N. Easterbrook G. Hughes, W.N. Mair, P.G. Partridge, H.C. Ranson, Int. J. Rapid Solidification 1 (1984-1985) 305.

[69] A. Kelly, Phil. Trans. R. Soc. A 322 (1987) 409.

[70] R.F. Bunshah, R. Nimmagadda, H.J. Doerr, B.A. Movchan, N.I. Grechanuk, E.V. Dabizha, Thin Solid Films 72 (1980) 261.

[71] B.J. Daniels, W.D. Nix, B.W. Clemens, Mater. Res. Soc. Symp. Proc. 343 (1994) 549.

[72] P.M. Anderson, C. Li, Nanostruct. Mater. 5 (1995) 349.

[73] S.I. Rao, P.M. Hazzledine, D. Dimiduk, Mater. Res. Soc. Symp. Proc. 362 (1995) 67.

[74] Y. Q. Sun, Phil. Mag. A, 77 (1998) 1107.

[75] L.B. Freund, J. Appl. Mech. 54 (1987) 553.

[76] W.D. Nix, Metall. Trans. A 20 (1989) 2217.

[77] A. Misra, M. Verdier, H. Kung, J.D. Embury, J. Hirth, Scripta Mater. 41 (1999) 973.

[78] E.O. Hall, Proc. Phys. Soc. B 64 (1951) 747.

[79] N.J. Petch, J. Iron Steel Inst. 173 (1953) 25.

[80] L. H. Friedman, D.C. Chrzan, Phys. Rev. Lett. 81 (1998) 2715.

[81] S. Suri, T. Neeraj, G.S. Daehn, D.-H. Hou, J.M. Scott, R.W. Hayes, M.J. Mills, Mater. Sci. Eng. A 234-236 (1997) 996.

[82] L.H. Friedman, Phil. Mag. 86 (2006) 1443.

[83] B.J. Daniels, W.D. Nix, B.M. Clemens, Thin Solid Films, 253 (1994) 218.

[84] A.F. Jankowski, J. Magn. Magn. Mater. 126 (1993) 185.

[85] C. Kim, S.B. Qadri, M.R. Scanlon, R.C. Cammarata, Thin Solid Films 240 (1994) 52.

[86] H. Huang, F. Spaepen, Acta Mater. 48 (2000) 3261.

[87] S.P. Baker, K.O. Nix, J. Mater. Res. 9 (1994) 3131.

[88] D. Josell, D. van Heerden, D. Read, J. Bonevich, D. Shechtman, J. Mater. Res. 13 (1998) 2902.

[89] Q. Li, P.M. Anderson, Acta Mater. 53 (2005) 1121.

[90] S.M. Keralavarma, A.A. Benzerga, Mater. Sci. Eng. 15 (2007) S239.

[91] L.B. Freund, J. Mech. Phys. Solids, 38 (1990) 657.

[92] M.A. Philips, BM Clements, W.D. Nix, Acta Mater. 51 (2003) 3157.

[93] A. Misra, J.P. Hirth, H. Kung, Phil. Mag. 82 (2002) 2935.

[94] R.G. Hoagland, R.J. Kurtz, C.H. Henager, Scripta Mater. 50 (2004) 775.

[95] S.P. Baker, L. Zhang, H.J. Gao, J. Mater. Res. 17 (2002) 1808.

[96] W.D. Nix, Scripta Mater. 39 (1998) 545.

[97] P. Pant, K.W. Schwarz, S.P. Baker, Acta Mater. 51 (2003) 3243.

[98] R.G. Hoagland, T.E. Mitchell, J.P. Hirth, H. Kung, Phil. Mag. 82 (2002) 643.

[99] S.I. Rao, P.M. Hazzledine, Phil. Mag. 80 (2000) 2011.

[100] S.A. Barnett, A. Madan, I. Kim, K. Martin, Mater. Res. Soc. Bull. 169 (2003) 28.

[101] N. Sridhar, J.M. rickman, D.J. Srolovitz, J. Appl. Phys. 82 (1997) 4852.

[102] J.C. alzahn Kampe, T.H. Courtney, Y. Leng, Acta Metall. 37 (1989) 1735.

[103] D. Josell, F. Spaepen, Mater. Res. Soc. Bull. 24 (1999) 39.

[104] G. Sharma, R.V. Ramanujan, G.P. Tiwari; Acta Mater. 48 (2000) 875.

[105] M. Bobeth, M. Hecker, W. Pompe, C.M. Schneider, J. Thomas, A Ullrich, K. Wetzig, Z. Metallk 92 (2001) 810.

[106] J.C. Malzahn Kampe, T.H. Courtney, Y. Leng, Acta Metall. 37 (1989) 1735.

[107] G. Sharma, R.V. Ramanujan, G.P. Tiwari; Acta Mater. 48 (2000) 875.

[108] D. Josell, S.R. Coriell, G.B. McFadden, Acta Metall. Mater. 43 (1995) 1987.

[109] A.C. Lewis, D. Josell, T.P. Weihs, Scripta Mater. 48 (2003) 1079.

[110] A. Misra, R.G. Hoagland, H. Kung, Phil. Mag. 84 (2004) 1021.

[111] G. Was, Fundamentals of Radiation Materials Science, Springer, New York, 2007.

[112] H. Ullmaier, Nucl. Fusion 24 (1984) 1039.

[113] S.J. Zinkle, B.N. Singh, J Nucl. Mater. 199 (1993) 173.

[114] W.J. Phythian, R.E. Stoller, A.J.E. Foreman, A.F. Calder, D.J. Bacon, J. Nucl. Mater. 223 (1995) 245.

[115] M.L. Jenkins, M.A. Kirk, W.J. Phythian, J. Nucl. Mater. 205 (1993) 16.

[116] M. Nastasi, J.W. Mayer, J.K. Hirvonen,. Ion-Solid Interactions: Fundamentals, Applications, Cambridge University Press, New York, 1996.

[117] T.D. Allen, Lecture of course NEEP 541, University of Wisconsin - Madison.

[118] L. Shao, Lecture of course NUEN 689, Texas A&M University, College Station.

[119] J. Lindhard, V. Nielsen, M. Scharff, Mat. Fys. Medd. Dan Vid. Selsk. 36 (1968) 10.

[120] K.B. Winterbon, Sigmund, J.B. Sanders, Mat. Fys Medd. Dan Vid. Selsk. 37 (1970) 14.

[121] J. Lindhard, M. Scharff, H.E. Schiott, Mat. Fys. Medd. Dan Vid. Selsk. 33 (1963) 3.

[122] J.F. Ziegler, J.P. Biersack, U. Littmark, The Stopping, Range of Ions in Solids, Pergamon Press, New York, 1985.

[123] O.B. Firsov, Sov. Phys. JETP 36 (1959) 1076.

[124] H. Sugiyama, J. Phys. Soc. Jpn. 50 (1981) 929.

[125] H. Sugiyama, Radiation Effects 56 (1981) 205.

[126] W.E. King, K.L. Merkle, M. Meshii, J. Nucl. Mater. 117 (1983) 12.

[127] D.R. Olander, Fundamental Aspects of Nuclear Reactor Fuel Elements (National Technical Information Service), Springfield, Virginia, 1976.

[128] G.H. Kinchin, R.S. Pease, Rept. Prog. Phys. 18 (1955) 1.

[129] M.W. Thompson, Defects and Radiation Damage in Metals, Cambridge University Press, Cambridge, 1969.

[130] M.T. Robinson, Phil. Mag. 12 (1965) 741.

[131] M.T. Robinson, O.S. Oen, J. Nucl. Mater. 110 (1982) 147.

[132] Sigmund, Radiation Effects, 1 (1969) 15.

[133] J. Lindhard, V. Nielsen, M. Scharff, P.V. Thomsen, Mat. Fys. Medd. Dan Vid. Selsk. 33 (1963) 10.

[134] M.J. Norgett, M.T. Robinson, I.M. Torrens, Nucl. Eng. Des. 33 (1975) 50.

[135] M.T. Robinson, The Energy Dependence of Neutron Radiation Damage in Solids, in Nuclear Fusion Reactors, British Nuclear Energy Society, London, 1970.

[136] E.L. Haines, A.B. Whitehead, Rev. Sci. Instrum. 37 (1966) 190.

[137] F. Seitz, J.S. Koehler, Displacement of Atoms During Irradiation, in Solid State Physics, Academic Press, New York, 1956.

[138] Sigmud, Appl. Phys. Lett. 25 (1974) 169.

[139] J.A. Brinkman, Am. J. Phys. 24 (1956) 246.

[140] J.F. Ziegler, M.D. Ziegler, J.P. Biersack, http://www.srim.org/, July 1, 2009.

[141] J.F. Ziegler, M.D. Ziegler, J.P. Biersack, http://www.srim.org/srim/srimintro.htm, July 1, 2009

[142] R. Schäublin, Z. Yao, N. Baluc, M. Victoria, Phil, Mag, 85 (2005) 769.

[143] Y. Dai, M. Victoria, Acta Mater. 45 (1997) 3495.

[144] Y. Matsukawa, Y.N. Osetsky, R.E. Stoller, S.J. Zinkle, Phil. Mag. 88 (2008) 581.

[145] M.L. Jenkins, Phil. Mag. 29 (1974) 813.

[146] S.J. Zinkle, L.L. Snead, J. Nucl. Mater. 225 (1995) 123.

[147] B.N. Singh, A. Horsewell, Toft , D.J. Edwards, J. Nucl. Mater.224 (1995) 131.

[148] Y. Shimomura, R. Nishiguchi, Radiation Effects, Defects in Solids, 141 (1997) 311.

[149] N. Hashimoto, T. S. Byun, K. Farrell, S. J. Zinkle, J. Nucl. Mater. 329-333 (2004) 947.

[150] R.L. Klueh, N. Hashimoto, M.A. Sokolov, P.J. Maziasz, K. Shiba, S. Jitsukawa, J. Nucl. Mater. 357 (2006) 169.

[151] L.K. Mansur, J. Nucl. Mater. 216 (1994) 97.

[152] F.A. Garner, M.B. Toloczko, B.H. Sencer, J. Nucl. Mater. 276 (2000) 123.

[153] S.I. Golubova, B.N. Singh, H. Trinkaus, J. Nucl. Mater. 276 (2000) 78.

[154] N. Hashimoto, T.S. Byun, K. Farrell, J. Nucl. Mater. 351 (2006) 295.

[155] K. Shiraishi, K. Fukaya, Y. Katano, J. Nucl. Mater. 54 (1974) 275.

[156] G.E. Lucas, J. Nucl. Mater. 206 (1993) 287.

[157] M. Victoria, N. Baluc, C. Bailat, Y. Dai, M.I. Luppo, R. Schäublin, B. N. Singh, J. Nucl. Mater. 276 (2000) 114.

[158] T.S. Byun, K. Farrell, J. Nucl. Mater. 326 (2004) 86.

[159] D.L. Porter, F.A. Garner, J. Nucl. Mater. 159 (1988) 114.

[160] Yu.N. Osetsky, D.J. Bacon, A. Serra, B.N. Singh, S.I. Golubov, J. Nucl. Mater. 276 (2000) 65.

[161] R.E. Stoller, J. Nucl. Mater. 276 (2000) 22.

[162] M. Kiritani, J. Nucl. Mater. 216 (1994) 200.

[163] K.C. Russell, R.W. Powell, Acta Met. 21 (1973) 187.

[164] M.R. Hayns, J. Nucl. Mater. 56 (1975) 267.

[165] C. Cawthorne, E. Fulton, Nature 216 (1967) 576.

[166] K.C. Russell, Acta Mater. 19 (1971) 753.

[167] R.W. Powell, K.C. Russell, Rad. Effect 12 (1972) 127.

[168] N.H. Packan, K. Farrell, J.O. Stregler, J. Nucl. Mater. 78 (1978) 143.

[169] K.C. Russell, Acta Mater. 26 (1979) 1615.

[170] H. Wiedersich, J.L. Katy, Adv. Colloid Interface Sci. 10 (1979) 33.

[171] J.L. Kata, H. Wiedersich, J. Nucl. Mater. 46 (1973) 41.

[172] K.C. Russell, Acta Met. 20 (1972) 899.

[173] A.D. Brailsford, R. Bullough, J. Nucl. Mater. 44 (1972) 121.

[174] A.G. Tyurin, Protection of Metals, 40 (2004) 240.

[175] S.I. Porollo, Yu. V. Konobeev, A.M. Dvoriashin, V.M. Krigan, F. A. Garner, 10th International Conference on Environmental Degradation of Materials in Nuclear Power Systems - Water Reactors, CD format, Lake Tahoe, Nevada, 2001.

[176] J.L. Brimhall, H.E. Kissinger, G.L. Kulcinski, In: Proceedings of Radiation-Induced Voids in Metals, CONF-710601, USAEC Technical Information Center, Oak Ridge, 1972.

[177] J.I. Cole, T.R. Allen, H. Kusanagi, K. Dohi, J. Ohta, Mat. Res. Soc. Symp. Proc. 650 (2001) R292.

[178] B.N. Singh, A.J.E. Foreman, H. Trinkaus, J. Nucl. Mater. 283-287 (1997) 103.

[179] R.E. Stoller, S.J. Zinkle, J. Nucl. Mater. 283-287 (2000) 349.

[180] F. Kroupa, P.B. Hirsch, Discuss. Faraday Soc. 38 (1964) 49.

[181] A. Seeger, On the Theory of Radiation Damage, Radiation Hardening. In: Proceedings of the Second United Nations International Conference on the Peaceful Uses of Atomic Energy, Geneva, United Nations, New York, 1958.

[182] G.S. Was, T.R. Allen, Mater. Character. 32 (1994) 239.

[183] S. M. Bruemmer, G. S. Was, J. Nucl. Mater. 216 (1994) 348.

[184] W.R. Grove, Phil. Trans. Roy. Soc. 142 (1852) 87.

[185] W. Eckstein, Surf. Inter. Anal. 14 (1989) 799.

[186] Y. Yamamura, Y. Itikawa, N. Itoh, Report IPPJ-AM-26, Institute of Plasma Physics, Nagoja University, Japan, (1983).

[187] H.F. Winters, H. Coufal, C.T. Rettner, D.S. Bethune, Phys. Rev. B 41 (1990) 6240.

[188] Institute of Materials & Machine Mechanics, Slovak Academy of Sciences, http://www.umms.sav.sk/index.php?ID=415, July 1, 2009

[189] S.M. Rossnagel, J. Vac. Sci. Technol. A 21 (2003) S74.

[190] J. A. Thornton, Alan S. Penfold, in Thin Film Processes, Academic Press, New York, 1978.

[191] D.B. Williams, C. B. Carter, Transmission Electron Microscopy, Plenum Press, New York, 1996.

[192] Atomic World, Department of Physics, The Chinese University of Hong Kong, http://www.hk-phy.org/atomic_world/tem/tem02_e.html, July 1, 2009

[193] Z.P. Luo, Lecture of Adv. TEM, BIOL 603, Texas A&M University, College Station, 2007

[194] W.D. Callister, Jr., Materials Science, Engineering: An Introduction, Sixth Edition, John Wiley & Sons, Inc., Hoboken, NJ, 2003.

[195] S. Baker, N. Burnham, 2000 MRS Fall meeting Tutorial Program, Symposium Q: Fundamentals of Nanoindentation, Nanotribology. Boston, MT, 2000.

[196] Czech and Slovak Crystallographic Association, (CSCA), http://www.xray.cz/xray/csca/kol2005/abst/ctvrtlik_files/image008.gif, July 1, 2009

[197] ASTM standard E 18, E10, E 92, E 384, "Standard Test Method for Rockwell Hardness, Brinell Hardness, Vickers Hardness, Microhardness of metallic materials"

[198] ISO 14577-12002, Metallic materials --- Instrumented Indentation Test for Hardness, Materials Parameters, International Standard.

[199] S.I. Bulychev, V.P. Alekhin, Zavodskaya Laboratoriya, 53 (1987) 76.

[200] M.F. Doerner, W.D. Nix, J. Mater. Res. 1 (1986) 601.

[201] W.C. Oliver, G.M. Pharr, J. Mater. Res. 7 (1992) 1564.

[202] J.B. Pethica, W.C. Oliver, Physica Scripta T19 (1987) 61.

[203] T.J. Bell, M.V. Swain, Thin Solid Films 220 (1992) 289.

[204] J.S. Field, M.V Swain, J. Mater. Res. 8 (1993) 297.

[205] The A-Z Nanotechnology, Nahttp://www.azonano.com/details.asp?ArticleID=1994, July 1, 2009

[206] G. Shafirstein, M. Gee, S. Osgerby, S. Saunders, Mater. Res. Soc. Symp. Proc. 356 (1995) 717.

[207] S.P. Baker, T.W. Barbee Jr, W.D. Nix, Mater. Res. Soc. Symp. Proc. 239 (1992) 319.

[208] W.D. Nix, H. Gao, J Mech Phys Solids 46 (1998) 411.

[209] Y. Huang, Z. Xue, H. Gao, W.D. Nix, Z.C. Xia, J. Mater. Res. 15 (2000)1786.

[210] Fischerscope HM200 Microhardness Measurement System Manual, Version 1.0, Fischer, 2003.

[211] E.G. Fu, Nan Li, A. Misra, R. Hoagland, H. Wang, X. Zhang, Mater. Sci. Eng. A 493 (2008) 283.

[212] N. Panich, Y. Sun, Surf. Coat. Technol. 182 (2004) 342.

[213] The Materials Characterization Facility (MCF), Texas A&M University (TAMU), Mhttp://mcf.tamu.edu/instruments/cleanroom, July 1, 2009

[214] J.D. Wood, A.J. Griffin, J.D, Embury, R. Zhou, M.Nastasi,, M.Veron, J. Mech. Phys. Solids 44 (1996) 737.

[215] K. Adachi, S. Tsubokawa, T. Takeuchi,, H.G. Suzuki, J. Jpn. Inst. Met. 61 (1997) 397.

[216] W.A. Spitzig, A.R. Pelton, F.C. Laabs, Acta Metall. 35 (1987) 2427.

[217] B.M. Clements, H. Kung, S.A. Barnett, MRS Bull. 24 (1999) 20.

[218] W.D. Nix, Mater. Sci. Eng. A 234-236 (1997) 37.

[219] D.J. Srolovitz, S.M. Yalisove, J.C. Bilello, Metall. Trans. A 26 (1995) 1805.

[220] S.V. Kamat, J.P. Hirth, B. Carnahan, Scr. Metall. Mater. 21 (1987) 1587.

[221] S.L. Lehoczky, J. Appl. Phys. 49 (1978) 5479.

[222] V.G. Gryaznov, V.A. Solov'ev, L.I.Trusov, Scr. Metall. Mater. 24 (1990) 1529.

[223] P.M. Anderson, I.H. Lin, R. Thomson, Scr. Metall. Mater. 27 (1992) 687.

[224] M. Shinn, L. Hultman, S.A. Barnett, J. Mater. Res. 7 (1992) 901.

[225] J.C.M. Li, G.C.T. Liu, Phil. Mag. 15 (1967) 1059.

[226] R.W. Amstrong, Y.T. Chou, R.M. Fisher, N. Louat, Phil. Mag. 14 (1966) 943.

[227] H.W. Liu, Q. Gao, Theor. Appl. Fract. Mech. 12 (1990) 195.

[228] J.G. Sevillano, in Plastic Deformation, Fracture of Materials, Materials Science, Technology- A comprehensive Treatment, Vol. 6, VCH, New York, 1993.

[229] F.R. de Boer, R. Boom, W.C.M. Mattens, A.R. Miedema, A.K. Niessen, Cohesion in Metal: Transition Metal Alloys, North-Holland, Amsterdam, 1989.

[230] S.P. Wen, R.L. Zong, F. Zeng, Y Gao, F. Pan, Acta Mater. 55 (2007) 345.

[231] R.G. Hoagland, J.P. Hirth, A. Misra, Phil. Mag. 86 (2006) 3537.

[232] D. Baral, J. E. Hilliard, J.B. Ketterson, K. Miyano, J. Appl. Phys. 53 (1982) 3552.

[233] L. Fournier, B.H. Sencer, G.S. Was, E.P. Simonen, S.M. Bruemmer, J. Nucl. Mater. 321 (2003) 192.

[234] T. Leguey, N. Baluc, R. Schäublin, M. Victoria, J. Nucl. Mater. 307-311 (2002) 696.

[235] T.R. Allen, J.I. Cole, C.L. Trybus, D.L. Porter, H. Tsai, F. Garner, E.A. Kenik, T. Yoshitake, Joji Ohta, J. Nucl. Mater. 348 (2006) 148.

[236] T. F. Morgeneyer, M.J. Starink, I. Sinclair, Acta Mater. 56 (2008) 1671.

[237] H. Trinkaus, B.N. Singh, J. Nucl. Mater. 323 (2003) 229.

[238] J. Carter, E.G. Fu, G. Bassiri, B.M. Dvorak, N. D. Theodore, G. Xie, D.A. Lucca, M. Martin, M. Hollander, X. Zhang, L. Shao, Nucl Instrum Meth B 267 (2009) 1518.

[239] F. A. Garner, B. Oliver, L.R. Greenwood, M.R. James, P.D. Ferguson, S.A. Maloy, W.F. Sommer, J. Nucl. Mater. 296 (2001) 66.

[240] B.M. Oliver, M.R. James, F.A. Garner, S.A. Maloy, J. Nucl. Mater. 307 (2002) 1471.

[241] I.I. Chernov, A.N. Kalashnikov, B.A. Kalin, S. Yu. Binyukova, J. Nucl. Mater. 323 (2003) 341.

[242] S.A. Fabritsiev, A.S. Pokrovsky, Fusion Engineering, Design, 65 (2003) 545.

[243] E. R. Bradley, R.H. Jones, J. Nucl. Mater. 103-104 (1981) 901.

[244] D. Kaletta, W. Schneider, J. Nucl. Mater. 122-123 (1984) 418.

[245] H. Matsui, K. Abe, S. Hirano, O. Yoshinari, M. Koiwa, J. Nucl. Mater. 133-134 (1985) 615.

[246] H. Takahashi, S. Ohnuki, H. Kinoshita, R. Nagasaki, K. Abe, J. Nucl. Mater. 155-157 (1988) 982.

[247] R.L. Klueh, D.S. Gelles, S. Jitsukawa, A. Kimura, GR Odette, B. van der Schaaf, M. Victoria, J. Nucl. Mater. 307-311 (2002) 455.

[248] T. Hasegawa, Y. Tomita, A.Kohyama, J. Nucl. Mater. 258-263 (1998) 1153.

[249] A. Hishinuma, A. Kohyama, R.L. Klueh, D.S. Gelles, W. Dietz, K. Ehrlich, J. Nucl. Mater. 258-23 (1998) 193.

[250] R.L. Klueh, K. Ehrlich, F. Abe, J. Nucl. Mater. 191-194 (1992) 116.

[251] K. Ehrlic, K. Anderko, J. Nucl. Mater. 171 (1990) 139.

[252] G.R. Odette, M.J. Alinger, B.D.Wirth, Annu. Rev. Mater. Res. 38 (2008) 471.

[253] M. Rose, A.G. Balogh, H. Hahn, Mater Sci Forum 248-249 (1997) 213.

[254] M. Rose, A.G. Balogh, H. Hahn, Nucl. Meth. Phys. Res. B 127-128 (1997) 119.

[255] Y. Chimi, A. Iwase, N. Ishikawa, M. Kobiyama, T. Inami, S.Okuda, J. Nucl. Mater. 297 (2001) 355.

[256] M. T. Robinson, J. Nucl. Mater. 216 (1994) 1.

[257] T. Hochbauer, A. Misra, K. Hattar, R.G. Hoagland, J. Appl. Phys. 98 (2005) 123516.

[258] X. Zhang, Nan Li, O. Anderoglu, H Wang, J.G. Swadener, T. Hochbauer, A Misra, R.G. Hoagland, Nucl. Meth. Phys. Res. B 261 (2007) 1129.

[259] M.J. Demkowicz, R.G. Hoagland, J.P. Hirth, Phys. Rev. Lett. 100 (2008) 136102.

[260] E.G. Fu, J. Carter, G. Swadener, A. Misra, L. Shao, H. Wang, X. Zhang, J. Nucl. Mater. 385 (2009) 629.

[261] H. Westendorp, Z-L. Wang, F.W. Saris, Nucl. Instrum. Meth. 194 (1982) 453.

[262] M. van Rossum, U. Shreter, W.L. Johnson, M. -A. Nicolet, Mater. Res Soc. Symp. Proc. 27 (1981) 127.

[263] Nan Li, E.G. Fu, H. Wang, A. Misra, R. G. Hoagland, J. J. Carter, M. Martin, L. Shao, X. Zhang, Nanostructure, J. Nucl. Mater. 389 (2009) 233.

[264] Nan Li, M.S. Martin, O. Anderoglu, A. Misra, L. Shao, H. Wang, X. Zhang, J. Appl. Phys. 105 (2009) 123522.

[265] X. Zhang, A. Misra, H. Wang, T.D. Shen, M. Nastasi, T.E. Mitchell, J.P Hirth, R.G. Hoagland, J. D. Embury, Acta Mater. 52 (2004) 995.

[266] X. Zhang, A. Misra, J. Appl. Phys. 96 (2004) 7173.

[267] H Trinkaus, J. Nucl. Mater. 318 (2003) 234.

[268] E Alonso, M.-J. Caturla, Díaz de la Rubia, J.M. Perlado, J. Nucl. Mater. 276 (2000) 221.

[269] A. Misra, M.J. Demkowicz, X. Zhang, R.G. Hoagland, JOM 59 (2007) 62.

[270] J.P. Hirth, J. Lothe, Theory of Dislocations, McGraw-Hill, New York, 1968.

[271] R. L. Mills, D.H. Lievenbergy, J.C. Bronson, Phys. Rev. B 21 (1980) 5137.

[272] A. Driessen, E. van der Poll, Phys. Rev. B 33 (1986) 3269.

[273] S.E. Donnelly, Radiation Effect 90 (1985) 1.

[274] G.R. Odette, D. Frey, J. Nucl. Mater. 85-86 (1979) 817.

[275] J. Friedel, Dislocations, Pergamon, New York, 1964.

[276] H. Ullmaier, E. Camus, J. Nucl. Mater. 251 (1997) 100.

[277] J.D. Hunn, E.H. Lee, T.S. Byun, L.K. Mansur, J. Nucl. Mater. 282 (2000) 131.

[278] E.H. Lee, T.S. Byun, J.D. Hunn, K. Farrell, L.K. Mansur, J. Nucl. Mater. 296 (2001) 183.

[279] S.J. Zinkle, Y. Matsukawa, J. Nucl. Mater. 329-333 (2004) 88.

[280] H.L. Heinisch, B. N. Singh, J. Nucl. Mater. 271-272 (1999) 46.

[281] Y. Satoh, I. Ishida, T. Yoshiie, M. Kiritani, J. Nucl. Mater. 155-157 (1988) 443.

[282] M.J. Makin, F.J. Minter, Acta Metall, 8 (1960) 691.

[283] T.H. Blewitt, R.R. Coltman, R.E. Jamison, J.K. Redman, J. Nucl. Mater. 2 (1960) 277.

[284] K. Farrell, T.S. Byun, J. Nucl. Mater. 150 (1987) 140.

[285] J.F Smith, Bulletin Alloy Phase Diagram, 6 (1985) 268.

[286] P. Troche, J. Hoffmann, K. Heinemann, F. Hartung, G. Schmitz, H.C. Freyhardt, D. Rudolph, J. Thieme, Guttmann, Thin Solid Films 353 (1999) 33.

[287] R. Venkatraman, J.C. Bravman, J. Mater. Res. 7 (1992) 2040.

[288] C.V. Thompson, J. Mater. Res. 8 (1993) 237.

[289] X. Zhang, A. Misra, H. Wang, A. L. Lima, M. F. Hundley, R. G. Hoagland, J . Appl. Phys. 97 (2005) 094302.

[290] E. Lugscheider, S. Bärwulf, C. Barimani, Surf. Coat. Technol. 120-121 (1999) 458.

VITA

Name: Engang Fu

Address: Department of Mechanical Engineering

Materials Science and Engineering Program

3123 TAMU

College Station, TX 77843-3123

Email Address: fuengang@gmail.com

Education:

B.E. Materials Science and Engineering
Dalian University of Technology, July 1997

M.E. Mechanical Engineering
Tsinghua University, July 2003

M.Phil. Physics
The University of Hong Kong, December 2006

Ph.D. Materials Science and Engineering
Texas A&M University, August 2009

The typist for this dissertation was Engang Fu.